

ALMA MATER STUDIORUM  
UNIVERSITÀ DEGLI STUDI DI BOLOGNA

---

Dipartimento di Fisica e Astronomia

DOTTORATO DI RICERCA IN  
ASTROFISICA

Ciclo XXX

Tesi di Dottorato

**“OFF PISTE” BEYOND THE DISC OF THE MILKY WAY:  
STRUCTURE OF THE STELLAR HALO AND DYNAMICS OF NEARBY  
DWARF GALAXIES**

**Presentata da: Giuliano Iorio**

**Coordinatore Dottorato:  
Francesco Rosario Ferraro**

**Supervisore:  
Carlo Nipoti**

**Co-supervisor:  
Filippo Fraternali  
Giuseppina Battaglia**

Esame finale anno 2018

---

Settore Concorsuale: 02/C1 – Astronomia, Astrofisica, Fisica della Terra e dei Pianeti  
Settore Scientifico Disciplinare: FIS/05 – Astronomia e Astrofisica



# Contents

<b>Contents</b>	<b>iii</b>
<b>1 Introduction</b>	<b>1</b>
1.1 A Universe of galaxies . . . . .	3
1.1.1 Galaxy Zoo . . . . .	3
1.1.2 Galaxy formation and evolution . . . . .	6
1.2 The stellar halo of the Milky Way . . . . .	7
1.2.1 Formation scenarios . . . . .	9
1.3 The HI in dwarf irregular galaxies . . . . .	12
1.3.1 The HI emission line . . . . .	13
1.3.2 HI disc kinematics: observations . . . . .	16
1.3.3 HI disc kinematics: the tilted-ring model . . . . .	18
1.3.4 HI disc kinematics: rotation curve . . . . .	20
1.4 This Thesis . . . . .	22
<b>2 First all-sky view of the Galactic halo</b>	<b>25</b>
2.1 The RR Lyrae Sample . . . . .	27
2.1.1 <i>Gaia</i> Data release 1 . . . . .	27
2.1.2 RR Lyrae in <i>Gaia</i> DR1 . . . . .	28
2.2 Distribution of the RRLs in the inner stellar Halo . . . . .	38
2.2.1 A first <i>Gaia</i> look at the stellar halo . . . . .	38
2.2.2 Setting the frame of reference . . . . .	39
2.2.3 Density distribution of the halo RRLs . . . . .	40
2.3 Model fitting . . . . .	46
2.3.1 Clean sample . . . . .	46
2.3.2 Halo models . . . . .	47
2.3.3 Comparing models with observations . . . . .	50
2.3.4 Results . . . . .	54

2.4	Discussion . . . . .	62
2.4.1	Best halo model . . . . .	62
2.4.2	Possible sources of bias in the maximum likelihood analysis . .	66
2.4.3	Halo substructures . . . . .	67
2.4.4	Comparison with other works . . . . .	69
2.5	Summary . . . . .	72
2.A	Jacobian . . . . .	75
2.B	Exploration of the parameters space . . . . .	76
<b>3</b>	<b>Kinematics of dwarf irregulars</b>	<b>77</b>
3.1	The Data . . . . .	78
3.1.1	Sample selection . . . . .	78
3.1.2	The Data . . . . .	80
3.2	<sup>3D</sup> BAROLO . . . . .	80
3.2.1	Assumptions . . . . .	82
3.3	Data Analysis . . . . .	83
3.3.1	HI total map . . . . .	83
3.3.2	Datacube fit . . . . .	86
3.3.3	The final circular velocity . . . . .	91
3.4	Results and discussion . . . . .	93
3.4.1	Notes on individual galaxies . . . . .	94
3.4.2	Comparison to the standard 2D approach . . . . .	99
3.5	Summary . . . . .	102
3.A	Atlas and Data . . . . .	103
3.A.1	Atlas . . . . .	103
3.A.2	Data . . . . .	122
3.B	An alternative scenario for DDO 216 . . . . .	134
3.C	Typical setup for <sup>3D</sup> BAROLO . . . . .	137
<b>4</b>	<b>Beyond Flatland: the thickness of the HI disc in dwarf irregulars</b>	<b>139</b>
4.1	Effect of the HI thickness on observables . . . . .	141
4.1.1	Datacube models . . . . .	141
4.1.2	Comparing thick and thin disc models . . . . .	142
4.2	An original method to account for gas thickness . . . . .	149
4.2.1	Theoretical background . . . . .	149
4.2.2	The method . . . . .	153
4.2.3	Tests . . . . .	162

4.3	Application to real galaxies . . . . .	163
4.3.1	The sample . . . . .	163
4.3.2	Results . . . . .	163
4.3.3	Testing working assumptions . . . . .	167
4.3.4	Understanding the HI emission near the minor axis . . . . .	169
4.4	Conclusions . . . . .	171
<b>5</b>	<b>Scaling relations of dwarf irregulars</b>	<b>173</b>
5.1	Test of the baryonic Tully-Fisher relation . . . . .	175
5.1.1	Estimate of the characteristic velocity and baryonic mass . . .	175
5.1.2	Results . . . . .	177
5.2	Test of the radial acceleration relation . . . . .	179
5.2.1	Estimate of the observed and baryonic acceleration . . . . .	180
5.2.2	Results and discussions . . . . .	182
5.3	What is feeding the turbulence? . . . . .	185
5.3.1	Star formation rate data . . . . .	186
5.3.2	Velocity dispersion . . . . .	187
5.3.3	Kinetic energy . . . . .	188
5.3.4	Kinetic energy from SN explosions . . . . .	190
5.4	Summary . . . . .	193
5.A	Rotation curve generated by the HI distribution . . . . .	194
<b>6</b>	<b>Concluding remarks</b>	<b>199</b>
6.1	Summary . . . . .	199
6.2	Related works . . . . .	201
6.3	Waiting for <i>Gaia</i> DR2 . . . . .	203
	<b>Bibliography</b>	<b>205</b>



# Chapter 1

---

## Introduction

If we embark on a journey beyond the disc of the Milky Way, we encounter a variety of interesting objects including the nearest galaxies that form the so-called Local Group as shown in Fig. 1.1. Within 100 kpc from the Sun, we can observe stars and globular clusters belonging to the diffuse stellar halo surrounding our Galaxy, in this same range and slightly farther away ( $< 300$  kpc) a number of dwarf spheroidal galaxies stream around the Milky Way (e.g. Fornax and Sculptor, see Fig. 1.1) together with the Magellanic Clouds (Small and Large Magellanic Clouds, see Fig. 1.1), the closest gas-rich dwarf galaxies. Going a little farther, we find the closest “sister” of the Milky Way, M31 also known as the Andromeda spiral galaxy with its “court” of dwarf spheroidal (e.g. Andromeda I and Andromeda II, see Fig. 1.1) and dwarf elliptical (e.g. M 110 and M 32, see Fig. 1.1) satellites orbiting around. Finally, from  $\sim 500$  kpc to beyond 1 Mpc a number of gas-rich dwarf irregular galaxies live a “solitary” life in a very lower-density environment. The nearest of them, as for example NGC 6822 ( $\sim 500$  kpc), IC 1613 ( $\sim 700$  kpc), WLM ( $\sim 1$  Mpc), DDO 210 (Aquarius dwarf,  $\sim 2$  Mpc) and DDO 216 (Pegasus dwarf,  $\sim 2$  Mpc) are shown in Fig. 1.1. These galaxies and their components (e.g. the stellar halo of the Milky Way or the gaseous discs of the dwarf irregulars) represent the nearest objects that we can study outside the disc of the Milky Way. Because of their vicinity, we can study them in great detail and this should facilitate our understating of how they

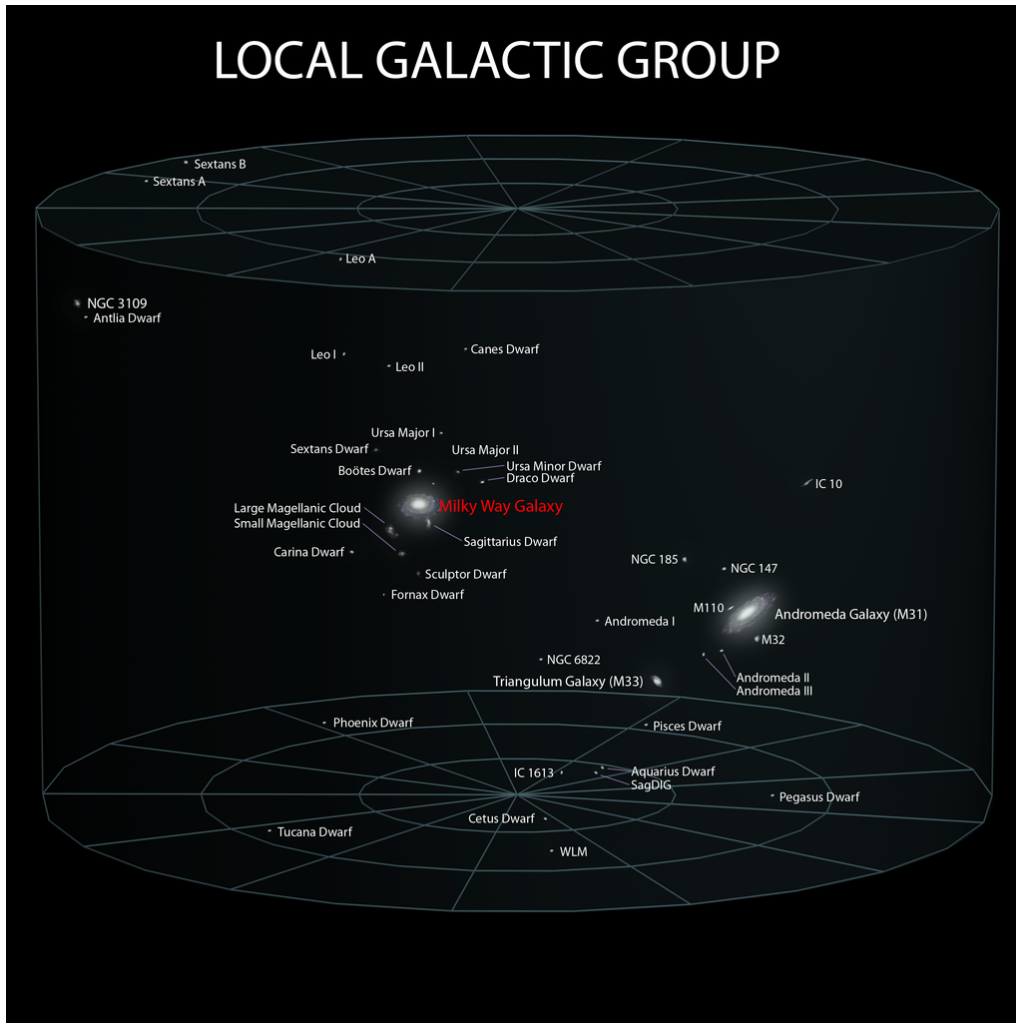


**Figure 1.1:** Spatial distribution of the galaxies in the Local Group. The distance between the Milky Way and Adromeda is 0.78 Mpc. Sagittarius dwarf, the nearest neighbour of the Milky Way, is at a distance of 0.02 Mpc from the Galaxy, while the distance between WLM and the Milky Way is 1 Mpc. Credit: Andrew Z. Colvin

form and evolve. Moreover, they can help us to interpret what we see, with lower level of details, in most distant objects.

The stellar halo of the Milky contains extremely old ( $\sim 12$  billion year) and metal-poor stars (Carollo et al., 2007) distributed both smoothly in a spheroidal volume around the Galactic disc (e.g. Deason, Belokurov & Evans 2011; Xue et al. 2015; Das, Williams & Binney 2016; Iorio et al. 2017a) and “clustered” in substructures (e.g. Helmi et al. 1999; Newberg et al. 2002; Belokurov et al. 2006). These stars are fossils of the time when our Galaxy formed, in particular the halo substructures are likely remnants of the past interactions of the Milky Way with smaller galaxies. Therefore, studying the distribution of the stars in the halo is important to understand the processes which led to the formation of the Galactic stellar halo and to

unravel the evolutionary history of the Milky Way (Helmi et al., 1999; Helmi, 2008).

The dwarf irregular galaxies are tiny gas-rich galaxies with ongoing star formation activity. Given that they are preferentially located in the outskirts of galaxy groups and in the field, the study of these objects is fundamental to understand how a galaxy can evolve in a low-dense environment with a small number of interactions with other objects (e.g. Lelli, Verheijen & Fraternali 2014b; Starkenburg, Helmi & Sales 2016). Another fundamental property is that these systems are the smallest galaxies harbouring a HI disc. The kinematics of the HI discs is one of most powerful tool to trace the total distribution of matter in the galaxies (Bosma, 1978; van Albada et al., 1985; Begeman, 1987; Swaters, 1999; de Blok et al., 2008; Oh et al., 2015). Therefore, the analysis of such discs is fundamental to test the prediction of the cosmological models at the extreme low-mass end of the galaxy mass function (e.g. Brook, Santos-Santos & Stinson 2016; Read et al. 2017; Sales et al. 2017).

In this thesis, we focus on the study of the stellar distribution in the inner parts of the Galactic stellar halo and on the study of the kinematics and dynamics of a sample of dwarf irregular galaxies. In the first case, we exploited the unprecedented dataset of the first data release of the *Gaia* satellite (Gaia Collaboration et al., 2016b). In the second case, we exploited the high resolution HI data obtained from the survey LITTLE THINGS (Hunter et al., 2012) and state-of-the-art techniques to analyse the HI discs of a sample of dwarf irregular galaxies.

In this Chapter, we briefly introduce our work. In Sec. 1.1, we summarise the properties and the differences among the observed galaxy types and the current theories of galaxy formation and evolution of galaxies. Then, in Sec. 1.2 and in Sec. 1.3, we introduce the Galactic stellar halo and the study of the HI emission in dwarf irregular galaxies, respectively. Finally, in Sec. 1.4, we outline the structure and the content of this thesis.

## 1.1 A Universe of galaxies

### 1.1.1 Galaxy Zoo

The first comprehensive classification of the galaxies in the Universe was made by Hubble (1936) through the so-called Hubble sequence (Fig. 1.2). Despite its name, this classification scheme does not imply an evolutive sequence from the left to right or vice-versa. It is a pure morphological classification going from the homogeneously smooth, feature-less elliptical galaxies (often referred to as early-type galaxies) and ending with spiral galaxies frequently exhibiting spiral arms and/or bars (also known as late-type galaxies). The morphological differences mark also different physical properties. In fact, the dichotomy between early-type galaxies and late-type galaxies is considered a benchmark of any galaxy formation and evolution theory, and it has

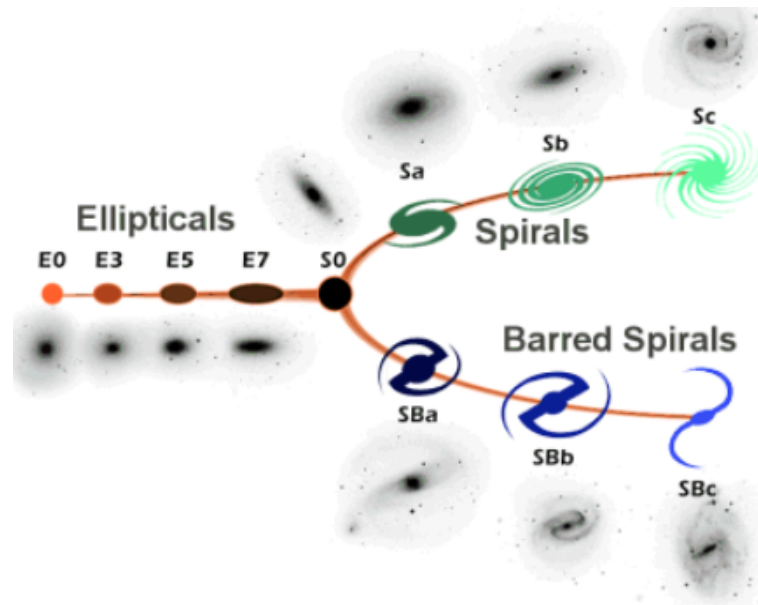


**Figure 1.2:** Schematic view of the Hubble classification of galaxies (Hubble, 1936). The elliptical galaxies are classified as  $En$  where  $n$  is related to the observed axial ratio  $q$  by  $q = 1 - n/10$ , hence E0 indicates a spherical shape and E7 an elliptical shape with axial ratio  $q = 0.3$ . The spiral galaxies are classified considering the presence (indicated with the capital B, bottom sequence) or the absence (top sequence) of a bar. Then, they are classified with the letters a,b,c considering the disc to bulge ratio and the opening angle of the spiral arms (both increasing from the left (Sa) to the right (Sc)). Credit: <https://www.wvu.edu/skywise/astronomy101.html>

been shown to be closely linked with other galactic properties such as stellar mass, halo mass, bolometric luminosity, black hole activity, galaxy size, and the relative ages of the stellar populations (Willett et al. 2017 and references therein).

Nowadays, more physical classification criteria have been proposed (e.g. Kormendy & Bender 2012; Romanowsky & Fall 2012), however the Hubble sequence remains a valid support to present the main properties of the galaxies observed in the local Universe.

Following Fig. 1.2 from the left to the right we find the following objects.

- **Elliptical galaxies:** these objects are smooth, featureless stellar systems containing little or no cool interstellar gas and with, in general, no significant stellar disc. The stars in these galaxies are old and metal-rich, compatible with the fact that these galaxies are likely to have formed most of their stars in a rapid star formation burst more than 10 Gyr ago (see e.g. Nelan et al. 2005; Renzini 2006; Citro et al. 2016). Thus, elliptical galaxies are fossils of the galaxy formation processes happened when the Universe was significantly younger than today.

- **Lenticular galaxies:** these galaxies show an “hybrid” morphology between ellipticals and spirals (see below): they have a predominant bulge and a rapidly rotating stellar disc without spiral structures and without signs of ongoing star formation. It is still a matter of debate whether these galaxies are the product of mergers (e.g. Falcón-Barroso, Lyubenova & van de Ven 2015; Querejeta et al. 2015) or just faded spirals in which the star formation have been halted (e.g. Laurikainen et al. 2010; Williams, Bureau & Cappellari 2010, see also the results of our recent work in Rizzo, Fraternali & Iorio 2017).
- **Spiral galaxies:** these are galaxies, like the Milky Way and M 31 (see Fig. 1.1), that contain a prominent disc composed of stars, gas, and dust. The spiral galaxies are currently forming stars, especially along the filamentary structure of the spiral arms. Most of them contain an inner bulge and/or a bar. At least some of these galaxies, for instance the Milky Way, are surrounded by a diffuse stellar halo (see e.g. Zibetti, White & Brinkmann 2004; Zibetti & Ferguson 2004; Mouhcine et al. 2005; Ibata et al. 2007; Helmi 2008; Harmsen et al. 2017) that can store important information about the galaxy formation history (see Sec. 1.2)

At smaller scales (stellar mass  $\lesssim 10^9 M_{\odot}$ ) the galaxies are defined as dwarf due to their smaller extent with respect to elliptical, spiral and lenticular galaxies. They can be divided in gas-poor quiescent dwarfs and gas-rich star forming dwarfs. Among the first we can find the **dwarf ellipticals** that can be considered the low-mass extensions of elliptical galaxies (Ferguson & Binggeli, 1994) and the **dwarf spheroidals** that have a luminosity similar to the dwarf ellipticals but a much shallower surface brightness (Mateo, 1998). Both these two families of objects show little or no evidence of gas and of star formation activity (McConnachie, 2012). Despite the common quiescent nature and the smooth spheroidal shape they are truly distinct kind of objects (Kormendy & Freeman, 2016). The gas-rich dwarfs are the smallest systems with ongoing star formation activity and they contain a rotating disc of cool gas. However, they do not have bulges or spiral arms. Considering the intensity of the star formation activity, they can be classified as **dwarf irregular galaxies** (dIrrs) with low star formation rates (Hunter & Elmegreen, 2004; Zhang et al., 2012) and **blue compact dwarfs** that can be considered starburst galaxies (Lelli, Verheijen & Fraternali, 2014a), see Sec. 1.3 for further details.

In the Local Group there is a strong spatial segregation between the dIrr and the dSph galaxies. The dSphs are preferentially found as satellites of more massive galaxies while the dIrrs are located in more distant and low-dense regions (Weisz et al., 2011). However, apart from their difference in gas content, dSphs and dIrrs appear to be similar in other properties, and they are probably closely related types of objects (Kormendy & Djorgovski, 1989; Da Costa, 1992; Kormendy & Freeman,

2016). Some scenarios suggest that the dIrrs evolve into dSphs losing their gas as they approach the massive galaxies (e.g. Mayer et al. 2001), while other models assume that these objects are truly distinct at birth and follow different evolutionary paths.

Despite the significant morphological differences, all galaxies are believed to be surrounded by a dark matter halo. This component is not visible, but its presence is needed to explain the observed kinematics in both rotating discs (spirals, dIrrs, e.g. Bosma 1978; Rubin, Ford & Thonnard 1980) and dispersion dominated galaxies (ellipticals, dSphs, e.g. Danziger 1997). In particular, the mass budget of both dSphs and dIrrs are totally dominated by the DM component (see e.g. Battaglia et al. 2008; Walker et al. 2009; Breddels & Helmi 2013; Oh et al. 2015), hence they are perfect DM probes, especially in the case of dIrrs where we can exploit the kinematics of the rotating gaseous disc (see Sec. 1.3). The study of the DM content of galaxies is fundamental to test the predictions of the various cosmological models (e.g. Read et al. 2017).

### 1.1.2 Galaxy formation and evolution

How structures in the Universe form and evolve from a primordial hot and dense state is today reasonably well understood, at least in general terms. After a very rapid phase of expansion called “inflation” (Guth, 1981), the evolution is driven by the gravity and by the presence of random small density fluctuations. Thus, the first stages of the Universe evolution are quite straightforward: the regions with a density higher than the average are able to contrast the expansion and become progressively denser; conversely, in regions with a density lower than the average the expansion proceeds faster and they become less and less dense. The first regions form the seeds of the first structures, while the second regions the seeds of the intergalactic voids. The presence of such primordial fluctuations is not only a theoretical speculation: the fluctuations can be indirectly measured by the anisotropies in the cosmic microwave background and from measurements of the distribution of matter at large scales (e.g. Peebles 1982a; Planck Collaboration et al. 2016a). When the densest regions become dense enough, they start to collapse decoupling from the universal expansion. During the collapse phase, which involves both the dark matter and the baryonic matter, the first proto-structures of the Universe are created. The current concordance cosmological model that describes the formation and the evolution of the Universe is the  $\Lambda$  cold dark matter ( $\Lambda$ CDM) framework (White & Rees, 1978; Peebles, 1982c,b). In this model, the components of the Universe are the dark energy ( $\sim 69\%$ <sup>1</sup>, responsible for the current Universe acceleration of expansion), the DM ( $\sim 26\%$ <sup>1</sup>) and the baryonic matter ( $\sim 5\%$ <sup>1</sup>). In particular, the DM

---

<sup>1</sup> Planck Collaboration et al. (2016b)

is assumed to be composed by massive and weakly interactive particles that had non-relativistic velocities at the time of decoupling from the Universe expansion. The “cold” behavior of the DM particles implies that the first structures to form are the one at the smallest scales; then, the larger structures are formed hierarchically by the merging of the smaller ones (see e.g. Lacey & Cole 1994; Navarro, Frenk & White 1996; Bullock et al. 2001; Ishiyama 2014).

During the collapse, when the gas starts to be dense enough, the first stars form and eventually explode as supernovae (SNe) releasing gas and metals into the interstellar medium. New stars are formed from the new metal-enriched gas and this cycle continues until the reservoir of cool gas runs out due to the internal (e.g. AGN/SNe feedback) or external (e.g. gas removal in dense environments) effects. The detailed understanding of the steps that lead from the collapse of the proto-structures to the creation of the variety of galaxies we see today (Sec. 1.1.1) is one of the main unsolved problem in astrophysics.

The first theory of the galaxy formation was proposed by Eggen, Lynden-Bell & Sandage (1962) and it is known as monolithic collapse. In this scenario, the formation of galaxies occurs very rapidly from the primordial collapsing gas, therefore all the stars of the galaxy are formed “*in situ*”. Few years later, Searle & Zinn (1978) proposed a theory in which galaxies form progressively assembling mass from smaller proto-structures. This last scenario is compatible with the hierarchical growth of structures predicted by  $\Lambda$ CDM. In this context, dwarf galaxies are expected to be the first systems to form, providing the building blocks for the formation of more massive systems through continuous merging and accretions. Therefore, the study of dIrr galaxies, especially of the most metal poor, is very important to understand the properties of the primordial building blocks (e.g. Sacchi et al. 2016). At the same time, the study of the stellar halo of galaxies in general, and of the Milky Way in particular, is useful to discern between different galactic formation scenarios. For example, if most of the stars in the stellar halo are smoothly distributed in space and show a radial gradient and/or a little spread in metallicity, it is likely that mergers have not been too important, at least in the recent time. Conversely, the predominance of clumpy substructures and/or of large spread in stellar metallicity favour a model in which the accretion of smaller structures have had a relevant role in shaping the halo and in the evolution of the galaxies (see Sec. 1.2).

## 1.2 The stellar halo of the Milky Way

The first glimpse of the existence of a stellar halo component in our Galaxy was caught when Roman (1955) found that the high-velocity stars around the Sun are systematically more metal poor than the Sun. Moreover the velocities of these objects imply that their orbits are highly eccentric and/or inclined with respect to

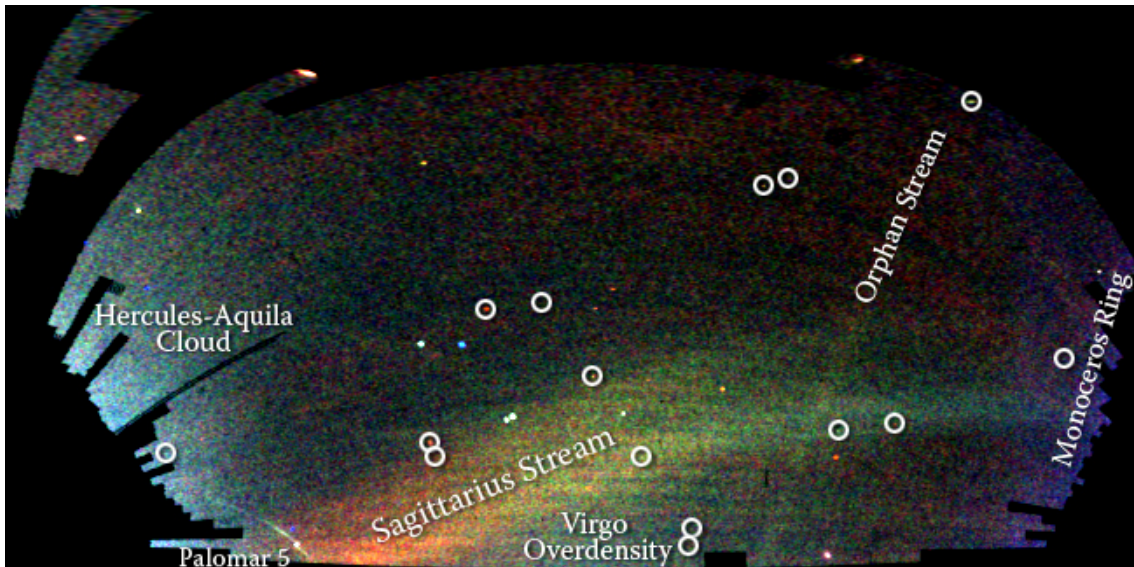


**Figure 1.3:** A map of some halo substructures in the outer part of the Milky Way, derived from the Sloan Digital Sky Survey (SDSS, Abazajian et al. 2009) images of the northern sky and adapted from Belokurov et al. (2006). The image is shown in a Mercator-like projection. The colour indicates the distance of the stars, while the intensity indicates the density of stars on the sky. Structures visible in this map include: streams of stars from the Sagittarius dwarf galaxy, the “orphan” stream (Belokurov et al., 2007b; Newberg et al., 2010), the “Monoceros Ring” that encircles the Milky Way disk (Newberg et al., 2002), trails of stars being stripped from the globular cluster Palomar 5 (Odenkirchen et al., 2001), and excesses of stars found towards the constellations Virgo and Hercules (Jurić et al., 2008; Vivas et al., 2001; Belokurov et al., 2007a). Circles enclose new Milky Way companions discovered by the SDSS; two of these are faint globular clusters, while the others are faint dwarf galaxies. Credit: V. Belokurov and the SDSS.

the plane in which the circular orbit of the Sun lies. Years later, Eggen, Lynden-Bell & Sandage (1962) discovered that among high-velocity stars the metallicity decreases for increasing orbital energy and angular momentum. Given this evidence, they stated that the most metal poor stars reside in a halo-like structure created during the initial stage of the formation of the Milky Way. In the eighties, Zinn (1985) and Armandroff (1989) found a clear bimodality in the metallicity of globular clusters and they advocated the existence of a new component of our Galaxy, different from the disk in both shape and formation history. Nowadays, we know that the stellar halo is a diffuse cloud of stars (and globular clusters) located all around the Milky Way. The stars belonging to the halo are old ( $\sim 13$  Gyr, Sneden et al. 1996; Hill et al. 2002; Frebel et al. 2007) and metal poor. The metallicity distribution peaks around  $[\text{Fe}/\text{H}] \sim -1.6$ , but it has significant tail at low metallicities extended well below  $[\text{Fe}/\text{H}] \sim -3$  (e.g. Ryan & Norris 1991; Carollo et al. 2007). The distribution of stars in the halo can be considered rather smooth, especially in the inner part of the Galaxy (e.g. Deason, Belokurov & Evans 2011; Xue et al. 2015; Das, Williams

& Binney 2016; Iorio et al. 2017a), but a series of substructures and streams are clearly visible spatially (see Fig. 1.3) and/or in the phase space (e.g. Helmi et al. 1999; Newberg et al. 2002; Belokurov et al. 2006). The kinematics inferred from local samples of halo stars indicates that the local halo shows a small amount of prograde rotation ( $V < 50 \text{ km s}^{-1}$ , e.g. Carney et al. 1996; Chiba & Beers 2000; Deason et al. 2017b) and is dominated by the velocity dispersion (Chiba & Beers, 2000).

The stellar halo contains only a very small fraction ( $\lesssim 2\%$ ) of the Galactic light and an even smaller fraction ( $\lesssim 0.2\%$ ) of the total Galactic mass (Bland-Hawthorn & Freeman, 2000). However, the stellar halo can be considered the “alter ego” of the much more massive structure, whose presence is inferred indirectly: the dark matter halo. The two halos emerge alongside each other, sharing the formation mechanism, i.e. a combination of the accretion onto the Galaxy and the subsequent relaxation and phase mixing. In particular the metal poor stars of the halo can be considered “fossil” of the early Galactic formation as nicely explained by Eggen, Lynden-Bell & Sandage (1962): “... a study of these subsystems allow us partially to reconstruct the Galactic past because the time required for stars in the Galactic system to exchange their energies and momenta is very long compared with the age of the Galaxy. Hence knowledge of the present energy and momenta of individual objects tell us something of the initial dynamic conditions under which there were formed.” Given that the stellar halo contributes negligibly to its host gravitational potential, the stars belonging to the halo are also perfect tracers for the DM content. For example, by positing the continuity of the phase-space flow, the dark matter distribution can be inferred if the stellar halo spatial shape is known and complemented by stellar kinematics (see e.g. Jeans 1915; Helmi 2008; Posti et al. 2015; Helmi et al. 2017). Therefore, the study of stellar halo of the Milky Way is important to understand the formation history and evolution of both the baryonic and the DM component of the Galaxy.

### 1.2.1 Formation scenarios

The formation scenarios of the galactic stellar halos in general, and of the stellar halo of the Milky in particular can be roughly classified following the “classical” galactic formation scenarios discussed in in Sec. 1.1.2. In the “monolithic collapse” scenario (Eggen, Lynden-Bell & Sandage, 1962), the stars in the halo are mostly formed during the initial collapse of the gas in the proto-galactic structure; while, in the “hierarchical” scenario (Searle & Zinn, 1978) the stars are deposited continuously in the halo through accretion of smaller structures. These two models are not really in contraposition, rather it is likely that both of them have a role in the formation and evolution of galaxies and their stellar halos (Helmi, 2008). Therefore, as suggested by Helmi (2008), it is more instructive to classify formation models in

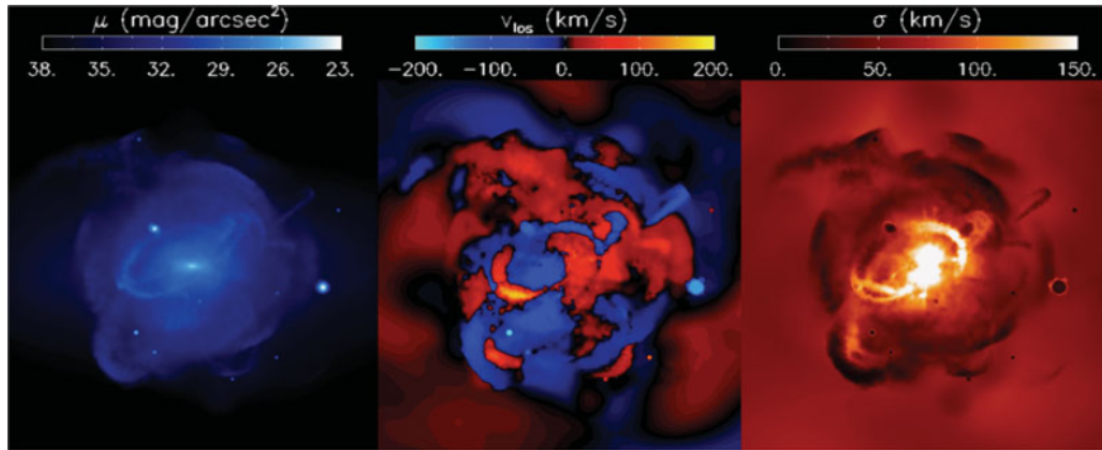


**Figure 1.4:** Surface brightness (**left-hand panel**), line-of-sight velocity (**middle panel**) and line-of-sight velocity dispersion (**right-hand panel**) of a simulation of purely accreted stellar halo from Bullock & Johnston (2005). Each box is  $300 \times 300$  kpc. The central galaxy, containing  $\sim 99\%$  of the stars, is not shown. Credit: Sanjib Sharma, Kathryn Johnston, James Bullock.

dissipative and non-dissipative scenarios: in the first case the stars in the halo are formed during a dissipative process (i.e. the collapse of gaseous clouds), while in the second case the stars are just put in the halo volume without involving dissipative processes. In order to link the information coming from the stellar halo to the theory of galaxy formation and evolution, the formation scenarios can be further classified considering the origin of the single stars (e.g. Johnston 2016). In this case, we can consider *in situ* models in which the stars born in the potential of the Milky Way (e.g. Zolotov et al. 2009) or *ex situ*/accreted models where the stars have an external origin (e.g. Pillepich, Madau & Mayer 2015). The latter case is compatible with the non-dissipative scenario, while the *in situ* stars can have both a dissipative and a non-dissipative origin. In the first case (dissipative) the stars were born in the halo volume from the primordial collapsing gas (as originally supposed by Eggen, Lynden-Bell & Sandage 1962); while, in the second case (non-dissipative) they were born in the disc and then they are “heated” or “kicked-out” in the halo changing significantly their circular-like orbits (e.g. Purcell, Bullock & Kazantzidis 2010). Moreover, there is also the possibility of an hybrid dissipative *in situ/ex situ* scenario in which the gas has an external origin (e.g. accreted through merging) and then the stars are formed inside the stellar halo volume (e.g. the “endo-debris” stars described in Tissera et al. 2013).

Discriminating between different formation models is not straightforward. Each scenario predicts certain stellar halo properties, as for example the spatial distribution of the halo stars or a certain spread or gradient in the stellar metallicity. However, these properties can be strongly degenerate among different scenarios.

For this reason a parallel exploitation of both data from observations and from N-body simulations is needed. For example, it is natural to think that the presence of a break in the density profile of the halo and/or the fact that the halo is more flattened in the outskirts than in the central parts, as is found in many works (e.g. Xue et al. 2015; Das, Williams & Binney 2016), could be the sign of the transition between an *in situ* dominated halo in the inner parts and an accretion dominated halo in the outer parts. However, many simulations of purely accreted stellar halos (see Fig. 1.4) show that a break in the density profile could be a natural consequence of a pure non-dissipative *ex situ* scenario (e.g. Bullock & Johnston 2005; De Lucia & Helmi 2008; Deason et al. 2013; Amorisco 2017). At the same time, pure *in situ* simulations are also able to reproduce to some extent the observed distributions of stars in the inner part of the halo (e.g. Samland & Gerhard 2003; Pérez-Villegas, Portail & Gerhard 2017).

In the outer part of the Milky Way stellar halo, the spatial distribution of the stars is very lumpy favouring a non-dissipative formation scenario via accretion of external galaxies. However, the nature of the accreted objects is still uncertain. In particular, it is still unclear whether the dSphs, like the ones that we see today around the Milky Way, can contribute significantly to the mass of the stellar halo. Although most of the metal-poor stellar halos ( $[\text{Fe}/\text{H}] < -2$ ) can have been accreted from low-mass dwarf galaxies (Deason, Mao & Wechsler, 2016), at higher metallicity the stars in the halo show significant difference with respect to the stellar populations found in dSphs (e.g. Fiorentino et al. 2015). In particular, the halo stars tend to be more  $\alpha$ -enhanced at a given metallicity compared to the stars in the dSphs (e.g. Tolstoy et al. 2006; Letarte 2007). As a consequence, these objects can not have been significant contributors of the mass assembly in the stellar halo (Shetrone, Côté & Sargent, 2001; Tolstoy et al., 2003; Venn et al., 2004; Deason, Mao & Wechsler, 2016). Recent works by Fiorentino et al. (2015) and Deason, Mao & Wechsler (2016) concluded that massive and the metal-rich satellites, such as the Large Magellanic clouds and the Sagittarius dSph, can have contributed to the Galactic halo formation more than classical dwarf spheroidals. In particular, one or two completely destroyed dwarfs with stellar masses between  $10^8 M_{\odot}$  and  $10^{10} M_{\odot}$  could have contributed to the majority of the accreted mass of the stellar halo (Deason, Mao & Wechsler, 2016). In this context, the Milky Way stellar halo is destined to transform dramatically with the dissolution of the debris from the Sagittarius dwarf and the Magellanic Clouds. Another possible scenario is that the building blocks of the halo and the dwarfs we see today are essentially different (Helmi, 2008). The first object can be associated to primordial high-density peaks (see Sec. 1.1.2) that collapse faster and at higher redshifts, while the current dwarf galaxies descend from less peaked density fluctuations with a slower evolution causing a lower level of  $\alpha$  enrichment.

To solve all these puzzles it is fundamental to have high quality data (e.g. phase

space positions, metallicity measurements) sampling the stellar halo from its innermost part ( $\sim 5$  kpc) to its extreme outer parts ( $\sim 100$  kpc). In this context, the forthcoming data from the *Gaia* mission promise prominent breakthroughs in the field. It is likely that, by the end of the mission ( $\sim 2020 - 2021$ ), our understanding of the formation of the Galactic halo and hence of the Milky Way formation will be drastically improved. In this thesis, we started to set the ground for this “revolution” by exploiting the already unprecedented richness of the first *Gaia* data release (see Sec. 1.4).

### 1.3 The HI in dwarf irregular galaxies

Dwarf galaxies are the most numerous galaxies in the Universe (Ferguson & Binggeli, 1994). For example, around the Local Group (Fig. 1.1), about 70% of the galaxies are dwarfs (McConnachie, 2012). The fraction remains this high also considering the Local Volume within 11 Mpc from the Milky Way (Dale et al., 2009). Understanding their structure, formation, and evolution is a fundamental goal for astrophysics and cosmology. Dwarf galaxies are low-mass systems with low surface brightness and, except for the most massive ones, they have low metallicities (Tremonti et al., 2004; Hunter et al., 2012). Among them, the gas-rich dwarf galaxies represent an extraordinary “mine” of information. They can be divided between dwarf irregular galaxies (dIrrs) and blue compact dwarfs (BCDs). The latter have typically higher surface brightness and intense blue colors in the optical band. As already discussed, gas-rich dwarfs are the smallest systems with an ongoing star formation activity, in particular the BCDs can be considered starburst galaxies (Lelli, Verheijen & Fraternali, 2014a). Therefore, dIrrs and BCDs are perfect laboratories to understand the physics of the star formation in the most extreme conditions, namely low metallicity, low content of molecular gas and no evident star formation triggers (e.g. Lelli, Verheijen & Fraternali 2014b; Starkenburg, Helmi & Sales 2016).

The interstellar medium of these galaxies is dominated by the presence of the atomic hydrogen (HI) that is extended well beyond the optical disc. While it was clear since the first observations that the HI medium in spiral galaxies is settled in a rotating disc, the situation for dIrrs/BCDs was initially more uncertain. Some dwarf galaxies studied in the early 1960s with single-dish radio telescopes showed sign of rotation (e.g. Volders & Högbom 1961; Epstein 1964), others did not (e.g. Roberts 1962). The advent of the radio interferometers, as the Westerbork Synthesis Radio Telescope, improved drastically the spatial resolution of the observations allowing to study the kinematics of the HI in dIrrs with unprecedented details. Nowadays, the modern interferometers, such as the Very Large Array or the Giant Metrewave Radio Telescope, have the sensitivity and the spatial resolution needed to detect and analyse in detail the HI discs of even the smallest dwarf galaxies (e.g. Begum et al.

2008b; Hunter et al. 2012). Based on several studies, the general picture emerged that also dIrrs host rotating HI discs, but they have a lower rotation amplitude with respect to the spirals and they have slowly rising rotation curves (e.g. Shostak 1974; Tully et al. 1978; Swaters 1999; Lelli, Verheijen & Fraternali 2014a; Oh et al. 2015; see also Fig. 1.8).

The presence of a rotating disc is a unique tool to investigate the dynamics and the content of dark matter of galaxies. The dIrrs, which are one of the focuses of this thesis, usually have a less “disturbed” HI kinematics with respect to the BCDs (Swaters, 1999; Lelli, Verheijen & Fraternali, 2014a), so they can be used to estimate quite robustly the galactic potential. Therefore, dIrrs represent also unique cosmological probes to test the predictions of the cosmological models at the low-mass end of the galaxy mass function. In this Section, we briefly introduce the physics behind the HI emission line from dIrr gaseous discs and the information that we can derive from it.

### 1.3.1 The HI emission line

Hydrogen is the most abundant element in the Universe: it is located in the stars, in the interstellar medium (ISM) and in the intergalactic medium (IGM). In the ISM of the galaxies, hydrogen is present in the thermal phases described below (Field, Goldsmith & Habing, 1969; Wolfire et al., 1995, 2003).

- Hot: in this phase the hydrogen is totally ionized (HII) and very hot ( $T \geq 10^6$  K) and diffuse ( $n \leq 10^{-2} \text{ cm}^{-3}$ ). This temperature can be reached as a consequence of a SN explosion or in the diffuse coronae around galaxies.
- Warm: in this phase the temperature ranges from 6000 K to 10000 K and the density is  $n \sim 0.1 - 1 \text{ cm}^{-3}$ . This hydrogen can be both ionized, by radiation from young stars (HII regions) or from the background radiation field, and neutral (warm neutral medium, WNM), heated by background radiation fields.
- Cold: At temperatures of the order 40 – 100 K the hydrogen is all neutral (cold neutral medium, CNM) and dense ( $n \sim 4 - 80 \text{ cm}^{-3}$ ).
- Molecular: at the lowest temperatures ( $T \leq 50$  K) and highest densities ( $n \geq 10^2 \text{ cm}^{-3}$ ), the hydrogen is found in molecular form ( $\text{H}_2$ ).

Both HII and  $\text{H}_2$  are strongly related to star forming regions, while the HI is more uniformly diffused in all the galaxy. In particular, in dIrrs the HI is settled on discs typically detected well beyond the stellar disc. The molecular gas is irrelevant in the mass budget of dIrrs (Tacconi & Young, 1987; Taylor, Kobulnicky & Skillman, 1998) and in most of the dIrrs the HI medium contains even more mass than the

stellar component (McConnachie, 2012).

In the typical conditions of the ISM, all the neutral hydrogen is in the ground state, so no electronic transitions can occur. However, van de Hulst (1945) theoretically predicted a HI emission line due to the interaction between the spin of the electron  $\vec{S}$  and the angular momentum of the proton  $\vec{I}$ . We can introduce the hyperfine quantum number  $\vec{F} = \vec{I} + \vec{S}$ : in case of parallel  $\vec{I}$  and  $\vec{S}$ ,  $F = 1$ , otherwise  $F = 0$ . The difference of energy from  $F = 1$  to  $F = 0$  leads to an emission line at  $\lambda_{\text{HI}} \simeq 21 \text{ cm}$  ( $\nu_{\text{HI}} \sim 1420 \text{ Mhz}$ ) with a Einstein coefficient of  $2.9 \times 10^{-15} \text{ s}^{-1}$ . This line is strongly forbidden, but the large amount of HI in the ISM of late-type galaxies allows us to detect it easily in the spiral and dIrr galaxies. Few years later, both Ewen & Purcell (1951) and Muller & Oort (1951) confirmed with radio observations the prediction of van de Hulst and the first pioneering work using radio observation with single-dish (e.g. van de Hulst, Raimond & van Woerden 1957; Argyle 1965) and interferometers (e.g. Rogstad & Shostak 1971; Allen, Goss & van Woerden 1973) started to explore the HI properties in the Milky Way and other nearby galaxies.

Radio observations at the wavelengths of the HI emission detect the spin-flip transition of the HI over the radio continuum of the galaxies (e.g. Heesen et al. 2011, 2014). Once the continuum is removed, the final data contain only the line emissions of the HI medium (see e.g. Hunter et al. 2012). The final products of single-dish/interferometers observations of the HI in galaxies are 3D dimensional arrays, typically called “datacubes”. A datacube has two spatial dimensions indicating the position of the emission in the sky and one spectral dimension indicating the actual frequency/wavelength/velocity at which the HI line is emitted due to the Doppler shift (see below). Therefore, each pixel of the datacubes (sometimes called “voxel”), stores the brightness ( $S$ ) of the HI emission (typically in units of  $^2[\text{Jy beam}^{-1}]$ ) at a given position on the sky and at a given frequency/velocity. In practice, a datacube can be read as a collection of HI line profiles at different spatial positions, or as a collection of 2D images, called “channel maps”, that represent the spatial distribution of the emitting source at a given velocity or frequency, namely at a given channel.

Considering the density and the temperature of the HI in the WNM and CNM, the HI emission can be assumed optically thin for column densities of the hydrogen lower than  $\sim 10^{22} \text{ cm}^{-2}$  (Spitzer, 1978; Haynes & Giovanelli, 1984; Watson & Deguchi, 1984), which is generally a value rarely found in dIrrs (Hunter et al., 2012). The negligible amount of HI self-absorption and the lack of dust extinction in the radio band imply that the HI flux can be directly related to the “quantity” of atoms

---

<sup>2</sup>The beam indicates the solid angle of the instrumental beam.

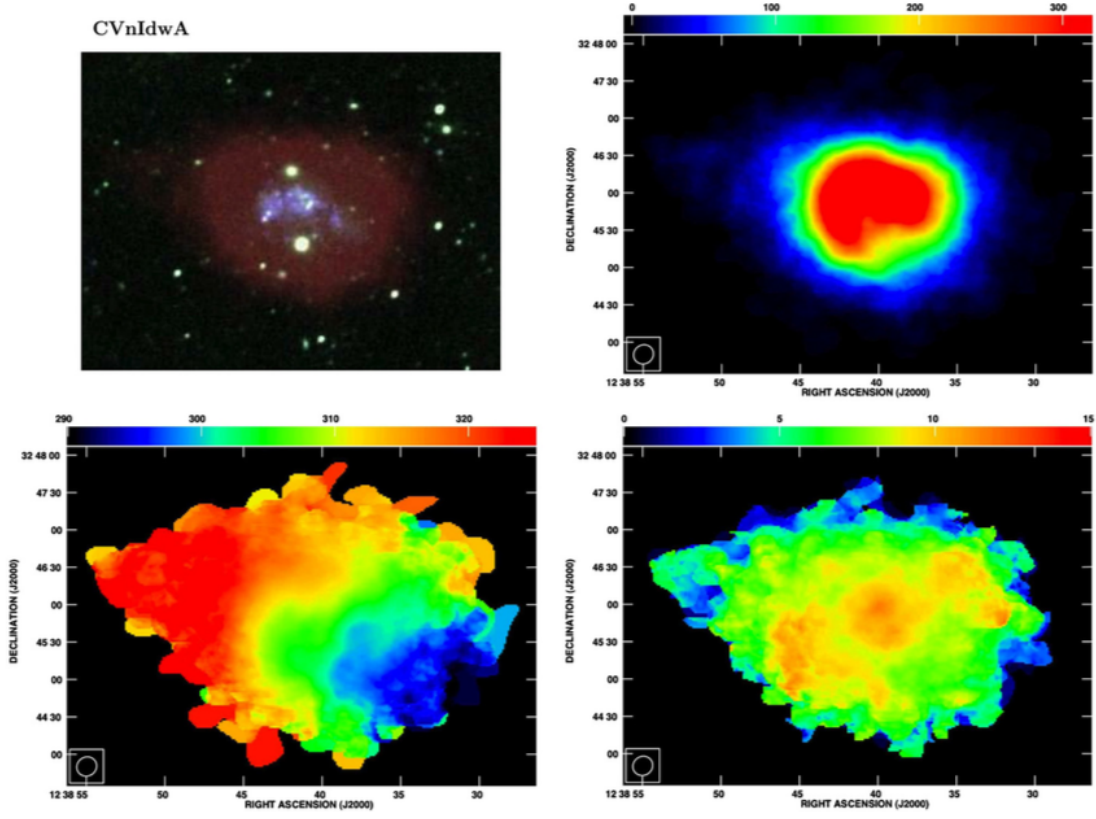


**Figure 1.5:** Information derived from the HI datacube of the dIrr CVnIdwA by Hunter et al. (2012). **Upper-left:** false color picture combining HI (red), V-band (green), and FUV (blue). **Upper-right:** integrated HI map. The colour wedge is in units of  $\text{Jy beam}^{-1} \text{ m s}^{-1}$ . **Bottom-left:** intensity-weighted velocity field (1st-moment map). **Bottom-right:** intensity-weighted velocity dispersion (2nd-moment map). The colour wedge for both bottom panels is in  $\text{km s}^{-1}$ . The circle in the bottom-left corner of the panels indicate the dimension of the beam. Credit: Deidre A. Hunter.

intercepted along the line of sight. In particular, the HI column density along the line of sight is (Roberts, 1975)

$$\frac{N_{\text{obs}}}{\text{cm}^{-2}} = \frac{1.106 \cdot 10^{24}}{\left(\frac{B_{\text{maj}}}{\text{arcsec}}\right) \times \left(\frac{B_{\text{min}}}{\text{arcsec}}\right)} \times \int \left(\frac{S}{\text{Jy beam}^{-1}}\right) \frac{dV}{\text{km s}^{-1}}, \quad (1.1)$$

while the surface density is

$$\frac{\Sigma_{\text{obs}}}{M_{\odot} \text{ pc}^{-2}} = \frac{8.794 \times 10^3}{\left(\frac{B_{\text{maj}}}{\text{arcsec}}\right) \times \left(\frac{B_{\text{min}}}{\text{arcsec}}\right)} \times \int \left(\frac{S}{\text{Jy beam}^{-1}}\right) \frac{dV}{\text{km s}^{-1}}. \quad (1.2)$$

In Eq. 1.1 and Eq. 1.2,  $B_{\text{maj}}$  and  $B_{\text{min}}$  represent the major and the minor full width

half maximum of the instrumental beam and the brightness  $S$  is integrated through all the datacube spectral channels. Notice that, applied to actual datacubes, the integrals are converted to summations over the channels. Integrating Eq. 1.2 over the surface of the emitting source, we obtain the total HI mass

$$M_{\text{HI}} = 2.356 \times 10^5 \left( \frac{\text{D}}{\text{Mpc}} \right)^2 \left( \frac{F_{\text{HI}}}{\text{Jy km s}^{-1}} \right), \quad (1.3)$$

where  $F_{\text{HI}}$  is the total flux of the source in the datacube multiplied by the channel width ( $\Delta V$ ). An example of an HI emission map is shown, for the dIrr CVnIrdwA, in the upper-right panel of Fig. 1.5 .

### 1.3.2 HI disc kinematics: observations

The emission profile (flux as a function of the frequency or velocity) of the hyper-fine HI transition (Sec. 1.3.1) has an extremely small natural quantum broadening ( $\sigma_q \ll 10^{-3} \text{ km s}^{-1}$ ). Hence, the emission profile from a single emitting atom can be considered a Dirac delta centred at the rest frequency  $\nu_{\text{HI}} = 1420 \text{ Mhz}$ . If the atom that emits the HI line is moving with respect to the observer, the line will be not received at the rest frequency but it will be shifted to large or smaller frequencies depending on whether the atom is moving toward or away from us. This phenomenon is simply due to the Doppler effect, so the observed shift in frequency,  $\Delta\nu$ , can be easily interpreted as a velocity,  $V$ , of the emitting source along the line of sight ( $V = c \frac{\Delta\nu}{\nu}$ , where  $c$  is the speed of light). Obviously, during an observation we do not discern the single atomic line emissions, rather the observed HI line profile is the result of the convolution of all the single emissions intercepted along the line of sight inside our instrumental beam. This final line can be considered as a density distribution (in terms of line intensity,  $I$ ) of the emitters as a function of their velocity (or frequency),  $I(V)$ . Therefore, the first moment of the distribution,

$$M_1 = V_{\text{los}} = \frac{\int I(V) V \text{ d}V}{\int I(V) \text{ d}V}, \quad (1.4)$$

namely the the mean of the velocities weighted over the line intensity, is a measure of the “bulk” velocity of the gas along the line of sight ( $V_{\text{los}}$ ). Similarly, the second moment of the distribution,

$$M_2 = \sigma_v = \sqrt{\frac{\int I(V) (V - V_{\text{los}})^2 \text{ d}V}{\int I(V) \text{ d}V}}, \quad (1.5)$$

namely the standard deviation of the velocities weighted over the line intensity, is a measure of the broadening of the emission line. The latter is also a measure of

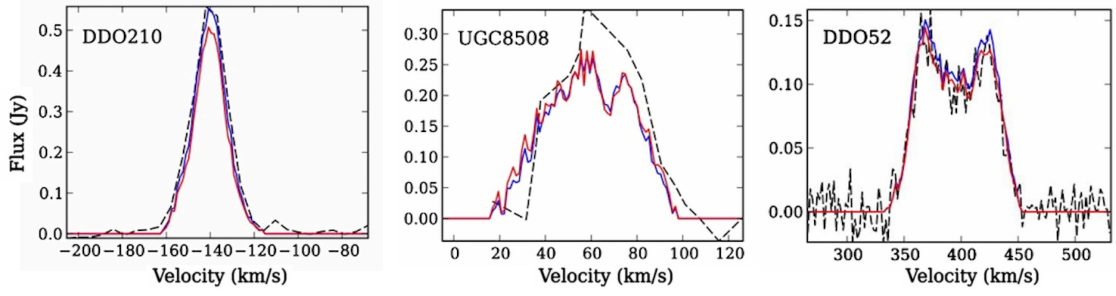


**Figure 1.6:** Global HI line emission profiles obtained by Hunter et al. (2012) summing the flux in each channel of the datacubes of the dIrr galaxies DDO210 (**left-hand panel**), UGC8508 (**middle panel**) and DDO52 (**right-hand panel**). The colored profiles are obtained from observations made with the Very Large Array interferometers using different methods to produce the final datacube (robust-weighted in blue and natural-weighted in red), while the black profiles have been obtained from single-dish observations (see Hunter et al. 2012 for further details). Figure adapted from the original in Hunter et al. (2012).

the velocity dispersion ( $\sigma_v$ ), along the line of sight, due to the chaotic thermal motion of the single particles ( $\sigma_{Th}$ ) and to the chaotic turbulent motions of the gas ( $\sigma_{Tu}$ ), see e.g. Sec. 5.3. Other spurious effects that can broaden the emission line are unresolved streaming and rotational motions inside the beam area ( $\sigma_{beam}$ , also known as “beam smearing”) and the convolution for the instrumental spectral resolution ( $\sigma_{instr}$ , typically of the order of the channel width). As for Eq. 1.1 and Eq. 1.2, in the analysis of actual datacubes, the integrals in Eq. 1.4 and Eq. 1.5 are converted to summations over the datacube channels.

If the HI disc is not spatially resolved (all the disc is inside the instrumental beam), as is the case of the first single-dish observations of dIrrs (e.g. Roberts 1962), the only reliable information at our disposal is the global HI emission profile from the whole disc. This can be calculated measuring the total flux in each channel of the datacube. If the HI emitting source is non rotating, or if the rotation is much lower than the velocity dispersion, the HI profile will be almost a Gaussian centered on the systemic velocity of the galaxy and the broadening of the line gives us information on the chaotic motions (convolved with the instrumental spectral resolution) of the gas. If the gas is rotating, the receding half of the galaxy will be shifted toward lower frequencies (larger velocities), while the approaching half toward higher frequency (larger velocities). In this case, the emission will be still centred on the systemic velocity of the galaxy, but the shape of the HI line profile will depend on the ratio between the amplitude of the rotation velocity projected along the line of sight,  $V_{amp}$  and the velocity dispersion,  $\sigma_v$ , of the gas:

- $V_{amp}/\sigma_v \sim 1$ : this case is similar to the non-rotating case, hence the HI line profile is nearly a Gaussian but the line broadening is due both to the chaotic motion of the gas and to the (non resolved) gas rotation (see the left-hand

panel of Fig. 1.6);

- $V_{\text{amp}}/\sigma_v \gg 1$ : in this case the HI line profile starts to deviate from a simple Gaussian, in particular the peaks is less and less pronounced for increasing values of  $V_{\text{amp}}/\sigma_v$  and it tends to become a “flat-topped” distribution (see the middle panel of Fig. 1.6). When the rotation of the gas is rapidly increasing in the inner parts and then almost constant in the outer parts, the HI line profile exhibits the typical “double-horn” shape (see the right-hand panel of Fig. 1.6), commonly seen in spiral galaxies.

If the rotation is dominant with respect to the velocity dispersion, a rough measure of the amplitude of the gas rotation can be obtained measuring the width of the line profile. A typically used value is  $W_{20}$ , the width at the 20% of the peak emission (e.g. Tully & Fisher 1977; Brook, Santos-Santos & Stinson 2016).

If the HI disc is spatially resolved we can measure the “local” kinematics ( $V_{\text{los}}, \sigma_v$ ) of the HI disc analysing the HI line profile in each pixel of the datacube. There are mainly two methods to extract the kinematic information from the observed HI line profiles. In the first case, we just apply Eq. 1.4 and Eq. 1.5 using the observed line intensity in each datacube channel. In the second case, we assume a certain density distribution (e.g. a Gaussian) which is fitted to the observed HI line profile; then, we use the best-fit parameters to estimate  $V_{\text{los}}$  and  $\sigma_v$ . Both the approaches have pros and cons: in the first case we do not need to make a priori assumptions, but the results could be heavily biased by the presence of the noise; in the second case, we are less influenced by the noise, but the final results could depend on the assumed density distribution. The optimal choice depends on the quality of the data and on the scientific interest. Applying one of the above methods in each spatial pixel, we obtain two 2D maps: a velocity field containing all the estimates of  $V_{\text{los}}$  and a velocity dispersion map containing all the estimates of  $\sigma_v$ . The bottom panels of Fig. 1.5 show the two maps obtained with the moments method for the dIrr CVnIdwA (Hunter et al., 2012). In particular, the velocity field (bottom-left panel) shows the typical “feature” of a rotating disc: half of the galaxy is approaching (green-blue colours) and the other half is receding (red-orange colours).

### 1.3.3 HI disc kinematics: the tilted-ring model

The observed velocity along the line of sight ( $V_{\text{los}}$ ) can be used to obtain the rotation curve of the HI discs, namely the one-dimensional representation of the rotational velocity of the gas as a function of the radius. Since Rogstad, Lockhart & Wright (1974), the most common approach to estimate the rotation curve of the HI discs from the observed kinematics (Sec. 1.3.2) is the so-called ‘tilted-ring model’. In practice the rotating disc is broken into a series of independent circular rings with radius  $R$ , each with its kinematic and geometric properties (see Fig. 1.7). The

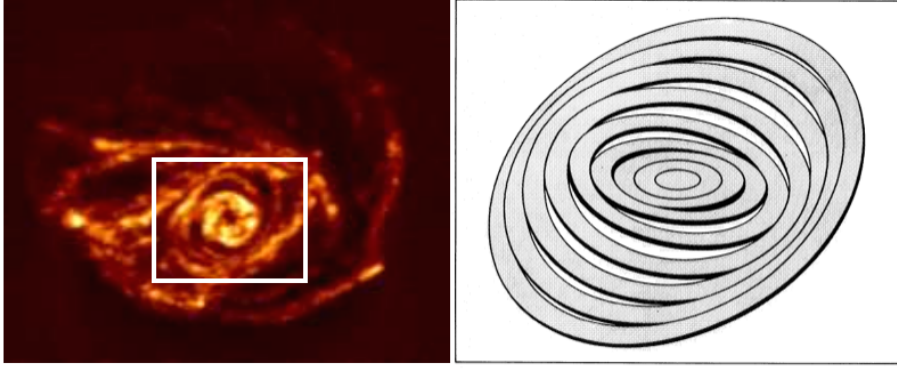


**Figure 1.7:** *Left:* HI total intensity map of the spiral galaxy M83 from Park et al. (2001). *Right:* Tilted-ring description of M83 by Rogstad, Lockhart & Wright (1974). The model refers to the region highlighted with the white rectangle.

projection of each ring on the sky is an elliptical ring with semi-major axis  $R$  and semi-minor axis  $R \cos i$ . Notice that using  $R$ , we indicate both the radius of the circular ring and the semi-major axis of its projection. For a given point with projected coordinates  $(x, y)$ , the projected velocity along the line of sight ( $V_{\text{los}}$ ) is

$$V_{\text{los}}(x, y) = V_{\text{sys}} + V_{\text{rot}}(R) \cos \theta \sin i, \quad (1.6)$$

where  $V_{\text{sys}}$  is the systemic velocity of the galaxy,  $V_{\text{rot}}$  is the rotation velocity of the gas at radius  $R$  and  $\theta$  is the azimuthal angle of the rings in the plane of the galaxy.  $\theta$  is related to  $i$ , to the galaxy centre (with coordinates  $x_0, y_0$ ) and to the position angle, PA, through:

$$\cos \theta = \frac{-(x - x_0) \sin \text{PA} + (y - y_0) \cos \phi}{R}$$

$$\sin \theta = \frac{-(x - x_0) \cos \text{PA} - (y - y_0) \sin \phi}{R \cos i}.$$

The PA is defined as the angle between the north direction on the sky and the projected major axis of the receding half of the rings. Eq. 1.6 indicates that the largest  $V_{\text{los}}$  (in absolute terms) are found along the disc major axis ( $\theta \sim 0^\circ$ ), while along the minor axis ( $\theta \sim 90^\circ$ ) the velocity of the gas is constant and equal to the systemic velocity of the galaxy. Using the ring decomposition it is possible also to obtain radial profiles from the integrated 2D maps (e.g. the HI surface density or the velocity dispersion profile).

It is worth noting that the Eq. 1.6 is strictly valid only assuming that the gas is settled in a razor-thin disc and it describes only the circular motion of the gas. Deviations from pure circular orbits can include radial motions due to inflow-outflow, non-circular motions due to deviation from symmetry of the galactic potential (spiral

arms, mergers, misaligned DM halo and so on; see e.g. Schoenmakers, Franx & de Zeeuw 1997 and Swaters et al. 1999) and small-scale perturbations due to the star formation activity (stellar winds, SNe, see e.g. Read et al. 2016). The tilted-ring model allows us to trace the radial variation of the HI disc geometry and model the so-called ‘warp’ as shown in Fig. 1.7 (García-Ruiz, Sancisi & Kuijken, 2002; Battaglia et al., 2006).

### 1.3.4 HI disc kinematics: rotation curve

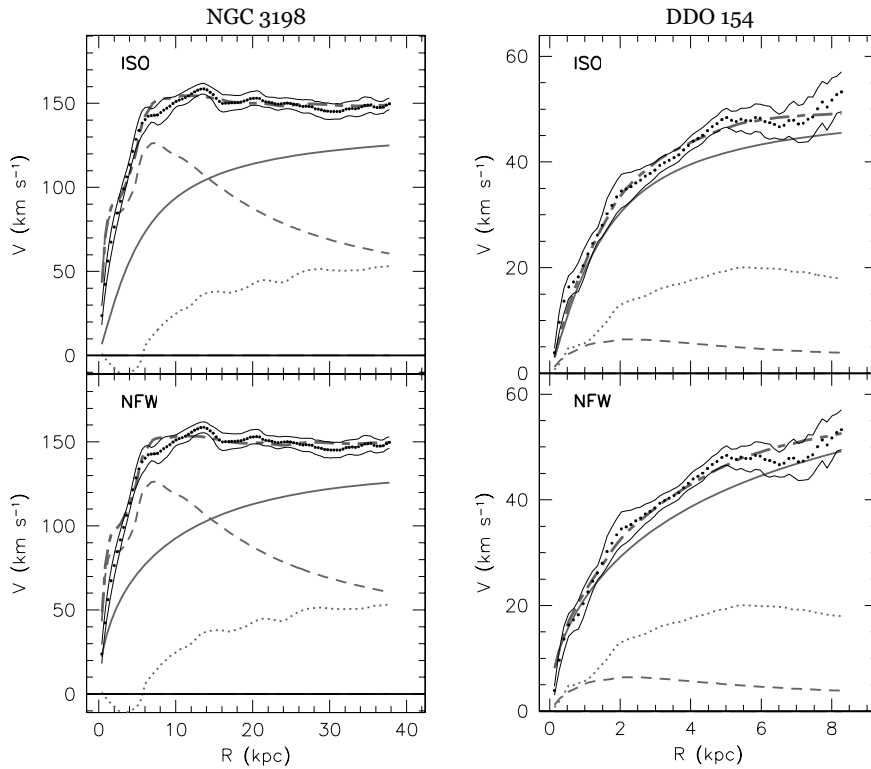


**Figure 1.8:** Rotation curve for the spiral galaxy NGC 3198 (**left-hand panel**) and the dIrr galaxy DDO 154 (**right-hand panel**). Plots are taken from de Blok et al. (2008). In all panels, black dots represent the observed curve and the thin full lines represent the uncertainties. The gray dotted curves and the thin dashed grey curves show the rotation generated from the observed distribution of gas and stars, respectively (see Appendix 5.A). The thick long-short dashed curves show the best-fit rotation curve models obtained assuming an isothermal (Eq. 4.26, **upper panels**) and an NFW (Eq. 4.27, **bottom panels**) profile for the dark matter halo (assumed spherical). The thick, grey full curves show the rotation curve generated by the dark matter halo only.

Using the tilted-ring model we can estimate the intrinsic geometrical parameters ( $i$ , PA) and the rotation curve ( $V_{\text{rot}}$ ) of HI discs both fitting the model to 2D velocity fields (bottom-left panel of Fig. 1.5) or comparing 3D tilted ring models to the data directly in the 3D space of the datacube.

The 2D approach has been used in several numerical algorithms such as ROTCUR (Begeman, 1987), RESWRI (Schoenmakers, Franx & de Zeeuw, 1997), KINEMETRY (Krajinović et al., 2006) and DISKFIT (Spekkens & Sellwood, 2007). All of these codes have been very useful to improve our understanding of the kinematics of late-type galaxies. However, working in 2D has a drawback: the results depend on the assumptions made when extracting the velocity field and are also affected by the instrumental resolution (the so-called beam smearing; Bosma 1978; Begeman 1987). These problems are especially relevant in the study of the kinematics of dIrrs since the HI line profiles can be heavily distorted by both non-circular motions and noise. As a consequence, the extraction of the velocity field can be challenging (see e.g. Oh et al. 2008).

The pioneering work of Swaters (1999) showed that these problems can be solved with an alternative approach: the properties of the HI disc can be retrieved with a direct modelling of the 3D datacube without explicitly extracting velocity fields. In practice, a 3D method consists of a data-model comparison of  $n_{\text{ch}}$  maps (where  $n_{\text{ch}}$  is the number of spectral channels) instead of the single map represented by the velocity field. The best advantage of this approach is that the datacube models are convolved with the instrumental response, so the final results are not affected by the beam smearing. Swaters (1999), Gentile et al. (2004), Lelli, Fraternali & Sancisi (2010) and Lelli, Verheijen & Fraternali (2014a) used a 3D visual comparison between datacubes and model cubes to correct and improve the results obtained with the classical 2D methods. However, a by-eye inspection of the data is time intensive and subjective. Modern software like TiRiFiC (Józsa et al., 2007) and <sup>3D</sup>BAROLO (Di Teodoro & Fraternali, 2015) can perform a full 3D numerical minimisation on the whole datacube. In this thesis, we exploit the code <sup>3D</sup>BAROLO to measure the rotation curve for a sample of dIrrs (see Chapter 3).

The rotation curves of discs are unique tools to trace the gravitational potential of galaxies. In fact, assuming centrifugal equilibrium, the rotation of the gas is related to the radial force generated by the total galactic mass distribution. If the observed baryons (gas+star) were the only component in the galaxy, the theoretical rotation curve generated by their matter distribution would be compatible with the rotation curve measured for the HI disc. This is not the case, for either spirals or dIrrs. In particular, the rotation curves of HI discs in spirals remain nearly flat also in the outermost disc, where the visible matter fades and one would expect a nearly Keplerian fall-off of the rotation curve (e.g. Bosma 1978; Bosma, Goss & Allen 1981; Bosma 1981; van Albada et al. 1985; Begeman 1987, 1989). The discrepancy between the “observed” rotation curve and the one expected from the baryonic matter can be used to estimate the radial profile of the dark matter halo (e.g. van Albada et al. 1985; Begeman 1987; de Blok et al. 2008; Oh et al. 2015).

However, the inner parts of the rotation curve of spirals can be dominated by the contribution of the stellar components (see the left-hand panels of Fig. 1.8). In these cases, the estimate of the DM profile is complicated by the large uncertainties in the estimate of the stellar mass-to-light for the bulge and/or the stellar disc (van Albada et al., 1985). Conversely, the potential of the dIrrs are totally dominated by the DM halo at all radii (see the right-hand panels of Fig. 1.8), moreover these galaxies are bulgeless. As a consequence, the uncertainties on the stellar mass-to-light ratio are totally negligible. In conclusion, the dIrrs represent excellent laboratories to study the basic properties of dark halos in the low mass regime (Swaters, 1999).

These scales are particularly interesting because of the presence of some tension between the observations and the predictions of cosmological  $\Lambda$ CDM (see Sec. 1.1.2) simulations. For example, pure dark matter cosmological simulations of structure formation predict that the dark matter density distribution within galaxies should have an inner cusp ( $\rho_{\text{DM}} \propto r^{-1}$ , Navarro, Frenk & White 1996); however, the rotation curves of dIrr and low surface brightness galaxies favour a central constant density core (e.g. Flores & Primack 1994; de Blok & Bosma 2002; Kuzio de Naray & Kaufmann 2011; Read et al. 2017). In order to understand whether this discrepancy owes to observational biases (e.g. Pineda et al. 2017) or to failures of the simulations in catching all the relevant physical processes (e.g. Read, Agertz & Collins 2016) or to a real failure of  $\Lambda$ CDM (e.g. Kamada et al. 2017), it is mandatory to estimate the dark matter density profile of galactic halos with high precision.

In conclusion, a robust determination of the HI rotation curves in dIrrs is fundamental to investigate the properties of the DM halo in galaxies and to compare these results with the predictions of the cosmological models (see e.g. Read et al. 2017).

## 1.4 This Thesis

As discussed in the previous Sections, the study of the Galactic stellar halo and the study of the HI disc of dIrrs are important to test the predictions of cosmological models. In particular, the study of the smooth structure of the stellar halo is fundamental both to discern among different formation scenarios (Sec. 1.2.1) and to highlight the presence of halo substructures that can be directly related to accreted objects in the Milky Way. On the other side, if the dwarf galaxies are really similar to the primordial building blocks predicted by cosmological models, it is important to understand their dynamics. In this context, the dIrrs are very unique objects in that they are the smallest systems with a rotating disc that can be used to trace the galaxy potential. We can roughly divide our “off piste tour” beyond the disc of the Milky Way in two parts.

In the first part, in [Chapter 2](#), we study the structure of the innermost regions of

the Galactic stellar halo exploiting the unprecedented “richness” of first data release of the *Gaia* mission. This first data release represents only the “tip of the iceberg” of what will be at our disposal by the end of the mission. Nonetheless, we present an original method to select RR Lyrae stars cross-matching the *Gaia* catalogue with the 2MASS catalogue and using only photometric quantity to define a proxy of the stellar variability. Thanks to this method, we obtain the first all-sky sample of RR Lyrae stars located in the inner part of the Galactic halo. We use these data to study, in detail, the spatial distribution of the stars in the halo both with parametric and non-parametric methods. Thanks to the excellent sky coverage of our sample, we are able to test also complex halo models not yet explored in the literature.

In the second part ([Chapter 3](#) - [Chapter 5](#)) we analyse the HI discs of a sample of dIrrs. In [Chapter 3](#), we make use of a new state-of-the-art code (<sup>3D</sup>BAROLO) to obtain the kinematics of dIrrs fitting directly the 3D datacubes. This approach represents a robust way to infer the kinematics since it takes into account the instrumental resolution and exploit the whole information in the datacube instead to work on the projected 2D maps as in previous methods. We also give particular attention to the correction for the pressure support that is especially relevant for these objects. In particular, for the first time, we propose a method to include the uncertainties in this correction process. The results of this work are reliable and ready-to-use rotation curves.

In [Chapter 4](#), we study the effect that the presence of thick gaseous disc can have on the analysis of the HI discs. Then, we present a new original technique to estimate the properties of the HI discs and the dynamics of the host galaxies taking into account the presence of the disc thickness, assuming vertical hydrostatical equilibrium. We applied our method to three of the galaxies analysed in [Chapter 3](#) assuming a razor-thin disc and discuss the differences of the obtained results.

In [Chapter 5](#), we use the data obtained in [Chapter 3](#) to test scaling relations at the low-mass end of the galaxy mass function. We investigate the Baryonic Tully-Fisher relation and the radial acceleration relation comparing our results with what is found for a sample of more massive galaxies. Then, we try to understand whether the energy injected in the ISM by the star formation activity can feed the turbulence that we see in the HI medium of dIrrs.

Finally, in [Chapter 6](#) a summary of the results of this work is presented.

*Get ready, check your equipment, our off piste tour beyond the disc of the Milky Way is about to begin!*



## The first all-sky view of the Milky Way stellar halo with *Gaia*+2MASS RR Lyrae<sup>†</sup>

Although the Galactic stellar halo stores less than the 2% of the Galactic baryons, it contains valuable information about the Milky Way (MW) formation history and the properties of the DM halo (see Sec. 1.2). Therefore, it is important to determine its shape and its density distribution. The radial density profile of the stellar halo has so far been measured with a variety of stellar tracers. Studies based on Main Sequence Turn-Off stars (e.g. Sesar, Jurić & Ivezić, 2011; Pila-Díez et al., 2015), Blue Straggler and Horizontal Branch stars (e.g. Deason, Belokurov & Evans, 2011) and RR Lyrae (e.g. Sesar et al., 2007; Watkins et al., 2009) seem to favour a “broken” power-law profile. According to these datasets, somewhere between 20 and 30 kpc from the MW centre, the density slope changes from a relatively shallow one, as described by power-law index of approximately  $-2.5$ , to a much steeper one, consistent with a power-law index of  $\approx -4$ .

While the radial density profile can also be gauged using data from a limited number of sight-lines through the Galaxy, the shape of the stellar halo requires a much more complete coverage of the sky. So far, much of the halo modelling has relied on the Sloan Digital Sky Survey data, which is biased towards the Northern celestial hemisphere. It is therefore possible that the incomplete view has troubled the efforts to simultaneously infer the details of the radial density distribution and the shape of the halo. For example, using A stars, Deason, Belokurov & Evans (2011) measured substantial flattening of the stellar halo in the direction perpendicular to

---

<sup>†</sup>Based on G. Iorio, V. Belokurov, D. Erkal, S. E. Koposov, C. Nipoti, F. Fraternali, 2017, *MNRAS*, in print (arXiv:1707.03833). This work has made use of data from the European Space Agency (ESA) mission *Gaia* (<http://www.cosmos.esa.int/gaia>), processed by the *Gaia* Data Processing and Analysis Consortium (DPAC, <http://www.cosmos.esa.int/web/gaia/dpac/consortium>). Funding for the DPAC has been provided by national institutions, in particular the institutions participating in the *Gaia* Multilateral Agreement.

the Galactic disc plane, but no change of the shape with radius. On the other hand, Xue et al. (2015) used a sample of spectroscopically-confirmed K giants and detected a noticeable change of flattening with radius. Furthermore, they argue that if the halo shape is allowed to vary with radius, then a break in the radial density profile is not required. Finally, to add to the puzzle, based on a set of BHB stars with spectra, Das, Williams & Binney (2016) reported both an evolving halo shape and a break in the radial density.

Looking at some of the earliest halo studies, which inevitably had to rely on much more limited samples of tracers, it is worth pointing out that, strikingly, glimpses of the variation of the halo shape were already caught by Kinman, Wirtanen & Janes (1966). This pioneering work took advantage of perhaps the most reliable halo tracer, the RR Lyrae stars (RRLs, hereafter). These old and metal-poor pulsating stars suffer virtually no contamination from other populations of the Milky Way and have been used to study the Galactic halo with unwavering success over the last 50 years (see e.g. Hawkins, 1984; Saha, 1984; Wetterer & McGraw, 1996; Ivezić et al., 2000; Vivas & Zinn, 2006; Catelan, 2009; Watkins et al., 2009; Sesar et al., 2010; Akhter et al., 2012; Soszyński et al., 2014; Torrealba et al., 2015; Soszyński et al., 2016).

While deep, wide-area samples of RRLs now exist, for example provided by the Catalina Sky Survey (CSS, Drake et al., 2013), Palomar Transient Factory (PTF, Sesar et al., 2014) and Pan-STARRS1 (PS1, Hernitschek et al., 2016; Sesar et al., 2017), they have yet to be used to model the Galactic halo globally. In case of CSS, this might be due to the varying completeness of the sample. For PTF and PS1 to the fact that the data are not publicly available. To remedy this, here we attempt to extract an all-sky sample of RRLs from the *Gaia* Data Release 1 (GDR1, Gaia Collaboration et al., 2016a) data. Our primary goal is to use the thus procured RRL candidates to model the global properties of the MW stellar halo. Therefore, we are not concerned with maximizing the completeness but instead strive to achieve homogeneous selection efficiency and reasonably high purity. While GDR1 does not contain any explicit variability information for stars across the sky, Belokurov et al. (2017) and Deason et al. (2017a) show that likely variable objects can be extracted from the `GaiaSource` table available as part of GDR1. We build on these ideas and combine *Gaia* and Two Micron All Sky Survey (2MASS) photometry (and astrometry) to produce a sample of  $\approx 21,600$  RRLs out to  $\approx 20$  kpc from the Sun, with constant completeness of  $\approx 20\%$  and purity of  $\approx 90\%$ .

Armed with this unprecedented dataset, we simultaneously extract the radial density profile as well as the shape of the Galactic stellar halo. Furthermore, taking advantage of the stable completeness and the all-sky view provided by *Gaia*+2MASS, we explore whether the density slope and the shape evolve with Galactocentric radius out to  $\approx 30$  kpc. Finally, we also allow the halo to be i) arbitrary oriented ii)

triaxial and iii) off-set from the nominal MW centre.

The analysis of the density distribution of the stars in our sample is based on the fit of density models, rather than on the fit of full dynamical models (see e.g. Das & Binney 2016; Das, Williams & Binney 2016). The main reason behind this choice is that we do not have any kinematic information, so the use of self-consistent dynamical models does not add any significant improvement to our study. Moreover, the knowledge of the spatial density distribution of the stellar halo is a useful piece of information not only if the halo is stationary, but also if it is not “phase-mixed”, as suggested by cosmological  $N$ -body simulations (Helmi et al., 2011).

This Chapter is organized as follows. In Section 2.1 we describe the *Gaia* data as well as the method used to select an all-sky sample of RRL candidates from a cross-match between *Gaia* and the 2MASS. Here, we also give the estimates of the purity and completeness of the resulting sample. In Section 2.2 we show and discuss the spatial distribution of the selected RRLs. Section 2.3 presents the details of the maximum likelihood approach employed to fit the data with different halo density models and the final results of this analysis. In Section 2.4 the best-fit halo model is discussed together with the possible biases that can affect our results. The summary of the results can be found in Section 2.5.

## 2.1 The RR Lyrae Sample

In this Section we describe the method used to select a sample of RRLs from GDR1.

### 2.1.1 *Gaia* Data release 1

*Gaia* is an all-sky scanning space observatory, currently collecting multi-epoch photometric and astrometric measurements of about a billion stars in the Galaxy. More details on the *Gaia* mission and on GDR1 can be found in Gaia Collaboration et al. (2016b). In the first data release, the information available for most faint sources is limited to basic properties, such as positions on the sky and fluxes in the broad *Gaia*  $G$  band, which covers most of the visible spectra from approximately 400 nm to 10000 nm (Jordi et al., 2010).

In this work, we used the table `GaiaSource` released as part of the GDR1 (Gaia Collaboration et al., 2016a). `GaiaSource` contains a number of auxiliary pieces of information, which provide plenty of added value to the GDR1. For example, the errors on the mean flux measurements can be used to separate constant and variable sources, and even gauge the amplitude of the variability (see, e.g. Belokurov et al., 2017; Deason et al., 2017a). Moreover, the quality of the astrometric fit, encapsulated by the so-called astrometric excess noise, contains information regarding the morphology of the source, and can be used to separate stars from galaxies (see

Koposov, Belokurov & Torrealba, 2017). The relevant `GaiaSource` quantities used here (other than the sky coordinates RA, Dec), are:

- $N_{\text{obs}}$ , the number of times a source has crossed a CCD in the *Gaia*'s focal plane;
- $F_G$ , the flux (electron per second) measured in the *G* band averaging over  $N_{\text{obs}}$  single flux measurements;
- $\sigma_{F_G}$ , the standard deviation of the  $N_{\text{obs}}$  flux measurements;
- $G$ , the mean magnitude in the *Gaia* *G* band (van Leeuwen et al., 2016) calculated from  $F_G$ ;
- AEN, the astrometric excess noise, which measures strong deviations from the best astrometric solution. The AEN should be large for objects whose behaviour deviates from that of point-like sources, as, for example, unresolved stellar binaries or galaxies (see Lindegren et al. 2012 for details).

Additionally, relying on the cross-match between *Gaia* and 2MASS, we calculated:

- PM, the total proper motion of each object.  $\text{PM} = \sqrt{\mu_\alpha^2 \cos^2 \delta + \mu_\delta^2}$ , where  $\mu_\alpha$  and  $\mu_\delta$  are the proper motions measured along RA and Dec, respectively.

### 2.1.2 RR Lyrae in *Gaia* DR1

We use the parameters provided in `GaiaSource` to select RRLs from the GDR1. Following the method outlined in Belokurov et al. (2017) and Deason et al. (2017a), we defined the quantity

$$\text{AMP} \equiv \log_{10} \left( \sqrt{N_{\text{obs}}} \frac{\sigma_{F_G}}{F_G} \right), \quad (2.1)$$

which can be used as a proxy for the amplitude of the stellar variability. Indeed, for variable stars with well sampled light curves,  $\sigma_{F_G}$  is proportional to the amplitude of the flux oscillation, while for non-variable stars it is just a measure of photon-count Poisson errors. Thus, it is possible to set a threshold value for AMP that will select only variable candidates. For instance, Belokurov et al. (2017) showed that most variable stars like Cepheids and RRLs have  $\text{AMP} > -1.3$ .

The selection of variables through the AMP parameter suffers from the limitations that AMP is a time-averaged information and does not allow to distinguish between various types of variable objects: RRLs, Cepheids or Mira variables. However, these different classes of pulsating stars populate a well-defined strip in the

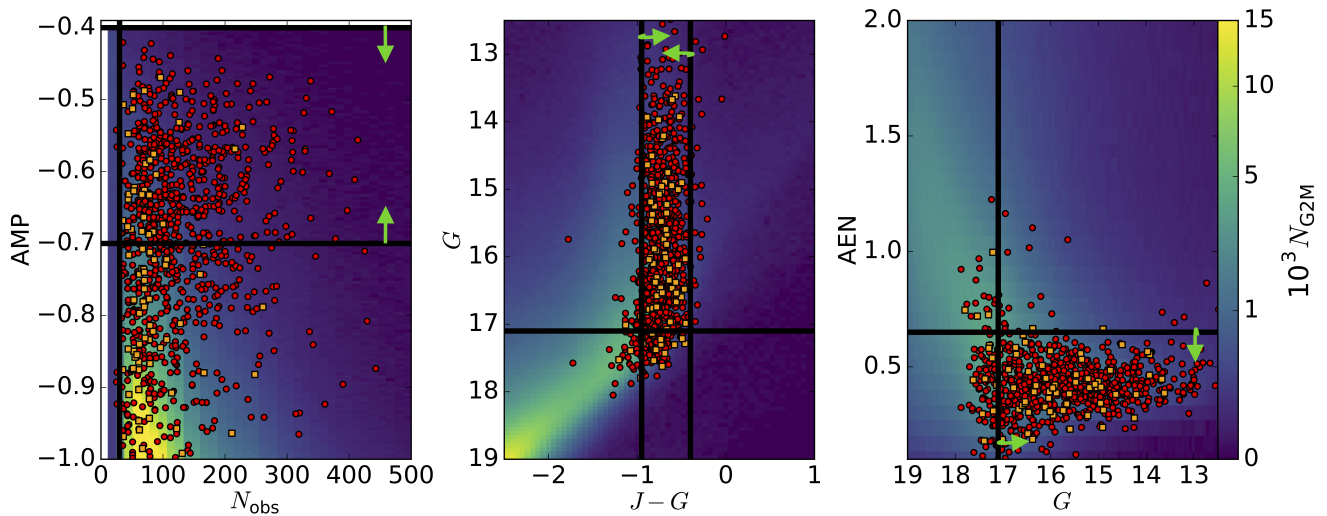


**Figure 2.1:** Diagnostic diagrams for the selection criteria of our RRL sample. **Left-hand panel:** distribution of stars in the AMP- $N_{\text{obs}}$  space; **middle panel:** distribution of stars in the colour-magnitude diagram ( $G$  magnitude from *Gaia*,  $J$  magnitude from 2MASS); **right-hand panel:** distribution of stars in the AEN- $G$  magnitude space. The colour-maps show the distribution of objects in the G2M catalogue, while points show a randomly selected subsample of bona fide RRLs from GCSS (red circles, 5% of the original sample) and GS82 (orange squares, 35% of the original sample) catalogues (see Sec. 2.1.2). The horizontal-black and vertical-black lines show the selection cuts used to obtain the final sample of RRLs (see Tab. 2.2), while the green arrows indicate the regions used to obtain the final sample.

colour-magnitude diagram. Therefore, as we show below, one can overcome this problem by applying selection cuts both in AMP and in colour obtaining a fairly clean sample of RRLs. Note that high values of AMP are also expected for contaminants (e.g. eclipsing binaries) and artefacts (e.g. spurious variations related to *Gaia* cross-match failures). We discuss their importance in Sec. 2.1.2.

### The *Gaia* + 2MASS sample

As mentioned, GDR1 reports photometric information only in the  $G$  band. We derived a colour ( $J - G$ ) for each source by cross-matching *GaiaSource* with the 2MASS survey data (Skrutskie et al., 2006) using the nearest-neighbour method with an aperture of 10 arcsec obtaining the final *GaiaSource* + 2MASS sample of stars (G2M, hereafter). We chose 2MASS mainly due to its uninterrupted all-sky coverage. The observed magnitudes have been corrected for extinction due to interstellar dust using the maps of Schlegel, Finkbeiner & Davis (1998) and the transformation  $A_G = 2.55E(B - V)$  for the  $G$  band (see Belokurov et al., 2017) and  $A_J = 0.86E(B - V)$  for the  $J$  band (Fitzpatrick, 1999).

### Auxiliary RR Lyrae datasets

In order to extract a reliable sample of RRL stars from the G2M catalogue, we must apply ad-hoc selection criteria. To this aim, we used two samples of bona fide RRLs: the CSS (Drake et al., 2013, 2014) and the Stripe 82 (S82, Sesar et al. 2010) catalogues. These samples allowed us to identify the optimal selection criteria, analyse the completeness and the contamination of the catalogue<sup>1</sup> and estimate the RRL absolute magnitude in the  $G$  band. The CSS contains about 22700 type-ab RRL stars distributed over a large area of the sky (about 33,000 deg<sup>2</sup> between  $0^\circ < \alpha < 360^\circ$  and  $-75^\circ < \delta < 65^\circ$ ) and extended up to a distance of 70 kpc. The completeness of this sample is constant (at  $\sim 65\%$ ) only for  $13 < V < 15$ , while it quickly decreases outside this range. Most importantly, as shown in Fig. 13 of Drake et al. (2013), for objects fainter than  $V \sim 15$ , the completeness is a strong function of the number of observations and thus varies appreciably across the sky. SDSS’s Stripe 82 covers a  $2.5^\circ$ -wide and  $100^\circ$ -long patch of sky aligned with the celestial equator and contains “only” 483 RRLs. However, the sample is very pure (with less than  $< 1\%$  of contaminants) and complete up to a distance of 100 kpc.

The large number of stars in CSS is useful to define the selection criteria (see Sec. 2.1.2) and to estimate the absolute magnitude in the  $G$  band (see Sec. 2.1.2), while the high quality of S82 sample is ideal to analyse the completeness and contamination of our final sample (see Sec. 2.1.2 and Sec. 2.1.2). A cross-matching of the CSS and S82 catalogues with G2M using an aperture of 1 arcsec led to the two samples CSS+G2M (GCSS hereafter) and S82+G2M (GS82 hereafter).

### RR Lyrae selection cuts

In this section we describe how the final sample of RRLs was obtained from the G2M catalogue. The selection was driven by the properties of the bona fide RRLs in the GCSS and GS82 catalogues (see Sec. 2.1.2) in order to maximise completeness of the sample and its spatial uniformity, while keeping the level of contamination low (see Sec. 2.1.2).

First of all, in order to exclude a region likely dominated by the Galactic disc, we removed all the stars in the G2M catalogue located between the Galactic latitudes  $b = -10^\circ$  and  $b = 10^\circ$ . Our limit in latitude ( $|b| = 10^\circ$ ) is lower with respect to other works in literature (e.g. Deason, Belokurov & Evans 2011; Das, Williams & Binney 2016), in which, however, the choice was mainly motivated by the limited sky-coverage of the used survey. Given the unprecedented sky-coverage of our data sample, we decided to push forward the study of the halo structure exploring also

---

<sup>1</sup>The completeness indicates the fraction of recovered true RRLs as a function of the apparent magnitude, while the contamination is an estimate of the fraction of spurious objects (non RRLs) that “pollute” our sample.

Selection cuts	
$ b $ [deg]	$> 10$
$G$ [mag]	$(10, 17.1)$
AMP	$(-0.7, -0.4)$
$J - G$	$(-0.95, -0.4)$
$N_{\text{obs}}$	$> 30$
AEN	$< 0.65$
PM [mas/yr]	$< 50$
$ \theta $ [deg] <sup>†</sup>	$> 20$
Structure cuts	
LMC	$D_{\text{LMC}} > 9^\circ$
SMC	$D_{\text{SMC}} > 7^\circ$
S1	$l \notin [167^\circ, 189^\circ] \vee b \notin [16^\circ, 22^\circ]$
S2	$l \notin [160^\circ, 190^\circ] \vee b \notin [63^\circ, 73^\circ]$
$N_{\text{stars}}$	21643 (13713 <sup>†</sup> )
$f_V$ [%]	58 (44 <sup>†</sup> )

**Table 2.2:** Summary of the selection cuts used to obtain the final sample of RRLs from the G2M catalogue. The description of parameters used in the sample selection and the details on the cut substructures can be found in Sec. 2.1.1.  $D_{\text{LMC}}$  and  $D_{\text{SMC}}$  are the sky angular distances from the LMC and SMC, respectively.  $\theta$  is the Galactocentric latitude (defined in Eq. 2.7) and was estimated by assuming an RRL absolute magnitude of  $M_{\text{RLL}} = 0.525$ . The <sup>†</sup> refers to the subsample used in the likelihood analysis in Sec. 2.3. The bottom part of the table gives a summary of the whole sample.  $N_{\text{stars}}$  is the number of stars in the sample and  $f_V$  is the fraction of the spherical volume of the halo sampled by our stars between Galactocentric distance 0 kpc and 28 kpc.

the region at low Galactic latitude that is usually not well sampled by other surveys. We are aware that our final sample could be polluted by Galactic disc contaminants, but in the following sections we carefully analyse the level of contamination and all our results are obtained taking into account the possible biases due to stars of the Galactic disc.

Figure 2.1 shows the distribution of the G2M stellar density (yellow-blue-purple colour-maps), a randomly selected subsample of RRLs in GCSS (red points) and in GS82 (orange squares) in the  $N_{\text{obs}}$ -AMP (left-hand panel), color-magnitude (middle panel) and AEN- $G$  (right-hand panel) planes. The bona fide RRLs occupy a well defined strip in colour, thus we excluded all the stars with the  $J - G$  colour index greater than  $-0.4$  and lower than  $-0.95$  as shown by the vertical black lines in the middle panel of Fig. 2.1. It is worth noting that most of the “normal” stars occupy this colour interval, therefore this cut mostly eliminates artefacts. The left-hand panel shows that the genuine RRLs are almost uniformly distributed in the AMP range of the G2M sample, however the contamination by spurious objects increases rapidly for  $\text{AMP} < -0.7$  (see Sec. 2.1.2 and Fig. 2.6), thus we only retained stars with variability amplitudes above this value. With regards to completeness, the faint magnitude limit plays an important role. According to our analysis,  $G = 17.1$  is the faintest magnitude that we can reach to obtain a sample with spatially uniform

completeness (see Sec. 2.1.2 for further details). The number of bright stars with  $G < 10$ , corresponding to RR Lyrae with distances less than 1 kpc from the Sun, is very small compared to the number of objects in our final catalogue. Therefore, instead of extending our completeness/contamination analysis at the very bright magnitudes (see Sec. 2.1.2 and 2.1.2), we decided to put the bright magnitude limit at  $G = 10$ .

The selection criteria described above involving colour, AMP and magnitude have the largest impact on the definition of our sample of RR Lyrae. However, we also applied a few minor refinements. The right-hand panel of Fig. 2.1 shows that most of the bona fide RRLs have a very small value of AEN, so we excluded all sources with  $AEN > 0.65$  as shown by the horizontal-black line. This cut likely removes contaminant extragalactic objects since they typically have  $AEN \approx 2$  (Belokurov et al., 2017) and some of the eclipsing binaries that survive the colour selection. Additionally, to further clean the sample from possible nearby Galactic disc contaminants, we cull all the stars with a total proper motion, PM, greater than 50 mas/yr. Given differences in the light-curves and its sampling, the significance of AMP (Eq. 2.1) might depend on the number of photometric measurements  $N_{\text{obs}}$ . With this in mind, we impose  $N_{\text{obs}} > 30$ : the focal plane of *Gaia* has an array of  $9 \times 7$  CCDs, so all objects with less than 3 complete *Gaia* transits are excluded.

It would be useful to have an estimate of the photometric metallicity to retain only genuine metal poor stars from the halo and effectively exclude metal rich contaminants from the Galactic disc. However, the photometric metallicity estimate requires a basic knowledge of the shapes of the RRL light curves which is not available in our dataset (see e.g. Jurcsik & Kovacs 1996).

Finally, we masked a few regions of the sky. First we removed the area near the Magellanic Clouds using two circular apertures: one centred on  $(l, b) = (280.47^\circ, -32.89^\circ)$  with an angular radius of  $9^\circ$  for the Large Magellanic Cloud (LMC) and the other centred on  $(l, b) = (302.80^\circ, -44.30^\circ)$  with a radius of  $7^\circ$  for the Small Magellanic Cloud (SMC). By inspecting the sky distribution of the stars in our RRL sample, we noticed the presence of two extended structures (S1 and S2, hereafter), that were not connected to any known halo substructures, but are likely objects instead produced by *Gaia* cross-match failures (see Sec. 2.1.2) that “survived” our selection cuts. We decided to mask these sky regions as well by removing all the stars in the following boxes:  $l = [167^\circ, 189^\circ]$   $b = [16^\circ, 22^\circ]$  for S1 and  $l = [160^\circ, 190^\circ]$   $b = [63^\circ, 73^\circ]$  for S2. The final sample has been further cleaned to exclude “hot pixels” using a simple median-filter method. We first built a sky-map using pixels of  $30'$ , then we replaced the number of stars in each pixel by the median of the star-counts calculated in a squared window of four pixels. Finally, we calculated the ratio between the original sky-map and the one processed with the median filter and all the objects in pixels with a ratio larger than 10 were removed. The properties of the median-filter has

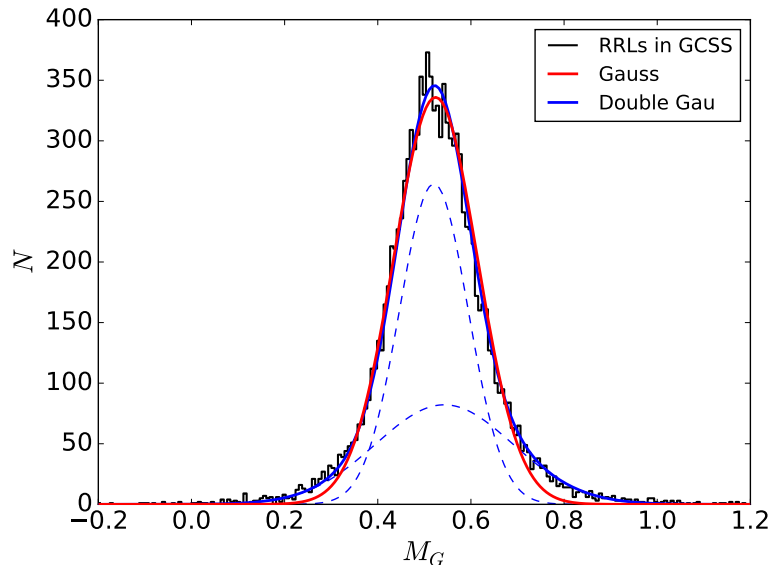


**Figure 2.3:** Distribution of  $G$  band absolute magnitudes for bona fide RRLs in the GCSS catalogue (*Gaia*+CSS, see Sec. 2.1.2). The coloured lines show the fit with a single Gaussian (red) and a double Gaussian (blue, with blue dashed lines showing individual Gaussian components of the fit).

been gauged to reveal small-scale features, since the most evident large-scale structures have been already removed (LMC, SMC, S1 and S2). The “spotted” hot-pixels correspond to known globular clusters (e.g. M3 and M5) or are connected to “remnants” of cross-match failure structures (see Sec. 2.1.2). In order to fully exploit the all-sky capacity of our sample, we decided not to exclude *a priori* any portion of the sky containing known substructures (e.g. unlike Deason, Belokurov & Evans 2011 which masked out the Sagittarius stream). The analysis of the most significant substructures found in this work can be found in Sec. 2.2 and 2.4.

The final sample contains about 21600 RRLs that can be used to have a direct look at the distribution of stars in the Galactic halo (Sec. 2.2). The final number of object is similar to the one in the CSS catalogue, however we cover a larger area of the sky (almost all-sky). Our sample populates 58% of the halo spherical volume within the Galactocentric distance of about 28 kpc which represents a significant improvement in volume fraction as compared to previous works (e.g. 20% in Deason, Belokurov & Evans 2011). A summary of the applied selection cuts can be found in Tab. 2.2.

### Absolute magnitude and distance estimate

Despite photometric variability, RRLs have an almost constant absolute magnitude and, having the apparent magnitudes  $G$ , we can directly estimate the heliocentric

distances through

$$\log\left(\frac{D_{\odot}}{\text{kpc}}\right) = \frac{G - M_G}{5} - 2, \quad (2.2)$$

where  $M_G$  is the absolute magnitude in the *Gaia*  $G$  band. To estimate  $M_G$  we used the RRLs in GCSS, as they have heliocentric distances estimated from the period-luminosity relation. The resulting  $M_G$  distribution is shown in Fig. 2.3: it has a well defined peak at  $M_G \approx 0.5$  and a small dispersion. We fit this distribution with a Gaussian function obtaining a mean of 0.525 and a dispersion of 0.090, comparable to the uncertainties of the V-band absolute magnitude of RRLs (see e.g. Vivas & Zinn 2006). The above Gaussian function perfectly describes the data in the central parts, but the distribution shows broader wings for  $M_G < 0.3$  and  $M_G > 0.7$ . The objects that populate the wings could be Oosteroff type II RRLs and objects influenced by the Blazhko effect (Drake et al. 2013 and references therein). A better fit can be obtained using a double Gaussian model, where two Gaussian components peak at about the same absolute magnitude of the single Gaussian fit (see Fig. 2.3). Given the small dispersion around the mean, we decided to set the absolute magnitude for all the RRLs in our sample to a single value  $M_{\text{RRL}} = 0.525$ . An analysis of the effect of this approximation on the results can be found in Sec. 2.4.2.

## Completeness

Before studying the properties of the stellar halo (as traced by RRLs), it is fundamental to consider the completeness of our sample of RRLs.

First of all, we checked that the scanning law of *Gaia* does not cause an intrinsic decrease of the completeness at low Galactic latitude. We compared the number of objects in *GaiaSource* with the number of stellar sources in the Data Release 7 of the Sloan Digital Sky Survey (SDR7, Abazajian et al. 2009) in a series of stripes at fixed Galactic longitudes, selected using the footprint of SDR7. The top panel of Fig. 2.4 shows the position of the stripes in Galactic coordinates. We selected all stellar sources in the SDR7 with  $16 < r < 18$ , where  $r$  is the  $r$ -band magnitude. In this magnitude range the SDR7 can be considered 100% complete<sup>2</sup>. We chose the  $r$  band because the peak of the filter response is almost coincident in wavelength with the one of the *Gaia*  $G$  band (see Sec. 2.1.1), therefore the two magnitudes are directly comparable. The bottom panel of Fig. 2.4 shows the ratio between the number of stars in *Gaia* and SDR7 in bins of Galactic latitude for individual SDSS stripes and considering all the stripes together. The ratio does not show significant variations as a function of  $b$  with values between 0.9 and 1.0. We conclude that there is no evidence for strong intrinsic completeness variations in the *Gaia* catalogue for  $b > 10^\circ$ .

<sup>2</sup><http://classic.sdss.org/dr7/products/general/completeness.html>

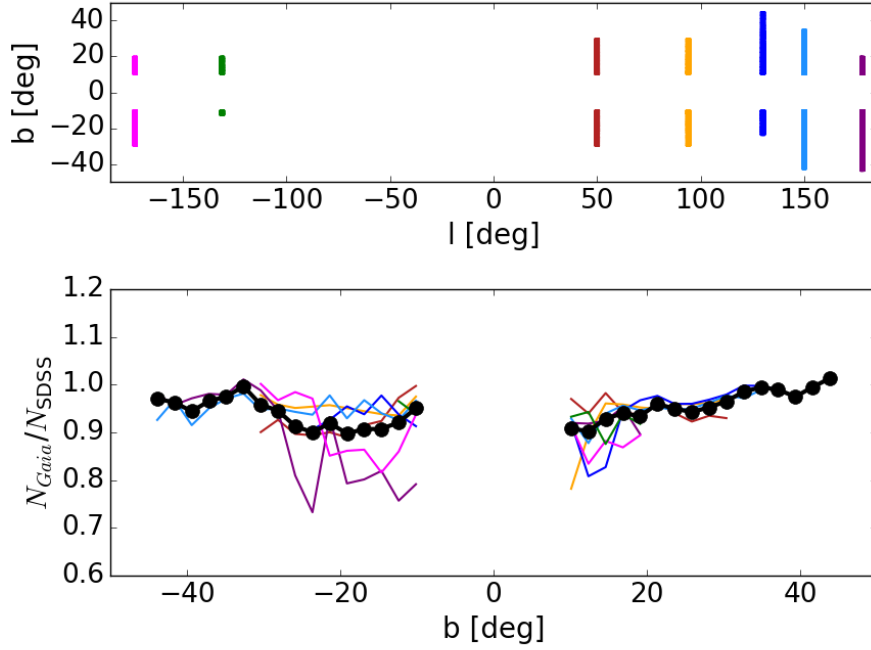


**Figure 2.4:** Completeness analysis of the sources in *GaiaSource* (Sec. 2.1.1) as a function of Galactic latitude. **Top panel:** regions of the sky considered in this analysis, each stripe has a constant Galactic longitude. **Bottom panel:** ratio between the number of stars in the *GaiaSource* ( $N_{Gaia}$ ) and stellar sources in the SDSS DR7 ( $N_{SDSS}$ , Abazajian et al. 2009) in bins of Galactic latitude. The lines refer to the ratio obtained for stars located in regions of the same colour shown in the top panel. The dots and the black line indicate the ratio obtained considering the stars in all the “stripes”. The stars in *Gaia* have been selected using the  $16 < G < 18$  cut, and the SDSS sources using the  $16 < r < 18$  cut (further details on the text).

We estimated the completeness (and the contamination) using the RRLs in our auxiliary catalogues: CSS and S82 (Sec. 2.1.2). In particular, S82 represents a complete ( $\sim 100\%$ ) and pure ( $\sim 99\%$ ) catalogue of RRLs located up to 100 kpc from the Sun, so it is perfect to test both the contamination and the completeness of our sample. We compared the number of stars in the original S82 sample with the ones contained in the GS82 after the selection cuts described in Sec. 2.1.2, in bins of heliocentric distance. Fig. 2.5 shows the level of completeness as a function of magnitude/distance assuming different lower limits in AMP ( $-0.65$  red triangles,  $-0.70$  blue circles,  $-0.75$  green diamonds) in the range of magnitudes  $15 < G < 17$ . The results are in agreement with the distance-based estimate of completeness as shown by the dashed lines. The level of completeness is relatively low, ranging from about 15% for  $AMP > -0.65$  to about 30% for  $AMP > -0.75$ , but it is reasonably constant up to about  $G = 17.5$  then it abruptly decreases to 0 at  $G \approx 18$ , so we decided to conservatively cut our sample at  $G = 17.1$  (vertical black line in Fig. 2.5,

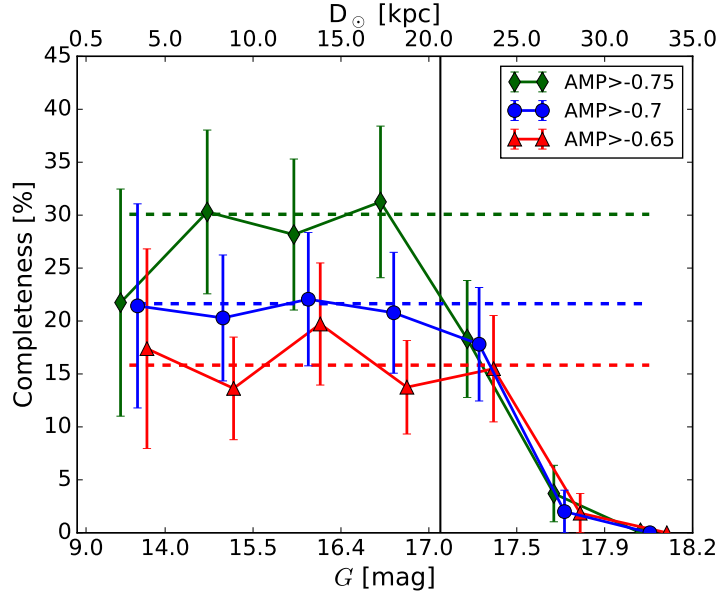


**Figure 2.5:** Completeness of our samples of RRLs as a function of distance from the Sun ( $D_{\odot}$ ) or  $G$  magnitude. The conversion from  $D_{\odot}$  to  $G$  has been obtained from Eq. 2.3 assuming a constant absolute magnitude  $M_{\text{RRL}} = 0.525$ . Different symbols indicate completeness for samples obtained using different AMP cuts: red-triangles for  $\text{AMP} > -0.65$ , blue circles for  $\text{AMP} > -0.70$  and green diamonds for  $\text{AMP} > -0.75$ . The error bars were calculated using the number of stars in each magnitude range and Poisson statistics. The dashed lines indicate the completeness estimated in the  $G$  magnitude range of  $15 < G < 17$ , while the vertical black line marks the  $G = 17.1$  faint magnitude limit of our final sample (see Sec. 2.1.2).

see Sec. 2.1.2).

We also used the GCSS catalogue and found no significant variation of the completeness as a function of the Galactic sky coordinates  $l$  and  $b$ , although we found a mild trend for increasing  $N_{\text{obs}}$ . This is expected since the larger the number of flux measurements the better the sampling of the light curves and, as a consequence, the AMP cut (Eq. 2.1) improves its effectiveness in selecting RRLs. However, the increase is not dramatic as all the differences are within 10%. In conclusion, for the purpose of this work, we considered the completeness of our catalogue of RRLs uniform across our sky coverage and the considered magnitude range (see Tab. 2.2).

## Contamination

We estimated the contamination of spurious sources as

$$\text{Contamination} = \frac{N_S - N_{\text{GS82}}}{N_S}, \quad (2.3)$$

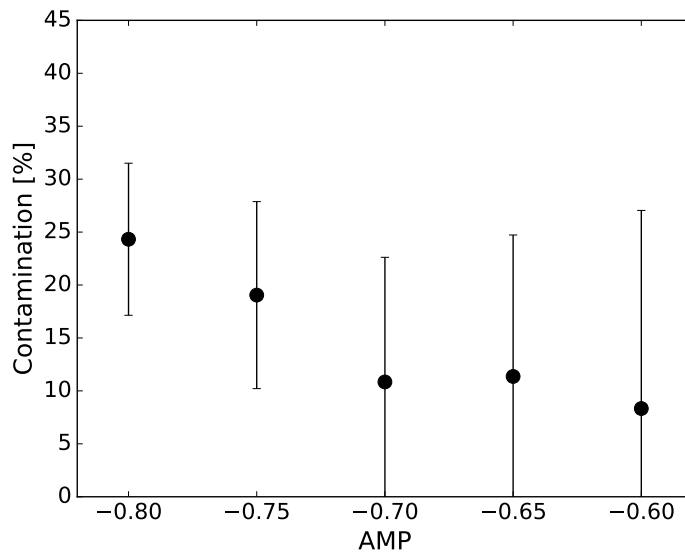


**Figure 2.6:** Contamination of the RRL sample as a function of the AMP cut. The contamination is estimated using the S82 catalogue (see Sec. 2.1.2) in the range of  $G$  magnitudes  $15 < G < 17$ . The error-bars have been calculated by propagating Poisson uncertainties from the number of stars in AMP bins.

where  $N_S$  and  $N_{GS82}$  indicate the number of stars in our samples and in GS82 catalogue after the selection cuts in Sec. 2.1.2. The S82 sample is pure (Sesar et al., 2010), so all the stars in our sample that are not present in the GS82 catalogue are likely contaminants. As before, we considered the magnitude range  $15 < G < 17$  for different lower limits of AMP. For AMP threshold larger than  $-0.7$  the level of contamination is lower than 10% (Fig. 2.6) with a mild increase toward low Galactic latitudes, where the contribution of the Galactic disc is larger. For AMP cut lower than  $-0.7$  the contamination fraction rapidly increases (about 25% for AMP =  $-0.8$ ). We expect that the contaminants of our sample are eclipsing-binaries in the Galactic disc and possible instrumental artefacts. As shown and discussed in detail in Belokurov et al. (2017) some regions of the *Gaia* all-sky map are crossed by sharp strips with a large excess of objects. These strips are similar in width to the field of view of *Gaia* and are regularly spaced on the sky. Belokurov et al. (2017) propose that these are spurious features due to failures in the cross-match procedure of *Gaia*, so that at some epochs the flux of a star comes from a different object. The spurious measurement of the flux increases  $\sigma_{F_G}$  and moves the stars in the region of high AMP “polluting” our samples. We found that for AMP  $> -0.8$  the contaminants are mostly related to cross-match failures. Unlike the disc contaminants, the cross-match failures have a complicated and poorly understood spatial distribution, so these structures are difficult to be taken in account in the study of the properties of the Galactic halo. For this reason, we decided to use AMP =  $-0.7$  as the lower

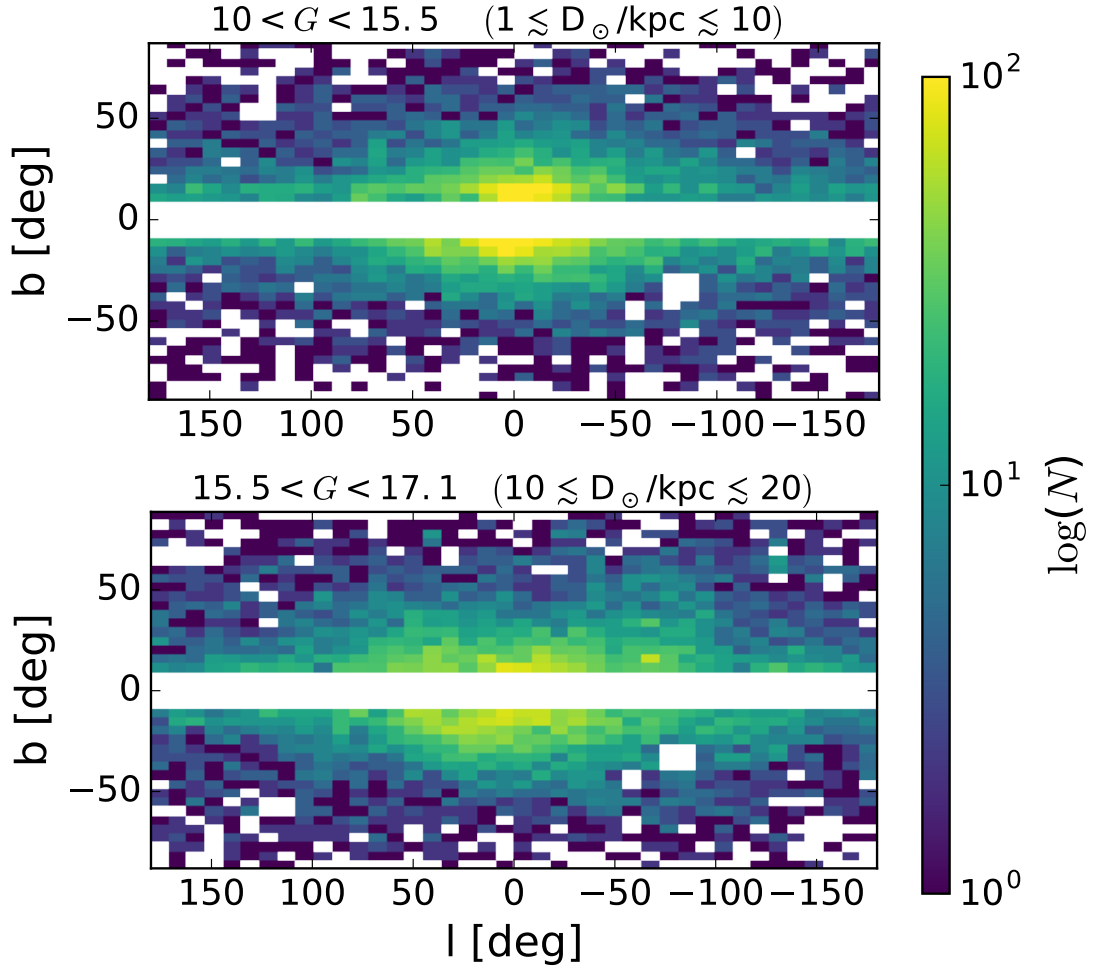


**Figure 2.7:** Star-count all-sky maps in the Galactic coordinates ( $l$ ,  $b$ ) for the RRLs in our sample (Sec. 2.1.2) in the magnitude intervals  $10 < G < 15.5$  (**upper panel**) and  $15.5 < G < 17.1$  (**lower panel**). The “holes” between  $l = -50^\circ$  and  $l = -100^\circ$  are due to the mask used to eliminate the contribution of the Large and Small Magellanic Clouds (see Sec. 2.1.2).

limit in our selection cut (see Sec. 2.1.2).

## 2.2 Distribution of the RRLs in the inner stellar Halo

### 2.2.1 A first Gaia look at the stellar halo

Fig. 2.7 shows the distribution of the RRLs of our final sample as a function of the Galactic coordinates ( $l$ ,  $b$ ). We split the stars in the sample into  $G$  magnitude intervals:  $10 < G < 15.5$ , corresponding to heliocentric distances between  $\sim 1$  kpc and 10 kpc (Eq. 2.2), and  $15.5 < G < 17.1$ , i.e. with heliocentric distances between

10 kpc and 20 kpc (assuming that all RRLs have absolute magnitude  $M_G = 0.525$ ). We stress that Fig. 2.7 represents the first all-sky view of the distribution of the RRLs in the inner halo.

The first magnitude range covers a portion of the Galaxy mostly located in the side of the Galaxy containing the Sun between the Galactic radii 1.4 kpc and 18 kpc. The distribution of stars in this region is quite regular: as expected most of the stars are in the direction of the Galactic centre ( $l \approx 0$ ) and there are not evident asymmetries with respect to the Galactic plane. The second magnitude range covers the Galactic distances between 18 kpc and 28 kpc in the side of the Galaxy containing the Sun and between 3 kpc and 12 kpc in the other side. In this distance range the distribution of the RRLs is less regular with clear asymmetries: in particular, an excess of stars is evident at high Galactic latitude around  $l = -50^\circ$ . In both magnitude intervals an over-dense band of stars at low Galactic latitude ( $|b| < 15^\circ - 20^\circ$ ) can be seen running all around the Galaxy. A discussion of the nature of these structures can be found in Sec. 2.4.3.

### 2.2.2 Setting the frame of reference

We set a left-handed Cartesian reference frame  $(X_g, Y_g, Z_g)$  centred in the Galactic centre and such that the Galactic disc lies in the plane  $(X_g, Y_g)$ , the Sun lies on the positive X-axis and the Sun rotation velocity is  $\dot{Y}_g > 0$ . The actual vertical position of the Sun with respect to the galactic disc is uncertain, but it is estimated to be smaller than 50 pc (Karim & Mamajek 2017 and reference therein), and thus negligible for the purpose of this work. In this Cartesian reference frame, the coordinates of an object with Galactic longitude  $l$ , Galactic latitude  $b$  and at a distance  $D_\odot$  from the Sun are

$$\begin{cases} X_g = X_{g,\odot} - D_\odot \cos b \cos l, \\ Y_g = D_\odot \cos b \sin l, \\ Z_g = D_\odot \sin b, \end{cases} \quad (2.4)$$

where  $X_{g,\odot}$  is the distance of the Sun from the Galactic centre. In this work we assume  $X_{g,\odot} = 8$  kpc (Bovy et al., 2012), but the main results of our work are unchanged for other values of  $X_{g,\odot}$ , within the observational uncertainties (between 7.5 kpc, e.g. Francis & Anderson 2014, and 8.5 kpc, e.g. Schönrich 2012).

For a star with Galactocentric Cartesian coordinates  $(X_g, Y_g, Z_g)$  we define the distance from the Galactic centre

$$D_g = \sqrt{X_g^2 + Y_g^2 + Z_g^2}, \quad (2.5)$$

the Galactocentric cylindrical radius

$$R = \sqrt{X_g^2 + Y_g^2}, \quad (2.6)$$

the Galactocentric latitude

$$\theta = \arctan \frac{Z_g}{R}, \quad (2.7)$$

and the Galactocentric longitude

$$\phi = \arctan \frac{Y_g}{X_g}. \quad (2.8)$$

Assuming that the stellar halo is stratified on concentric ellipsoids, it is useful to introduce another Cartesian frame  $(X, Y, Z)$ , aligned with the ellipsoid principal axes, and to define the elliptical radius

$$r_e = \sqrt{X^2 + Y^2 p^{-2} + Z^2 q^{-2}}, \quad (2.9)$$

where  $p$  and  $q$  are, respectively, the Y-to-X and Z-to-X ellipsoid axial ratios. In general we will allow the  $(X, Y, Z)$  to differ from  $(X_g, Y_g, Z_g)$  in both orientation and position of the origin. When the origin of  $(X, Y, Z)$  is the Galactic centre and  $p = 1$ , as we will assume in this section, the system  $(X, Y, Z)$  can be identified with  $(X_g, Y_g, Z_g)$  without loss of generality.

### 2.2.3 Density distribution of the halo RRLs

Given the all-sky RRL sample illustrated in Fig. 2.7, we can compute their volume number density distribution  $\rho$ . In particular we define the number density of halo RRLs in a cell  $\Delta\vec{\epsilon}$  centred at  $\vec{\epsilon}$ , where  $\vec{\epsilon}$  is a coordinate vector, such as for instance  $(R, Z_g)$ , as

$$\rho(\vec{\epsilon}, \Delta\vec{\epsilon}) \approx N(\vec{\epsilon}, \Delta\vec{\epsilon}) f_V^{-1}(\vec{\epsilon}, \Delta\vec{\epsilon}) V^{-1}(\vec{\epsilon}, \Delta\vec{\epsilon}), \quad (2.10)$$

where  $N(\vec{\epsilon}, \Delta\vec{\epsilon})$  is the number of stars observed in the cell,  $V$  is the volume of the cell and  $f_V$  is the fraction of this volume accessible to our analysis, which depends on the sky coverage, on the selection cuts and the mask that we applied (see Sec. 2.1.2), and on the off-set between the Sun and the Galactic centre. We estimate  $f_V$  numerically as follows. First, we define a Cartesian Galactic grid sampling each of the axes  $(X_g, Y_g, Z_g)$  with 300 points linearly spaced between  $-D_{g,\max}$  and  $D_{g,\max}$  ( $D_{g,\max} \simeq 28$  kpc is the maximum value of  $D_g$ , given our magnitude limit at  $G = 17.1$ ), so the reference Galactic volume (a cube of 56 kpc side centred on the Galactic centre) is sampled with 27 million points with a density of about 125 points per kpc<sup>3</sup>. Each of the points of the grid is a ‘‘probe’’ of the Galactic volume. We assign to each of them Galactic coordinates, heliocentric coordinates and observational coordinates

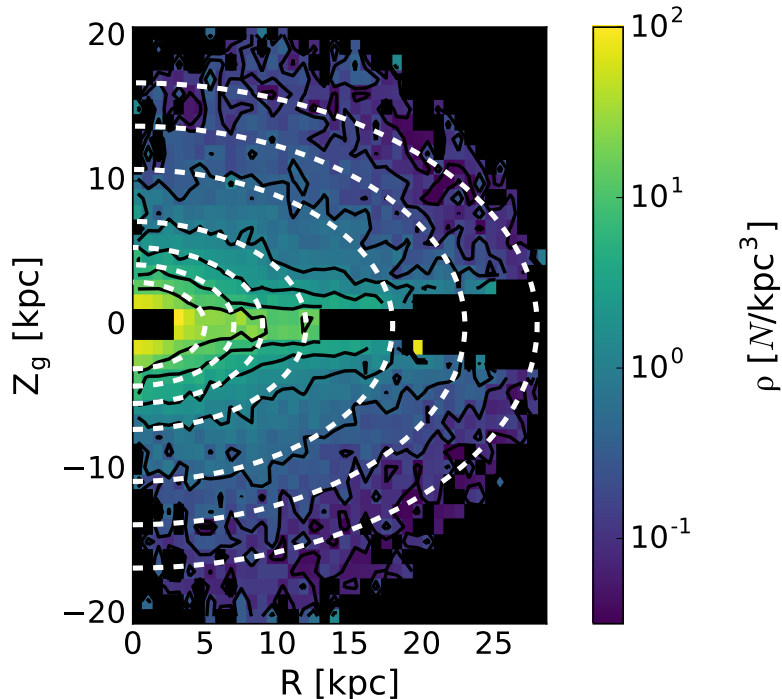


**Figure 2.8:** Number density in the Galactic  $R - Z_g$  plane for the RRLs in our sample. The number density is calculated dividing the number of stars found in a cylindrical ring by the volume of the ring corrected for the non-complete volume sampling of the data (Eq. 2.10). The black contours are plotted with spacing  $\Delta \log \rho = 0.4$  from  $\log \rho = -1.2$  to  $\log \rho = 1.6$ , where  $\rho$  is in units of  $\text{kpc}^{-3}$ ; the white dashed lines represent elliptical contours with an axial ratio  $q = 0.6$ .

( $l, b, \alpha, \delta$ ). A secondary (non-uniform) grid is built by applying the selection cuts in Tab. 1 to the points on the primary grid, so we end up with a grid sampling the complete Galactic volume and a grid sampling the portion of the volume accessible to our analysis. Given a cell in a certain coordinates space (e.g.  $R, Z_g$ ), we define  $f_V$  as the ratio between the number of points of the secondary grid and the number of points of the primary grid contained in the cell. In summary, when we estimate the number density in a 1D or 2D space we build three binned maps: the first contains the number of stars in each bin/cell ( $N$ ), the second the total volume of each bin/cell ( $V$ ) and the third the fraction of this volume that we are actually sampling ( $f_V$ ). These three quantities are inserted in Eq. 10 to estimate the stellar number density. We tested this method with both simple analytic distributions and mock catalogues (see Sec. 2.3.3).

### Meridional plane

Fig. 2.8 shows the number density of the RRLs of our sample in the Galactic meridional plane  $R - Z_g$ . The shape of the iso-density contours clearly shows the presence

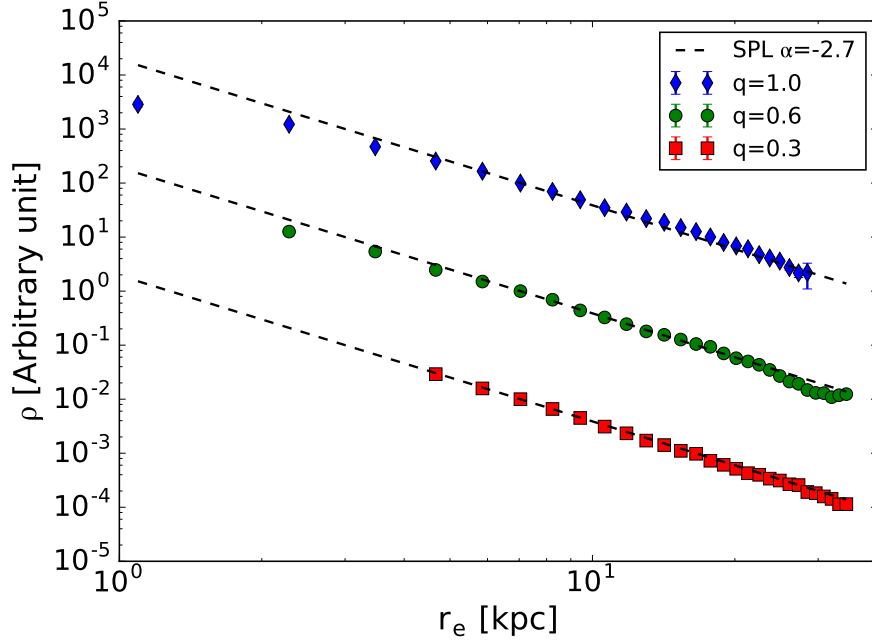


**Figure 2.9:** 1D number density profiles of the halo RRLs as functions of the elliptical radius  $r_e$  (Eq. 2.9) assuming that the halo is stratified on spheroids with  $p = 1$  and different values of  $q$ :  $q = 1.0$  (blue diamonds),  $q = 0.6$  (green dots) and  $q = 0.3$  (red squares). The black-dashed line shows, for comparison, a single power law with index  $\alpha = -2.7$ . The Poisson errors are smaller than the size of the symbols. The density normalisation is arbitrary and different for each profile.

of two components: a spheroidal component and a discy component. The discy component causes the flattening of the contours at low  $Z_g$ . The nature of this component is uncertain: it could represent the disc RRL stars, it could be a low-latitude substructure of the MW halo or, finally, it could be due to non-RRL contaminants from the Galactic disc (both genuine variables such as eclipsing binaries as well as artefacts, e.g. due to cross-match failures). A more detailed analysis of this low-latitude substructure can be found in Sec. 2.4.3. The density at higher  $Z_g$  is less contaminated by the discy component and it represents more directly the density behaviour of the RRLs in the halo. The iso-density contours nicely follow the the  $q = 0.6$  elliptical contours (overplotted in Fig. 2.8) out to  $R \approx 15 - 20$  kpc. At larger radii the contours tend to be rounder. The overall density distribution looks reasonably symmetric with respect to the Galactic plane, although there is an over-dense region at  $Z_g > 10$  kpc, which does not seem to have a counterpart below the Galactic plane (see Sec. 2.2.3 for further details).

## Density profile

Fig. 2.8 demonstrates that the RRLs in the inner halo are consistent with being stratified on spheroids (except in the region close to the Galactic plane), thus we estimate the 1D RRL density profile by counting the stars in spheroidal ( $p = 1$ ) shells and dividing this number by the shell volume corrected by the coverage of our sample (Eq. 2.10). The profiles are shown in Fig. 2.9 for  $q = 1.0$ ,  $q = 0.6$  and  $q = 0.3$ . Independently of the assumed value of  $q$ , the density of RRLs follows a single power law with no significant evidence of change of slope out to an elliptical radius of 35 kpc. It must be noted that the most distant region is only sampled by a low number of stars located in a small portion of the total volume, so it is possible that a change of slope starting near the edge of our elliptical radial range could be missed with this analysis. As the elliptical radius depends on the assumed axial ratios, the results of this analysis are not straightforwardly comparable with previous works (see Sec. 2.4.4 for a detailed comparison with results obtained in the literature).

The slope of this power law is similar in the three cases and very close to  $\alpha = -2.7$  (see Fig. 2.9), but, based on this simple analysis, all values of  $\alpha$  in the range  $-3 < \alpha < -2.5$  are consistent with the data.

## Halo flattening

The distribution of RRLs in the meridional Galactic plane (Fig. 2.8) suggests that the inner halo should be reasonably well represented by a spheroidal stratification with  $q \approx 0.6$ . However, in order to more rigorously study the halo flattening, we estimate the density in the  $r_e - \theta$  plane (see equations 2.4 and 2.9). In practice, for a given value of  $q$ , we scan the density as a function of  $\theta$  at fixed  $r_e$ . If the RRLs are truly stratified on similar spheroids with axial ratio  $q$ , the density is independent of  $\theta$ , so the isodensity contours in the  $r_e - \theta$  plane are vertical stripes. If the assumed value of  $q$  is smaller than the true value  $q_{\text{true}}$ ,  $r_e$  is underestimated, the estimated density is a monotonic decreasing function of  $\theta$  and the isodensity contours in the  $r_e - \theta$  plane are bent in the direction of  $|\theta|$  increasing with  $r_e$  (provided that the density is a decreasing function of  $r_e$ ). The isodensity contours are bent in the opposite direction, if one assumes  $q > q_{\text{true}}$ . The shape of the isodensity contours in the  $r_e - \theta$  plane is a very efficient and direct diagnostic of the evolution of  $q$  as function of the elliptical radius.

The number density maps in the  $r_e - \theta$  plane of the RRLs in our sample are shown in Fig. 2.10 for  $q = 0.75$ ,  $q = 0.55$  and  $q = 0.35$ , assuming  $p = 1$ . Below  $|\theta| = 20^\circ$  (indicated by the white-dashed lines) the contours are nearly horizontal, because the density is dominated by the highly flattened discy component (see Fig. 2.8) for which  $q$  is over-estimated in all the panels. At higher latitudes ( $|\theta| > 20^\circ$ ) the

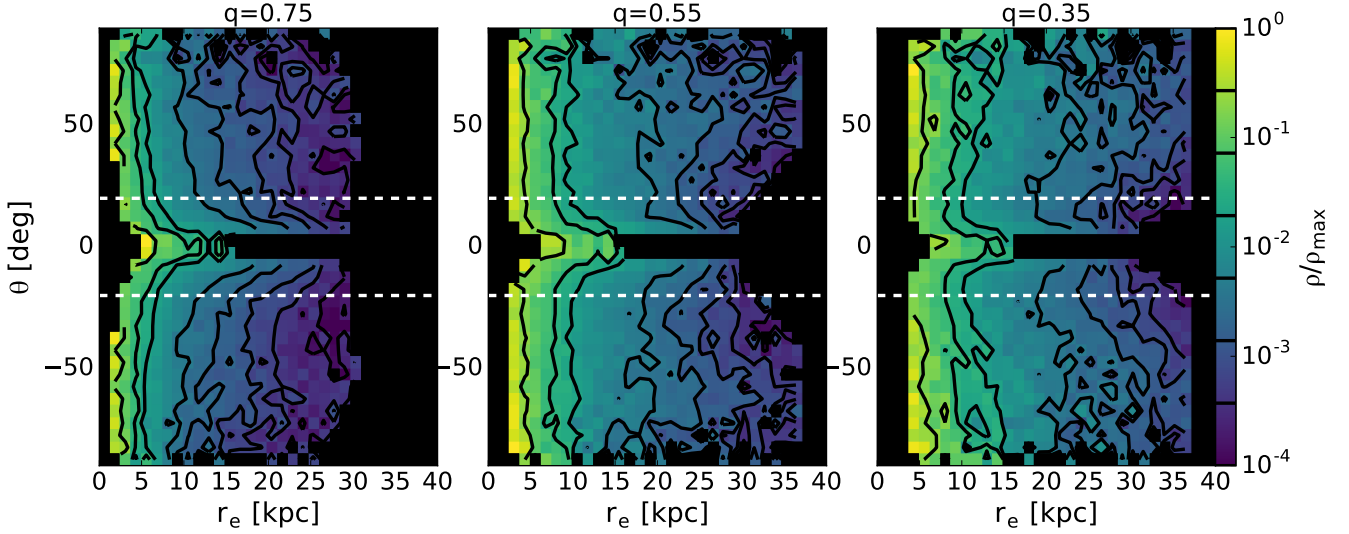


**Figure 2.10:** Number density of RRLs in the elliptical radius ( $r_e$ ) - Galactocentric latitude ( $\theta$ ) space for  $q = 0.75$  (left-hand panel),  $q = 0.55$  (middle panel) and  $q = 0.35$  (right-hand panel), assuming  $p = 1$ . The density is normalized to the maximum value of each panel. The contours show the normalised density levels (0.0002, 0.00055, 0.001, 0.002, 0.004, 0.02, 0.04, 0.2), while the dashed lines indicate  $|\theta| = 20^\circ$ .

contours give a direct indication on the flattening of the halo: in the right-hand panel of Fig. 2.10 ( $q = 0.35$ ) the iso-density contours are significantly inclined in a way that implies  $q_{\text{true}} > 0.35$ . For  $r_e < 20$  kpc a flattening of about 0.55 gives a good description of the data as shown by the vertical iso-density contours in the middle panel of Fig. 2.10 ( $q = 0.55$ ), but beyond 20 kpc the contours start to bend so that  $q_{\text{true}} > 0.55$ . The last two iso-density contours in the left-hand panel ( $q \approx 0.75$ ) look vertical enough to assert that at the outer radii the halo becomes more spherical. This analysis, together with the recent works of Liu et al. (2017), shows the first direct evidence of a change of shape of the stellar halo going from the inner to the outer halo. Moreover the unique all-sky view of our sample allows us to confirm that this trend is symmetric with respect to the Galactic plane. A variation of the halo flattening was also proposed in previous works (e.g. Xue et al. 2015 and Das, Williams & Binney 2016). In Sec. 2.3.4 we perform a comprehensive model fitting analysis of the RRL dataset and compare our results to those found in the literature.

### Vertical asymmetries

Contours of the RRL density shown in Fig. 2.8 and Fig. 2.10 display an overall symmetry between the Northern and Southern Galactic hemispheres, however at  $Z_g > 10$  kpc and around  $\theta \approx 60^\circ$  an over-density of RRLs above the disc plane is

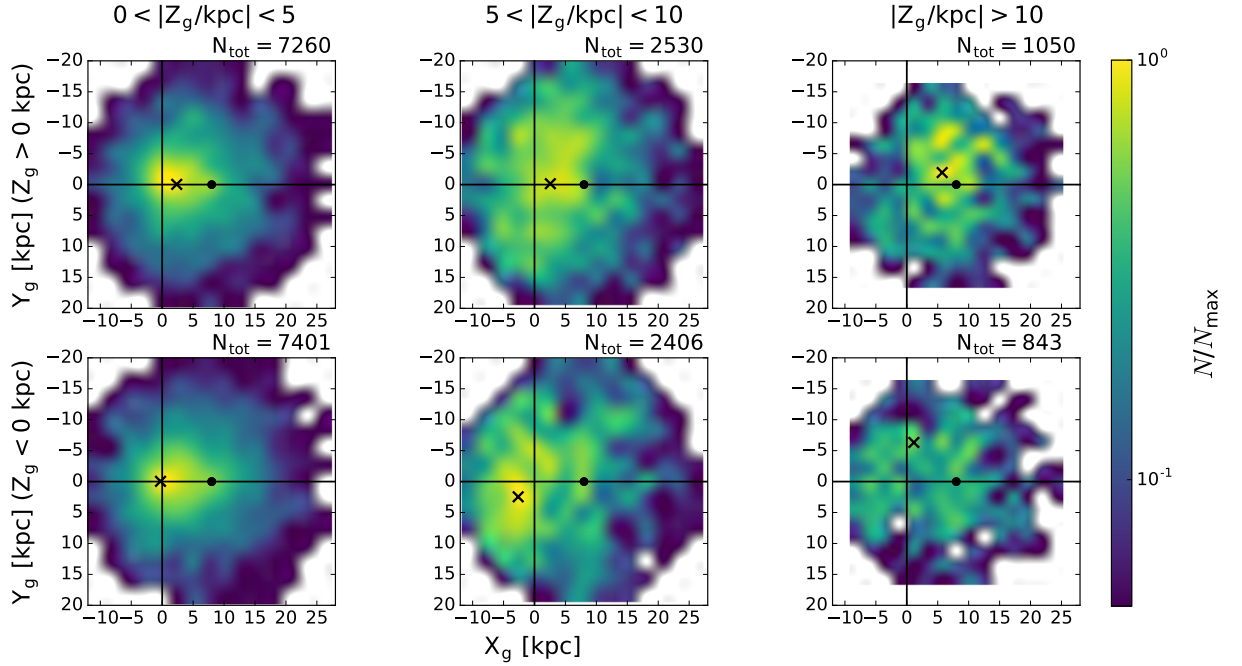


**Figure 2.11:** Number counts of stars in the  $X_g$ – $Y_g$  plane for different  $Z_g$ -slabs: **left-hand panels** with  $0 < |Z_g/\text{kpc}| < 5$ , **middle panels** with  $5 < |Z_g/\text{kpc}| < 10$  and **right-hand panels** with  $|Z_g/\text{kpc}| > 10$ . The top and bottom panels show the layers above ( $Z_g > 0$ ) and below ( $Z_g < 0$ ) the Galactic plane, respectively. The colour maps are normalised to the maximum number in each column of plots.  $N_{\text{tot}}$  is the total number of stars found on each  $Z_g$ -slab. The black dots show the position of the Sun (at  $Z_g = 0$ ), while the crosses indicate the maximum of the star counts. The maps have been smoothed with a spline kernel.

evident. Thanks to the unprecedented sky coverage of our sample we can directly analyse the distribution of stars in different  $Z_g$ -slabs to understand whether the over-density is compatible with the Poisson star-count fluctuations or it is due to a genuine halo substructure.

Fig. 2.11 shows star-count maps in the  $X_g$ – $Y_g$  plane integrated along three different  $Z_g$ -slabs. Close to the plane (left-hand panels) the two maps look very similar and the difference between the total number of stars is small (less than 2%) and compatible within the Poisson errors. In these maps, an elongated component (also visible in the other density maps, Figs. 2.8 and 2.10) can be seen stretching from the Galactic centre to the Sun and beyond: this component appears symmetric with respect to the Galactic plane but is present only in the side of the Galaxy containing the Sun. In the intermediate  $Z_g$ -slabs (middle panels) the difference between the number of stars in the region above and below the Galactic plane is small (less than 5%) as in the previous case, but the maps look less symmetric. In particular the peaks of the star counts are now apart by about 10 kpc. Finally, the slabs at the highest  $Z_g$  (right-hand panels) show a significant difference in the total number of

stars (about 20%) that can not be explained by Poisson fluctuations only. Moreover the excess of stars above the Galactic plane is strongly clustered in the regions between  $X_g \approx (5, 15)$  kpc and  $Y_g \approx (0, 10)$  kpc.

Note that some of the differences between the star counts in the regions above and below the Galactic plane could be due to the mask used to eliminate the contribution of the Magellanic Clouds (see Sec. 2.1.2). Indeed, some mismatch is expected given that we have excluded a relatively large region of the halo volume below the Galactic plane. In order to quantify the differences introduced by the mask, we produce mock catalogues (see Sec. 2.3.3) of different halo models and find that the Magellanic Clouds mask introduces a difference of about the 7% in the number of objects above and below the Galactic plane for  $|Z_g| > 10$  kpc, significantly less than the value of 20% obtained here. Therefore, the structure seen at high positive  $Z_g$  appears to be genuine, and is most likely related to the “Virgo over-density” (Jurić et al., 2008; Vivas et al., 2016). Across all  $Z_g > 0$  slabs, portions of the Virgo Cloud are visible as an excess of stars at positive  $X_g$ . Virgo’s counterpart underneath the disc is the Hercules-Aquila Cloud (see Belokurov et al., 2007a; Simion et al., 2014), discernible in middle bottom panel as strong over-density at negative  $X_g$  (and  $Z_g$ ).

## 2.3 Model fitting

In this section we present the stellar halo models and we compare them with the observed sample of RRLs.

### 2.3.1 Clean sample

Fig. 2.8 and Fig. 2.10 show the presence of a highly “flattened” structure close to the Galactic plane. The properties of this structure are clearly at odds with the distribution of stars at high Galactic latitude that are more likely a “genuine” tracer of the halo population. The “flattened” component contains about 35% of the RRLs in our sample, so it must be taken into account to infer the properties of the stellar halo. Therefore, we built a “clean” sample of RRLs eliminating all the stars belonging to the substructure from our original catalogue (Sec. 2.1.2). Fig. 2.10 suggests that the substructure can be effectively eliminated with a selection in angle  $\theta$  (see Eq. 2.7).

In particular, at  $|\theta| = 20^\circ$  there is a transition between a very flattened component and a more spheroidal structure. Therefore, we define our clean sample of halo RRLs as the stars with  $|\theta| > 20^\circ$ : this subsample contains 13713 objects and covers approximately 44% of the halo volume within a sphere of radius 28 kpc (see Tab. 2.2). We stress that this cut is based on values of  $\theta$  obtained from Eq. 2.2 and Eq. 2.7 assuming the same value of the absolute magnitude,  $M = M_{\text{RRL}} = 0.525$ ,

for all the stars (see Sec. 2.1.2).

We also tried to exclude the flattened structure with alternative cuts, e.g. using a higher cut on the Galactic latitude  $b$  or a direct cut on  $Z_g$ . We found that the results obtained for the sample with  $|\theta| > 20^\circ$  (see Sec. 2.3.4) are qualitatively similar to the results obtained using a sample with  $|b| > 30^\circ$  (the lowest Galactic latitude used in most of the previous works, e.g. Deason, Belokurov & Evans 2011) or a sample with  $|Z_g| > 6$  kpc (Fermani & Schönrich 2013 uses  $|Z_g| > 4$  kpc to cut disc stars). The cuts on  $b$  and  $Z_g$  significantly reduce the number of tracers in the inner part of the halo and the final number of stars is smaller, in both cases, with respect to the one obtained cutting the original sample at  $|\theta| = 20^\circ$ .

In the following subsections we present the method used to fit halo models to this subsample of RRLs and the final results.

### 2.3.2 Halo models

As in Sec. 2.2.1, we assume here that the number density of the halo RRLs is stratified on ellipsoids with axial ratios  $p$  and  $q$ . Therefore, a halo model is defined by a functional form for the density profile (number density as a function of the elliptical radius) and a “geometrical” model for the ellipsoidal iso-density surfaces (in practice, characterized by values of  $p$  and  $q$ , and the orientation of the principal axes with respect to the Galactic disc).

#### Density profiles

We consider five families of number density profiles: double power-law (DPL), single power-law (SPL), cored power-law (CPL), broken power-law (BPL) and Einasto profiles (EIN). The DPL profile has a number density

$$\rho(r_e) \propto \left( \frac{r_e}{r_{eb}} \right)^{-\alpha_{inn}} \left( 1 + \frac{r_e}{r_{eb}} \right)^{-(\alpha_{out} - \alpha_{inn})}, \quad (2.11)$$

where  $\alpha_{inn}$  and  $\alpha_{out}$  indicate the inner and outer power-law slopes and  $r_{eb}$  is the scale length. The number density of the SPL is given by Eq. 2.11 when  $\alpha_{inn} = \alpha_{out}$ , while the number density of the CPL has  $\alpha_{inn} = 0$ , in which case  $r_{eb}$  represents the length of the inner core. The BPL number density profile is given by a piecewise function:

$$\rho(r_e) \propto \begin{cases} r_e^{-\alpha_{inn}} & r_e \leq r_{eb} \\ r_{eb}^{\alpha_{out} - \alpha_{inn}} r_e^{-\alpha_{out}} & r_e \geq r_{eb} \end{cases}. \quad (2.12)$$

The EIN profile (Einasto, 1965) is given by

$$\rho(r_e) \propto \exp \left[ -d_n \left( \left( \frac{r_e}{r_{eb}} \right)^{\frac{1}{n}} - 1 \right) \right], \quad (2.13)$$

where  $d_n = 3n - 0.3333 + 0.0079/n$  for  $n \geq 0.5$  (Graham et al., 2006). The steepness of the EIN profile,  $\alpha_{\text{EIN}}$ , changes continuously as a function of  $r_e$  tuned by the parameter  $n$ ,

$$\alpha_{\text{EIN}} = -\frac{d_n}{n} \left( \frac{r_e}{r_{eb}} \right)^{\frac{1}{n}}. \quad (2.14)$$

The EIN profile is the only density law among those considered here that assures a halo model with a finite total mass for any choice of the parameters. The power-law profiles with  $\alpha_{\text{inn}} < -3$  or with  $\alpha_{\text{out}} > -3$  imply halos with infinite total mass, however our study focuses only on a limited radial range and we do not exclude *a priori* any solution. We anticipate that our best density model is a SPL with  $\alpha_{\text{inn}} < -3$  (see Sec. 2.3.4), therefore there should be a physical radius, outside our radial range, beyond which the profile becomes, either abruptly (e.g. BPL or an exponential truncation) or gently (e.g. DPL), steeper.

### Iso-density ellipsoidal surfaces

Concerning the iso-density ellipsoidal surfaces we define four different models:

- spherical (SH): we set  $p = 1$  and  $q = 1$  in Eq. 2.9, so that  $r_e$  is just the spherical radius  $D_g$  (see definition 2.5) in the Galactic frame of reference;
- disc-normal axisymmetric (DN): we set  $p = 1$ , the axis of symmetry is normal to the Galactic disc, and  $q$  is a free-parameter;
- disc-plane axisymmetric (DP): we set  $q = 1$ , the axis of symmetry is within the Galactic plane making an (anticlockwise) angle  $\gamma$  with respect to the Galactic Y-axis, and  $p$  is a free-parameter,.
- triaxial (TR): both  $p$  and  $q$  are considered free-parameters, the Z-axis of symmetry is coincident with the normal to the Galactic plane and the X and Y axes are within the plane making an (anticlockwise) angle  $\gamma$  with respect to the Galactic X and Y axes, respectively.

Given the unprecedented sky coverage of our sample, we also tested more complex models for the iso-density ellipsoidal surfaces:

- *qv*:  $q$  depends on the elliptical radius as

$$q(r_e) = q_\infty - (q_\infty - q_0) \exp \left[ 1 - \frac{\sqrt{r_e^2 + r_{eq}^2}}{r_{eq}} \right], \quad (2.15)$$

so  $q$  varies from  $q_0$  at the centre to the asymptotic value  $q_\infty$  at large radii and the variation is tuned by the exponential scale length  $r_{eq}$ ;

- (*tl*): in this model we assume that the principal axes of the ellipsoids are tilted with respect to the Galactic plane; in practice, before calculating the elliptical radii (Eq. 2.9), we transform the Galactic coordinates (see Eq. 2.4) of each star by applying a rotation matrix  $R(\gamma, \beta, \eta)$  following a ZYX formalism so that  $\gamma$  is the rotation angle around the original Z-axis,  $\beta$  the one around the new Y-axis and finally  $\eta$  is the rotation angle around the final X-axis; all the rotation are defined in the anticlockwise direction;
- (*off*): in this model the elliptical radius of each star is estimated with respect to a point offset by  $(X_{off}, Y_{off}, Z_{off})$  with respect to the Galactic centre.

The specific functional form of Eq. 2.15 is empirical: the same expression was adopted by in Xue et al. (2015) and Das, Williams & Binney (2016), where, however,  $q$  is a function of the spherical radius ( $D_g$ ). We decided to maintain the dependence on  $r_e$  given that this approach is self-consistent with our assumption that the RRLs are stratified on ellipsoidal surfaces. It follows that, for our models with a varying  $q$ , the elliptical radius  $r_e$  of a star with coordinates  $(X_g, Y_g, Z_g)$  is the root of

$$r_e^2 - X_g^2 - Y_g^2 p^{-2} - Z_g^2 q(r_e)^{-2} = 0, \quad (2.16)$$

where  $q(r_e)$  is defined in Eq. 2.15. In our fitting code we solve this equation numerically with a Newton-Raphson root finder.

### Complete halo model

Each complete halo model is defined by a model for the density law (SPL, DPL, CPL, BPL, EIN) plus a model for the shape of the iso-density surfaces (SH, DN, DP, TR) and any combination of geometrical variants (*qv*, *tl* and *off*). For instance, a SPL-SH model has a spherical distribution of stars with a single power-law density profile, while a EIN-TR<sup>*qv,tl*</sup> model is a triaxial tilted model with varying flattening along the Z-axis of symmetry and an Einasto density profile (see Tab. 2.12 for a reference on the various model labels). In the next sections when we discuss the properties or the results of density models (e.g. SPL models), unless otherwise stated, we are implicitly referring to all the models that share the same density model whatever the geometrical and geometrical variants properties are. The same applies when we

focus on geometrical models only. We fit our data with all possible combinations of density laws (SPL, DPL, CPL, BPL, EIN), geometrical models (SH, DN, DP, TR) and model variants (*qv*, *tl*, *off*). See Tab. 2.13 for a summary of results obtained with a sample of such models.

### 2.3.3 Comparing models with observations

#### Density of stars in the observed volume

Given a certain halo model (Sec. 2.3.2), the normalised number density of stars in an infinitesimal volume  $dV_g = dX_g dY_g dZ_g$  is given by

$$\tilde{\rho}(X_g, Y_g, Z_g | \vec{\mu}) \propto \frac{dN}{dV_g}, \quad (2.17)$$

where  $\vec{\mu}$  is the vector containing all the model parameters (e.g.  $\vec{\mu} = (\alpha_{\text{inn}}, q)$  for an SPL+disc-normal axisymmetric model, see Sec. 2.3.2) and  $\tilde{\rho}$  is defined such that

$$\int \tilde{\rho}(X_g, Y_g, Z_g | \vec{\mu}) dV = 1. \quad (2.18)$$

It is useful to define the normalised star number density

$$\tilde{\nu}(m, l, b | M, \vec{\mu}) = |J| \tilde{\rho}(X_g, Y_g, Z_g | m, l, b, M, \vec{\mu}) \quad (2.19)$$

within the infinitesimal projected (onto the sky) volume element  $dS = dm dl db$  centred at  $(m, l, b)$ , where  $m$  is the observed magnitude,  $l$  and  $b$  are the Galactic longitude and latitude, and

$$|J| = \frac{\ln 10}{5} D_{\odot}^3(m, M) \cos b \quad (2.20)$$

is the determinant of the Jacobian matrix  $J = \left[ \frac{dV_g}{dS} \right]$  (Appendix 2.A). The number density  $\tilde{\nu}$  depends also on the additional parameter  $M$ , which is the absolute magnitude needed to pass from the observable variables  $(m, l, b)$  to the Cartesian variables (see Eqs. 2.2 and 2.4). Substituting Eq. 2.20 in Eq. 2.19 we obtain

$$\tilde{\nu}(m, l, b | M, \vec{\mu}) = \frac{\ln 10}{5} \tilde{\rho}(X_g, Y_g, Z_g | m, l, b, M, \vec{\mu}) D_{\odot}^3(m, M) \cos b. \quad (2.21)$$

#### Likelihood of a single star

From the normalised density function (Eq. 2.21) we can define the expected rate function for finding a star with  $(m, l, b)$  given the absolute magnitude  $M$  and a halo

Model component	Model label	Density parameters			Iso-density surfaces parameters				
		$\alpha_{\text{inn}}/n$	$\alpha_{\text{out}}$	$r_{\text{eb}}$ (kpc)	$p$	$q(q_0/q_{\text{sc}})$	$r_q$ (kpc)	$X_{\text{off}}/Y_{\text{off}}/Z_{\text{off}}$ (kpc)	$\gamma/\beta/\eta$ (degree)
Single power-law	SPL	U[0,20]	$\delta(\alpha_{\text{inn}})$	$\delta(1)$					
Cored power-law	CPL	$\delta(0)$	U[0,20]	U[0.01,10]					
Double power-law	DPL	U[0,20]	U[0,20]	U[ $r_e^{\text{min}}, r_e^{\text{max}}$ ]	†				
Broken power-law	BPL	U[0,20]	U[0,20]	U[ $r_e^{\text{min}}, r_e^{\text{max}}$ ]	†				
Einasto	EIN	U[0,100]		U[0.1,500]					
Spherical	SH				$\delta(1)$	$\delta(1)$			
Disc-normal axsym	DN				$\delta(1)$	U[0.1,10]			
Disc-plane axsym	DP				U[0.1,10]	$\delta(1)$			U[-80,80]
Triaxial	TR				U[0.1,10]	U[0.1,10]			U[-80,80]
q-var	$qv$						U[0.1,100]		
Offset	$off$							U[0,10]	
Tilted	$tl$								U[-80,80]

**Table 2.12: Prior distribution  $\Pi$  (Eq. 2.28) of the halo model parameters.** Each row refers to a given component of the halo models, each column indicates a single parameter or a group of parameters if they share the same prior distribution. The second column indicates the labels used to indicate the halo models throughout the text (Sec. 2.3.2). The third column refers to the parameter  $n$  for the Einasto profile and to the parameter  $\alpha_{\text{inn}}$  for the other density models. The U indicates a uniform distribution within the values shown inside the square brackets; a  $\delta$  indicates a Dirac delta distribution. † The prior range of the parameter  $r_{\text{eb}}$  for the BPL and DPL density models is not the same in all models, depending on the minimum ( $r_e^{\text{min}}$ ) and maximum ( $r_e^{\text{max}}$ ) elliptical radius of the stars in the sample.

model with parameters  $\vec{\mu}$

$$\lambda(m, l, b, M|\vec{\mu}) = A\tilde{\nu}(m, l, b|M, \vec{\mu})W(m, l, b|M_{\text{RRL}})P(M). \quad (2.22)$$

In Eq. 2.22,  $A$  is a constant,  $P(M)$  represents the probability density function (pdf) of the absolute magnitude of the stars, while the function  $W$  is the selection function that takes into account the incomplete coverage of the Galactic volume. It is a function of  $l$ ,  $b$  and  $m$  and returns a result in the Boolean domain  $B = (0, 1)$ . In particular,  $W$  is always equal to 1 except for the points  $(m, l, b)$  that are outside the volume covered by our clean sample (see Tab. 2.2).

In this work, we decided to set the absolute magnitude of the RRLs to a single value,  $M_{\text{RRL}} = 0.525$  (Sec. 2.1.2), so we are assuming that  $P(M)$  in Eq. 2.22 is a Dirac delta. As a consequence, we can marginalize Eq. 2.22 over  $M$  to obtain

$$\lambda(m, l, b|M_{\text{RRL}}, \vec{\mu}) = A\tilde{\nu}(m, l, b|M_{\text{RRL}}, \vec{\mu})W(m, l, b|M_{\text{RRL}}), \quad (2.23)$$

and we define the normalised rate function as

$$\tilde{\lambda}(m, l, b|M_{\text{RRL}}, \vec{\mu}) = \frac{\lambda(m, l, b|M_{\text{RRL}}, \vec{\mu})}{\int \lambda(m, l, b|M_{\text{RRL}}, \vec{\mu})dm dl db}. \quad (2.24)$$

The normalised rate function in Eq. 2.24 is the pdf of stars, i.e. the likelihood per star, at a certain position  $(m, l, b)$  for halo model parameters  $\vec{\mu}$ .

### The total likelihood

Consider a sample of stars  $D$  with coordinates  $(m, l, b)$  and a halo model with parameters  $\vec{\mu}$ . Given the pdf of the stellar distribution  $\tilde{\lambda}(m, l, b)$  (Eq. 2.24) the logarithmic likelihood is

$$\ln \mathcal{L} = \sum_{i=1}^{N_s} \ln \tilde{\lambda}(m_i, l_i, b_i | \vec{\mu}), \quad (2.25)$$

where  $N_s$  is the number of stars in our sample. Plugging Eq. 2.21 and Eq. 2.23 into Eq. 2.24 we can write the logarithmic likelihood as

$$\ln \mathcal{L} = \sum_{i=1}^{N_s} \ln \frac{\tilde{\rho}(X_g, Y_g, Z_g | m_i, l_i, b_i, M_{\text{RRL}}, \vec{\mu}) D_{\odot}^3(m_i, M_{\text{RRL}}) \cos b}{V_c(\vec{\mu})}, \quad (2.26)$$

where

$$V_c(\vec{\mu}) = \int_{-90^\circ}^{90^\circ} \cos b \, db \int_0^{360^\circ} dl \int_{G_{\min}}^{G_{\max}} \tilde{\rho} D_{\odot}^3 W \, dm \quad (2.27)$$

is the normalisation integral. Notice that the numerator of Eq. 2.26 is evaluated only in regions of the sky where  $W = 1$  (i.e. where we observe stars).

### Sampling of the parameter space

Considering the Bayes's law, the logarithmic posterior probability of the parameters  $\vec{\mu}$  of an halo model given the data is

$$\ln P(\vec{\mu} | D) = \ln P(D | \vec{\mu}) + \ln \Pi(\vec{\mu}) = \ln \mathcal{L} + \ln \Pi(\vec{\mu}), \quad (2.28)$$

where  $P(D | \vec{\mu}) = \mathcal{L}$  is the probability of the data,  $D$ , given the parameters  $\vec{\mu}$  (See Sec. 2.3.3) and  $\Pi(\vec{\mu})$  represents the prior probability of  $\vec{\mu}$  (Tab. 2.12). In Eq. 2.28 we omit the Bayesian evidence term  $P(D)$  that is defined as the integral of the likelihood over the whole parameter space. This term is negligible in the determination of the best set of parameters for a given model (see below).

Using Eq. 2.26 we can write the posterior probability as

$$\ln P(\vec{\mu} | D) = \sum_{i=1}^{N_s} \ln \frac{\tilde{\rho}(X_g, Y_g, Z_g | m_i, l_i, b_i, M_{\text{RRL}}, \vec{\mu}) D_{\odot}^3(m_i, M_{\text{RRL}}) \cos b}{V_c(\vec{\mu})} + \ln \Pi(\vec{\mu}). \quad (2.29)$$

In order to explore the parameter space without biases, we decided to use very large priors for most of our parameters (see Tab. 2.12). In particular, the very large ranges for  $\alpha_{\text{inn}}$  and  $\alpha_{\text{out}}$  approximate uniform infinite priors.

Concerning the parameter  $r_{\text{eb}}$ , we assume, for both the BPL and DPL density models, that the prior distribution is uniform between  $r_e^{\min}$  and  $r_e^{\max}$  which represent

the minimum and maximum elliptical radii (Eq. 2.9) of stars in our sample. For most of our models,  $r_e^{\min}$  remains constant at about 2.4 kpc, while  $r_e^{\max}$  ranges between roughly 31 kpc and 38 kpc.

We analysed the posterior probability of the parameters,  $\vec{\mu}$ , for a given halo model using the Eq. 2.29 and we sampled the parameters space with Goodman & Weare’s Affine Invariant Markov chain Monte Carlo (mcmc, Goodman & Weare 2010), making use of the Python module emcee<sup>3</sup> (Foreman-Mackey et al., 2013). The technical details of our approach can be found in Appendix 2.B.

The final best-fit values of the model parameters have been estimated using the 50th percentile of the posterior distributions and the 16th and 84th percentiles have been used to estimate the  $1\sigma$  uncertainties.

### Tests on mock catalogues

In order to test our fitting method, we developed a simple Python script to generate mock catalogues with the same properties (e.g. number of stars, magnitude limits) as our clean sample of RRLs (Sec. 2.3.1). This algorithm distributes the stars using a combination of the density laws (Sec. 2.3.2) and according to the assumptions on the properties of the iso-density ellipsoidal surfaces (Sec. 2.3.2). The absolute magnitude of the stars in the mock catalogues are distributed using the best-fit double Gaussian functional form shown in Fig. 2.3. The final mock catalogues do not include *Gaia* and 2MASS photometric and sky-coordinates errors because the uncertainties they cause on the estimate of the distance are negligible.

We applied our fitting method to mock catalogues finding that we are able to recover the input parameters for all possible model combinations, including in the sample a fraction of Galactic disc contaminants (see Sec. 2.4.2).

Analysing the mock catalogues, we can estimate what properties of the halo we are able to measure and constrain using the stars in our catalogue. We found that we are able to detect a core in the density profile (CPL density model) all the way down to 100 pc. However for a very small core size most of the information comes from a relative small region where the transition between the inner core and the outer density profile takes place. The detection of a change of slope depends on the halo flattening: for  $p = 1$  and  $q = 1$  we can detect a break in the density profile within about  $r_{\text{eb}} = 28$  kpc (Eq. 21). For more flattened models ( $q$  around 0.5/0.6) this range extends up to about  $r_{\text{eb}} = 35$  kpc. However, in this latter case most of the information for regions where  $r_e > 28$  kpc comes from a small number of stars at very high Galactic latitude, therefore the fit can be easily biased by the presence of substructures such as the one highlighted in Sec. 2.2.3 and Fig. 9. In conclusion, we are confident that we are able to robustly detect significant deviations from a

<sup>3</sup><https://github.com/dfm/emcee>

Model		Parameters	$\Delta \ln(\mathcal{L}_{\max})$	$\Delta \text{BIC}$
Density law	Surface			
SPL	SH	$\alpha_{\text{inn}} = 2.61 \pm 0.01$ (2.61)†	-868	1688
SPL	DP	$\alpha_{\text{inn}} = 2.64 \pm 0.01$ (2.64)†, $p = 1.59 \pm 0.03$ (1.59), $\gamma = -22.0 \pm 1.7$ deg (-22.3 deg)‡	-405	779
SPL	DN	$\alpha_{\text{inn}} = 2.71 \pm 0.01$ (2.71)†, $q = 0.58 \pm 0.01$ (0.58)	-81	124
BPL	DN	$\alpha_{\text{inn}} = 2.70 \pm 0.01$ (2.70), $\alpha_{\text{out}} = 2.90 \pm 0.11$ (2.87), $r_{\text{eb}} = 22.3^{+3.3}_{-2.8}$ (22.2) kpc, $q = 0.58 \pm 0.01$ (0.58)	-79	141
DPL	DN	$\alpha_{\text{inn}} = 2.70 \pm 0.03$ (2.71), $\alpha_{\text{out}} = 2.74^{+0.04}_{-0.02}$ (2.72), $r_{\text{eb}} = 21.1^{+5.7}_{-9.9}$ (23.1) kpc, $q = 0.58 \pm 0.01$ (0.58)	-81	143
CPL	DN	$\alpha_{\text{out}} = 2.72 \pm 0.02$ (2.71), $r_{\text{eb}} = 0.03^{+0.03}_{-0.01}$ (0.03) kpc, $q = 0.58 \pm 0.01$ (0.58)	-81	134
EIN	DN	$n = 37.5^{+3.5}_{-4.6}$ (40), $r_{\text{eb}} = 391.1^{+84.6}_{-169.8}$ (474.0) kpc, $q = 0.58 \pm 0.01$ (0.58)	-87	145
SPL	DN <sup>qv</sup>	$\alpha_{\text{inn}} = 2.93 \pm 0.05$ (2.93)†, $q_0 = 0.52 \pm 0.02$ (0.52), $q_{\infty} = 0.74 \pm 0.05$ (0.75), $r_{\text{eq}} = 14.8 \pm 1.9$ (15.0) kpc	-66	113
SPL	TR	$\alpha_{\text{inn}} = 2.71 \pm 0.01$ (2.71)†, $p = 1.27 \pm 0.03$ (1.27), $\gamma = -21.1 \pm 2.6$ deg (-21.1 deg)‡ $q = 0.65 \pm 0.01$ (0.65)‡	-22	23
SPL	TR <sup>qv</sup>	$\alpha_{\text{inn}} = 2.96 \pm 0.05$ (2.96)†, $p = 1.27 \pm 0.03$ (1.27), $\gamma = -21.3 \pm 2.6$ deg (-21.3 deg)‡ $q_0 = 0.57 \pm 0.02$ (0.57), $q_{\infty} = 0.84 \pm 0.06$ (0.84), $r_{\text{eq}} = 12.2^{+2.4}_{-1.8}$ (12.2) kpc	0	0

**Table 2.13: Summary of properties and results for a sample of families of halo models.** For each family we report the assumed density law (Sec. 2.3.2) and geometry of the iso-density surfaces (Sec. 2.3.2). See Tab. 2.12 for a reference on the model labels. For each fitted parameter we report the median and the uncertainties estimated as the 16th and 84th percentiles of the posterior distribution, the values in parentheses indicate the value for which we obtain the maximum value of the likelihood  $\mathcal{L}_{\max}$  (Eq. 2.26). The last two columns indicate the logarithmic likelihood and BIC differences between the best model of the family and the best of of all the presented models. † In the SPL models  $\alpha_{\text{inn}} = \alpha_{\text{out}}$ , see Sec. 2.3.2. ‡ The (anticlockwise) angle  $\gamma$  indicates the tilt of the X and Y axes of symmetry of the halo with respect to the Galactic X and Y axes, see Sec. 2.3.2.

SPL within a range of elliptical radii from less than 1 kpc to about 30 kpc. Finally, we verified that the method described above can recover a variation of the halo flattening given a realistic mock dataset.

### 2.3.4 Results

In this section we present the main results obtained applying the method described in Sec. 2.3.3 to the RRLs in our clean sample (Sec. 2.3.1).

### Model comparison

In addition to estimating the parameters for a single model, it is important to compare the results of different models to determine which of them gives the best description of the data. The most robust way to perform a model comparison is through the ratio of the Bayesian evidences. Under the assumption that the posterior distributions are almost Gaussian, the Bayesian evidence can be approximated by the Bayesian information criterion (BIC, Schwarz 1978) defined as

$$\text{BIC} = \dim(\vec{\mu}) \ln(N_S) - 2 \ln(\mathcal{L}_{\max}), \quad (2.30)$$

where  $N_S$  is the number of objects in the sample and  $\mathcal{L}_{\max}$  is the maximum value of the likelihood (Eq. 2.26).

The BIC is often used to compare different models with different dimensions in parameter space and the model with the lowest BIC is preferred. The BIC is similar to the maximum likelihood criterion, but it includes a penalty depending on the number of free parameters  $\dim(\vec{\mu})$ , such that for two models with the same likelihood, the one with more parameters is penalised. The best-fit parameters together with a comparison of the maximum likelihood and the BIC for a representative sample of halo models can be found in Tab. 2.13. These quantities have been calculated taking the maximum of the 14400 likelihood estimates obtained with the final mcmc sampling (see Sec. 2.3.3).

Other than the BIC, we also compared the ability of the different models to describe the observed properties of the RRLs (e.g. distribution of the stars in the sky).

### RRLs density law

We tested different density profiles assuming a DN geometrical model: the SPL (Eq. 2.11 with  $\alpha_{\text{inn}} = \alpha_{\text{out}}$ ), the DPL (Eq. 2.11), the BPL (Eq. 2.12), the CPL (Eq. 2.11 with  $\alpha_{\text{inn}} = 0$ ) and the EIN profile (Eq. 2.13).

The logarithmic maximum likelihoods and the BICs obtained for these different models are very similar as shown in Tab. 2.13, moreover Fig. 2.14 shows that the predicted fraction of RRLs in bins of magnitude, for the different density models, are practically coincident. Therefore, the DPL, BPL, CPL and EIN models do not offer any significant improvement in the description of the RRLs distribution with respect to the simpler SPL. Fig. 2.15 shows the comparison between the (elliptical) radial profiles of the density slope for different halo models. The slopes have been calculated as the logarithmic (elliptical) radial derivative of the logarithmic density, therefore the result for a SPL is just a constant (as shown by the black-dashed line in the four panels). The best-fit broken radius for the BPL is  $r_{\text{eb}} \approx 22$  kpc: in

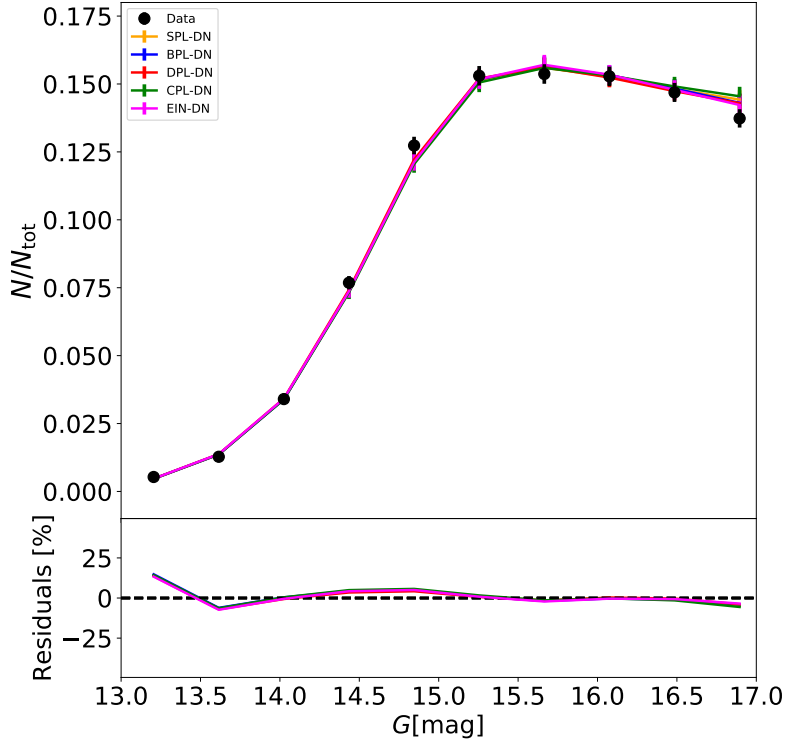


**Figure 2.14:** Top panel: the black points show the fraction of stars in magnitude bins, while the curves show the same fraction expected for halo models with different density laws: SPL (blue), BPL (orange), DPL (green), CPL (red) and EIN (magenta). Error bars on the data points and on the model distributions indicate Poisson uncertainties. Bottom panel: relative residual (Data-Model/Model). In all the cases we assumed a DN geometrical halo model (see Tab. 2.13).

the inner part the best-fit slope is practically the same as the SPL model then it decreases to a slightly larger slope of about 2.9.

Concerning the DPL, the posterior distributions of the slopes are compatible with  $\alpha_{\text{out}} = \alpha_{\text{inn}}$ , such that the final density profile is again an SPL with a slope compatible with the best-fit SPL model (panel B in Fig. 2.15), moreover the posterior distribution of  $r_e$  is almost uniform in the prior range interval (Tab. 2.12). Similarly, the core radius of the CPL model is very small and the final CPL model is compatible with no-core and the outer slope is the same of the SPL model (panel C panel in Fig. 2.15).

Finally, for the EIN the fit favours very large values both for  $n$  ( $\approx 38$ ) and for  $r_{\text{eb}}$  ( $\approx 390$  kpc), so that in the analysed radial range the variation of the slope is minimal and the density profiles effectively mimic an SPL. However, since the BIC of the EIN model is higher than the BIC of the SPL models, there is no evidence in favour of an EIN profile for the inner part of the stellar halo.

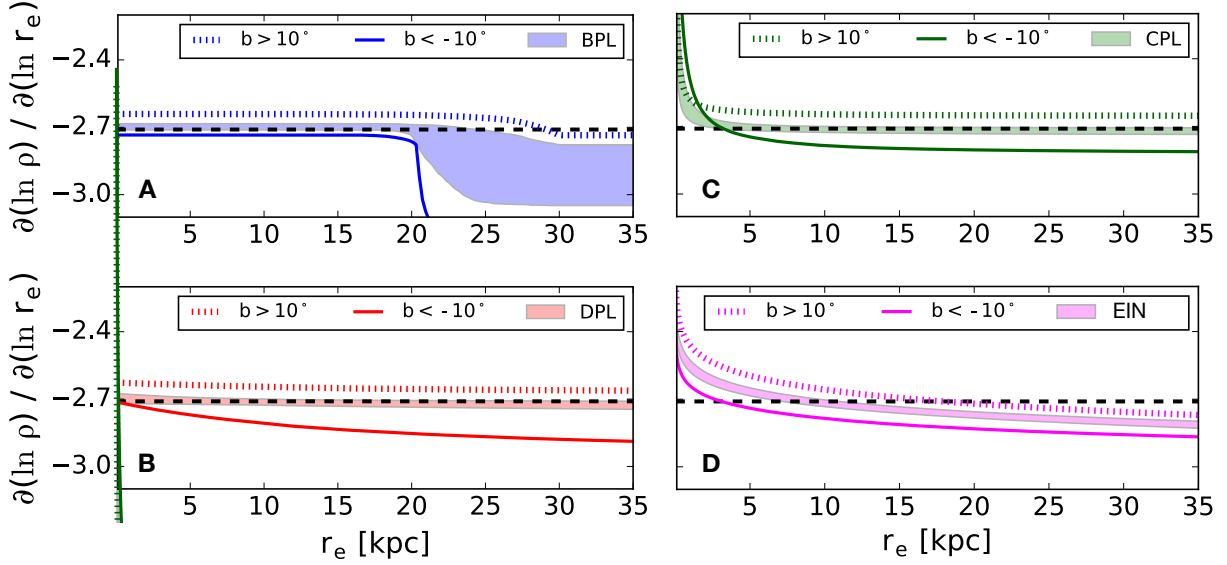


**Figure 2.15:** Radial profile of the density slope ( $\partial(\ln \rho)/\partial(\ln r_e)$ ) for different density law models: BPL (**panel A**), DPL (**panel B**), CPL (**panel C**) and EIN (**panel D**). The bands represent the posterior distribution between 16th and 84th percentiles. The coloured lines represent the median of the posterior obtained fitting only the stars above ( $b > 10^\circ$ , dotted line) and below ( $b < -10^\circ$ , solid line) the Galactic plane. The dashed-black line shows the best-fit slope obtained for the SPL model. In all the cases we assumed a DN geometrical halo model (Tab. 2.13).

The break radius of the BPL model is compatible with the one obtained in Xue et al. (2015) after the subtraction of halo substructures, although the change of slope is much more significant in their work with respect to our result (see Tab. 2.24). In principle, the over-density of stars described in Sec. 2.2.3 might make it difficult to detect the break, so we repeated the maximum likelihood analysis using the RRLs only above and below the Galactic plane. The results are shown in Fig. 2.15 by the solid ( $b < -10^\circ$ ) and dashed ( $b > 10^\circ$ ) coloured curve: in general the stars above the Galactic plane prefer a mean slope of about 2.65 while the ones below have a mean slope of about 2.78. Concerning the change of slope above the Galactic plane, the posterior distribution of the parameters of the BPL, DPL and CPL models are such that these models are similar to the SPL profile. Below the Galactic plane both the BPL and the DPL favour a change of slope, however the one of the BPL model is much more significant going from about 2.73 in the inner part to about 3.3 beyond  $r_e \approx 20$  kpc. It is evident that the stars below the Galactic plane have a steeper decrease of the density with respect to the stars above the Galactic plane. This result could be due to the excess of stars at high latitude, however in both the sub-samples the minimum BIC is still obtained for the SPL model. Therefore, the change of slope is not highly significant and the fact that the DPL and the BPL show a different behaviour could indicate that the change of slope could be due to

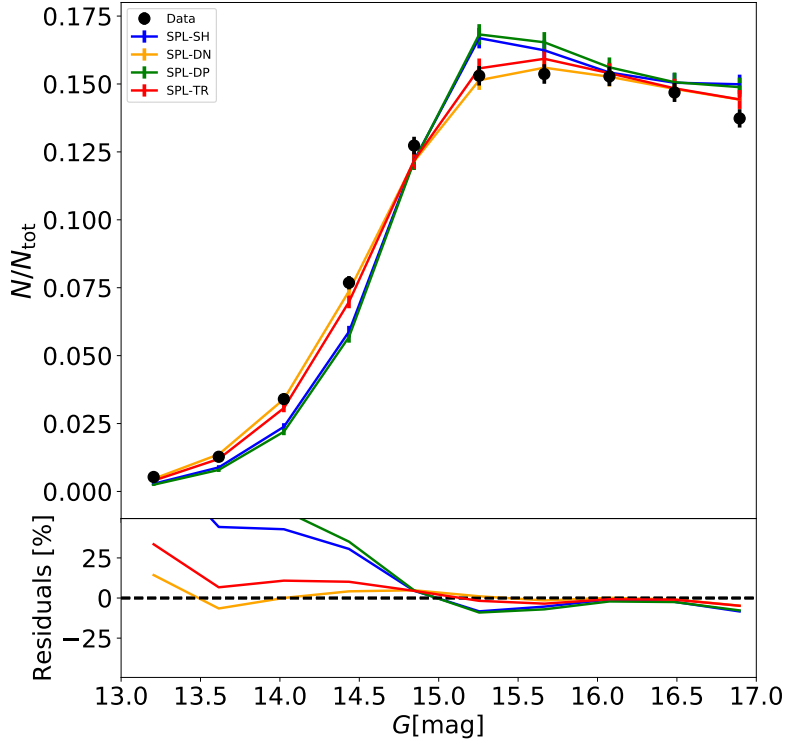


**Figure 2.16:** As in Fig. 2.15 but for halo models SH (blue,  $q = 1$  and  $p = 1$ ), DN (orange,  $q = 0.58$  and  $p = 1$ ), DP (green,  $q = 1$  and  $p = 1.59$ ) and TR (red,  $q = 0.65$  and  $p = 1.27$ ). In all cases we assumed a SPL for the density profile of the RRLs (with parameters given in Tab. 2.13).

some local artefact (such as a local decrease of the completeness).

The comparisons discussed above refer only to DN halo models, however we obtained similar results also for DP and TR halo models. In particular, we found that the SPL density model always provides the lowest BIC value, independent of the assumed halo geometry.

In conclusion, there is no significant evidence of deviation from a SPL density law: the RRLs follows an SPL with an exponent that ranges between 2.6, assuming a SH model, to 3 assuming a  $\text{TR}^{qv}$  halo. These results agree with the estimate of the density profiles obtained in Sec. 2.2.3 counting stars in ellipsoidal shells (Fig. 2.9).

### Iso-density surfaces

As shown by the BIC comparison in Tab. 2.13, the SH and DP models give significantly worse fits with respect to the DN and TR models. This result is confirmed by a comparison of the properties of the RRLs in our sample with the ones expected for the best-fit models. For example, Fig. 2.16 shows the fraction of RRLs in our sample in different observed magnitude bins (black points) compared to the predicted

distribution for different halo models (assuming a SPL, see Tab. 2.13). The SH and the SP models predict too low a fraction of stars at lower  $G$  and a significant excess around  $G = 15$ , while the DN and the TR models give a good match to the data.

As a further refinement we tested the  $\text{DN}^q$  and  $\text{TR}^q$  models. Allowing  $q$  to vary, we obtained a better description of the distribution of RRLs as shown by the decreases of the BICs in Tab. 2.13. The variation of the flattening is quite significant as it is shown in Fig. 2.17. The halo is largely flattened ( $q \approx 0.57$ ) in the very inner part and then it becomes more spherical reaching a flattening of about 0.75 at the border of the Galactic volume analysed in this work ( $r_e \approx 30$  kpc). These results are in agreement with what we have seen directly in the distribution of stars in the  $r_e$ - $\theta$  plane in Sec. 2.2.3 and Fig. 2.10. Essentially the same result is obtained by considering the stars only above or only below the Galactic plane. Fig. 2.18 shows the comparison between the magnitude distribution of the stars in our sample and the one expected for the varying  $q$  model.

In the (non-tilted) TR and the DP models the elongated axis makes an (anticlockwise) angle  $\gamma \approx -20^\circ$  with respect to the positive part of the Galactic Y-axis. It is interesting to compare the orientation of the halo principal axes to the one of the Galactic bar. The orientation of the Galactic bar  $\Phi_{\text{bar}}$ <sup>4</sup> is uncertain (Antoja et al., 2014), depending on the works it ranges from about  $-10^\circ$  (e.g. Robin et al. 2012) to about  $-45^\circ$  (e.g. Benjamin et al. 2005). Given these large uncertainties, the angle  $\gamma$  can be considered compatible with  $\Phi_{\text{bar}}$ . Since gamma represents the angle between the X-axis/Y-axis of the halo and the X-axis/Y-axis of the Galactic frame of reference, the orientation of the bar is compatible with the X-axis of the halo. In other terms, the elongated axis (Y-axis) of the halo is almost perpendicular to the orientation of the Galactic bar. It is unclear if this correlation is a coincidence, due to the large errors, or if it reflects a real link between the two structures. For the purpose of this work, we note that the fact that the elongated axis is almost perpendicular to the Galactic bar rules out the hypothesis that the fit has been influenced by some contaminants coming from the inner Galactic bar.

### Tilt and offset

As a final analysis, we considered halo models that can be tilted with respect to the Galactic plane and offset from the Galactic centre (see Sec. 2.3.2). We added these refinements to the SPL-TR model.

For the offset model, the best-fit parameters are

- $X_{\text{off}} = 0.39 \pm 0.05$  kpc,
- $Y_{\text{off}} = -0.17 \pm 0.06$  kpc,

---

<sup>4</sup> $\Phi_{\text{bar}}$  is defined as the anticlockwise angle between the direction of the bar and the Galactic X-axis.

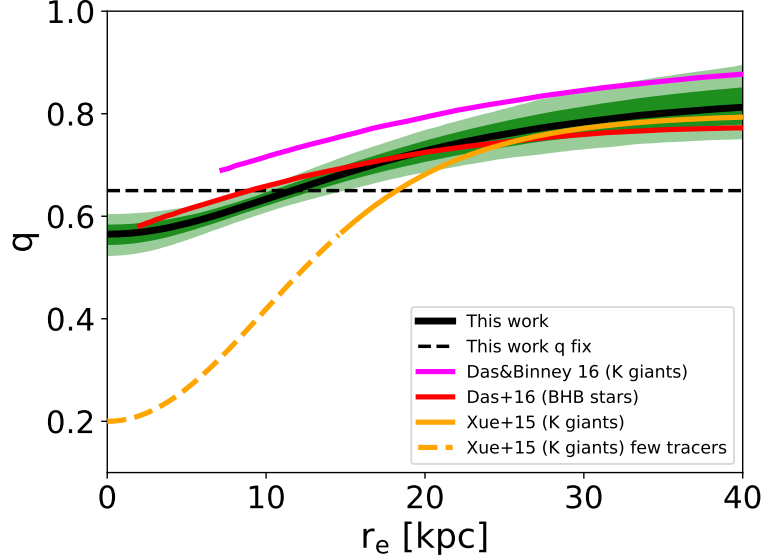


**Figure 2.17:** Halo flattening,  $q$ , as a function of the elliptical radius  $r_e$  (Eq. 2.9). The black solid-line shows the median of the functional-form distribution of  $q$  obtained for our best halo model (SPL-TR<sup>qv</sup>; last row in Tab. 2.13) while the dark and light green bands indicate the 68% and 95% confidence intervals. The dashed line indicates the best-fit  $q$  obtained for the SPL-TR halo model (8th row in Tab. 2.13). The orange curve shows the best-fit functional form of  $q$  found in Xue et al. (2015) using a sample of K giants. The other curves show the non-parametric estimate of  $q$  from Das & Binney (2016) (magenta line) using a sample of K giants stars and from Das, Williams & Binney (2016) (red line) using a sample of BHB stars. Concerning the best-fit parametric functional forms of Das, Williams & Binney (2016), we note that they found a profile that is very similar to the one of Xue et al. (2015) (practically coincident, except at the innermost radii). In the work of Xue et al. (2015),  $q$  is a function of the spherical radius  $D_g$  rather than the elliptical radius  $r_e$ . In order to compare their and our results the orange line has been calculated along the Galactic vertical direction where  $X_g = Y_g = 0$ ,  $D_g = Z_g$  (Eq. 2.5) and  $r_e q(r_e) = Z_g$  (Eq. 2.9). In this case our estimate of the flattening  $q$  at  $r_e$  should be compared with their estimates calculated at  $D_g = qr_e$ .

- $Z_{\text{off}} = -0.01 \pm 0.01$  kpc,

and the size of the displacement vector with respect to the Galactic centre is  $D_{\text{off}} = 0.43 \pm 0.07$ . The offset we found is small and quite insignificant compared to the radial extent of the halo. Indeed these small values could also be due to the over-fitting of some local substructure at small elliptical radii. Moreover, both the posterior distribution of  $Y_{\text{off}}$  and  $Z_{\text{off}}$  are compatible (within  $3\sigma$  and  $1\sigma$ , respectively) with 0 and most of the displacement is along the Galactic X-axis. This axis connects the Sun to the Galactic centre, therefore the offset in this direction can be also interpreted as changing the distance of the Sun from the Galactic centre. Considering our results, the estimated Sun position is  $X_{\odot} = 7.61 \pm 0.05$  kpc, which is totally compatible with the Sun-distance estimates in literature (e.g. McMillan &

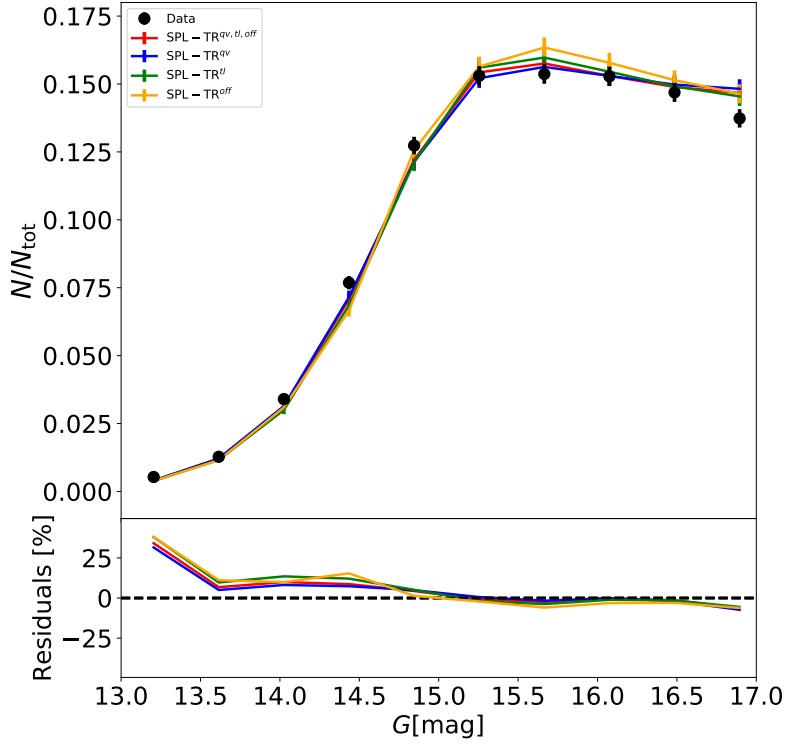


**Figure 2.18:** As in Fig. 2.14 but for triaxial halo models with varying  $q$  (blue), halo tilt (green), centre offset (yellow) and a combination of the previous models (red), see Sec. 2.3.4 for further details.

Binney 2010).

For the tilt model, we take the triaxial model and allow the axes of symmetry to be arbitrarily oriented. The best-fit results for the (anticlockwise) angles describing the orientation of the halo (see Sec. 2.3.2) are

- $\gamma = -20.1^\circ \pm 2.7^\circ$  (rotation around the Z-axis),
- $\beta = 5.7^\circ \pm 0.8^\circ$  (rotation around the new Y-axis),
- $\eta = 3.13^\circ \pm 0.5^\circ$  (rotation around the final X-axis).

The angle  $\gamma$  represents the tilt of the elongated axis of the halo with respect to the Galactic Y-axis and it is compatible with the orientation found for the non-tilted DN and TR disc-plane models (Tab. 2.13). The angles  $\beta$  and  $\eta$  measure the tilt of the halo meridional plane with respect to the plane of the Galactic disc. Even though the BIC indicates a mild improvement with respect to the non-tilted triaxial model ( $\Delta\text{BIC} \approx -40$ ), the tilt is quite small.

Finally, we compared the ability of tilted and non-tilted models to reproduce the observed distribution of stars. Fig. 2.18 shows the comparison between data and

different models for the magnitude distribution of the stars. The models are  $TR^{qv}$ ,  $TR^{tl}$ ,  $TR^{off}$  and  $TR^{qv,tl,off}$ . Note that all of them are capable to give a good match to the data.

In conclusion, we conservatively assume that there is no need for a significant tilt to describe the RRL distribution in the inner halo.

## 2.4 Discussion

### 2.4.1 Best halo model

We have explored the properties of the Galactic stellar halo using two independent methods. First, we analysed the density of the RR Lyrae candidates binned along the Z and R dimensions. This direct method was followed by an approach where the probability of observing each individual star in the space spanned by celestial coordinates and the apparent magnitude was described by a 3D model, whose parameters were optimized using mcmc likelihood sampling. Additionally, we augmented each method with a model comparison exercise. The results of the direct analysis (Sec. 2.2) and the maximum likelihood fit (Sec. 2.3) are highly compatible. Namely, i) the density of the RRL stars in the inner 25 kpc of the halo appears to be stratified on ellipsoids with a pronounced flattening along the Galactic Z-axis (Fig. 2.8), and ii) the radial density profile can be described by a single power-law (SPL, Fig. 2.9). While - as evidenced by Tab. 2.13 - this simple model gives an adequate description of the RRLs density distribution, it can be further refined by adding a mild elongation in the Galactic plane in combination with a radially varying flattening (along the Z-axis). Based on the BIC analysis (Sec. 2.3.4) as well as the direct comparison between the properties of the data and the best-fit models, we chose to highlight this SPL- $TR^{qv}$  (last row in Tab. 2.13) as the best-performing model amongst the family examined.

The distribution of the RRLs in the inner halo as described by the above best-fit model has the following properties: the radial density is an SPL power-law with an exponent  $\alpha = 2.96 \pm 0.05$  and the iso-density surfaces of triaxial shape. The minor axis of the density ellipsoids is aligned with the Galactic Z-axis. We find strong evidence for an evolution of the vertical density flattening: the inner parts are squashed with ( $q \approx 0.57$ ), however the flattening becomes less pronounced ( $q \approx 0.75$ ) at the border of the Galactic volume analysed in this work ( $r_e \approx 30$  kpc). Note that the signs of the evolution of the halo flattening can be observed in the data directly as demonstrated in Fig. 2.10. In the plane of Galactocentric latitude and elliptical radius, the iso-density contours should appear vertical for the correct (and constant) value of  $q$ . Clearly, the contours are slanted in the left and the right panels of the Figure, where the halo flattening is over- and under-estimated correspondingly.

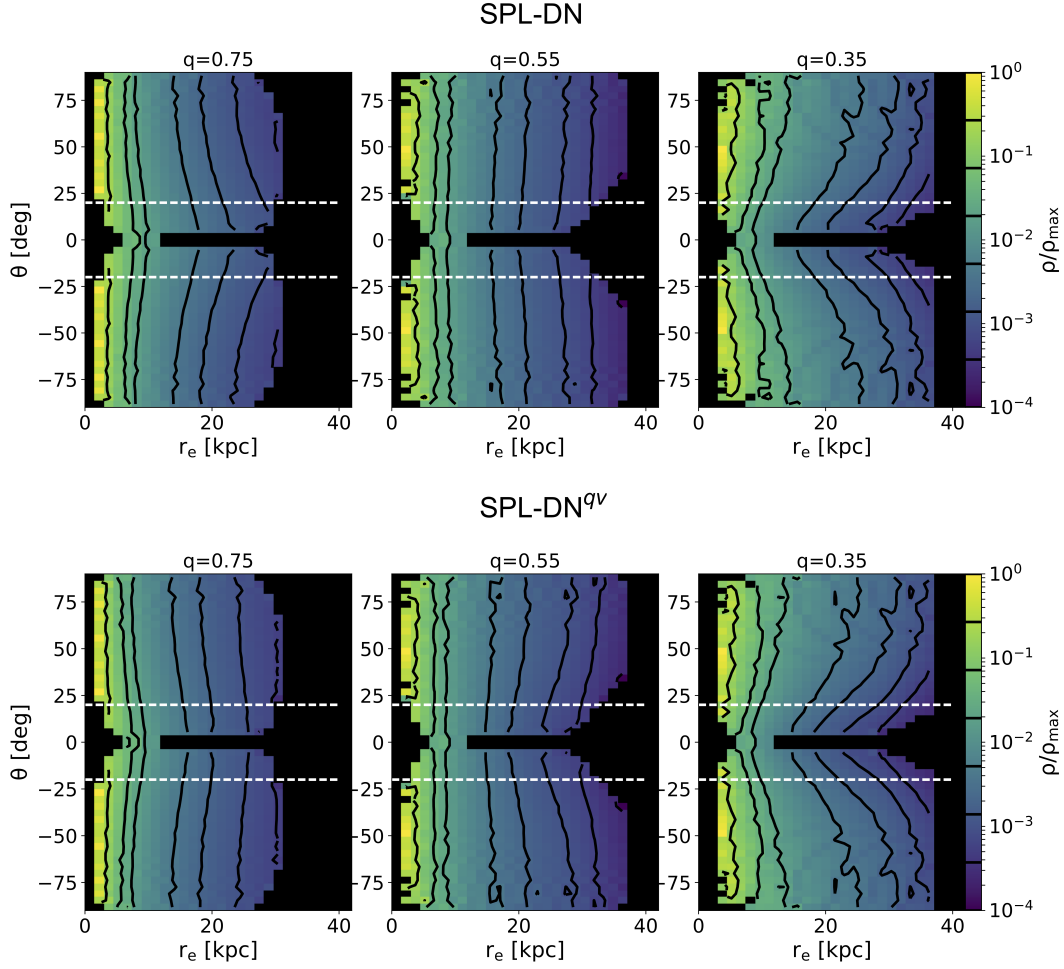


**Figure 2.19:** Same as in Fig. 2.10 but for mock stellar halos. **Top:** density maps for the best-fit SPL-DN model. **Bottom:** density maps for the best-fit SPL-DN<sup>qv</sup> (see Tab. 2.13). The maps have been obtained by averaging over 1000 halo mock realisations. Note that for a halo with a fixed flattening, for the (almost) correct value of  $q$  (middle panel) the iso-density contours remain vertical across the whole range of elliptical radii. This is at odds with the RRL distribution in the Milky Way. As the middle panel of Fig. 2.10 demonstrates, the contours indeed start vertical for  $r_e < 20$  kpc, but at larger radii there is a noticeable bending away from the centre. Our best-fit model with varying  $q$  displays exactly the same behaviour (see middle panel of bottom row).

However, in the middle panel (corresponding to our best-fit fixed  $q$  model), for a large range of radii, the iso-density contours do look vertical. Beyond 20 kpc, the contours start to bend away from the Galactic centre, signalling a change in the halo shape. Fig. 2.19 illustrates the effect of the radial halo shape evolution with the  $\theta - r_e$  views of the mock RRL realisations for two of our best-fit (in each class) models. Note that the middle panel in the bottom row of the Figure displays the same trend as the middle panel of Fig. 2.10, albeit with a lot less noise. With regards to the halo’s major axis, in the Galactic plane, we measure a mild elongation

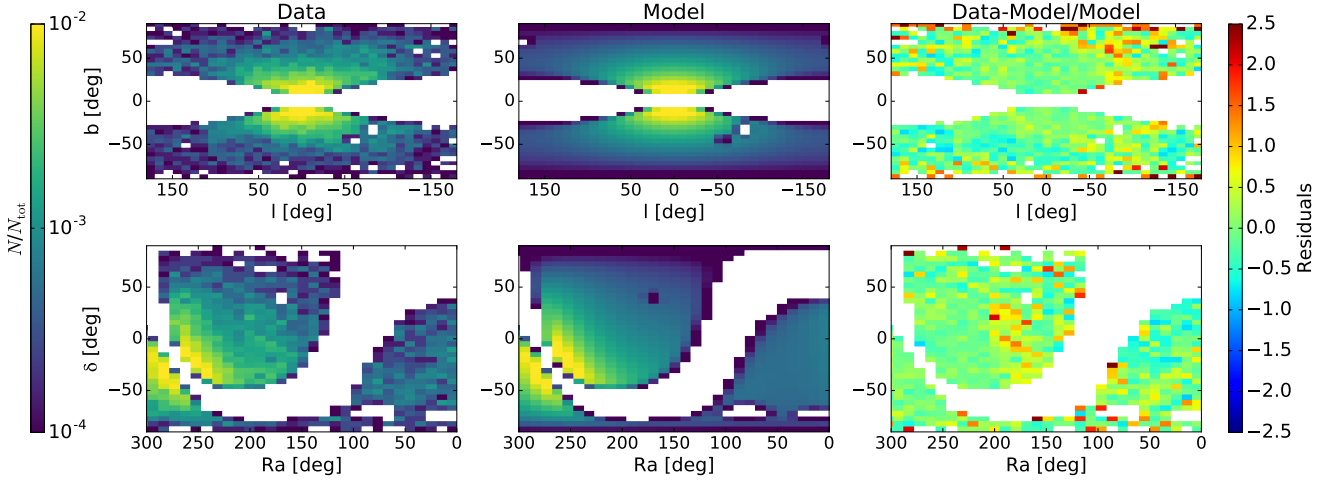


**Figure 2.20:** **Top panels:** all-sky star number density maps in Galactic coordinates. **Bottom panels:** sky-maps density plots in equatorial coordinates. The **left-hand panels** show the data, while the **middle panels** show our best model (SPL-TR<sup>qv</sup>, see Sec. 2.4.1 and Tab. 2.13), the **right-hand panels** show the relative data-model residuals. The model maps have been obtained integrating the star density distribution (Eq. 2.21) through the magnitude interval  $10 < G < 17.1$  assuming a constant absolute magnitude  $M = M_{\text{RRL}} = 0.525$ .

( $p = 1.27 \pm 0.03$ ) in the direction which is rotated with respect to the Galactic Y-axis by  $\gamma = -21.3^\circ \pm 2.6^\circ$  (anticlockwise).

The measured RRL (as represented by the clean sample, see Sec. 2.3.1) distribution can be compared to the best-fit model in Figs. 2.20, 2.21 and 2.22. Fig. 2.20 presents all-sky maps in both Galactic (top panels) and equatorial (bottom) coordinates. Fig. 2.21 gives the number density in the meridional plane, and, finally, Fig. 2.22 shows the number density in the  $r_e - \theta$  space. In each Figure, the right-most column displays the map of residuals in the corresponding projection.

Reassuringly, the residual maps indicate that the model gives a reasonable description of the RRL distribution in the G2M sample. Overall, the Milky Way's inner halo appears smooth, but some systematic model-data mismatches are visible. The most prominent (with residuals in some pixels corresponding to a density excess of order of 200%) is the overdensity of stars visible in Fig. 2.20 at Galactic longitudes around  $-70^\circ$  or RA of about  $190^\circ$ . This structure is also discernible in Fig. 2.21 for  $Z_g > 15$  kpc and at about  $r_e = 35$  kpc and above  $\theta = 50^\circ$  in Fig. 2.22. Most likely, this large stellar cloud is related to the Virgo over-density, as discussed in Sec. 2.2.3.

Amongst other differences, a mild deficiency of stars is visible at the edge of the Galactic volume (available to us) in the anti-centre direction, i.e. around  $l=180^\circ$ .

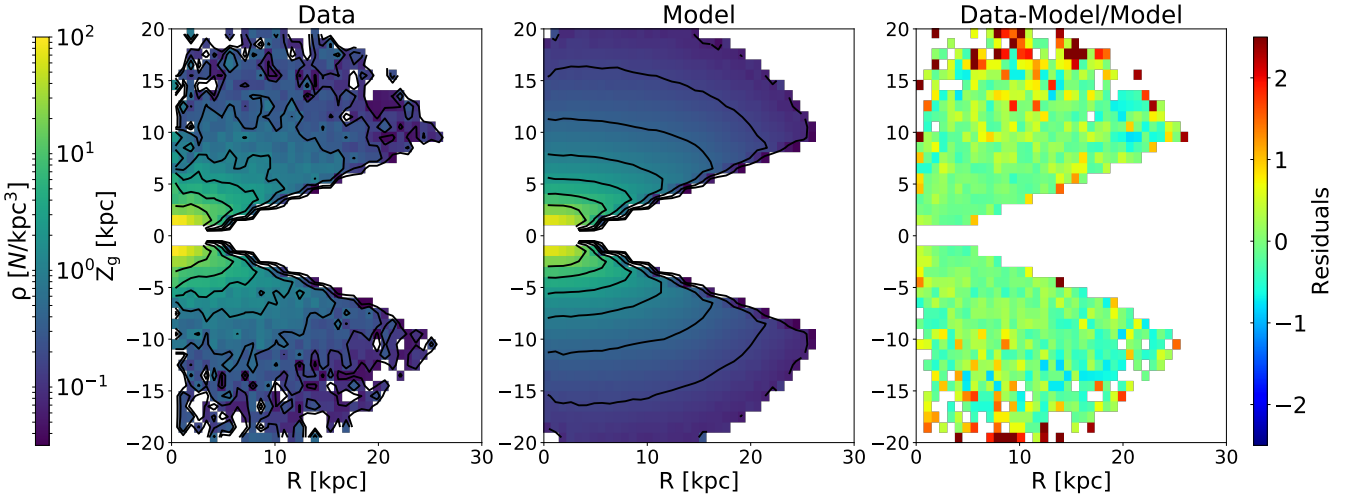


**Figure 2.21:** Number density in the Galactic  $R - Z_g$  plane. **Left-hand panel:** density map for the RRLs in our clean sample (Sec. 2.3.1); **middle panel:** density map for our best model (SPL-TR<sup>qv</sup>, see Sec. 2.4.1); **right-hand panel:** relative data-model residuals. The black iso-density contours are plotted with interval of  $\Delta \log \rho = 0.4$  from  $\log \rho = -3$  to  $\log \rho = 4$ , where  $\rho$  has the dimension  $\text{kpc}^{-3}$ . The model map has been obtained averaging the maps of 1000 different mock catalogues made assuming the best-fit parameters obtained for the SPL-TR<sup>qv</sup> halo model (see Tab.2.13).

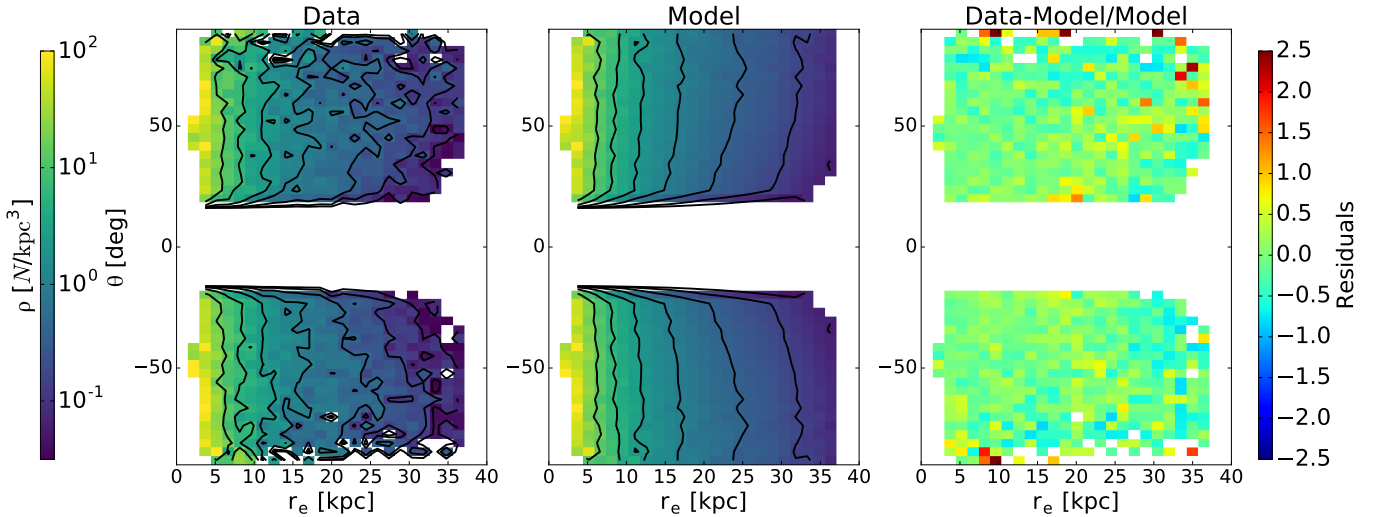


**Figure 2.22:** Same as in Fig. 2.21 but for the number density in the Galactic  $r_e - \theta$  plane. The  $r_e$  in the plot have been obtained assuming  $q = 0.6$  and  $p = 1$  (see Sec. 2.2.3).

This mild depletion is especially noticeable below the Galactic plane, however the amplitude of these outer Galaxy residuals is much smaller as compared to the mismatch caused by the Virgo over-density. We argue that this deficiency of stars may be a hint of the steepening of the radial density profile, but, as discussed in Sec. 2.3,

it does not obey the smooth parametric model considered here.

### 2.4.2 Possible sources of bias in the maximum likelihood analysis

#### Assumption on the absolute magnitude

Our halo fitting method (Sec. 2.3.4) relies on the assumption that all RRLs in the sample have the same absolute magnitude  $M_{\text{RRL}} = 0.525$ . However, as Fig. 2.3 demonstrates, this is not strictly true as indicated by the Gaussian-like wings in the  $M_G$  distribution. To understand the possible bias introduced by this simplification, we assumed that the pdf of the absolute magnitude  $P(M)$  in Eq. 2.22 is represented by the best-fit double Gaussian (blue line in Fig. 2.3). With this addition to the model, we repeated the fit of our best halo model (Sec. 2.3.3), this time marginalising the likelihood over  $M$ . Perhaps unsurprisingly, the final posterior distributions of the model parameters are totally compatible with the ones obtained assuming a constant absolute magnitude.

#### Dust

Regions with high dust extinction add severe uncertainties in the study of distribution of stars in the Galaxy. In these regions it is difficult to recover the faintest stars and the completeness could be much lower compared to the rest of the sky. Note however, that applying the cut on  $\theta$  (Sec. 2.3.1), we eliminated most of the regions with high Galactic dust extinction: the 85% of the stars in our “clean” sample has  $E(B - V) < 0.25$  and only the 1% are located in regions with  $E(B - V) > 0.8$ . To be sure that our results are not influenced by the regions with high reddening, we repeated the fit of our best halo model (Sec. 2.4.1) masking the regions with  $E(B - V) > 0.4$ . We did not find any appreciable differences with respect to the un-masked analysis.

#### Contamination from the Galactic disc

The final results of the fitting analysis (Sec. 2.3.4) have been obtained considering the presence of only one smooth stellar component, however disc RRLs (if any) and other disc variables, including artefacts (see Sec. 2.1.2) could pollute our sample. Although the cut on Galactic  $b$  (Sec. 2.1.2) and  $\theta$  (Sec. 2.3.1) is employed to limit such contamination, we repeated the modelling with the addition of an extra disc component. Thus, this new model has contribution from an ellipsoidal halo with normalised density  $\tilde{\rho}_h$  (Sec. 2.3.2) as well as a double-exponential disc with normalised density  $\tilde{\rho}_d \propto \exp[-R/R_d] \exp[-|Z|/Z_d]$ . Here  $R_d$  and  $Z_d$  are the radial and the vertical disc scale-lengths. Considering the two components, the global pdf of

the stellar distribution is

$$\tilde{\lambda}(m, l, b | f, \vec{\mu}_h, \vec{\mu}_d) = (1 - f)\tilde{\lambda}_h(m, l, b | \vec{\mu}_h) + f\tilde{\lambda}_d(m, l, b | \vec{\mu}_d), \quad (2.31)$$

where  $\tilde{\lambda}_h$  and  $\tilde{\lambda}_d$  represent the pdf of the halo and the disc stars, while  $f$  is the the disc-to-total stellar number ratio. The pdfs that appear in Eq. 2.31 above have been already marginalised over the absolute magnitude distribution of the halo and disc stars. For the halo we used a Dirac delta centred on  $M = M_{\text{RRL}} = 0.525$  (Sec. 2.1.2), while for the disc a uniform distribution between  $M = -2$  and  $M = 5$ . The absolute magnitude distribution of the stars in the disc could be much more complicated with respect to a uniform distribution. However, making use of mock catalogues we found that our assumption is a good choice to minimise the bias also in the presence of a truly complicated multi-peak distribution.

The RRL sample was modelled (Sec. 2.3.3) using Eq. 2.31 in the logarithmic likelihood in Eq. 2.25: we considered  $f$  as a free parameter, but fixed the disc’s stellar density profile assuming values for  $R_d$  and  $Z_d$ . We tested a wide range of thin and thick disc models using  $R_d$  values between 2 and 4 kpc and  $Z_d$  values between 0.1 and 1 kpc. In general, we did not find significant differences with respect to the results shown in Tab. 2.13, except for the SH and DP models. In these two cases, the models try to reproduce the vertical flattening observed in the data with an high-percentage of disc stars, but the final fits are poor as evidenced by the presence of large residuals. For all the other models considered we found that the final posterior distribution for  $f$  is lower than 3% and is consistent with 0. Therefore, we conclude that our “clean” sample (Sec. 2.3.1) does not harbour stars coming from the Galactic disc and the observed flattening along the vertical direction is a genuine property of the distribution of RRLs in the halo.

### 2.4.3 Halo substructures

The main focus of this work is the study of the overall distribution of RRLs in the inner halo. Reinforcing the principal assumption behind the modelling, the distribution of RRLs in our sample appears smooth. Nonetheless, several substructures are present, of which the following two are the most obvious: i) a highly flattened distribution of stars at low Galactic latitudes and ii) an excess of stars at high  $Z_g$ . The first substructure is clearly evident in Fig. 2.8 and in Fig. 2.10 below  $\theta = 20^\circ$ . In our investigation of this substructure we have attempted two approaches: first, we tried to exclude the regions most affected, i.e. those close to the disc from influencing the halo fit, and, second, we aimed to model the excess as a contamination coming from the Galactic disc. In particular, we repeated the fit using our original catalogue of about 22600 RRLs (see Tab. 2.2) and the halo+disc stellar pdf defined in Eq. 2.31. The disc in the model was a realistic double exponential distribution:

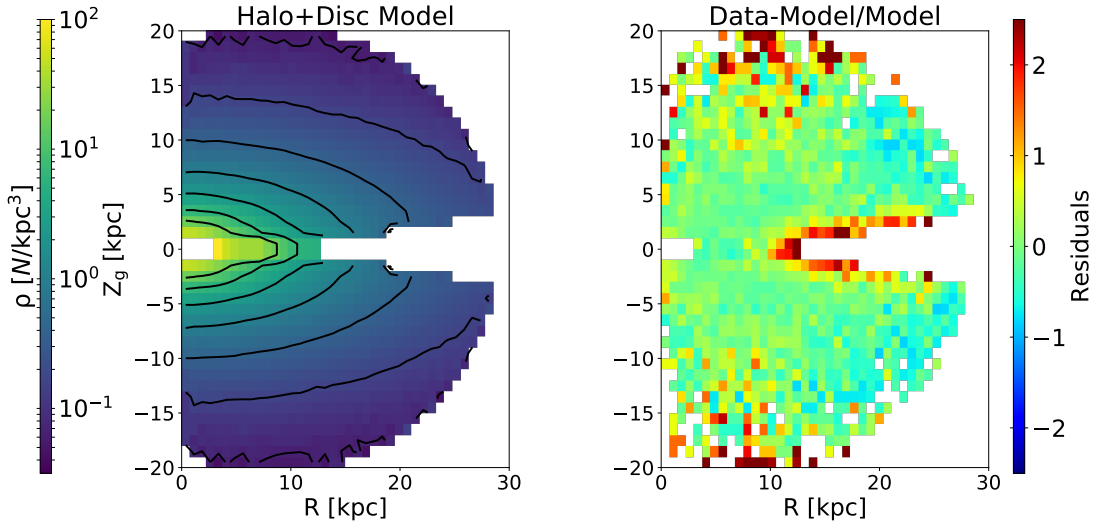


**Figure 2.23: Left-hand panel:** number density of stars in the Galactic  $R - Z_g$  plane for a multi-component model with an halo and a disc; the black iso-density contours are plotted with interval of  $\Delta \log \rho = 0.4$  from  $\log \rho = -3$  to  $\log \rho = 4$ , where  $\rho$  are in unit of  $\text{kpc}^{-3}$ . **Right-hand panel:** relative residuals ( $\text{Data-Model}/\text{Model}$ ) between the density in the  $R - Z_g$  plane for our complete sample of RRLs as shown in Fig. 2.8 and the model shown in the left-hand panel. The model map has been obtained averaging the maps of 1000 different mock catalogues made assuming the best-fit parameters obtained for the disc + SPL-DN halo model (See 2.4.3). The stars in the disc follow a double exponential distribution with a radial scale length  $R_d = 2.7$  kpc and a vertical scale height  $Z_d = 0.2$  kpc.

we fixed the radial ( $R_d$ ) and vertical ( $Z_d$ ) thin and thick disc scale-lengths to the classical values found in literature (e.g. Das, Williams & Binney 2016). Fig. 2.23 gives the density distribution in the  $R - Z_g$  plane for a disc+halo model in which the disc has  $R_d = 2.7$  kpc and  $Z_d = 0.2$  kpc. As illustrated by the residual map (right panel), the halo+disc model is able to explain the flattened distribution of stars but only within about 10 kpc. As a consequence, the posterior distribution of the halo parameters favours a more flattened density ( $q \approx 0.4$ ), thus concealing the evidence of the radial variation of  $q$ , as measured and discussed above (Tab.2.13) as part of the analysis of the “clean” sample of RRLs (Sec. 2.3.1). The residuals suggest that the two-component model gives a poor fit with a significant mismatch both at low  $Z_g$  for  $R > 10$  kpc and at high  $Z_g$  for  $R < 10$  kpc. Note that these results do not change if different values for the disc scale lengths are assumed ( $R_d$  between 2 and 4 kpc and  $Z_d$  between 0.1 and 1 kpc). As a further test, we repeated the fit leaving the scale lengths of the disc model as free parameters. This test yielded unrealistically large values of  $R_d \approx 25$  kpc and  $Z_d \approx 3$  kpc. This can be compared to the results of the study of the thick disc’s RR Lyrae by Mateu et al. (2011) who find the disc to be “anti-truncated”, i.e. having a flatter density profile

in the outer parts. In conclusion, it seems that this flat and elongated structure can not be modelled simply by adding a double exponential disc with the properties expected for the Milky Way. Instead, we conjecture that the observed excess could possibly be related to the Monoceros Ring (Newberg et al., 2002). Notice, however that it is still debated (see de Boer, Belokurov & Koposov, 2017, and references therein) whether Monoceros represents a portion of the accreted halo (e.g. Sollima et al. 2011) or a structure related to the Galactic disc such as a warp and/or a flare in the outer disc (e.g. López-Corredoira & Molgó 2014).

Another, a more prosaic, explanation could simply mean that the excess of stars at low latitude is due to *Gaia* artefacts such as the cross-match failures (discussed in Belokurov et al. 2017). Such conclusion is supported by the fact that no survey so far has reported a clear detection of RRL in the Monoceros Ring. Additionally, this structure is not observed in a sample of metal poor K-Giants  $[\text{Fe}/\text{h}] < -1$  from the LAMOST (Large Sky Area Multi-Object Fibre Spectroscopic Telescope) survey (Liu et al., 2017). Of course, Monoceros Ring is indeed a prominent feature of the stellar density maps in the direction of the Galactic anti-centre. However, so far it has only been traced by typical disc stellar populations such as metal-rich MS stars (Yanny et al., 2003; Jurić et al., 2008; Morganson et al., 2016) or M giants (see e.g. Crane et al., 2003).

The second substructure is a significant over-density of stars above the Galactic plane: it is visible in the density map in Fig. 2.8 for  $Z_g > 15$  kpc and in Fig. 2.10 for  $\theta > 50^\circ$  and large elliptical radii; it is the cause of the mismatch between the star counts above and below the Galactic plane for  $|Z_g| > 10$  kpc (right-hand panels in Fig. 2.11). Moreover, it is also traced by the significant increases of the residuals in the data-model comparison in Fig. 2.20 and Fig. 2.21. The spatial location and shape of this structure indicate that it is most likely related to the Virgo over-density (Jurić et al., 2008), a large and diffuse halo substructure detected with a variety of tracers, but most notably with horizontal branch stars, such as BHBs and RRL (see Duffau et al., 2006; Vivas & Zinn, 2006; Deason, Belokurov & Evans, 2011; Vivas et al., 2016). As far as the quality of the halo models is concerned, by repeating the fit using the stars only below the Galactic plane, we find that the Virgo Cloud does not strongly influence our final results (see Sec. 2.3.4).

#### 2.4.4 Comparison with other works

Thanks to the all-sky view, stable completeness and substantial purity, we have been able to test Galactic stellar halo models with a degree of complexity previously unexplored. Indeed, our best halo model (SPL-TR<sup>qv</sup>, see Sec. 2.4.1) can not be directly compared with results from other works. In fact, to date, only Deason, Belokurov & Evans (2011) attempted to fit a triaxial model to the stellar halo. They found that the triaxial model does increase the quality of the model of the distribution

Authors	Tracer (1)	Range [kpc] (2)	Slope ( $\alpha$ ) (3)	Axial ratios (4)	Catalogue (5)
Das, Williams & Binney (2016)	BHB	10-70	$\approx -4.7 \pm 0.3$	$q = 0.39 \pm 0.09 \rightarrow 0.81 \pm 0.05$	SegueII
Xue et al. (2015)	K-Giants	10-80	$-4.2 \pm 0.1$	$q = 0.2 \pm 0.1 \rightarrow 0.80 \pm 0.03$	SDSS
Sesar et al. (2013)	RRLs	5-30	$\approx -2.4$	$q \approx 0.65$	LINEAR
Deason, Belokurov & Evans (2011)	BHB	10-80	$-2.3 \pm 0.1$ $R_b \approx 27$ kpc, $-4.6 \pm 0.2$	$q = 0.59 \pm 0.02$	SDSS
De Propris, Harrison & Mares (2010)	BHB	10-100	$\approx -2.5$	$q \approx 1.0$	2dF QSO
Watkins et al. (2009)	RRLs	5-110	$-2.4$ $R_b \approx 25$ kpc, $-4.5$	$q=1$ (assumed)	Stripe82
Jurić et al. (2008)	MSTO	0-20	$\approx -2.8$	$q \approx 0.6$	SDSS
Miceli et al. (2008)	RRLs	3-30	$-3.15 \pm 0.07$	$q = 0.5 \rightarrow 1.0$ (assumed)	SegueII
Vivas & Zinn (2006)	RRLs	4-60	$\approx -2.8$	$q \approx 0.6$	QUEST-1
<b>This work</b>	RRLs	1.5-28	$-2.96 \pm 0.05$	$q = 0.57 \pm 0.02 \rightarrow 0.84 \pm 0.06$ $p = 1.27 \pm 0.03$	<i>Gaia</i> DR1 + 2MASS

**Table 2.24: Galactic halo properties found in a sample of literature works. 1:** used halo tracers, Blue horizontal branch stars (BHB), K-Giants stars (K-Giants), RR Lyrae stars (RRLs), stars near the main-sequence turn-off (MSTO). **2:** range of sampled Galactocentric distances. **3:** exponent of the power-law describing the density profile of the stars in the halo; when two values are present they represent the exponents in the inner part and in the outer part of the halo separated by the transition cylindrical radius  $R_b$ . **4:** results on the shape of the halo iso-density surfaces,  $q$  represents the the Z-to-X axial ratio,  $p$  the Y-to-X axial ratio (if not shown  $p = 1$ ); when two values are present they represent the axial ratio in the inner part and in the outer part of the halo. **5:** Survey or Catalogue used, SDSS (Abazajian et al., 2009), Stripe82 (Sesar et al., 2010), SegueII (Yanny et al., 2009), 2dF QSO (Shanks et al., 2000), QUEST-1 (Vivas et al., 2004), LINEAR (Stokes et al., 2000), *Gaia* DR1 (Gaia Collaboration et al., 2016a), 2MASS (Skrutskie et al., 2006).

of A-colored stars, however they considered this to be an overfit, mainly due to the presence of substructures such as Monoceros and the Sagittarius stream. We have taken care to remove stars that may be related to Monoceros in our modelling (Sec. 2.2 and 2.3.1). With regards to the Sagittarius stream, we have not found any worrying levels of contamination by its members in the volume covered in this analysis. Indeed, a recent work by Liu et al. (2017) shows that the residuals due to the Sagittarius stream are in regions not sampled in our work. Comparing the two triaxial models, the best-fit  $p$  in Deason, Belokurov & Evans (2011) is smaller than 1, while we infer  $p \approx 1.3$ . Pérez-Villegas, Portail & Gerhard (2017) found that, due to the gravitational effect of the bar/bulge, a triaxial distribution of RRLs arises also from an initially oblate distribution of stars. This effect is restricted to a very small Galactic region ( $D_g < 5$  kpc), however gravitational effects at large scale (e.g. the influence of the LMC and/or of the spiral arms) could also cause halo triaxiality outside the innermost region of the Galaxy. In this context, in the future, it will be interesting to study the trend of  $p$  as a function of the elliptical radius as already done in this and previous works for the vertical flattening  $q$  (see below).

Perhaps not totally unexpectedly, we have found strong evidence for the evolution of the shape of the stellar halo as a function of the position in the Galaxy. Both parametric (Sec. 2.3.4) and non-parametric (Sec. 2.2.3) analysis require the flattening of the halo along the Galactic Z-axis to decrease from the inner to the outer regions, i.e.  $q$  to increase at larger distances. Most recently, similar claims

have been put forward in the works of Xue et al. (2015), Das, Williams & Binney (2016), Das & Binney (2016) and Liu et al. (2017) (see Sec. 2.2.3 and Fig. 2.17). The results of Xue et al. (2015) have been obtained by employing the same functional form  $q(r_e)$  used in this work (Eq. 2.15), while Das & Binney (2016) used a non-parametric measure of  $q(r_e)$  estimated by the iso-density contours of their best-fit dynamical model. Finally, Das, Williams & Binney (2016) estimated the flattening using both the methods described above. Fig. 2.17 shows the results of these works compared to our best-fit flattening profile: the non-parametric radial profile of Das, Williams & Binney (2016) is compatible with our results, while the results found in Das & Binney (2016) point towards a distribution of stars that is systematically more spherical. While the best fit parametric functional forms of both Xue et al. (2015) and Das, Williams & Binney (2016) are compatible with our measurement of the flattening trend for  $r_e > 20$  kpc, there are several important differences. First of all, these studies postulated the dependence of  $q$  on the spherical radius. Here, to make our models self-consistent, we chose to express  $q$  as a function of the elliptical radius  $r_e$  (see Eqs. 2.9 and 2.15). Second, the largest discrepancies are at small radii ( $r_e < 15$  kpc): in our best-fitting model  $q$  is almost constant at  $\sim 0.6$ , while in the other works the halo flattening keeps increasing ( $q$  decreasing) towards the centre. For example, around the Galactic centre, ( $q \approx 0.4$  in Das, Williams & Binney 2016 and  $q \approx 0.2$  in Xue et al. 2015). Note however that the samples used in both these studies are actually depleted in stars within 10 kpc from the Galactic centre, and thus the reported behaviour of  $q$  there is an extrapolation rather than a measurement. It is interesting to report that, in a recent work, Xu et al. (2018) analysed the distribution of a sample of metal poor K giants with a novel non-parametric technique and found that the halo becomes almost spherical ( $q > 0.8$ ) already at small elliptical radii ( $r_e \approx 20$  kpc). Curiously, Deason, Belokurov & Evans (2011) found no evidence for the variation of the halo flattening within 40 kpc from the Galactic centre. The reason of these discrepancies is not clear, but we note that both the sky coverage and the halo tracer population is different compared to our study. In conclusion, we are still a long way from a general convergence about the details of the flattening of the stellar halo, even for the same halo tracers. In this respect, we stress again that the superior sky coverage of our study (and of *Gaia* in general) should assure very robust results, especially in the study of the halo flattening.

Our best SPL-DN model (see Tab. 2.13) is highly compatible with the previous results relying on RRLs (see Tab. 2.24) such as Miceli et al. (2008) and Vivas & Zinn (2006), but partially in contrast with the result of Sesar et al. (2013) who found a similar slope outside of 16 kpc but a flatter radial density profile ( $\alpha \approx -1$ ) in the very inner part of the halo. However, the distribution of their RRLs in this region is very clumpy and can not be properly fitted by a simple smooth power-law model. Similarly, Watkins et al. (2009) found that the overall distribution of RRLs

can not be described by a smooth model, but we note that their results are based on a drastically lower sky coverage with respect to this and other RRL-based studies.

Comparing to inference with tracers other than RRL, our best SPL-DN model is in good agreement with the work of Liu et al. (2017) based on RGB stars and to Jurić et al. (2008) who used MS main-sequence and MSTO main-sequence turn-off stars. The studies employing other tracers such as BHB and K-Giants (Das, Williams & Binney, 2016; Xue et al., 2015; Deason, Belokurov & Evans, 2011) derive similar flattening of the halo, but usually report a steeper profile for the density law ( $\alpha > -4$ ) beyond 20-30 kpc. Note however that the work of De Propriis, Harrison & Mares (2010) found a more shallow profile ( $\alpha \approx -2.5$ ) up to 100 kpc. Some of the differences can simply be due to different stars used to trace the Galactic halo. In particular the RRLs tend to be more metal-rich as compared to the BHBs - an important difference given that there is evidence of a metallicity gradient in the halo (Carollo et al., 2007). While we are not sensitive to the changes in the radial density profile outside of 25 kpc, there have been claims that such “break” is an artifact of not taking the shape evolution into account (see e.g. Liu et al., 2017; Xue et al., 2015). Further discussion can be found in Sec. 2.3.4. Table 2.24 summarises the properties of the Galactic stellar halo as reported in the literature.

As a final note, it is important to mention that the distribution of our RRLs is nicely in agreement (in terms of both density profile and halo shape) with the one estimated by Pietrukowicz et al. (2015) for a sample of genuine RRL stars in the Galactic bulge. This result seems to strengthen the hypothesis that the RRL population in the bulge is consistent with being the inward extension of the Galactic stellar halo, as also found in N-body simulations by Pérez-Villegas, Portail & Gerhard (2017).

## 2.5 Summary

In this Chapter, we presented the very first use of the *Gaia* DR1 photometric catalogue to study the properties of the Galactic stellar halo as traced by RR Lyrae. The key points of our study are listed below.

1. We used the method proposed by Belokurov et al. (2017) to mine the *Gaia* DR1 for variable stars in advance of the official variable object release by the Collaboration. It is based on the estimate of the object’s variability, AMP (Eq. 2.1) derived from the *Gaia*’s mean flux and its associated error.
2. Our principal selection cuts are those based on the AMP statistics and the colour index,  $J - G$  obtained from the cross-match between *Gaia* and 2MASS. It is the depth of the latter survey which governs the reach of our most distant RR Lyrae. Our sample extends over the whole sky and contains 21643

stars within a sphere of 20 kpc centred on the Sun, covering an unprecedented fraction of the volume ( $\sim 58\%$ ) of the inner halo ( $R < 28$  kpc). While the overall completeness of our sample can not compete with the levels attained by dedicated RRL surveys, it is stable across the sky and the magnitude range explored - the property most important for robust measurements of the stellar density in the halo. Additionally, we demonstrate that the sample's contamination of non RRL stars is close to zero, and is not expected to exceed  $\sim 10\%$ .

3. Assuming a constant absolute magnitude for all RRLs in our sample ( $M_{\text{RRL}} = 0.525$ ), we analysed their density distribution in the inner Galaxy. To that end, Figure 2.7 presents the first all-sky stellar halo maps. These heliocentric slices reveal a relatively smooth nearby halo, with prominent inter-quadrant asymmetries starting to become noticeable beyond 10 kpc from the Sun.
4. We point out two main substructures superimposed on the otherwise smooth distribution of the Galactic RRLs. One is visible as a highly flattened distribution of stars close to the disc plane, at odds with the more ellipsoidal distribution observed at high  $Z_g$ . It contains a little less than half of the stars in our sample, but given its large radial extent it can not be explained as a contamination of the Galactic disc. It may be related to the Monoceros ring (Newberg et al., 2002), but most likely it is caused by artefacts in the *Gaia* data at low Galactic latitude (see discussion in Belokurov et al., 2017). At high Galactic latitudes, a large over-density of stars is evident, clustered in a region with  $Z_g \approx 15$  kpc and between a Galactic radius of 5-10 kpc, as illustrated in Figure 2.11. This is likely a portion of the well-known Virgo over-density (Jurić et al., 2008) and in a recent work we found that this excess of stars could be related to the Magellanic stream (Boubert et al., 2017). Its counterpart at negative  $Z$  is the Hercules-Aquila Cloud, also discernible in the Figure, on the other side of the Galaxy, beyond the bulge.
5. The RRL density distribution is stratified on ellipsoidal surfaces flattened along the direction perpendicular to the Galactic disc. The density decreases regularly following a power-law, without evidence of an inner-core or any change of slope within the radial range accessible, as demonstrated in Figure 2.9.
6. For the first time, we are able to show the evolution of the halo flattening with radius directly in the data (see Figure 2.10). The Milky Way's stellar halo is rather flat in the inner parts but becomes more spherical at  $R \sim 20$  kpc. A similar property has been glimpsed in the sample of RGB halo stars considered by Liu et al. (2017).
7. To mitigate possible biases associated with the low-latitude excess of the RRL candidates, we extracted a subset of 13713 stars from the original sample. We

applied to this “clean” sample a maximum likelihood fitting method, testing a large variety of halo models. The parameters of our final best-fit model are in good agreement with the results obtained by the non-parametric analysis of the RRLs distribution. The halo is mildly triaxial with its major and intermediate axes in the Galactic plane ( $p = 1.27$ ) and a significant flattening along the Galactic Z-axis which varies from  $q \approx 0.57$  in the centre to  $q \approx 0.75$  at the edge of the radial range analysed. The halo’s major axis is rotated in the anticlockwise direction by a angle  $\gamma \approx -21^\circ$  with respect to the direction of the Galactic Y-axis. The density slope is well approximated by a single power-law with exponent  $\alpha = -2.96$ .

We have demonstrated the power of the *Gaia* data for the Galactic stellar halo exploration. The wealth of the information available in GDR1 is unexpected and signals that a paradigm shift in the halo studies is imminent. One only has to wait for the GDR2 to be unleashed (see Sec. 6.3).

## 2.A Jacobian

The Jacobian needed to go from the set of Cartesian coordinate  $(X,Y,Z)$  to the observed one  $(m,l,b)$  is the determinant of the following matrix (see Sec. 2.3.3):

$$J = \begin{bmatrix} \frac{\partial X}{\partial m} & \frac{\partial X}{\partial l} & \frac{\partial X}{\partial b} \\ \frac{\partial Y}{\partial m} & \frac{\partial Y}{\partial l} & \frac{\partial Y}{\partial b} \\ \frac{\partial Z}{\partial m} & \frac{\partial Z}{\partial l} & \frac{\partial Z}{\partial b} \end{bmatrix}.$$

Therefore, the intrinsic and observed coordinates are related as

$$\begin{cases} X = D_{\odot} \cos l \cos b \\ Y = D_{\odot} \sin l \cos b \\ Z = D_{\odot} \sin b \end{cases}, \quad (2.32)$$

where  $D_{\odot} = 10^{\frac{m-M}{5}-2}$  kpc is the distance of the object from the Sun. The Jacobian matrix becomes

$$J = \begin{bmatrix} dD_{\odot} \cos l \cos b & -D_{\odot} \sin l \cos b & -D_{\odot} \cos l \sin b \\ dD_{\odot} \sin l \cos b & D_{\odot} \cos l \cos b & -D_{\odot} \sin l \sin b \\ dD_{\odot} \sin b & 0 & D_{\odot} \cos b \end{bmatrix}.$$

The determinant is

$$|J| = D_{\odot}^2 dD_{\odot} \cos b = \frac{\ln 10}{5} D_{\odot}^3 \cos b. \quad (2.33)$$

The result of Eq. 2.33 has been obtained for a frame of reference centred at the Sun, however it is also valid for a Galactocentric frame of reference. The two coordinate systems differ only by an additive constant (the distance of the Sun from the Galactic centre) in the first row of the system 2.32, so the determinant is the same in the two cases.

## 2.B Exploration of the parameters space

The exploration of the parameter space is performed evaluating the likelihood in Eq. 2.29, which is a very time-consuming step. The bottleneck of the process is the calculation of the normalisation integral  $V_c$  in Eq. 2.27. Given the presence of the selection function  $W$ , the integrand function is not continuous and shows abrupt decreases to 0 in some regions of the integration domain. For this reason, the classical multi-dimensional quadrature methods are not able to give robust results, so we decided to make use of a Monte Carlo integration technique. In particular, we used the *vegas* algorithm (Lepage, 1978) through its `Python` implementation<sup>5</sup>. The final estimate of the integral comes from the average of  $N_{\text{it}}$  *vegas* runs with  $N_{\text{eval}}$  integrand evaluations. The values of  $N_{\text{it}}$  and  $N_{\text{eval}}$  have been chosen after comparing the results of *vegas* and an adaptive quadrature technique<sup>6</sup> setting  $W=1$  in the integrand (Eq. 2.27). In particular we used two settings:

- *fast* with  $N_{\text{eval}} = 10^5$  and  $N_{\text{it}} = 20$ ;
- *robust* with  $N_{\text{eval}} = 5 \cdot 10^5$  and  $N_{\text{it}} = 100$ .

In principle, we can also divide our integration domain into multiple regions where  $W = 1$  and use the faster quadrature methods. However, given our cut in  $\theta$ , the integral extremes  $G$ ,  $l$  and  $b$  become non-trivially interconnected and further time is expended on their calculation. Moreover, we also note that the time spent by a quadrature integral solver is roughly independent of the dimension of the sample space, therefore  $N$  different evaluations increase the computational time by about  $N$  times. In conclusion, using this approach we do not obtain a significant decrease of the computational time.

In order to have the best compromise between computational time and good sampling of the parameter space we adopt a two-stage procedure.

1. In the first “explorative” stage we sample the parameter space using 200 walkers with 300 steps each after 100 “burn-in” steps and using the *fast* estimate of the normalisation integral (see Sec. 2.3.3). The initial positions of the walkers are randomly extracted from their prior distributions (Tab. 2.12). Given the wide prior ranges (see Tab. 2.12), a large number of walkers is needed to have an unbiased sampling of the posterior distributions.
2. In the second stage we use 48 walkers with 300 steps each after 100 “burn-in” steps using the *robust* estimate of the normalisation integral (see Sec. 2.3.3). The walkers are initially placed in a small region around the parameters for which we obtained the maximum value of the likelihood in the first stage.

<sup>5</sup><https://github.com/gplepage/vegas>

<sup>6</sup><https://github.com/saullocaastro/cubature>

# Chapter 3

---

## LITTLE THINGS in 3D: robust determination of the kinematics of dwarf irregular galaxies<sup>†</sup>

The HI 21 cm emission line is a powerful tool for studying the dynamics of late-type galaxies since it is typically detected well beyond the optical disc and is not affected by dust extinction (see Sec. 1.3). The flat rotation curves of spirals are one of the most robust indications for the existence of dark matter (DM); in particular, gas-rich late-type galaxies are ideal laboratories for studying the properties of DM halos. In this context, dwarf irregular galaxies (dIrrs) are particularly interesting. Unlike large spirals, they appear to be dominated by DM down to their very central regions. Thus, the determination of the DM density distribution is nearly independent of the mass-to-light ratio of the stellar disc (e.g. Casertano & van Gorkom 1991; Côté, Carignan & Freeman 2000).

There are two main approaches to estimate the rotation curve of a HI disc and both are based on the fitting of a tilted-ring model (see Sec. 1.3.3) to the data. In the first (“standard”) method the “data” consist in a 2D velocity field (e.g. Begeman 1987; Schoenmakers, Franx & de Zeeuw 1997); conversely, in the second method the “data” is the full 3D datacube (two spatial dimensions and one spectral dimension, see Sec. 1.3.1).

In this Chapter, we exploit the power of a state-of-the-art 3D fitting software, <sup>3D</sup>BAROLO (hereafter 3DB; Di Teodoro & Fraternali 2015), to study the kinematics of a sample of 17 dIrrs taken from the LITTLE THINGS (hereafter LT) sample (Hunter et al., 2012) and already analysed with a 2D approach in Oh et al.

---

<sup>†</sup>Based on G. Iorio, F. Fraternali, C. Nipoti, E. Di Teodoro, J. I. Read, Battaglia G., 2017, *MNRAS*, 466, 4159. This research made use of the LITTLE THINGS data sample (Hunter et al., 2012).

(2015) (hereafter O15). 3DB has been extensively tested on mock HI datacubes corresponding to low mass isolated dIrrs. In Read et al. (2016) we have shown that the rotation curve is well-recovered even for a star-bursting dwarf, provided that the inclination of the HI disc is higher than  $40^\circ$ . We focus in particular on the correction of the rotational velocity for the pressure support of the chaotic motion of the gas, this process is conceptually similar to the asymmetric-drift correction applied in the study of the velocity distributions of the stars in the galactic disc (Marchuk & Sotnikova, 2017), but it is simplified by the fact that the HI velocity dispersion in discs can be considered isotropic. This correction term is usually applied without considering the errors made in its calculation, but if the velocity dispersion is comparable with the rotational velocity, as is the case of the less massive dIrrs, the uncertainties can be very large and should be taken into account. We developed a method to calculate and propagate the pressure support correction errors: as a result, the quoted errors on the final corrected rotation curves (circular velocity) are a robust description of the real uncertainties.

This chapter is organised as follows. In Section 3.1, we illustrate the sample and the data used in this work. In Section 3.2, we briefly introduce the code 3DB and our working assumptions. In Section 3.3, we describe in detail the analysis applied to our data. In Section 3.4 we discuss the individual galaxies and we compare our results with previous work. A summary is given in Section 3.5. The plots and the tables containing the results for all the galaxies in our sample can be found in the Atlas (Appendix 3.A).

## 3.1 The Data

### 3.1.1 Sample selection

The galaxies used in this work represent a subsample of the galaxies of the LT survey (Hunter et al., 2012) which is a sample of 37 dIrrs and 4 Blue Compact Dwarfs (BCDs) located in the Local Volume within 11 Mpc from the Milky Way. LT combines archival and new HI observations taken with the Very Large Array (VLA) to obtain a very high spatial and spectral resolution dataset (see Table 3.2). The objects in the LT sample have been chosen to be both isolated and representative of the full range of dIrr properties (Hunter et al., 2012).

We built our sample selecting dIrrs that are well-suited to study the circular motion of the HI discs. To this end, we excluded from our selection all the objects seen at low inclination angles and the 4 BCDs. The inclination angle  $i$  is defined as the angle between the plane of the disc and the line of sight such that  $i = 90^\circ$  for an edge-on galaxy and  $i = 0^\circ$  for a face-on galaxy. The estimate of  $i$  in nearly face-on galaxies ( $i < 40^\circ$ ) is extremely difficult both from the kinematic fit (Begeman, 1987)

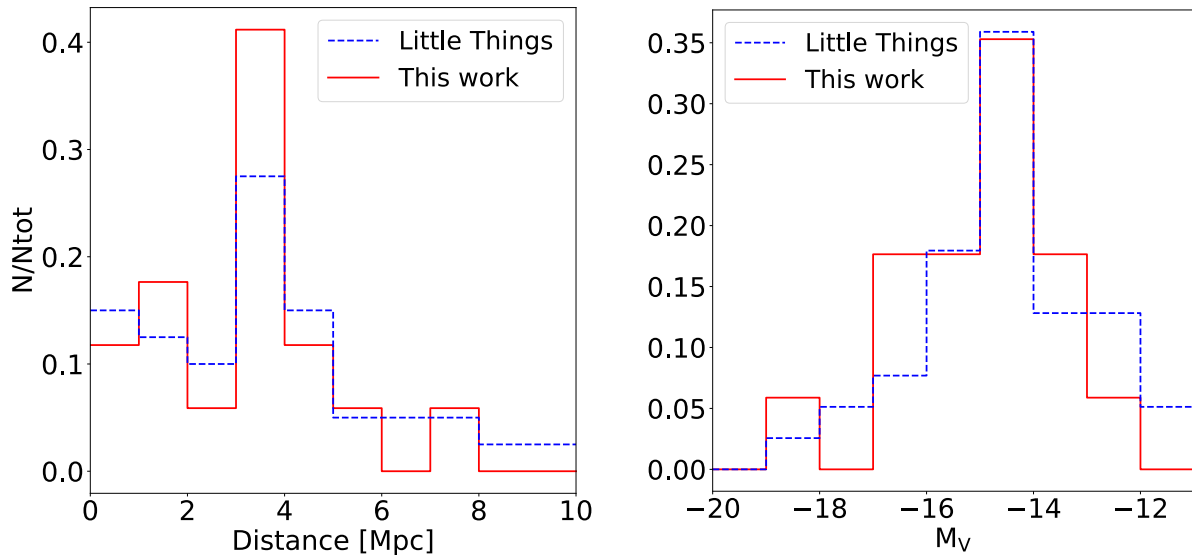


**Figure 3.1:** Distribution of the Galactocentric distances (**left-hand panel**) and of the absolute magnitudes (**right-hand panel**) for the sample of galaxies studied in this work (red histograms) and for the whole LT sample (blue dashed histograms). Data from Hunter et al. (2012) and reference therein.

and from the analysis of the HI map (Read et al., 2016). Moreover, for  $i < 40^\circ$ , relatively small errors on  $i$  have a great impact on the deprojection of the observed rotational velocity (see Eq. 1.6). As a consequence, the final rotation curves of these nearly face-on galaxies could be biased and unreliable with both 2D (Oman et al., 2016) and 3D methods (Read et al., 2016). Among the objects with  $i > 40^\circ$ , we selected 17 dIrrs.

We checked, using a Kolmogorov-Smirnov (KS) test, that our subsample preserves the statistical distribution of the galactic properties such as distance (KS p-value 0.96), absolute magnitude (KS p-value 0.99), star formation rate density (SFRD, KS p-value 0.92) and baryonic mass (KS p-value 0.99). Because of our rejection criterion, the average  $i$  in our subsample ( $58^\circ$ ) is higher than the one measured in the LT sample ( $50^\circ$ ). Figure 3.1 shows the distributions of the distances and of the absolute magnitudes of our sample and the original LT sample.

It is worth pointing out that our rejection criterion is based on  $i$  estimated for the stellar disc using the  $V$ -band photometry (Hunter & Elmegreen, 2006). When we re-estimated  $i$  from the HI datacubes (see Sec. 3.3.2), we found that four galaxies (DDO 47, DDO 50, DDO 53, and DDO 133) have an average  $i$  lower than  $40^\circ$  (see Tab. 3.8). We did not exclude these galaxies from our sample, but our results for these objects should be treated with caution. In particular the formal errors on the velocities and on  $i$  could underestimate the real uncertainties (see notes on the

individual galaxies in Sec. 3.4).

In conclusion, our sample comprises 17 objects covering the stellar mass range  $5 \times 10^5 \lesssim M_*/M_\odot \lesssim 10^8$ , with a mean SFRD of about  $0.006 M_\odot \text{yr}^{-1} \text{kpc}^{-2}$  and a mean specific SFRD (SSFRD) of about  $2.26 \times 10^{-10} \text{yr}^{-1} \text{kpc}^{-2}$  (data from Hunter et al. 2012 and reference therein). For comparison the SFRD and the SSFRD of the complete LT sample are  $0.007 M_\odot \text{yr}^{-1} \text{kpc}^{-2}$  and  $2.95 \times 10^{-10} \text{yr}^{-1} \text{kpc}^{-2}$  respectively (Hunter et al. 2012 and references therein).

### 3.1.2 The Data

The HI datacubes were taken from the publicly available archive of the LT survey<sup>1</sup>. For each galaxy, LT provides two datacubes that differ in the weight scheme used to reduce the raw data: the natural datacube offers the best signal-to-noise ratio, the robust datacube gives the best angular resolution. We preferred the natural datacubes for two main reasons: (i) a high signal-to-noise ratio allows us to have enough sensitivity to extend the study of the kinematics to large radii; (ii) 3D methods are not dramatically influenced by the resolution of the data (see Sec. 3.2). In some cases (DDO 50, DDO 154, NGC 1569, NGC 2366, UGC 8508 and WLM) the galaxies are so extended in the sky that we further smoothed the datacube maintaining a good spatial resolution. Instead, we have chosen the robust datacube when the natural datacube gives too few resolution elements to sample the HI disc (five cases, see Tab. 3.2). The mean spatial resolution is about 240 pc ranging from about 60 pc (DDO 210) to about 460 pc (DDO 87). These data are summarised in Cols. 4-6 of Table 3.2. The rotation curves of all the galaxies in our sample have been already derived with the classical 2D approach in O15. The masses and the surface density profiles of the stellar discs for all the galaxies can be found in Zhang et al. (2012), except for DDO 47 for which they can be found in Makarova (1999) and in Walter & Brinks (2001).

## 3.2 3D BAROLO

In this work we measure the kinematic and geometric properties of the galaxies in our sample with the publicly available software 3DB<sup>2</sup> (Di Teodoro & Fraternali, 2015).

3DB is a 3D method that performs a tilted-ring analysis (see Sec. 1.3.3) on the whole datacube. In practice, for each sampling radius it builds a ring model based on Eq. 1.6, then it calculates the residuals between the emission of the model and of the data pixel-by-pixel along the ring in the datacube. The final parameters of each

<sup>1</sup><https://science.nrao.edu/science/surveys/littlethings>

<sup>2</sup><http://editeodoro.github.io/Bbarolo/>.

Galaxy	D (Mpc) (1)	M <sub>V</sub> (mag) (2)	f <sub>c</sub> (pc arcsec <sup>-1</sup> ) (3)	cube (4)	Beam (arcsec×arcsec) (5)	Ch. sep (km s <sup>-1</sup> ) (6)	M <sub>HI</sub> (10 <sup>7</sup> M <sub>⊙</sub> ) (7)	σ <sub>ch</sub> (mJy beam <sup>-1</sup> ) (8)	σ <sub>3T</sub> (M <sub>⊙</sub> pc <sup>-2</sup> ) (9)
CVnIdwA	3.6	-12.4	17.4	ro	10.9 x 10.5	1.3	4.5 ± 0.1	0.63	0.96
DDO 47	5.2	-15.5	25.2	na	16.1 x 15.3	2.6	35.3 ± 0.6	0.61	0.41
DDO 50	3.4	-16.6	16.5	na†	15.0 x 15.0	2.6	59.5 ± 1.6	0.82	0.65
DDO 52	10.3	-15.4	49.9	na	11.8 x 7.2	2.6	22.3 ± 0.1	0.46	1.20
DDO 53	3.6	-13.8	17.4	ro	6.3 x 5.7	2.6	4.7 ± 0.3	0.57	3.80
DDO 87	7.4	-15.0	35.9	na	12.8 x 11.9	2.6	20.7 ± 1.0	0.51	0.90
DDO 101	6.4	-15.0	31.0	ro	8.3 x 7.0	2.6	1.8 ± 0.2	0.50	0.90
DDO 126	4.9	-14.9	23.7	na	12.2 x 9.3	2.6	12.8 ± 0.1	0.41	1.27
DDO 133	3.5	-14.8	17.0	ro	12.4 x 10.8	2.6	10.0 ± 0.2	0.35	0.89
DDO 154	3.7	-14.2	18.0	na†	15.0 x 15.0	2.6	25.1 ± 0.1	0.44	0.52
DDO 168	4.3	-15.7	20.8	na	15.0 x 15.0	2.6	25.1 ± 0.1	0.47	0.54
DDO 210	0.9	-10.9	4.4	na	16.6 x 14.1	1.3	0.2 ± 0.1	0.75	0.59
DDO 216	1.1	-13.7	5.3	ro	16.2 x 15.4	1.3	0.5 ± 0.1	0.91	0.40
NGC 1569	3.4	-18.2	16.5	na†	15.0 x 15.0	2.6	17.3 ± 0.1	0.77	1.10
NGC 2366	3.4	-16.8	16.5	na†	15.0 x 15.0	2.6	64.0 ± 1.2	0.52	0.59
UGC 8508	2.6	-13.6	12.6	na†	15.0 x 15.0	1.3	1.7 ± 0.1	1.31	0.54
WLM	1.0	-14.4	4.8	na†	25.0 x 25.0	2.6	5.6 ± 0.1	2.00	0.58

**Table 3.2: Properties of the galaxies studied in this work.** - (1) distance in Mpc (Hunter et al. 2012 and references therein); (2) V band absolute magnitude (Hunter et al. 2012 and references therein); (3) conversion factor from arcsec to pc; (4) weighted scheme used to produce the final datacube: "na" for natural "ro" for robust. A † means that we have further smoothed the original datacube to the beam indicated in Col. 5; (5) beam major x minor axis in arcsec of the data used for the kinematic fits (see Sec. 3.1.2); (6) channel separation in km s<sup>-1</sup> (this value indicates also the velocity resolution of the datacube in terms of FWHM); (7) total HI mass (see Sec. 3.3.1); (8) rms noise per channel estimated with 3DB; (9) 3σ pseudo noise in the total map (see Sec. 3.1.1). Note that DDO 87 has a slightly different distance with respect to the one reported in Hunter et al. (2012) because their value is a typo (the correct value is given in Croxall et al. 2009)

ring are found through the minimisation of these residuals. Before the comparison between the datacube and the model, the latter is smoothed to the spatial and spectral instrumental resolution. This ensures full control of the observational effects and in particular a proper account of beam smearing that can strongly affect the derivation of the rotation velocities in the inner regions of dwarf galaxies (see e.g. Swaters 1999). Moreover 3DB fits, at the same time, the rotation velocity and the velocity dispersion instead of treating them as separate components as done in the classical 2D approach (e.g. Tamburro et al. 2009, O15).

In conclusion, 3DB fits up to 8 parameters for each ring in which the galaxy is decomposed: central coordinates, V<sub>sys</sub>, i, PA, HI surface density (Σ), HI thickness (z<sub>d</sub>), V<sub>rot</sub> and the velocity dispersion (σ<sub>v</sub>). 3DB separates the genuine HI emission from the noise by building a mask: only the pixels containing a signal above a certain threshold from the noise are taken into account. The noise estimated with 3DB for each galaxy is reported in the Col. 8 of Table 3.2. Further details on 3DB can be found in Di Teodoro & Fraternali (2015).

3DB works well both on high-resolution and low-resolution data (Di Teodoro & Fraternali, 2015). This allows us to use the optimal compromise between spatial resolution and sensitivity, as already discussed in Sec. 3.1.2. In Read et al. (2016) we showed that 3DB is capable of obtaining a good estimate of the kinematic parameters of mock HI datacubes corresponding to low-mass isolated dIrrs, similar to those that we will study here.

### 3.2.1 Assumptions

As the focus of this work is the kinematics ( $V_{\text{rot}}$  and  $\sigma_v$ ) of the HI discs, we can consider the other 6 variables fitted by 3DB as “nuisance parameters”. We decided to reduce the relatively high number of parameters making assumptions on the HI surface density, HI scale height, systemic velocity and the position of the galactic centre.

- *HI surface density:* we remove the surface density from the list of the free parameters by normalising the flux locally to the value of the total HI map. This approach is also convenient to take into account the asymmetry of the HI distribution and to avoid that regions with peculiar emission (e.g. clumps or holes) affect the global fit (see Lelli et al. 2012a and Lelli et al. 2012b). For a full description of this normalisation technique, see the 3DB reference paper (Di Teodoro & Fraternali 2015).
- *HI scale height:* 3DB includes the possibility to fit the HI scale height. This is something exclusive to 3D methods since there is no information about the scale height in the integrated 2D velocity field. However, the assumption of a thick disc is somewhat inconsistent with the ‘tilted-ring model’ (see Sec. 1.3.3): in the presence of a thick disc along the line of sight we are accumulating emission from different rings, hence a ring-by-ring analysis can not incorporate this effect. To be fully consistent, we should set the value of the scale height  $z_d$  to 0: however, it turns out that, assuming  $z_d = 0$  the galactic models made with 3DB have a too sharp cut-off at the border of rings. Therefore, we assume a Gaussian vertical profile for the gas and we set for all the galaxies a scale height of 100 pc, constant in radius. In Chapter 5 (Sec. 4.3) we show the effect of the presence of a thick disc in the kinematic analysis for three galaxies of our sample.
- *Systemic velocity:* we fix the systemic velocity for all rings to the value calculated as

$$V_{\text{sys}} = 0.5(V_{20_{\text{app}}} + V_{20_{\text{rec}}}), \quad (3.1)$$

where  $V_{20}$  is the velocity where the flux of the global HI profile is 20% of the flux peak, while ‘app’ and ‘rec’ indicate the approaching and the receding

halves of the galaxy.

- *Centre of the galaxy:* we fix the position of the galactic centre for all rings to the value found with one of the methods described in Sec. 3.3.2.

## 3.3 Data Analysis

### 3.3.1 HI total map

Before starting the kinematic fit procedure, for each galaxy we produce HI total maps from the datacubes. This step is needed both to have an initial rough estimate of the geometrical properties of the HI discs and to define the maximum radius to use in the kinematic fit. Moreover, we use it to extract the HI surface density profiles using the best-fit parameters of the disc (Sec. 3.3.2). The HI surface density profile is crucial to correct the estimated rotation curve for the asymmetric drift (Sec. 3.3.3).

### HI spatial distribution

Integrating the signal of each pixel along the spectral axis one obtains a 2D total map that represents the spatial distribution (on the sky) of the HI emission. To build these maps, we masked the original datacube with the following procedure: first we smoothed the original data to obtain a low-resolution cube (between 2 and 3 times the original beam, depending on the galaxy); then, a pixel is included in the mask only if its emission is above a certain threshold (2.5 of the noise  $\sigma_{\text{ch}}$  of the smoothed cube) in at least three adjacent channels. Finally we sum, along the spectral axis, all the flux of the pixel included in the mask obtaining a 2D map. This method produces a very clean final map with only a small contribution from the noise.

Using Eq. 1.2, we can directly relate the intensity of the radio emission ( $S$ ) to the projected surface density of the gas ( $\Sigma_{\text{obs}}$ ) as

$$\frac{\Sigma_{\text{obs}}(x, y)}{\text{M}_{\odot} \text{ pc}^{-2}} = 8794 \left( \frac{S(x, y)}{\text{Jy beam}^{-1}} \right) \left( \frac{\Delta V}{\text{km s}^{-1}} \right) \left( \frac{B_{\text{maj}} B_{\text{min}}}{\text{arcsec}^2} \right)^{-1}, \quad (3.2)$$

where  $B_{\text{maj}}$  and  $B_{\text{min}}$  are the FWHM of the major and minor axis of the beam and  $\Delta V$  is the channel separation of the datacube. We obtained the radial profile of  $\Sigma_{\text{obs}}$  averaging the total map along elliptical rings defined by the disc geometrical parameters (see Sec. 3.3.2). The errors on  $\Sigma_{\text{obs}}$  are calculated as the standard deviation of the averaged values<sup>3</sup>.

<sup>3</sup> Pixels in datacubes are correlated by the convolution with the instrumental beam occurring during the observations. As a consequence, the estimated errors are an underestimate of the real uncertainties (see Sicking 1997). However, the estimated errors for the surface density are already

The intrinsic surface density ( $\Sigma_{\text{int}}$ ) is defined as the density of the HI disc integrated along the vertical axis of the galaxy. Assuming a razor-thin HI disc, the relation between  $\Sigma_{\text{obs}}$  and  $\Sigma_{\text{int}}$  is simply

$$\Sigma_{\text{int}}(R) = \Sigma_{\text{obs}}(R) \cos i, \quad (3.3)$$

because the area of the projected ring is smaller than the one of the intrinsic ring by a factor  $\cos i$ . Throughout this Chapter,  $R$  indicates both the radius of the circular ring and the semi-major axis of its projection (see Sec. 1.3.3). Finally, we can have a measure of the total mass of the HI disc summing the observed surface densities of all pixels in the total map multiplied by the physical area of the pixels

$$\frac{M_{\text{HI}}}{M_{\odot}} = 23.5 \left( \frac{\delta}{\text{arcsec}} \right)^2 \left( \frac{D}{\text{Mpc}} \right)^2 \sum_{\text{pixels}} \left( \frac{\Sigma_{\text{obs}}(x, y)}{M_{\odot} \text{pc}^{-2}} \right), \quad (3.4)$$

where  $\delta$  is the size of the pixel and  $D$  is the distance of the galaxy. To have an estimate of the uncertainties in this measure we have built two other maps: a low-resolution map using the smoothed cube that we used to build the mask and an extremely low-resolution map smoothing again the cube to a beam of 40-60 arcsec. As described above, we clean these maps removing all the pixels that have not a flux larger  $2.5\sigma_{\text{ch}}$  in at least three consecutive channels. We applied the primary beam correction to the total HI map using the task PBCORR of GIPSY (van der Hulst et al., 1992). For each map the mass is estimated using Eq. 3.4 and the method described above. In particular, we take as measure of the disc mass the average and the associated error the standard deviation of the values obtained in the three maps. The final estimates of  $M_{\text{HI}}$  are listed in Table 3.2 (Col. 7). The intrinsic surface density profile and the HI map contours are shown respectively in the box B (bottom right panel) and in the box C (left panel) of the summary plot of each galaxy in the Atlas (Appendix 3.A.1).

Figure 3.3 shows the comparison between the mass estimated with our method and those estimated by O15 and Hunter et al. (2012). The relative difference between our measures and those of O15 is on average 20%, with the largest discrepancies (up to 50%) found at the low-mass end; these differences are mainly due to the different method used to estimate the total mass. The method used in Hunter et al. (2012) is similar to the one used in this work (Hunter et al. 2012 used only robust datacubes while we used both robust and natural datacubes; see Col. 4 in Tab. 3.2): in this case the average relative difference is about 10%. Because of the data-reduction methods used in Hunter et al. (2012), the natural datacubes have systematically

---

very large and we did not correct them. Moreover, the elliptical rings are usually much larger than the beam, so the correlation of the data is not expected to affect significantly the final estimate of the average and the error of the surface density.

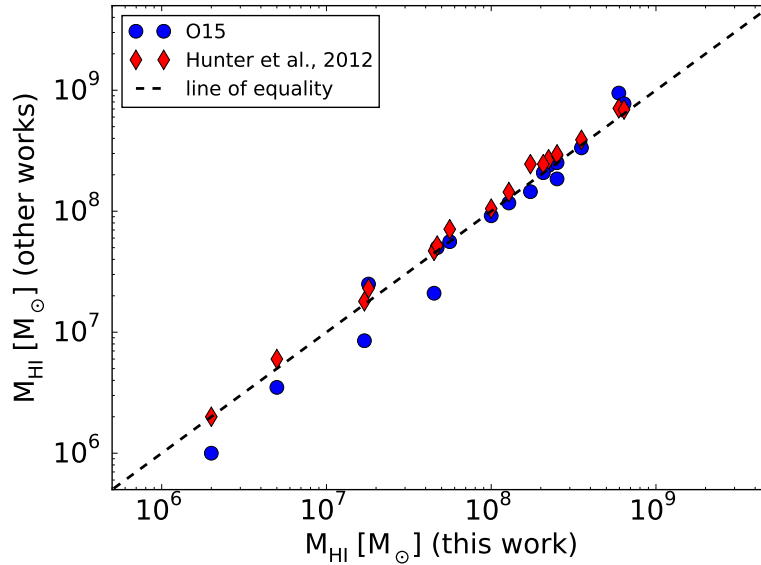


**Figure 3.3:** Comparison of the HI mass estimated in this work and in other works (O15, blue circles; Hunter et al. 2012, red diamonds.)

lower flux with respect to the robust ones (see Hunter et al. 2012 for the details), therefore our values are slightly lower.

### Noise in the total map and maximum radius

In order to define a maximum radius for the HI disc, we need to calculate the noise level in the total map. If we sum  $N$  independent channels each with noise  $\sigma_{\text{ch}}$  the final noise will be equal to  $\sigma_{\text{ch}}\sqrt{N}$ . However, using a mask, the number of summed channels is different from pixel to pixel, moreover the datacubes in our sample have been Hanning-smoothed and adjacent channels are not independent (see Verheijen & Sancisi 2001). To have a final estimate of the noise in the total map we follow the approach of Verheijen & Sancisi (2001) and Lelli, Verheijen & Fraternali (2014b): we constructed a signal-to-noise map and we defined as the  $3\sigma$  pseudo level ( $\sigma_{3T}$ ) the mean value of the pixels with a S/N between 2.75 and 3.25. We fit our kinematic model only to the portion of the datacube within the contour defined by  $\sigma_{3T}$  and avoiding to use rings which do not intercept, around the major axis, HI emission coming from the disc. This ensures a robust estimate of the galactic kinematics avoiding regions of the galaxy dominated by the noise and with poor information about the gas rotation. The  $3\sigma$  pseudo noise levels  $\sigma_{3T}$  are listed in Table 3.2 (Col. 9), while the maximum radii  $R_{\text{max}}$  used in the fit are reported in Table 3.8 (Cols. 1-2).

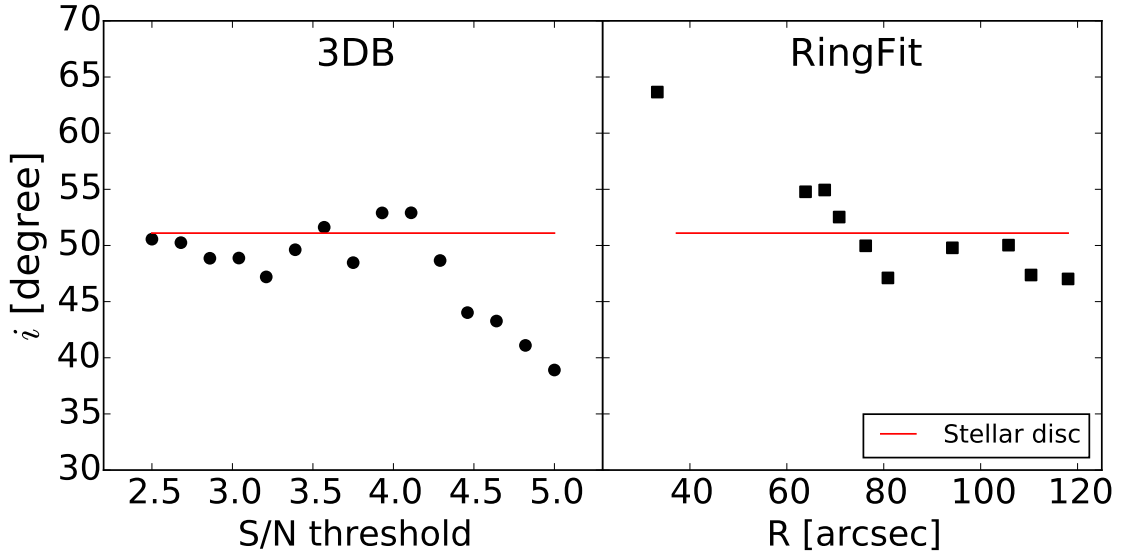


**Figure 3.4:** Initial estimate of the inclination angle for DDO 52 with 3DB (**left-hand panel**) and with the fit of the iso-density contours of the HI total map (**right-hand panel**). The red lines show the inclination of the optical disc. See the text for details.

### 3.3.2 Datacube fit

Given the assumptions we made (Sec. 3.2.1), we are left with two geometrical ( $i$ , PA) and two kinematic ( $V_{\text{rot}}$  and  $\sigma_v$ ) parameters. Eq. 1.6 shows that the rotational velocity and the geometrical parameters are coupled: in particular they become degenerate for galaxies with rising rotation curves (Kamphuis et al., 2015) as it is the case for most of the dIrrs. As a consequence, the fitting algorithm tends to be sensitive to the initial guesses, so it is important to initialise the fit with educated guess values.

#### Initial guesses

We estimate the initial values of the the geometrical parameters (centre,  $i$  and PA) using three different methods:

- *3DB*: 3DB can automatically estimate the geometrical parameters analysing the 0th moment (HI total map) and the 1st moment (velocity field) of the datacube. The  $i$  is estimated by fitting HI model maps to the observed HI total map, while the PA is calculated as the orientation of the line that maximises the velocity gradient in the velocity field. Finally, the centre is estimated as the flux-weighted average position of the source. 3DB builds the total map and the velocity field using a source-finding algorithm (DUCHAMP, Whiting 2012), separating the source pixels from the noise pixels on the basis of a S/N threshold. As a consequence, the final maps and the estimate of the disc

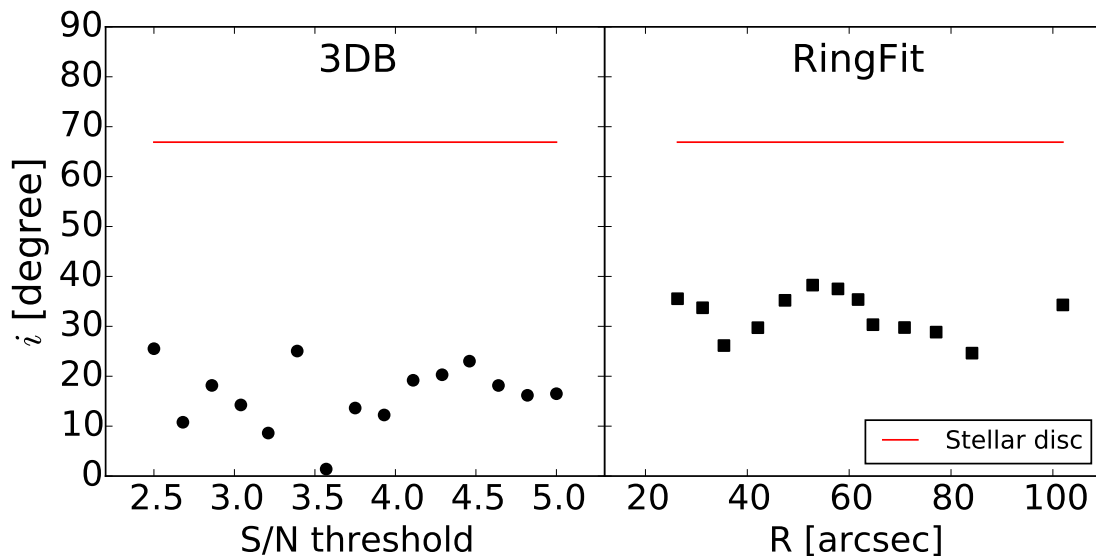


Figure 3.5: Same as Fig. 3.4 but for DDO 210.

parameters depend on the choice of this threshold. For this reason we repeat this analysis using S/N threshold ranging from 2.5 to 5. Finally, we average the values on the range of S/N where the estimated parameters are almost constant.

- *RingFit*: We developed a simple script, called RingFit, to fit ellipses to the iso-density contours at different radii of our total HI maps (Sec. 3.3.1). From the properties of the fitted ellipses we can estimate the geometrical parameters of the HI disc at different radii.
- *Isophotal fitting of the optical maps*: The geometrical parameters are derived from the V-Band photometry by Hunter & Elmegreen (2006).

Figs. 3.4 and 3.5 show two examples of the estimate of  $i$  with the three different methods. In the first case (DDO 52) the methods are in good agreement, while in the second case (DDO 210) the results are not compatible (notice that in this case the HI contours deviate strongly from elliptical shape, see Box C in Fig. 3.21). Usually, the optical disc has a more regular morphology with respect to the HI disc, therefore we give more weight to the geometrical parameters estimated by Hunter & Elmegreen (2006). When the geometry of the stellar and of the HI disc do not show a clear agreement (Fig. 3.5) or the stellar disc presents peculiar features such as strong bars, we use the other two methods. More details can be found in the description of the individual galaxies in Sec. 3.4.

3DB allows to use an azimuthal weighting function  $w(\theta)$  (see Eq. 1.6) to “weigh” the residuals non-uniformly across the rings (see Di Teodoro & Fraternali 2015). We decided to use  $w(\theta) = \cos \theta$  to weigh the most the regions around the major axis,

where most of the information on the galactic rotation lies. If we fit at the same time the four parameters, we can obtain rotation curves and velocity-dispersion profiles that show unphysical discontinuities due to the scatter noise of the geometrical parameters. For this reason, we run 3DB with the option *TWOSTAGE* (see Appendix 3.C) turned on: first a fit with four free parameters is obtained, then the geometrical parameters are regularised with a polynomial, and finally a new fit of only  $V_{\text{rot}}$  and  $\sigma_v$  is obtained. We chose to use the lowest polynomial order allowed by the data: in practice, we set the geometrical parameters to a constant value, unless there is a clear evidence of radial trends of  $i$  and/or of PA as for example in DDO 133 and in DDO 154.

The result of the fit is compared by eye with the real datacube both analysing the position-velocity diagrams (PV, hereafter) along the major axis and the minor axis, and channel by channel. Figures 3.6 and 3.7 show the comparison in the channel maps between the observations and the best-fit model found with 3DB for DDO 154 and NGC 2366: the emission of DDO 154 is reproduced quite well, while the best-fit model found for NGC 2366 traces the global kinematics but it is not able to reproduce the extended feature in the North-West of the galaxy (see e.g. channel at 120 km/s). The presence of such kind of peculiarities makes the study of the dIrrs HI disc kinematics challenging and requires careful visual inspection. Whenever we notice that the model was not a good representation of the data, we restart the fit changing the initial guesses and/or varying the order of the polynomial regularisation.

Concerning the errors on the estimated parameters, it is worth spending a few words about the differences between the standard 2D approach and 3DB. In the first case the errors are a combination of (i) nominal errors coming from the tilted ring fit (typically using a Levenberg-Marquardt algorithm) and (ii) the differences between the fit of the approaching and receding sides. It is well known that nominal errors are very small. The uncertainties are dominated by the difference between the approaching and receding sides, an ‘asymmetric-error’ that is not straightforward to quantify. 3DB uses a Monte Carlo method to estimate the errors further exploring the parameters space around the best fit solutions (see Di Teodoro & Fraternali 2015 for further details), therefore our quoted errors should be a robust and statistically significant measure of the uncertainties of the kinematic parameters.

Given that we use the errors estimated with 3DB, we did not fit separately the approaching and receding halves of the galaxy as often done in the classical 2D methods. The only exception is DDO 126: in this case the best-fit model found with 3DB using the whole galaxy does not give a good representation of the datacube because of the strong kinematic asymmetries (see Sec. 3.4).

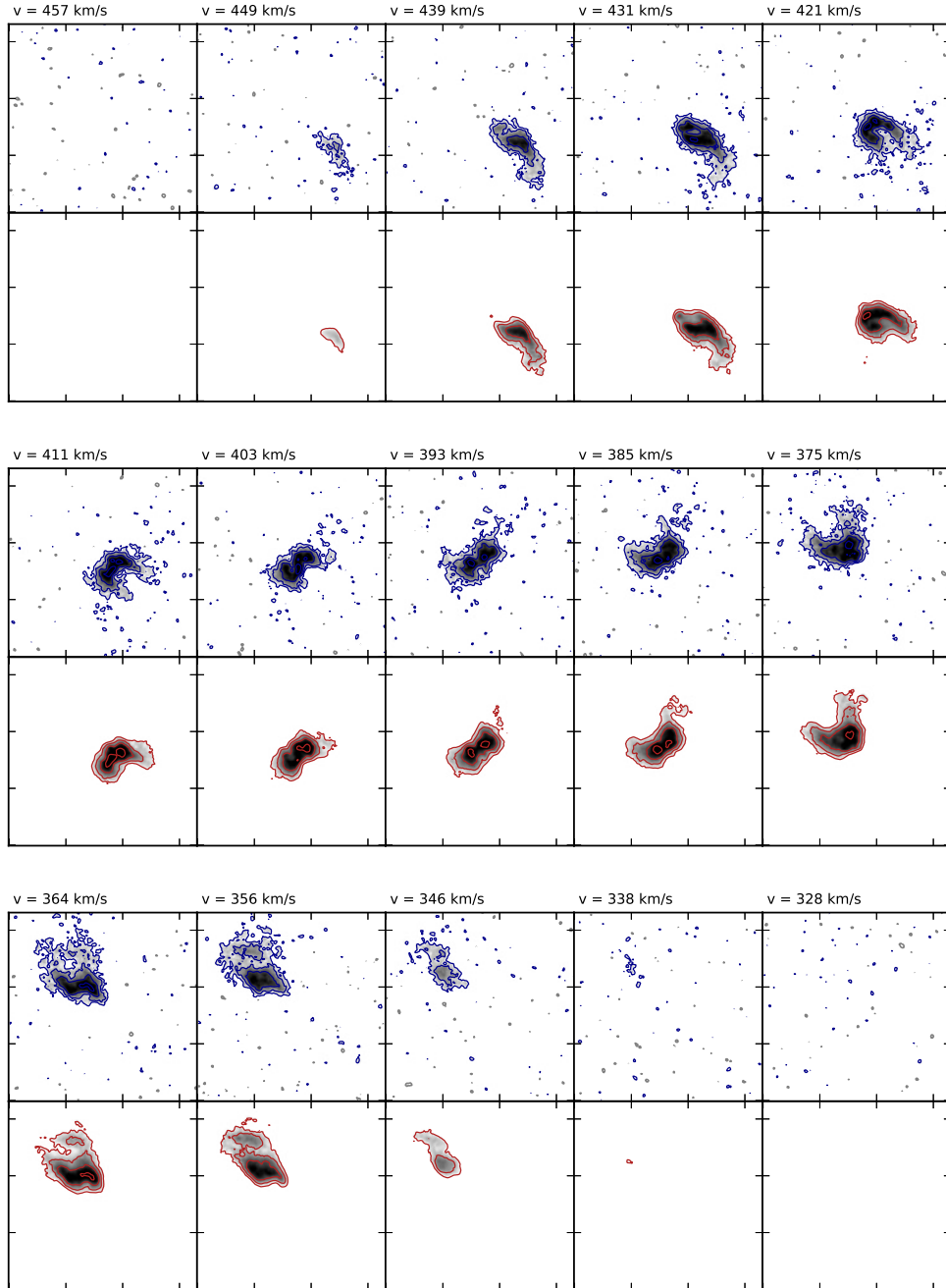


**Figure 3.6:** Channel maps showing the HI emission for DDO 154: data (**top panels**, blue contours) and the best-fit model found with 3DB (**bottom panels**, red contours). The velocity of each channel is reported above the panels. The minimum contour is  $3\sigma_{\text{ch}}$  (Col. 8 in Tab. 3.2) and adjacent contours differ by a factor of 2 in emissivity; the grey contours in the the data channels indicate the emission at  $-3\sigma_{\text{ch}}$ . The size of the field is about  $14' \times 14'$ .

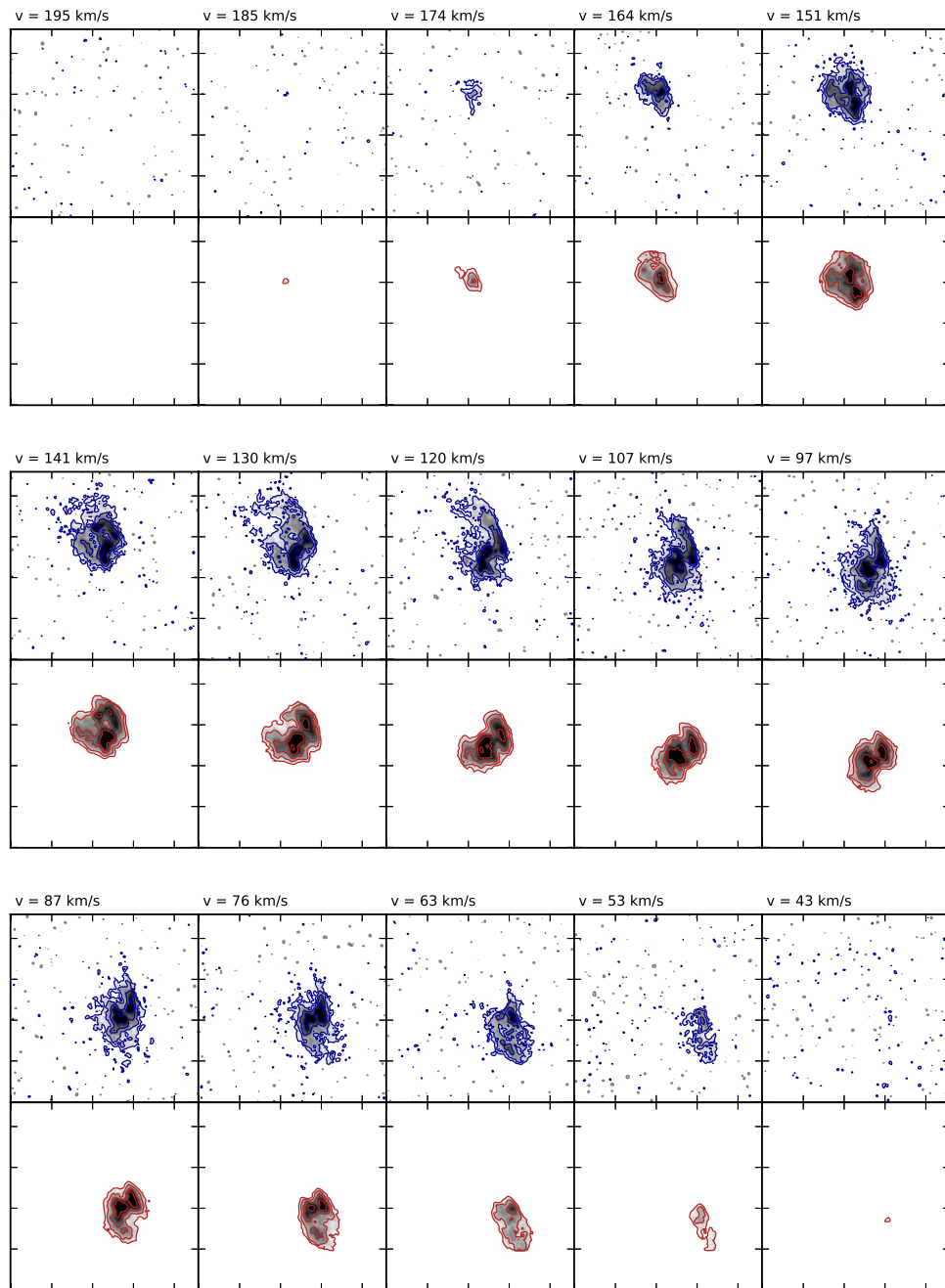


**Figure 3.7:** Same as Fig. 3.6 but for NGC 2366. The size of the field is about 20' x 20'.

### 3.3.3 The final circular velocity

Assuming that the gas is in equilibrium, the rotation velocity of the gas ( $V_{\text{rot}}$ ) can be related to the galactic gravitational potential ( $\Phi$ ) through the radial component of the momentum equation

$$\frac{1}{\rho} \frac{\partial \rho \sigma_v^2}{\partial R} = -\frac{\partial \Phi}{\partial R} + \frac{V_{\text{rot}}^2}{R}, \quad (3.5)$$

where  $\rho$  is the volumetric density of the gas and  $\sigma_v$  is the velocity dispersion. Therefore, the observed  $V_{\text{rot}}$  is not a direct tracer of the galactic potential when the pressure support term ( $\rho \sigma_v^2$ ) due to the random gas motions is non-negligible.

#### Pressure support correction

Eq. 3.5 can be re-written as

$$V_c^2 - V_{\text{rot}}^2 = -\frac{R}{\rho} \frac{\partial \rho \sigma_v^2}{\partial R} = -R \sigma_v^2 \frac{\partial \ln(\rho \sigma_v^2)}{\partial R} = V_A^2, \quad (3.6)$$

where  $V_c = \sqrt{R \frac{\partial \Phi}{\partial R}}$  is the circular velocity and  $V_A$  is the pressure support or asymmetric-drift term, which becomes increasingly important at large radii and is heavily dependent on the value of the velocity dispersion. When the rotation velocity is much higher than the velocity dispersion the asymmetric-drift correction is negligible. This is the case in spiral galaxies where typically  $V_{\text{rot}} \sigma_v^{-1} > 10$  (e.g. de Blok et al. 2008). Instead, for several dIrrs the rotation velocity is comparable to the velocity dispersion, making the asymmetric-drift correction indispensable for an unbiased estimate of the galactic potential.

The volumetric density in the equatorial plane ( $z=0$ ) is proportional to the ratio of the intrinsic surface density and the vertical scale height ( $z_d$ ), therefore the asymmetric drift  $V_A^2$  is given by

$$V_A^2 = -R \sigma_v^2 \frac{\partial \ln(\sigma_v^2 \Sigma_{\text{int}} z_d^{-1})}{\partial R}. \quad (3.7)$$

We can ignore the term with the radial derivative of  $z_d$  assuming that the thickness of the gaseous layer is independent of radius (but see Sec. 4.3). Furthermore, assuming that the HI disc is thin, the ratio between the intrinsic and the observed surface density is just the cosine of  $i$  (Eq. 3.3). Under these assumptions, from Eq. 3.7 we derive the classical formulation of the asymmetric-drift correction (see e.g. O15):

$$V_A^2 = -R \sigma_v^2 \frac{\partial \ln(\sigma_v^2 \Sigma_{\text{obs}} \cos i)}{\partial R}. \quad (3.8)$$

Except for DDO 168, NGC 1569 and UGC 8508, all the analysed galaxies have a constant  $i$  and the cosine in Eq. 3.8 can also be ignored.

### Application to real data

Fluctuations of the observed surface density and of the measured velocity dispersion at similar radii can have dramatic effects on the numerical calculation of the radial derivative in Eq. 3.8. As a consequence, the final asymmetric-drift correction can be very scattered causing abrupt variations in the final estimate of the circular velocity. For this reason, we decided to use functional forms to describe both the velocity dispersion and the argument of the logarithm in Eq. 3.8. The velocity dispersion is regularised with a polynomial  $\sigma_p(R, n_p)$  with degree  $n_p$  lower than 3. If there is not a clear radial trend, we consider a fixed velocity dispersion taking the median of  $\sigma_v(R)$ . The radial variation of the velocity dispersion is usually small, therefore the radial trend of  $\Sigma_{\text{int}}\sigma_v^2$  is dominated by the behaviour of the surface density: this falls off exponentially at large radii, while in the centre it is almost constant or it shows an inner depression. In analogy with Bureau & Carignan (2002) we chose to fit  $\Sigma_{\text{int}}\sigma_v^2$  with the function

$$f(R) = f_0 \left( \frac{R_c}{\text{arcsec}} + 1 \right) \left( \frac{R_c}{\text{arcsec}} + e^{\frac{R}{R_d}} \right)^{-1}, \quad (3.9)$$

where  $f_0$  is a normalisation coefficient, and  $R_c$  and  $R_d$  are characteristic radii. The function  $f$  is characterised by an exponential decline at large radii and by an inner core almost equal to  $f_0$ . Read et al. (2016) showed that the Eq. 3.9 is a good compromise between a pure exponential that overestimates the asymmetric-drift correction in the inner radii, and a functional form with an inner depression that can produce unphysical negative values of  $V_{\text{rot}}^2$ . Combining Eq. 3.9 and Eq. 3.8 we can write the asymmetric-drift correction as

$$V_A^2 = R \frac{\sigma_p^2(R, n_p) e^{\frac{R}{R_d}}}{R_d} \left( \frac{R_c}{\text{arcsec}} + e^{\frac{R}{R_d}} \right)^{-1}. \quad (3.10)$$

### Error estimates

We can calculate the final errors on  $V_c$  by applying the propagation of errors to Eq. 3.6 to obtain

$$\delta_c = \frac{\sqrt{V_{\text{rot}}^2 \delta_{\text{rot}}^2 + V_A^2 \delta_A^2}}{V_c}, \quad (3.11)$$

where  $\delta_{\text{rot}}$  is the error found with 3DB and  $\delta_A$  is the uncertainty associated with the estimated values of the asymmetric-drift term. Usually  $\delta_A$  is simply ignored (e.g.

Bureau & Carignan 2002; O15), thus the uncertainties on the final corrected rotation curve are equal to  $\delta_{\text{rot}}$ . This is a reasonable assumption if the rotational terms in Eq. 3.11 are dominant, but for some galaxies in our sample (e.g. DDO 210) the final circular rotation curve is heavily dependent on the asymmetric-drift correction. In these cases it is important that  $\delta_c$  includes the uncertainties introduced by the operations described in Sec. 3.3.3. We decided to estimate  $\delta_c$  with a Monte Carlo approach:

1. First we make  $N$  realisations of the radial profile of both the velocity dispersion and of the surface density. For each sampling radius  $R$  the values of a single realisation  $\sigma_v^i(R)$  or  $\Sigma_{\text{int}}^i(R)$  are extracted randomly from a normal distribution with the centre and the dispersion taken respectively from the values and errors of the parent populations.
2. For each of the  $N$  realisations we apply the method described in Sec. 3.3.3 to obtain the asymmetric-drift correction at each sampling radius  $V_A^i(R)$ .
3. The final asymmetric-drift correction is calculated as  $V_A(R) = \text{median}_i(V_A^i(R))$ , where each  $V_A^i$  is obtained with the Eq. 3.10. The associated errors are  $\delta_A(R) = K \times \text{MAD}(V_A^i(R))$  where the MAD is the median absolute deviation around the median. The factor  $K$  links the MAD with the standard deviation of the sample ( $K \approx 1.48$  for a normal distribution). We chose to use the median and the MAD because they are less biased by the presence of outliers with respect to the mean and the standard deviation.

We found that  $N = 1000$  is enough to obtain a good description of the error introduced by the asymmetric-drift correction.

## 3.4 Results and discussion

We applied the techniques described in Sec. 3.3 to each of the dIrrs presented in Sec. 3.1. The final results are ready-to-use high quality kinematic data that we made publicly available (see the on-line version of Iorio et al. 2017b<sup>4</sup>).

In the following sections we discuss the individual galaxies (Sec. 3.4.1) and we compare our estimated rotation curves with the one obtained with classical 2D method in O15 (Sec. 3.4.2).

The assumptions made in the analysis and the general properties derived for each of the dIrrs can be found in in Tab. 3.8, in particular in Col. 8 we report the value of the velocity of the outer disc ( $V_o$ ) defined as the mean circular velocity of

---

<sup>4</sup>The data tables can be downloaded also from <http://www.filippofraternali.com/resources/finalrot.zip>

the last three fitted rings (see Sec. 3.3.2). The error on  $V_o$  is conservatively assumed as the maximum error between these three values.

In the Appendix 3.A we present the summary plots (Appendix 3.A.1) and the Tables (Appendix 3.A.2) with the radius-by-radius kinematic (circular velocity, velocity dispersion) and HI mass distribution information (intrinsic surface density) for each analysed galaxy.

### 3.4.1 Notes on individual galaxies

- **CVnIdwA.** The HI morphology of CVnIdwA (Fig. 3.10) looks regular, but the orientation of the HI iso-density contours is quite different with respect to the direction of the velocity gradient. The emission of the stellar disc is very patchy, so we estimated the geometrical parameters of the HI disc using 3DB (see Sec. 3.3.2).
- **DDO 47.** The HI disc of DDO 47 (Fig. 3.11) is nearly face-on, while the stellar disc looks highly inclined at  $64^\circ$  (Hunter & Elmegreen, 2006) and probably hosts a bar-like structure (Georgiev, Karachentsev & Tikhonov, 1997). We decided to use only the HI data to estimate  $i_{\text{ini}}$ ,  $\text{PA}_{\text{ini}}$  and the galactic centre. The best-fit  $i$  (see Tab. 3.8) is consistent with previous works ( $35^\circ$  in Gentile et al. 2005,  $30^\circ$  in de Blok & Bosma 2002 and Stil & Israel 2002a) and seems a reasonable upper limit for this galaxy (see ellipses in Box C in Fig. 3.11). In the very outer part of the disc, the inclination is probably even lower, therefore given the large uncertain estimate of the rotational velocities in nearly face-on discs (see Sec. 3.1.1), we decided to limit our analysis to the maximum radius of 210 arcsec. The final rotation curve shows a flattening at  $R < 60''$ : analysing the PVs and the channel maps we found that at these radii the emission is dominated by small high-density regions that can bias the kinematic fit. For this reason, we consider the velocities for  $R < 120''$  not completely reliable (empty circles in Box A in Fig. 3.11).
- **DDO 50.** The gaseous disc of DDO 50 (Fig. 3.12) is “drilled” by medium-large HI holes ranging from 100 pc to 1.7 kpc (Puche et al., 1992). Despite this peculiarity, the large scale kinematics is quite regular and typical of a flat rotation curve. The estimates of the  $i$  and PA are difficult given that this galaxy is nearly face-on. The  $i$  of the optical disc ( $47^\circ$ ) looks too high to be compatible with the HI contours: the best agreement between the datacube and the model has been found using initial values of  $30^\circ$  for  $i_{\text{ini}}$  and  $180^\circ$  for  $\text{PA}_{\text{ini}}$ . The centre was set using the coordinates of the centre of the stellar disc (Hunter & Elmegreen, 2006).
- **DDO 52.** The best-fit  $i$  of DDO 52 (Fig. 3.13) tends to be more edge-on

Galaxy	R <sub>max</sub>	R <sub>max</sub>	ΔR	centre			V <sub>sys</sub>	i <sub>ini</sub>	PA <sub>ini</sub>	V <sub>o</sub>	⟨σ <sub>v</sub> ⟩	⟨i⟩	⟨PA⟩
	(arcsec)	(kpc)	(pc)	RA	DEC	(km/s)	(°)	(°)	(km/s)	(km/s)	(°)	(°)	
	(1)	(2)	(3)	(4a)	(4b)	(5)	(6)	(7)	(8)	(9)	(10)	(11)	
CVnIdwA	90	1.6	170	12 38 40.2 <sup>B</sup>	32 45 52 <sup>B</sup>	307.9 <sup>B</sup>	41 <sup>B</sup>	55 <sup>B</sup>	21.5 ± 3.9	7.7 ± 0.5	49.2 ± 10.9	60.6 ± 18.5	
DDO 47	210	5.3	380	7 41 54.6 <sup>H</sup>	16 48 10 <sup>H</sup>	272.8 <sup>B</sup>	35 <sup>H</sup>	310 <sup>H</sup>	62.6 ± 5.2 <sup>†</sup>	7.9 ± 0.2	37.4 ± 1.7 <sup>†</sup>	317.4 ± 7.3	
DDO 50	390	6.4	190	8 19 08.7 <sup>S</sup>	70 43 25 <sup>S</sup>	156.7 <sup>B</sup>	30 <sup>T</sup>	180 <sup>T</sup>	38.7 ± 10.1 <sup>†</sup>	9.0 ± 1.5	33.1 ± 4.6 <sup>†</sup>	174.9 ± 5.9	
DDO 52	108	5.4	450	8 28 28.5 <sup>S</sup>	41 51 21 <sup>S</sup>	396.2 <sup>B</sup>	51 <sup>S</sup>	5 <sup>S</sup>	51.1 ± 6.3	8.0 ± 0.8	55.1 ± 2.9	6.5 ± 2.0	
DDO 53	60	1.1	110	8 34 08.0 <sup>S</sup>	66 10 37 <sup>S</sup>	20.4 <sup>B</sup>	35 <sup>T</sup>	120 <sup>T</sup>	20.3 ± 6.6 <sup>†</sup>	7.9 ± 0.1	37.0 ± 2.0 <sup>†</sup>	123.4 ± 3.8	
DDO 87	144	5.2	430	10 49 34.7 <sup>S</sup>	65 31 46 <sup>S</sup>	338.7 <sup>B</sup>	40 <sup>T</sup>	240 <sup>B</sup>	50.3 ± 9.1	6.3 ± 2.4	42.7 ± 7.3	238.6 ± 4.7	
DDO 101	60	1.9	190	11 55 39.4 <sup>S</sup>	31 31 8 <sup>S</sup>	586.6 <sup>B</sup>	49 <sup>S</sup>	290 <sup>S</sup>	59.2 ± 3.6	4.8 ± 1.7	52.4 ± 1.7	287.4 ± 3.6	
DDO 126	140	3.3	240	12 27 06.3 <sup>H</sup>	37 08 23 <sup>H</sup>	214.3 <sup>B</sup>	63 <sup>B</sup>	138 <sup>B</sup>	38.6 ± 3.1	9.1 ± 1.6	62.2 ± 2.9	140.7 ± 3.5	
DDO 133	165	2.8	190	12 32 55.4 <sup>S</sup>	31 32 14 <sup>S</sup>	331.3 <sup>B</sup>	38 <sup>B</sup>	20 <sup>B</sup>	47.2 ± 5.1 <sup>†</sup>	8.1 ± 0.7	38.9 ± 3.7 <sup>†</sup>	-3.8 ± 8.9	
DDO 154	390	7.0	270	12 54 06.2 <sup>S</sup>	27 09 02 <sup>S</sup>	375.2 <sup>B</sup>	65 <sup>S</sup>	224 <sup>S</sup>	47.1 ± 5.1	8.5 ± 0.9	67.9 ± 1.1	226.1 ± 2.6	
DDO 168	225	4.7	310	13 14 27.9 <sup>B</sup>	45 55 24 <sup>B</sup>	191.9 <sup>B</sup>	60 <sup>T</sup>	300 - 270 <sup>T</sup>	56.2 ± 6.9	8.8 ± 1.3	62.0 ± 2.6	272.7 ± 4.2	
DDO 210	100	0.4	40	20 46 52.0 <sup>S</sup>	-12 50 51 <sup>S</sup>	-140.0 <sup>B</sup>	60 <sup>T</sup>	65 <sup>T</sup>	16.4 ± 9.5	6.2 ± 0.6	63.2 ± 3.2	77.3 ± 15.2	
DDO 216	195	1.0	80	23 28 32.1 <sup>H</sup>	14 44 50 <sup>H</sup>	-188.0 <sup>T</sup>	65 <sup>H</sup>	130 <sup>H</sup>	13.6 ± 5.5	5.6 ± 0.5	70.0 ± 5.0	130.4 ± 9.0	
NGC 1569	150	2.5	250	4 30 49.8 <sup>S</sup>	64 50 51 <sup>S</sup>	-75.6 <sup>B</sup>	61 <sup>S</sup>	122 <sup>S</sup>	55.6 ± 22.4	21.0 ± 4.0	67.0 ± 5.6	114.6 ± 4.0	
NGC 2366	384	6.3	260	7 28 48.8 <sup>S</sup>	69 12 22 <sup>S</sup>	100.8 <sup>B</sup>	65 <sup>B</sup>	35 <sup>B</sup>	57.7 ± 5.4	12.6 ± 1.8	65.1 ± 4.2	39.8 ± 2.8	
UGC 8508	110	1.4	130	13 30 44.9 <sup>S</sup>	54 54 29 <sup>S</sup>	59.9 <sup>B</sup>	65 <sup>H</sup>	120 <sup>H</sup>	33.8 ± 6.4	9.1 ± 1.8	67.6 ± 5.3	123.2 ± 1.7	
WLM	600	2.9	120	0 01 59.2 <sup>S</sup>	-15 27 41 <sup>S</sup>	-124.0 <sup>B</sup>	70 <sup>S</sup>	178 <sup>S</sup>	38.7 ± 3.4	7.7 ± 0.8	74.0 ± 2.3	174.0 ± 3.1	

**Table 3.8: Fit results:** - (1) outermost radius in arcsec (see Sec. 3.3.1); (2) outermost radius in kpc (see Sec. 3.3.1); (3) sampling radius used in the datacube fitting; (4a)(4b) assumed galactic centre in RA (hh mm ss.s) and DEC (dd mm ss) coordinate system (J2000); (5) assumed systemic velocity (see Sec. 3.2.1); (6) initial guesses for  $i$ ; (7) initial guesses for PA. <sup>S</sup> indicates that the values is estimated from the stellar disc (Hunter & Elmegreen, 2006), <sup>B</sup> using 3DB, <sup>H</sup> using the fit of the contours of the HI total map (see Sec. 3.3.2 for details). <sup>T</sup> indicates peculiar cases (see the individual galactic description for details). **Results:** (8) mean circular velocity of the outer disc, calculated as the median of the  $V_c$  at three most external radii; (9) median of the best-fit velocity dispersion found with 3DB; (10) median of the best-fit PA found with 3DB; (11) median of the best-fit  $i$  found with 3DB. <sup>†</sup> indicates nearly face-on galaxies in which the quoted errors on  $\langle i \rangle$  and  $V_o$  could underestimate the real uncertainties.

at the end of the disc. However, the analysis of the channels and of the PVs indicates that the model with a constant  $i$  gives a better representation of the data.

- **DDO 53.** The stellar disc and the HI disc of DDO 53 (Fig. 3.14) are misaligned and the galaxy is nearly face-on. As a consequence,  $i$  and PA are very difficult to constrain: we tried different values in the range  $30^\circ$ - $50^\circ$  for  $i_{\text{ini}}$  and  $100^\circ$ - $140^\circ$  for  $\text{PA}_{\text{ini}}$ . The best match with the data has been found using  $i_{\text{ini}} = 35^\circ$  and  $\text{PA} = 120^\circ$ , but the rotational and the circular velocities should be taken with caution. In the northern part of the galaxy there is some extra emission possibly connected with an inflow/outflow: this region is clearly visible in the PV along the minor axis around  $-50$  arcsec at a velocity of about  $5 \text{ km s}^{-1}$ .
- **DDO 87.** The morphology of DDO 87 (Fig. 3.15) is clearly irregular in the inner part, but the outer disc looks more regular. We decided to set the initial guesses for the PA using 3DB (see Appendix 3.3.2). We tried different initial guesses for  $i$ : the best representation of the data has been obtained with  $i_{\text{ini}} = 40^\circ$  and  $\text{PA}_{\text{ini}} = 240^\circ$ , approximately  $15^\circ$  lower than the orientation of the optical disc (Hunter & Elmegreen, 2006).
- **DDO 101.** The HI disc of DDO 101 (Fig. 3.16) is extended only slightly beyond the optical disc and the HI emission is almost constant with some high density structures around 1.0 kpc. Notice that the estimates of the distance for this galaxy are very uncertain (ranging from 5 to 16 Mpc) since they all rely on a poor distance estimator (Tully-Fisher relation, e.g. Karachentsev, Makarov & Kaisina 2013).
- **DDO 126.** DDO 126 (Fig. 3.17) shows kinematic asymmetries, so we separately run 3DB also on the approaching and the receding halves of the galaxy. Beyond 1.5 kpc the fit on the whole galaxy gives a good representation of the datacube and the errors found with 3DB are larger than (or comparable to) the differences due to the kinematic asymmetries (black circles in Box A in Fig. 3.17). The inner regions are less regular and the best model has been found taking the mean between the approaching and receding rotation curves (empty circles in Box A in Fig. 3.17), while the errors have been calculated as half the difference between the two values following the recipe of Swaters (1999).
- **DDO 133.** The HI disc of DDO 133 (Fig. 3.18) has a regular kinematics, although there is evidence of non-circular motions, especially in the region of the stellar bar (Hunter et al., 2011). The final PA found with 3DB is about  $20^\circ$  in the inner part of the disc ( $R < 0.5$  kpc) and it becomes almost zero in the outer disc. We decided to take the radial trend of the PA into account

with a fourth order polynomial. This galaxy is close to face-on, therefore the rotational and circular velocities should be taken with some caution.

- **DDO 154.** The HI morphology and the kinematics of DDO 154 (Fig. 3.19) is quite regular. However, the contours of the HI map clearly show a radial trend of the PA, as confirmed by the values found with 3DB. We followed this radial trend with a fourth order polynomial. The polynomial gives too large values of the PA at small radii ( $R < 1$  kpc), so we decided to fix the PA in this region to the mean values of the first three points (see Box B in Fig. 3.19). As in O15, we do not confirm the almost Keplerian fall-off of the rotation curve claimed by Carignan & Purton (1998) beyond 5 kpc. The channel maps are shown in Fig. 3.6
- **DDO 168.** The velocity gradient of DDO 168 (Fig. 3.20) is misaligned with respect to both the HI and the stellar disc. Moreover, the presence of a prominent bar visible both in the stellar disc (Hunter & Elmegreen, 2006) and in the inner part of the HI disc makes the initial estimate of the geometrical parameters very uncertain. We obtained a first estimate of the PA using the 2D tilted-ring fitting of the velocity field shown in Fig. 3.20: the resultant PA decreases from  $300^\circ$  to about  $270^\circ$ . We used these values as initial guesses for all sampling radii in 3DB (see Appendix 3.3.2). The centre was set to the value found with 3DB which roughly corresponds to the optical centre. We tried different values for  $i_{\text{ini}}$  between  $40^\circ - 70^\circ$ : the best reproduction of the datacube has been obtained with  $i_{\text{ini}} = 60^\circ$ . The final results still show a variation of PA that we regularised with a second order polynomial. The outer disc of DDO 168 is quite irregular. There is extra emission at velocities close to  $V_{\text{sys}}$  possibly related to inflow/outflow, while the distortions of the iso-velocity contours (Box C. in Fig. 3.20) could be due to the presence of an outer warp.
- **DDO 210.** DDO 210 (also know as Aquarius dIrr, Fig. 3.21) is the least massive galaxy in our sample and it is classified as a transitional dwarf galaxy (McConnachie 2012 and reference therein). The kinematics is dominated by the velocity dispersion, however a weak velocity gradient is visible. The velocity gradient looks misaligned with both the stellar and the HI disc, so we set the initial values of  $i$  and PA ( $60^\circ$  and  $65^\circ$ , respectively) using a by-eye inspection of the velocity field. The estimate of the galactic centre is very uncertain and we decided to set it to the optical value (Hunter & Elmegreen, 2006), but we excluded from our analysis the first two points (10 and 20 arcsec). This procedure is quite arbitrary, but it is important to note that the final circular-velocity curve is quite independent of our procedure since it is totally dominated by the asymmetric-drift correction (see Sec. 3.3.3). Notice

that along the minor axis there is an extended region with HI emission apparently not connected with the rotating disc. As in the case of DDO 53 this emission could trace an inflow/outflow.

- **DDO 216.** DDO 216 (also known as Pegasus dIrr, Fig. 3.22) is defined as a transitional dwarf galaxy (Cole et al., 1999). The galaxy shows a velocity gradient aligned with the HI and the optical disc, but it could be entirely due to a single ‘cloud’ at a discrepant velocity in the approaching side of the galaxy (Stil & Israel, 2002b). For the purpose of our work, we assumed the gradient genuine and caused entirely by the gas rotation. The analysis of the alternative scenario can be found in Appendix 3.B. Given the kinematic peculiarities (see Appendix 3.B), we did not use 3DB to estimate the  $V_{\text{sys}}$  (Sec. 3.2.1). We tried different values between  $-186$  and  $-190$   $\text{km s}^{-1}$  and we decided to use  $V_{\text{sys}} = -188$   $\text{km s}^{-1}$  because this value minimises the kinematic asymmetries between the receding and the approaching halves of the galaxy. We set the centre,  $i_{\text{ini}}$  ( $65^\circ$ ) and  $\text{PA}_{\text{ini}}$  ( $130^\circ$ ) using the values obtained from the elliptical fit of the outermost HI contours ( $R > 600$  pc). The best-fit PA decreases from about  $140^\circ$  to about  $125^\circ$ .
- **NGC 1569** NGC 1569 (Fig. 3.23) is a starburst galaxy with a very disturbed HI kinematics and morphology (Stil & Israel, 2002a; Johnson et al., 2012; Lelli, Verheijen & Fraternali, 2014a). We found that the best-fit model shows a slight increase of  $i$  and a slight decrease of PA as a function of radius. The best-fit model is a good representation of the large scale structure and kinematics of the HI disc, but it fails to reproduce the small scale local features. The ISM of this galaxy is highly turbulent: the velocity dispersion found with 3DB is about  $20$   $\text{km s}^{-1}$  and the asymmetric-drift correction dominates at all radii. For this reason the kinematic data reported here should be used with caution especially at the inner radii (empty circles in Box A in Fig. 3.23) where no significant rotation of the gas is observed (see also Lelli, Verheijen & Fraternali 2014a).
- **NGC 2366.** The HI disc of NGC 2366 (Fig. 3.24) is quite regular, although it shows some peculiar features. The HI emission on the channel maps (Fig. 3.7) indicates the presence of two ridges located in the North-West and South-East (less prominent) of the disc running parallel to the major axis. The ridges show different kinematics with respect to the disc (see Oh et al. 2008) and their origin is not clear (see Hunter, Elmegreen & van Woerden 2001 for a detailed discussion). We checked that 3DB was not affected by the presence of this feature. From the PV along the major axis (Panel D in Fig. 3.24) it is clear that the 3DB model does not reproduce some emission close to the systemic velocity, especially in the receding side where the gas is seen also

at ‘forbidden’ velocities below  $V_{\text{sys}}$ . As already stated by Lelli, Verheijen & Fraternali (2014a) this is probably due to the presence of some extraplanar gas that is rotating at lower velocity with respect to the gas in the disc (see e.g. Fraternali et al. 2002). As in Lelli, Verheijen & Fraternali (2014a) and in O15 we do not find that the rotation curve declines beyond 5 kpc, as instead claimed by both Hunter, Elmegreen & van Woerden (2001) and van Eymeren et al. (2009).

- **UGC 8508.** The HI and the stellar disc of UGC 8508 (Fig. 3.25) are aligned but the analysis of the HI map favours an  $i$  slightly higher than the value obtained from the stellar disc (Hunter & Elmegreen, 2006). We found that the datacube is better reproduced with a linearly increasing  $i$ . Notice that in the inner part of the galaxy ( $R < 0.6$  kpc) the kinematics is very peculiar as it is visible by the S-shaped iso-velocity contours (left-panel C in Fig. 3.25). This kind of distortions can be related to an abrupt variation of the PA and/or to the presence of radial motions (Fraternali et al., 2001) as well as to a deviation from axisymmetry of the galactic potential (Swaters et al., 1999). We tested the hypothesis of a radially varying PA and the presence of non-zero radial velocities ( $V_{\text{rad}}$ ) performing a 2D analysis of the velocity field with ROTCUR (Begeman, 1987). We found that the combination of the two effects can partially explain the distortions of the velocity field, but their magnitude is too large to be physically plausible. Fortunately, the final rotation curves obtained including radial motions and/or the varying PA are compatibles with the results we found with 3DB, though the inner points (empty circles in Box A in Fig. 3.25) should be treated with caution.
- **WLM.** The HI and the optical discs of WLM (Fig. 3.26) are well aligned, but the best-fit  $i$  looks slightly too edge-on with respect to the HI contours (see ellipses in Fig. 3.26). The excess of the emission around the minor axis could be due to the HI disc thickness (see Fig. 4.14 and Sec. 4.3.4, see also Leaman et al. 2012). Further details on the analysis of WLM can be found in Read et al. (2016).

### 3.4.2 Comparison to the standard 2D approach

In this Section we compare the rotation curves obtained with our method with the ones obtained in O15 for the same dataset with the classical 2D approach. As a general feature, the rotation curves of O15 reach larger radii: the median difference on the radial extension is about 700 pc and the galaxies with the largest discrepancies are: DDO 50 (3.4 kpc), DDO 87 (2.2 kpc) and NGC 2366 (1.8 kpc). DDO 216 has rotation curves of similar extensions, while our rotation curves for DDO 210 and DDO 168 are more extended by about 200 pc and 700 pc respectively. These

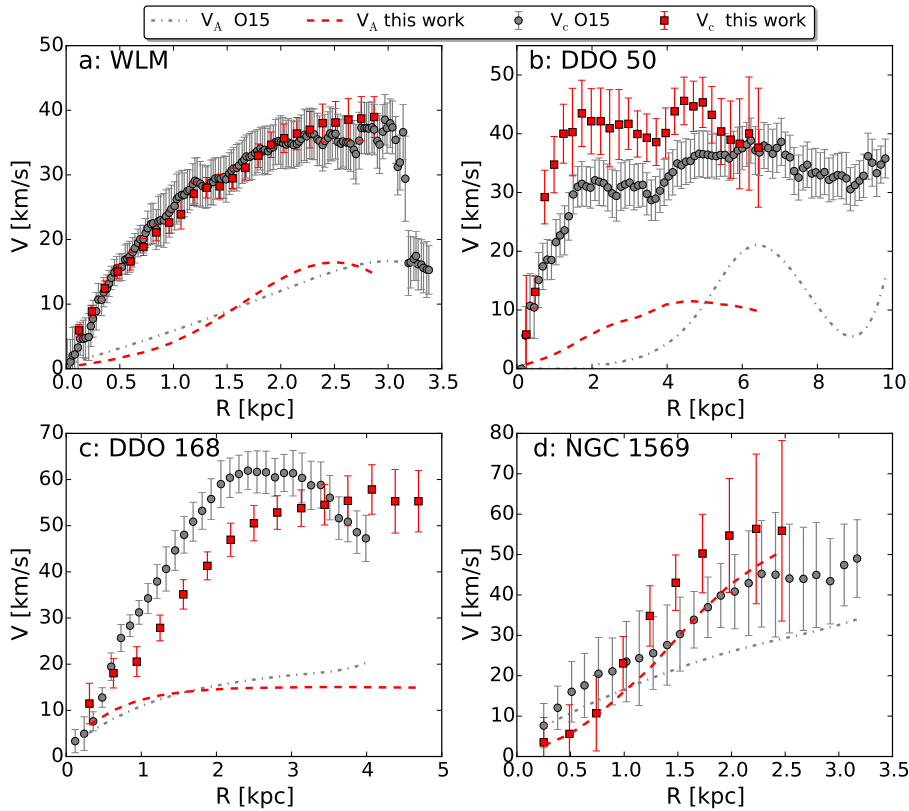


**Figure 3.9:** Circular velocity ( $V_c$ ) and asymmetric-drift term ( $V_A$ ) for four representative galaxies in our sample (**a:** WLM, **b:** DDO50, **c:** DDO 168, **d:** NGC 1569). The red squares and the red curves show the results found in this work, while the grey circles and the grey curves show the results obtained in O15.

differences are due to the different approach in the choices on the outermost radii considered in the kinematic fit. We decided to include only the part of the galaxy with clear information on the rotation motion and not dominated by the noise (see Sec. 3.3.1), as shown by the elliptical rings over plotted to the HI maps and HI velocity fields (Box C in Figs. 3.10-3.26). In contrast, O15 extended the fit as much as possible, but in some cases the outer part of the rotation curves might be extracted mainly from emission around the minor axis which have poor information on the rotational motion. The peril of this approach is that the rotation curves at large radii can be quite unreliable or show artifacts as for example in WLM (Fig. 3.9a) where the rotation curve of O15 shows an abrupt drop-off after the outermost radii used in our analysis.

Concerning the shapes of rotation curves, about half of our results are compatible with O15 within the errors. When differences are present they can be due to a combination of three different reasons: (i) an intrinsic difference in the best-fit

projected rotational velocities ( $V_{\text{rot}} \sin i$ ), (ii) a difference in the best-fit  $i$ , PA or centre and (iii) a difference in the asymmetric-drift correction terms ( $V_A$ ). Most of the cases are due to (ii) and (iii); only one galaxy (DDO 168) seems to have a significant discrepancy caused by the two different fitting methods. This galaxy is shown in Fig. 3.9c, while examples of (ii) and (iii) are shown in Figs. 3.9b and 3.9d. The galaxies showing the largest discrepancies are listed below.

- **CVnidwa.** Our final rotation curve is systematically higher than that of O15 by about  $5 \text{ km s}^{-1}$ . This difference is totally dominated by the discrepancy in the asymmetric-drift correction term. Our  $V_A$  is already significant at the inner radii, while the  $V_A$  of O15 is negligible out to 2 kpc. These differences are ascribed to the different radial trend of the intrinsic surface density profile caused by discrepancies in the best-fit PA .
- **DDO 47.** The circular velocity shows a discrepancy of about  $7 \text{ km s}^{-1}$  in the inner part of the disc ( $R < 2 \text{ kpc}$ ) due to a discrepancy on the best-fit  $i$ : O15 used  $i \approx 55^\circ$  while we used  $i = 37^\circ$  independent of radius.
- **DDO 50.** Discrepancies of about  $10 \text{ km s}^{-1}$  (see Fig. 3.9b) are due to the different assumption on the value of  $i$  (about  $50^\circ$  in O15 and  $33^\circ$  in this work). Our curve is also less extended (see Fig. 3.12).
- **DDO 52.** The final rotation curve of O15 is systemically higher due to the different values of  $i$  (about  $37^\circ$  in O15 and  $55^\circ$  in this work).
- **DDO 87.** Our final rotation curve shows a steeper rising due to a discrepancy in the assumed  $i$ : we used  $i = 40^\circ$  independent of radius, while in O15  $i$  varies between  $60^\circ$  and  $40^\circ$ .
- **DDO 168.** The final rotation curves are quite different (see Fig. 3.9c). In O15 the curve flattens at about 2 kpc and starts to decrease at 3 kpc, while our rotation curve shows a less steep rising in the inner part and a flattening at about 3.5 kpc. These discrepancies are due mainly to an intrinsic difference in the best-fit projected rotation curve found with the two methods. The differences are further increased by the different assumptions on  $i$  ( $i \approx 60^\circ$  in this work,  $i \approx 40^\circ$  in O15).
- **NGC 1569.** The circular rotation curve found in this work rises steeper with respect to the rotation curve reported in O15 (see Fig. 3.9d). The difference is caused by the asymmetric-drift correction given that with our 3D method we find a different radial trend of both the velocity dispersion and the intrinsic surface density.

- **NGC 2366.** Our final rotation curve is systematically lower in the inner disc ( $R < 2$  kpc). The cause is a combination of a different position of the galactic centre and different PA. We used a constant PA of about  $40^\circ$ , while in O15 the PA grows from  $20^\circ$  to  $40^\circ$  in the first two kpc.

### 3.5 Summary

We presented a study of the kinematics of the HI discs for 17 dwarf irregular galaxies taken from the public survey LITTLE THINGS (Hunter et al., 2012). The main goal of this work is to make available to the community a sample of high-quality rotation curves of dIrrs ready-to-use to perform dynamical studies. The tabulated quantities ( $V_{\text{rot}}$ ,  $V_{\text{c}}$ ,  $V_{\text{A}}$ ,  $\sigma_v$ ) and HI surface-density profile ( $\Sigma_{\text{int}}$ ) are available in the Appendix 3.A.2 and in the on-line version of Iorio et al. (2017b). The key points of this work are listed below.

1. We derived the rotation curves from the HI datacubes with a state-of-art technique: the publicly available software <sup>3D</sup>BAROLO (Di Teodoro & Fraternali, 2015). It fits 3D models to the datacubes without explicitly extracting velocity fields. The fit in the 3D space of the datacubes ensures full control of the observational effects and in particular a proper account of beam smearing.
2. The maximum radii used in the fits have been chosen with great care from the HI total map. This ensures a robust estimate of the kinematics avoiding regions of the galaxy dominated by the noise and with scant information about the gas rotation.
3. We developed a method to take into account the uncertainties of the asymmetric-drift correction. As a consequence, the quoted errors on the rotation curves are representative of the real uncertainties. The inclusion of these errors are fundamental in galaxies for which the calculation of the circular velocity is highly dominated by the asymmetric-drift correction (e.g. DDO 210).

In Chapter 4, we will use a new original method to explore whether the presence of a significant HI disc thickness can introduce biases in the results presented in this work. In Chapter 5, we will further exploit the results obtained in this Chapter to test scaling relations for the smallest galaxies in the Universe.

## 3.A Atlas and Data

### 3.A.1 Atlas

This Appendix includes the summary plots for all the galaxies in our sample. The general descriptions for the different boxes shown in the Figures are reported below.

- **Box A:** Rotation velocity estimated with 3DB ( $V_{\text{rot}}$ , blue line), asymmetric-drift correction ( $V_A$ , grey circles) and final corrected circular velocity ( $V_c$ , black circles).

- **Box B:**

**Top:** Inclination (left-hand panel) and position angle (right-hand panel) found with 3DB as functions of radius  $R$ . The red lines show the fit used to obtain the rotation velocity (see Sec. 3.3.2), while the black dashed line indicates the median of the data.

**Bottom:** HI velocity dispersion estimated with 3DB (left-hand panel) and intrinsic surface density of the HI disc not corrected for Helium (right-hand panel) as a function of the radius  $R$ . In the left-hand panel the black dashed line indicates the median of the data. The empty circles (if present) represent the points excluded both from the calculation of the asymmetric-drift correction (see Sec. 3.3.3) and from the calculation of the median. The excluded points belong to rings where the velocity dispersion found with 3DB is discrepant or peculiar with respect to global trend.

- **Box C:**

*Left-hand panel:* Stellar emission overlaid with the iso-density contours of the total HI emission. The thick contour indicates  $\sigma_{3T}$ , the  $3\sigma$  pseudo noise of the total map (see Sec. 3.3.1 and Tab. 3.2).

*Right-hand panel:* Velocity field obtained as the 1th moment of the data cube. The thick contour highlights the systemic velocity (see Tab. 3.8). A physical scale is plotted on the bottom right corner of the panel, while the beam of the HI observation is shown in the bottom left corner.

The crosses and the ellipses show the assumed galactic centre and the last used ring respectively (see Tab. 3.8).

- **Box D:** PV diagram along the major (left-handed panel) and the minor (right-handed panel) axis of the HI disc. The black and the red contours show respectively the iso-density contours of the galaxy and the best-fit model found with 3DB. The horizontal black dashed lines indicate the systemic velocity.

The physical radii have been calculated assuming the distance in Tab. 3.2. Further information on the step of the iso-density and of the iso-velocity contours can be found in the caption below each Figure.

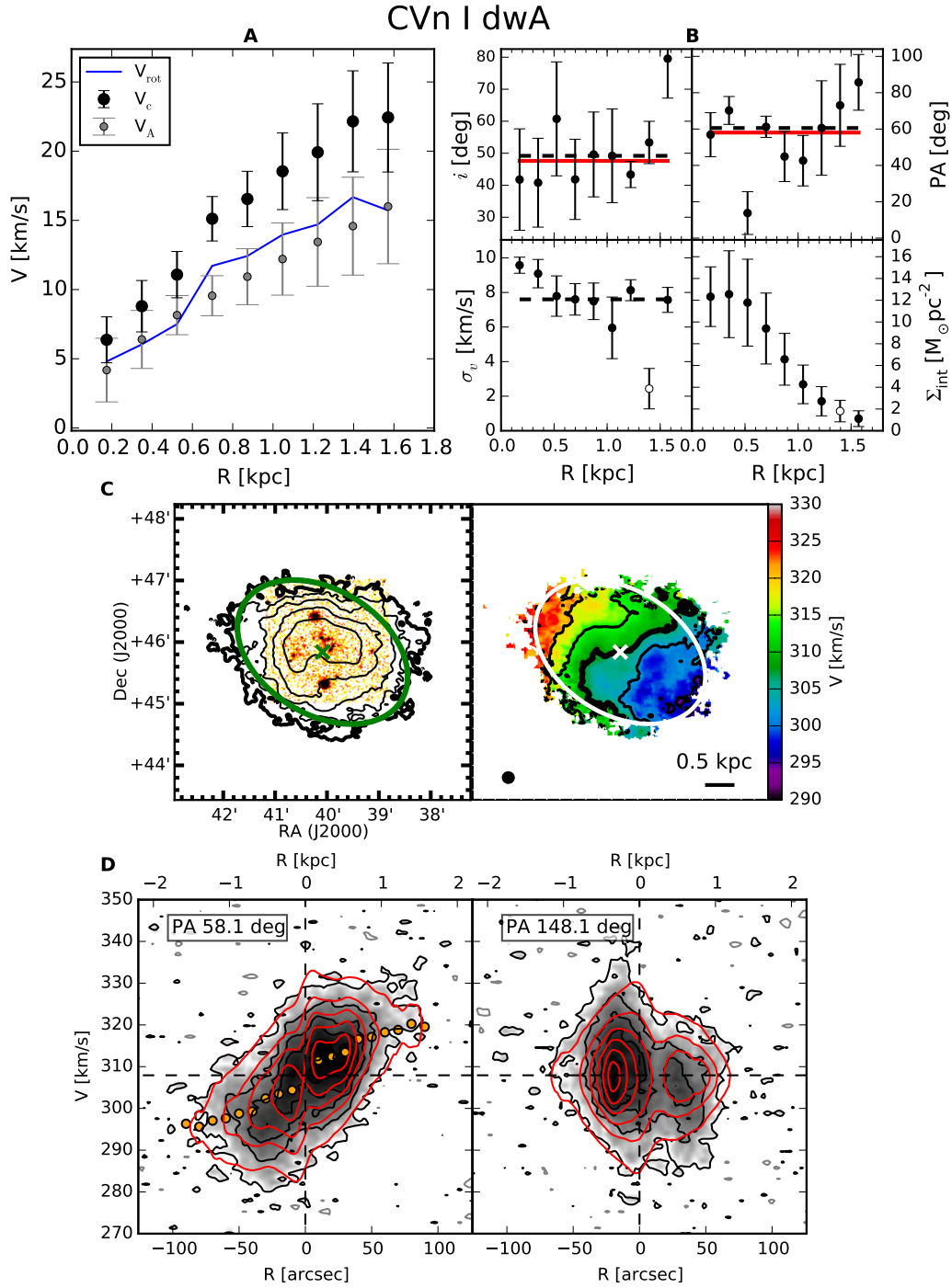


**Figure 3.10:** Notes. **C (left-hand panel):** Contours at  $2^n \sigma_{3T}$  and  $\sigma_{3T} = 0.96 M_{\odot} \text{pc}^{-2}$  (thick contour), stellar map in SDSS r band (Baillard et al., 2011); **C (right-hand panel):** Contours at  $V_{\text{sys}} \pm \Delta V$  where  $\Delta V = 6.0 \text{ km s}^{-1}$  and  $V_{\text{sys}} = 307.9 \text{ km s}^{-1}$  (thick contour). **D:** Contours at  $(2 + 4n)\sigma_{\text{ch}}$ , where  $\sigma_{\text{ch}} = 0.63 \text{ mJy beam}^{-1}$ , the grey contours are at  $-\sigma_{\text{ch}}$ .

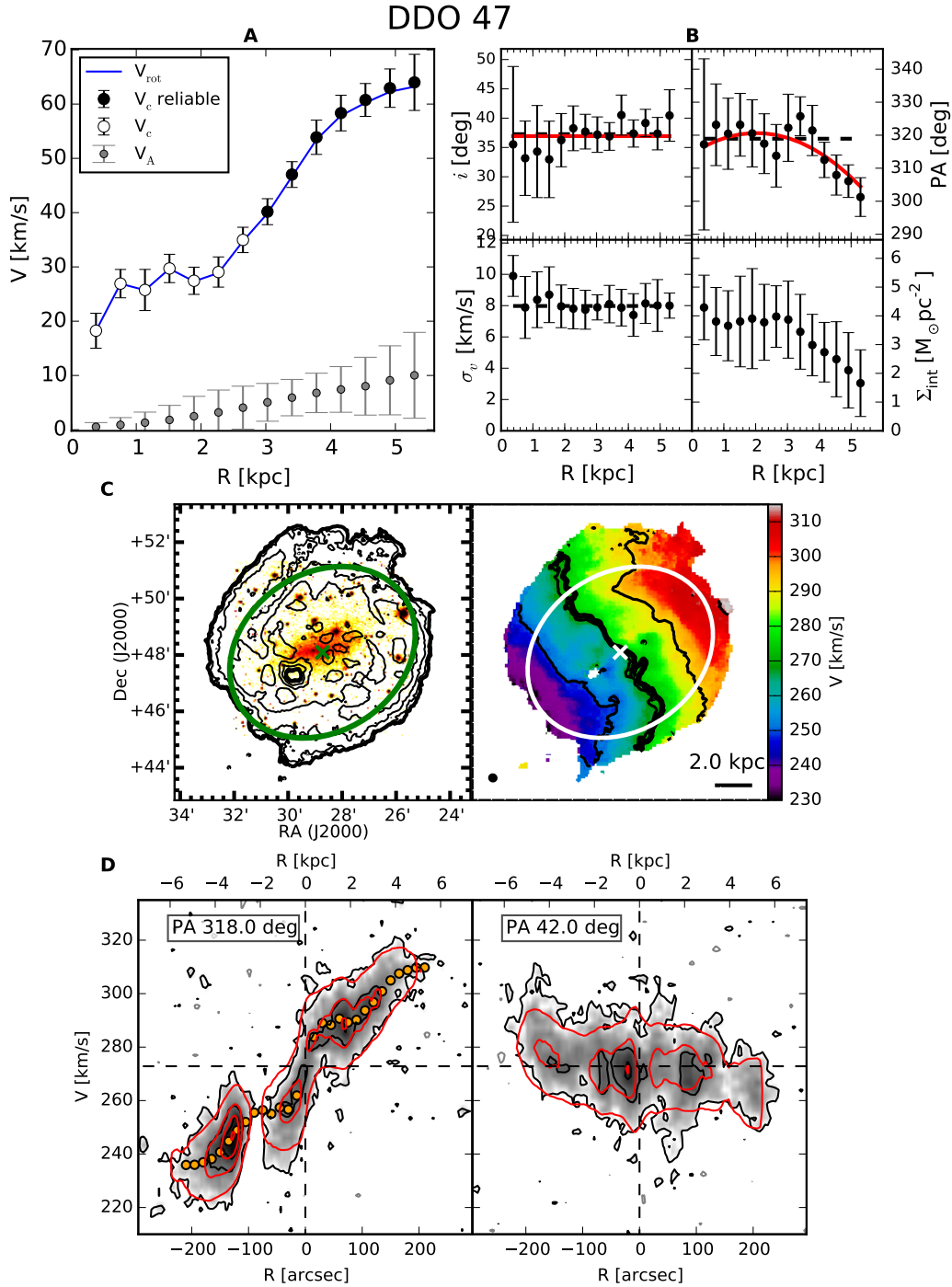


**Figure 3.11:** Notes. **A:** The empty circles indicate the region in which the estimate of the rotation curve can be biased by small HI regions at anomalous velocity along the major axis (see the text for further details); **C (left-hand panel):** Contours at  $2^{\text{nd}}\sigma_{3\text{T}}$  and  $\sigma_{3\text{T}} = 0.41 M_{\odot} \text{pc}^{-2}$  (thick contour), stellar map in SDSS r band (Baillard et al., 2011); **C (right-hand panel):** Contours at  $V_{\text{sys}} \pm \Delta V$  where  $\Delta V = 20.0 \text{ km s}^{-1}$  and  $V_{\text{sys}} = 272.8 \text{ km s}^{-1}$  (thick contour). **D:** Contours at  $(2 + 6n)\sigma_{\text{ch}}$ , where  $\sigma_{\text{ch}} = 0.61 \text{ mJy beam}^{-1}$ , the grey contours are at  $-2\sigma_{\text{ch}}$ .

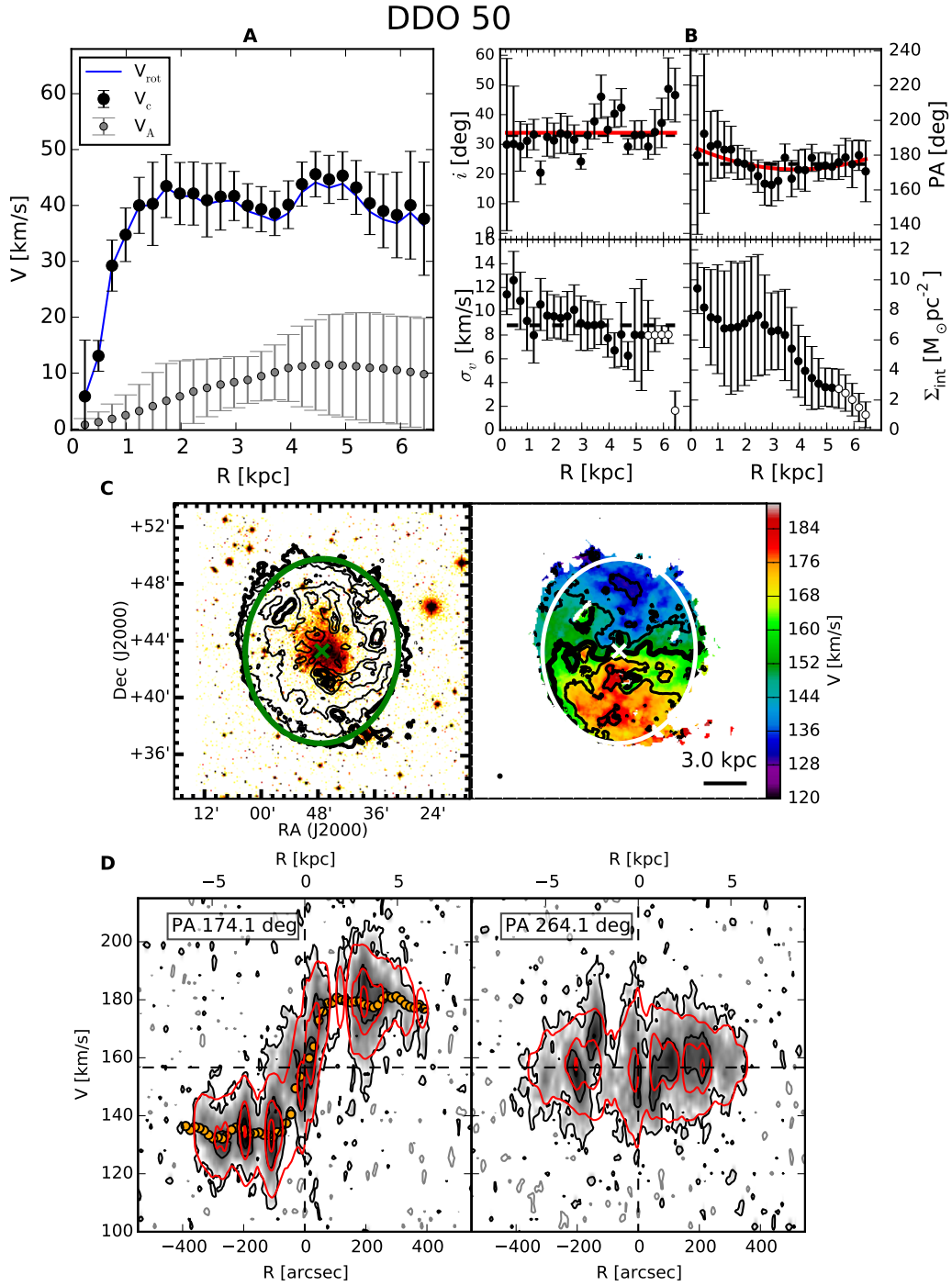


**Figure 3.12:** Notes. **C (left-hand panel):** Contours at  $3^n \sigma_{3T}$  and  $\sigma_{3T} = 0.65 M_{\odot} \text{pc}^{-2}$  (thick contour), stellar map in R band from Cook et al. (2014); **C (right-hand panel):** Contours at  $V_{\text{sys}} \pm \Delta V$  where  $\Delta V = 12.0 \text{ km s}^{-1}$  and  $V_{\text{sys}} = 156.7 \text{ km s}^{-1}$  (thick contour). **D:** Contours at  $(2 + 7n)\sigma_{\text{ch}}$ , where  $\sigma_{\text{ch}} = 0.82 \text{ mJy beam}^{-1}$ , the grey contours are at  $-2\sigma_{\text{ch}}$ .

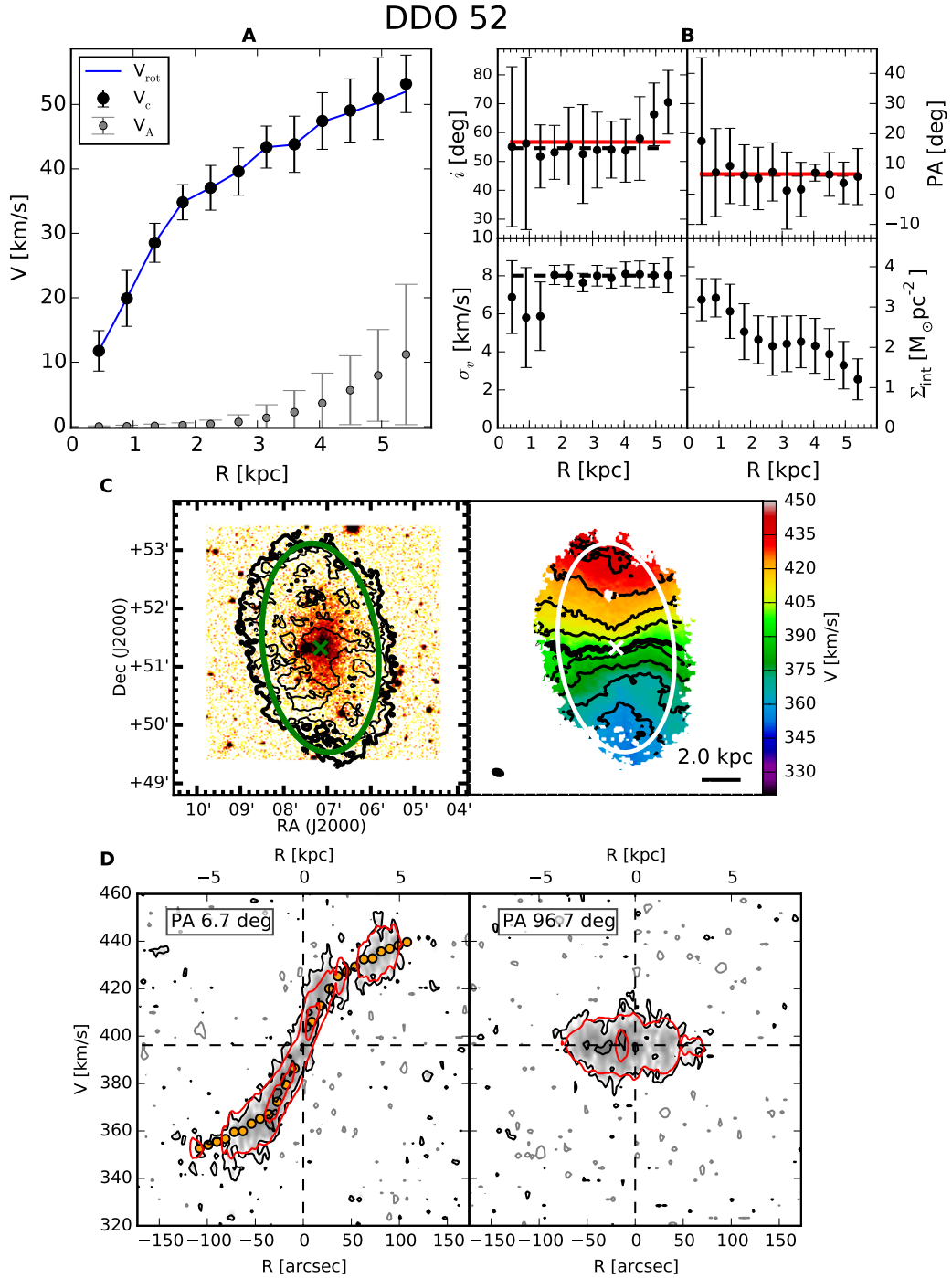


**Figure 3.13:** Notes. **C (left-hand panel):** Contours at  $2^n \sigma_{3T}$  and  $\sigma_{3T} = 1.20 M_{\odot} \text{pc}^{-2}$  (thick contour), stellar map in SDSS  $r$  band (Baillard et al., 2011); **C (right-hand panel):** Contours at  $V_{\text{sys}} \pm \Delta V$  where  $\Delta V = 10.0 \text{ km s}^{-1}$  and  $V_{\text{sys}} = 396.2 \text{ km s}^{-1}$  (thick contour). **D:** The contours start from  $(2 + 4n)\sigma_{\text{ch}}$ , where  $\sigma_{\text{ch}} = 0.46 \text{ mJy beam}^{-1}$ , the grey contours are at  $-2\sigma_{\text{ch}}$ .

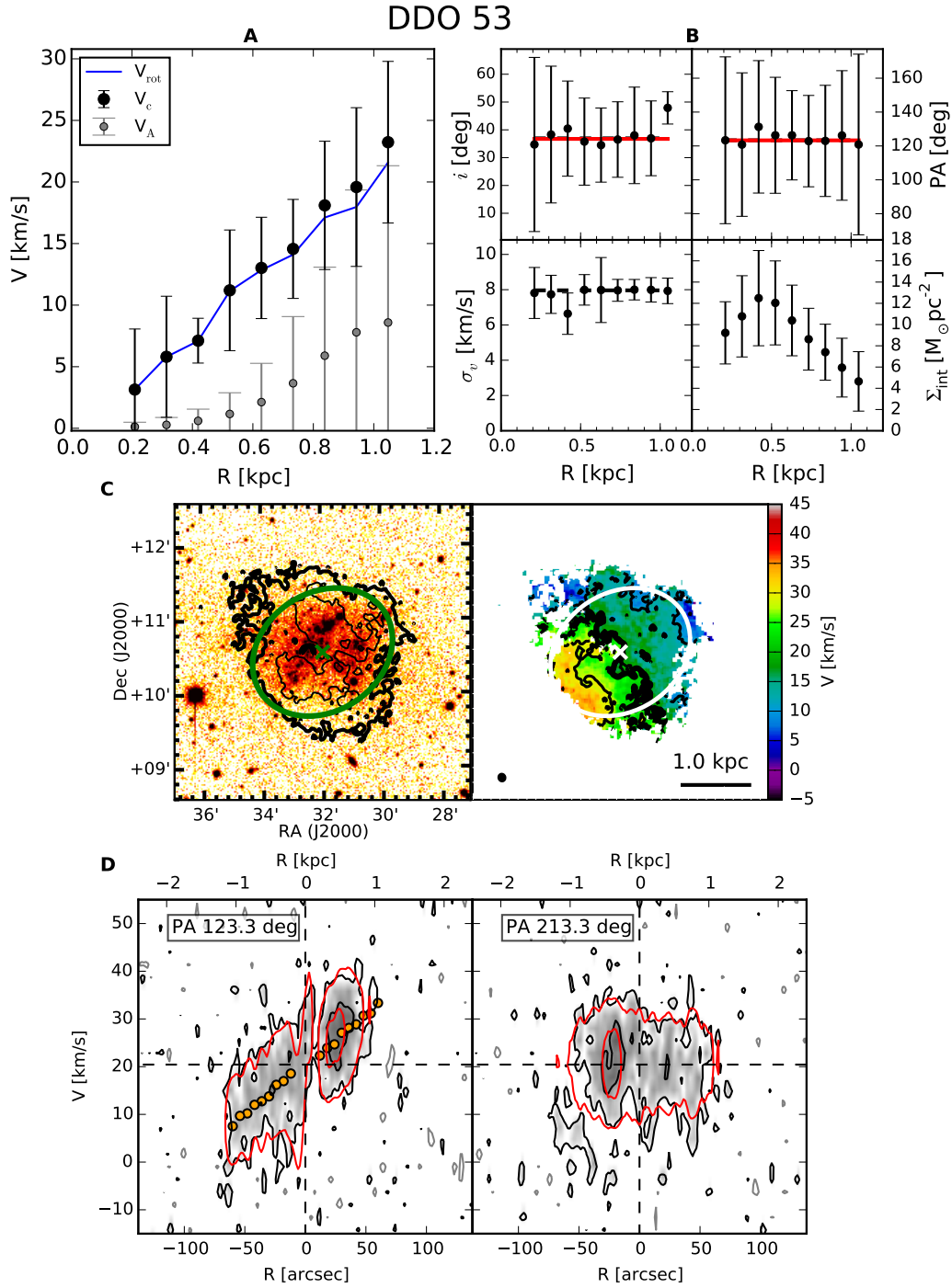


**Figure 3.14:** Notes. **C (left-hand panel):** Contours at  $2^n \sigma_{3T}$  and  $\sigma_{3T} = 3.80 M_{\odot} \text{pc}^{-2}$  (thick contour), stellar map in R band from Cook et al. (2014); **C (right-hand panel):** Contours at  $V_{\text{sys}} \pm \Delta V$  where  $\Delta V = 8.0 \text{ km s}^{-1}$  and  $V_{\text{sys}} = 20.4 \text{ km s}^{-1}$  (thick contour). **D:** Contours at  $(2 + 4n) \sigma_{\text{ch}}$ , where  $\sigma_{\text{ch}} = 0.57 \text{ mJy beam}^{-1}$ , the grey contours are at  $-\sigma_{\text{ch}}$ .

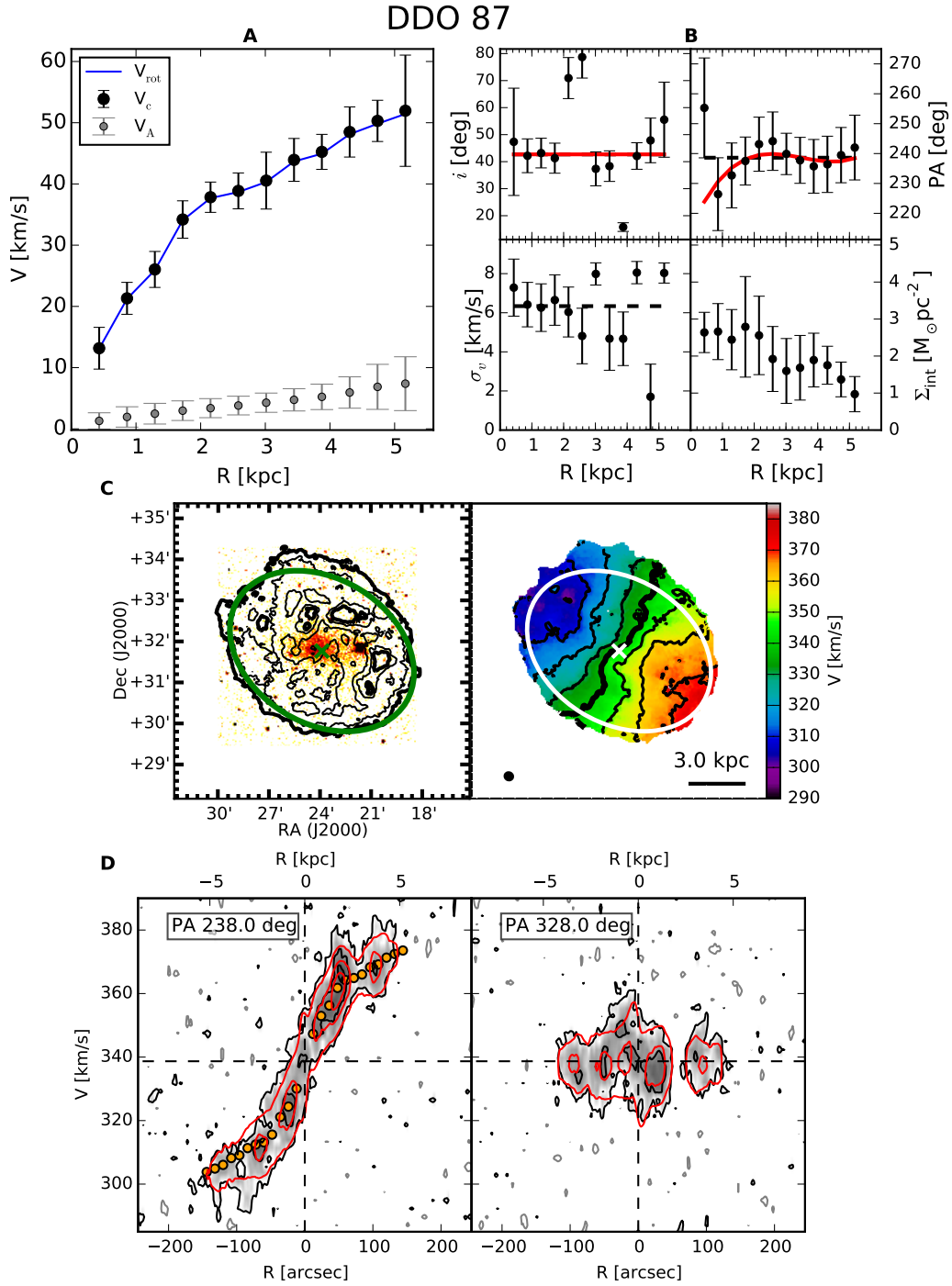


**Figure 3.15:** Notes. **C (left-hand panel):** Contours at  $2^n \sigma_{3T}$  and  $\sigma_{3T} = 0.90 M_{\odot} \text{pc}^{-2}$  (thick contour), stellar map in SDSS r band (Baillard et al., 2011); **C (right-hand panel):** Contours at  $V_{\text{sys}} \pm \Delta V$  where  $\Delta V = 10.0 \text{ km s}^{-1}$  and  $V_{\text{sys}} = 338.7 \text{ km s}^{-1}$  (thick contour). **D:** Contours at  $(2+4n)\sigma_{\text{ch}}$ , where  $\sigma_{\text{ch}} = 0.51 \text{ mJy beam}^{-1}$ , the grey contours are at  $-\sigma_{\text{ch}}$ .

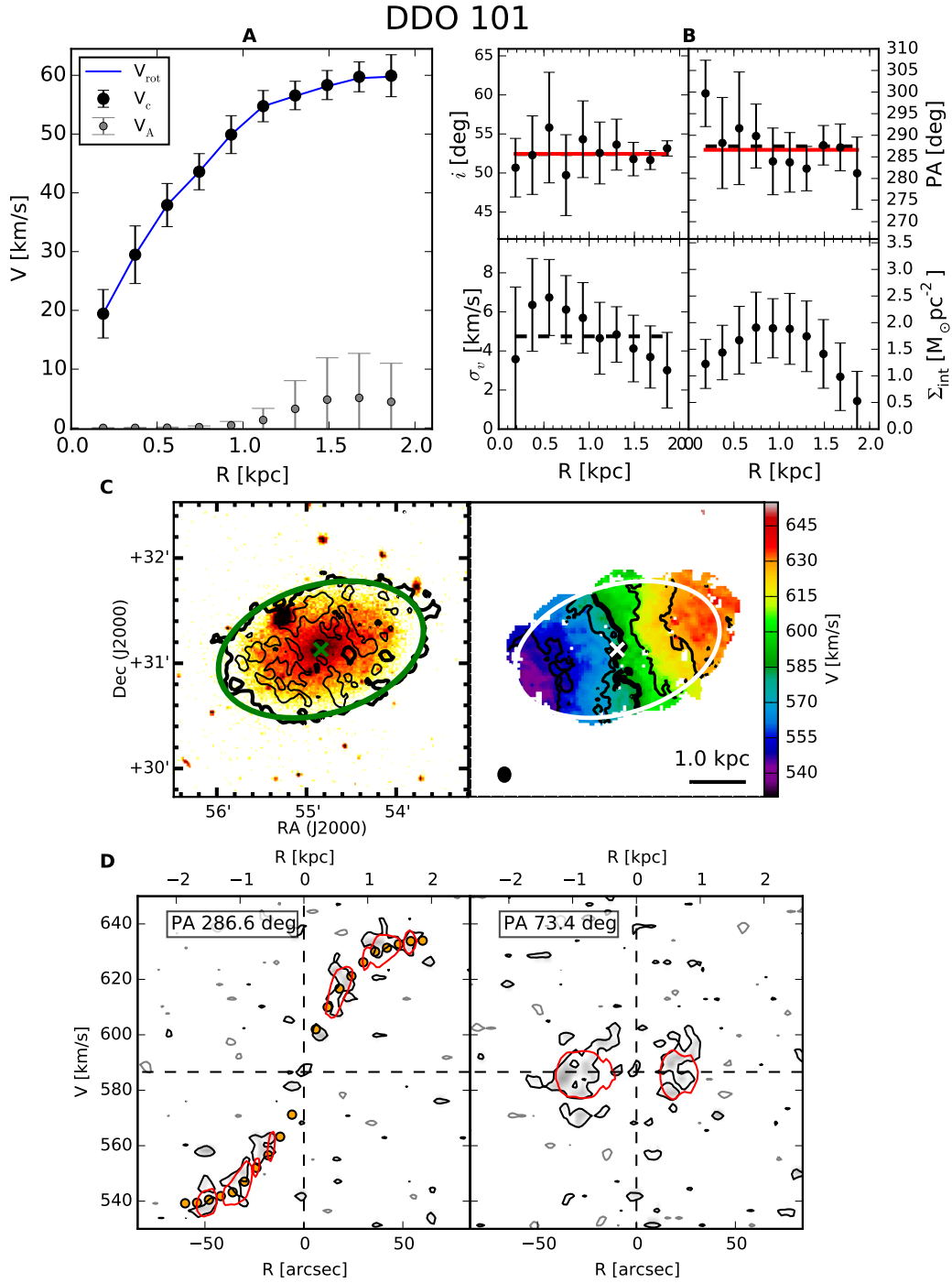


**Figure 3.16:** Notes. **C (left-hand panel):** Contours at  $4^n \sigma_{3T}$  and  $\sigma_{3T} = 0.90 M_{\odot} \text{pc}^{-2}$  (thick contour), stellar map in SDSS r band (Baillard et al., 2011); **C (right-hand panel):** Contours at  $V_{\text{sys}} \pm \Delta V$  where  $\Delta V = 20.0 \text{ km s}^{-1}$  and  $V_{\text{sys}} = 586.6 \text{ km s}^{-1}$  (thick contour). **D:** Contours at  $(2 + 6n)\sigma_{\text{ch}}$ , where  $\sigma_{\text{ch}} = 0.50 \text{ mJy beam}^{-1}$ , the grey contours are at  $-\sigma_{\text{ch}}$ .

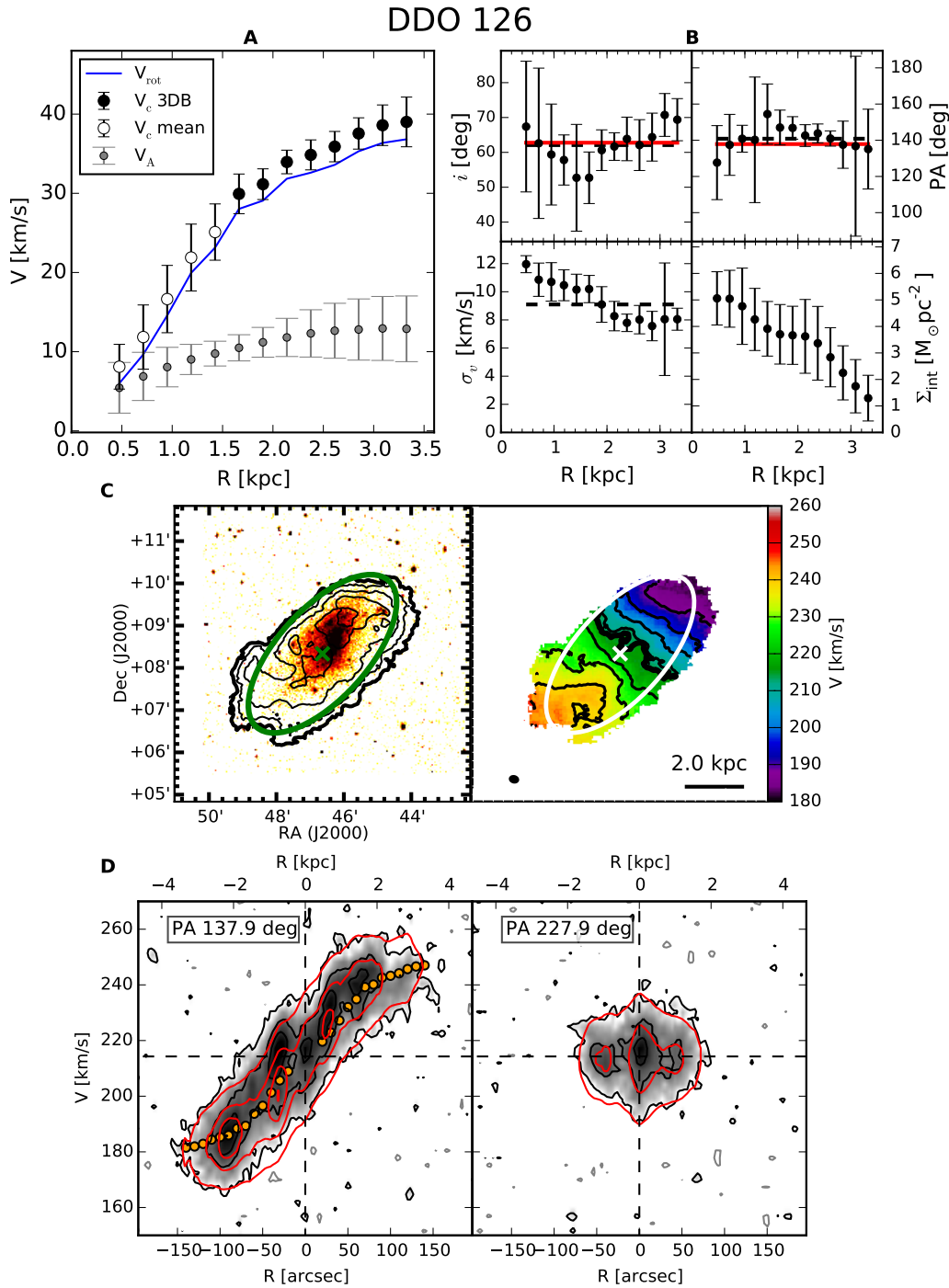


**Figure 3.17:** Notes. **A:** The empty circles indicates the region in which the circular velocity has been calculated as the mean between the approaching and receding rotation curves; **C (left-hand panel):** Contours at  $2^{\text{n}}\sigma_{3\text{T}}$  and  $\sigma_{3\text{T}} = 1.27 M_{\odot} \text{pc}^{-2}$  (thick contour), stellar map in SDSS r band (Baillard et al., 2011); **C (right-hand panel):** Contours at  $V_{\text{sys}} \pm \Delta V$  where  $\Delta V = 8.0 \text{ km s}^{-1}$  and  $V_{\text{sys}} = 214.3 \text{ km s}^{-1}$  (thick contour). **D:** Contours at  $(2 + 6n)\sigma_{\text{ch}}$ , where  $\sigma_{\text{ch}} = 0.41 \text{ mJy beam}^{-1}$ , the grey contours are at  $-2\sigma_{\text{ch}}$ .

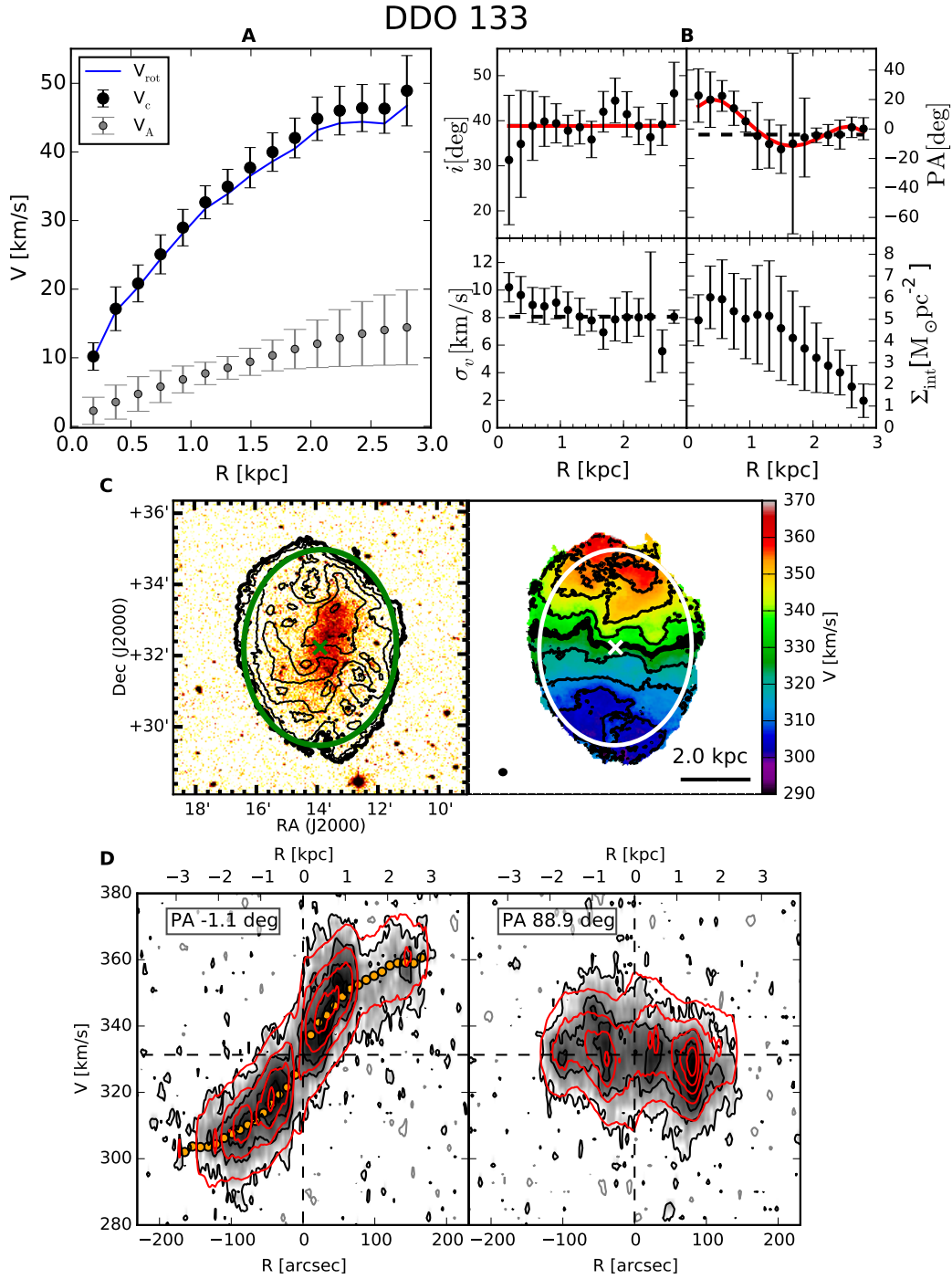


**Figure 3.18:** Notes. **C (left-hand panel):** Contours at  $2^n \sigma_{3T}$  and  $\sigma_{3T} = 0.89 M_{\odot} \text{pc}^{-2}$  (thick contour), stellar map in R band from Cook et al. (2014); **C (right-hand panel):** Contours at  $V_{\text{sys}} \pm \Delta V$  where  $\Delta V = 8.0 \text{ km s}^{-1}$  and  $V_{\text{sys}} = 331.3 \text{ km s}^{-1}$  (thick contour). **D:** Contours at  $(2 + 5n)\sigma_{\text{ch}}$ , where  $\sigma_{\text{ch}} = 0.35 \text{ mJy beam}^{-1}$ , the grey contours are at  $-2\sigma_{\text{ch}}$ .

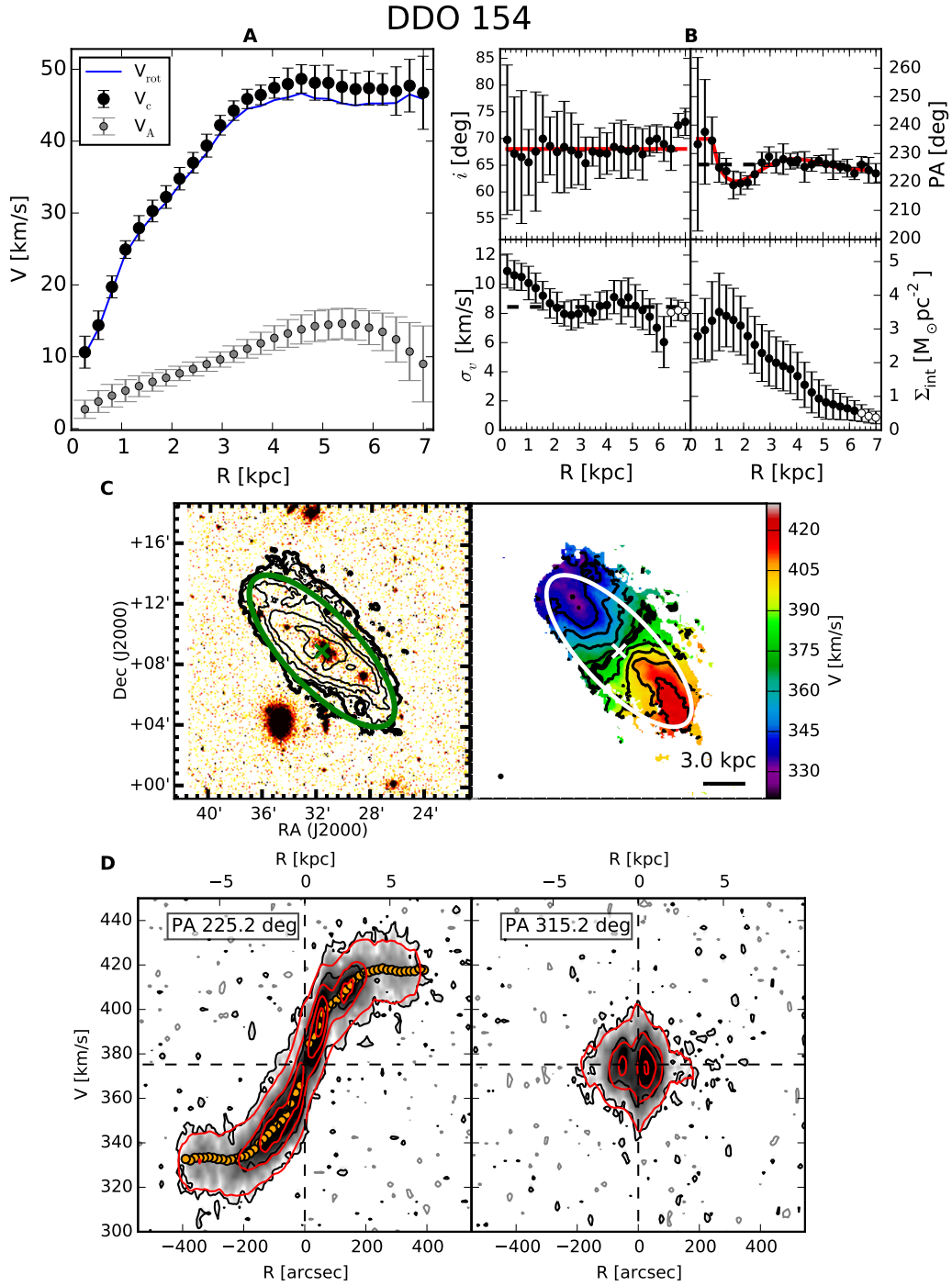


**Figure 3.19:** Notes. **C (left-hand panel):** Contours at  $2^n \sigma_{3T}$  and  $\sigma_{3T} = 0.52 M_{\odot} \text{pc}^{-2}$  (thick contour), stellar map in R band from Cook et al. (2014); **C (right-hand panel):** Contours at  $V_{\text{sys}} \pm \Delta V$  where  $\Delta V = 10.0 \text{ km s}^{-1}$  and  $V_{\text{sys}} = 375.2 \text{ km s}^{-1}$  (thick contour). **D:** Contours at  $(2 + 8n) \sigma_{\text{ch}}$ , where  $\sigma_{\text{ch}} = 0.44 \text{ mJy beam}^{-1}$ , the grey contours are at  $-2\sigma_{\text{ch}}$ .

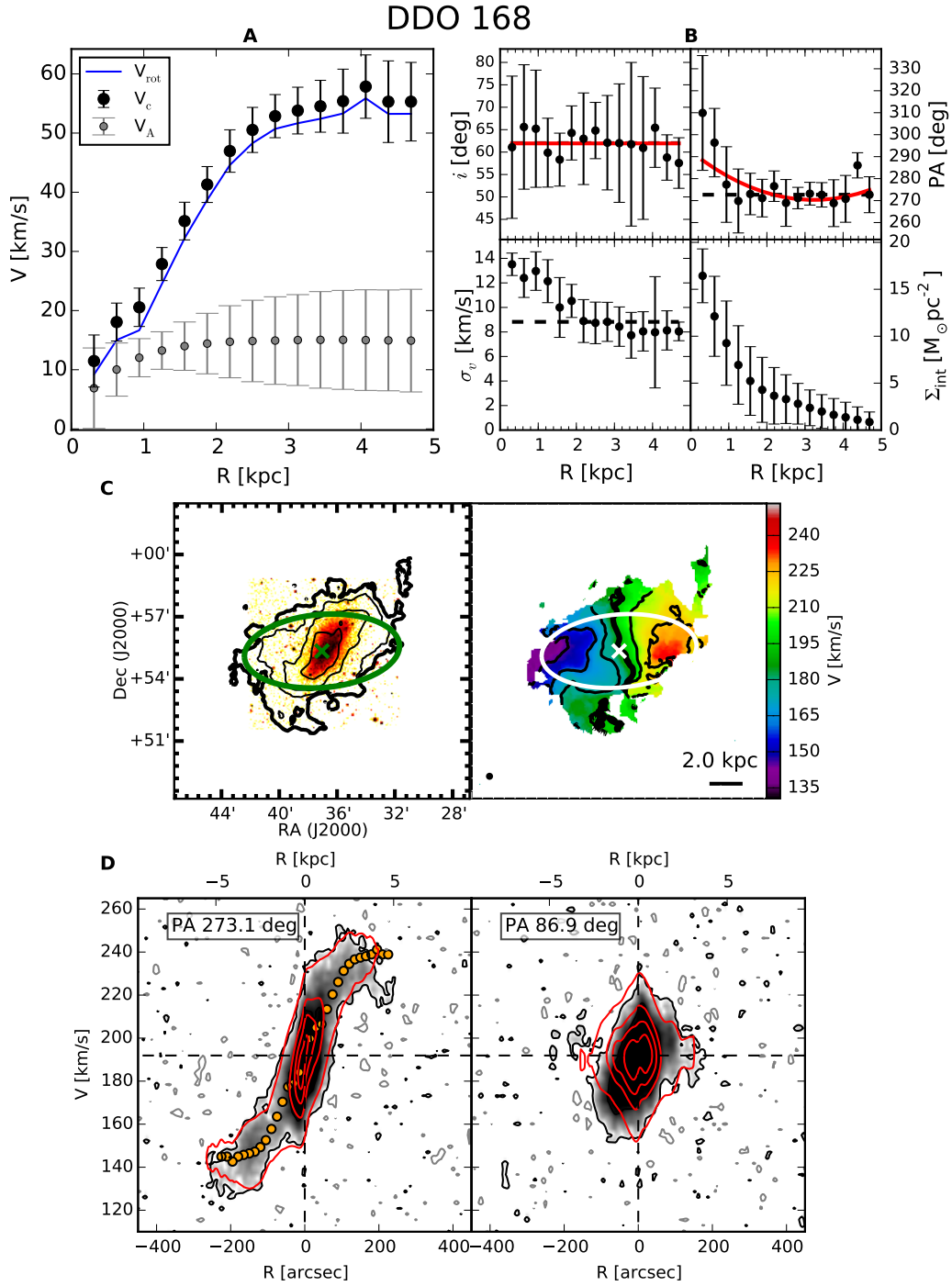


**Figure 3.20:** Notes. **C (left-hand panel):** Contours at  $3^n \sigma_{3T}$  and  $\sigma_{3T} = 0.54 M_{\odot} \text{pc}^{-2}$  (thick contour), stellar map in r band from (Baillard et al., 2011); **C (right-hand panel):** Contours at  $V_{\text{sys}} \pm \Delta V$  where  $\Delta V = 15.0 \text{ km s}^{-1}$  and  $V_{\text{sys}} = 191.9 \text{ km s}^{-1}$  (thick contour). **D:** Contours at  $(2+15n)\sigma_{\text{ch}}$ , where  $\sigma_{\text{ch}} = 0.47 \text{ mJy beam}^{-1}$ , the grey contours are at  $-\sigma_{\text{ch}}$ .

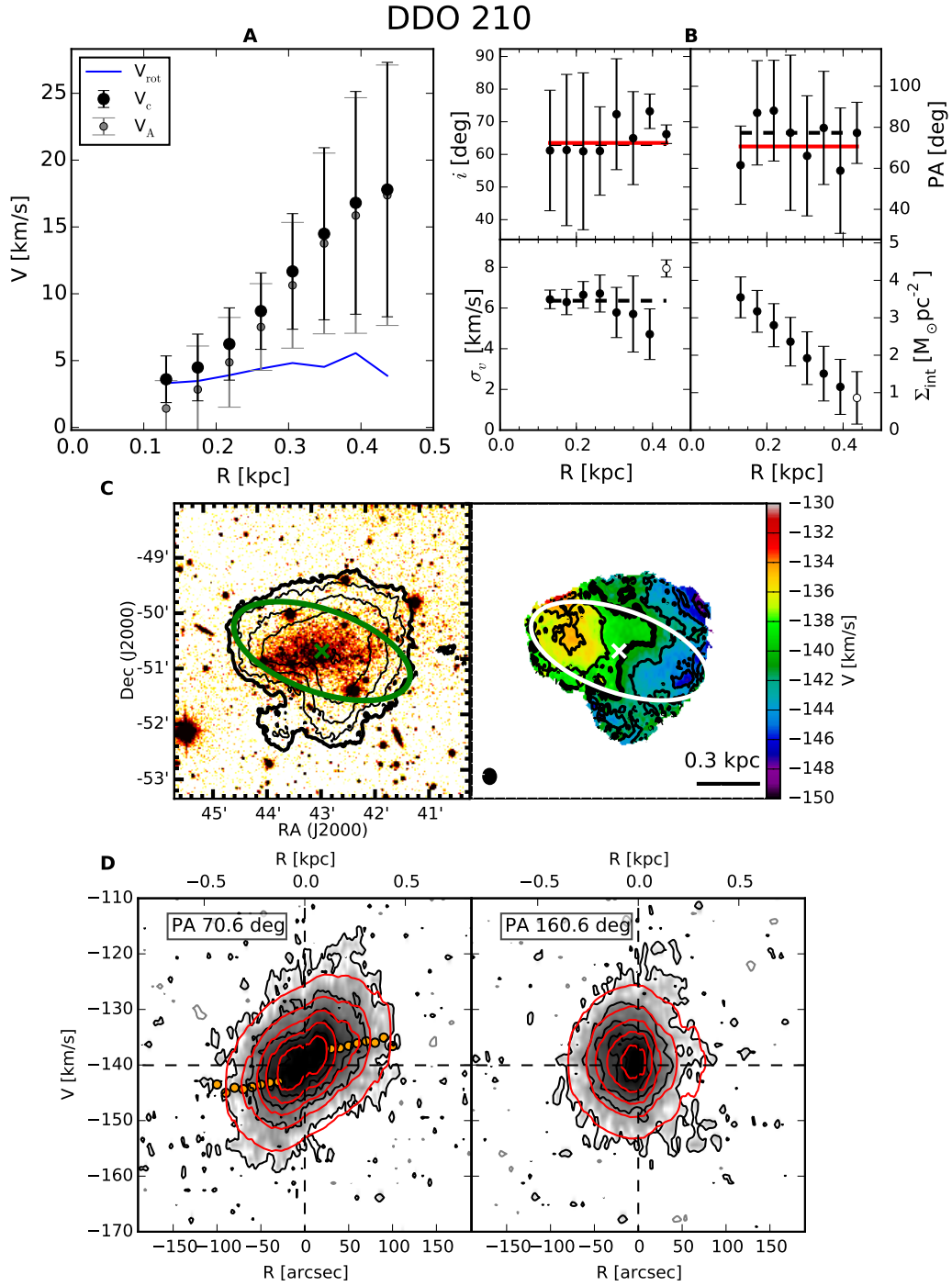


**Figure 3.21:** Notes. **C (left-hand panel):** Contours at  $2^n\sigma_{3T}$  and  $\sigma_{3T} = 0.59 M_{\odot}\text{pc}^{-2}$  (thick contour), stellar map in R band from Cook et al. (2014); **C (right-hand panel):** Contours at  $V_{\text{sys}} \pm \Delta V$  where  $\Delta V = 2.5 \text{ km s}^{-1}$  and  $V_{\text{sys}} = -140.0 \text{ km s}^{-1}$  (thick contour). **D:** Contours at  $(2 + 4n)\sigma_{\text{ch}}$ , where  $\sigma_{\text{ch}} = 0.75 \text{ mJy beam}^{-1}$ , the grey contours are at  $-2\sigma_{\text{ch}}$ .

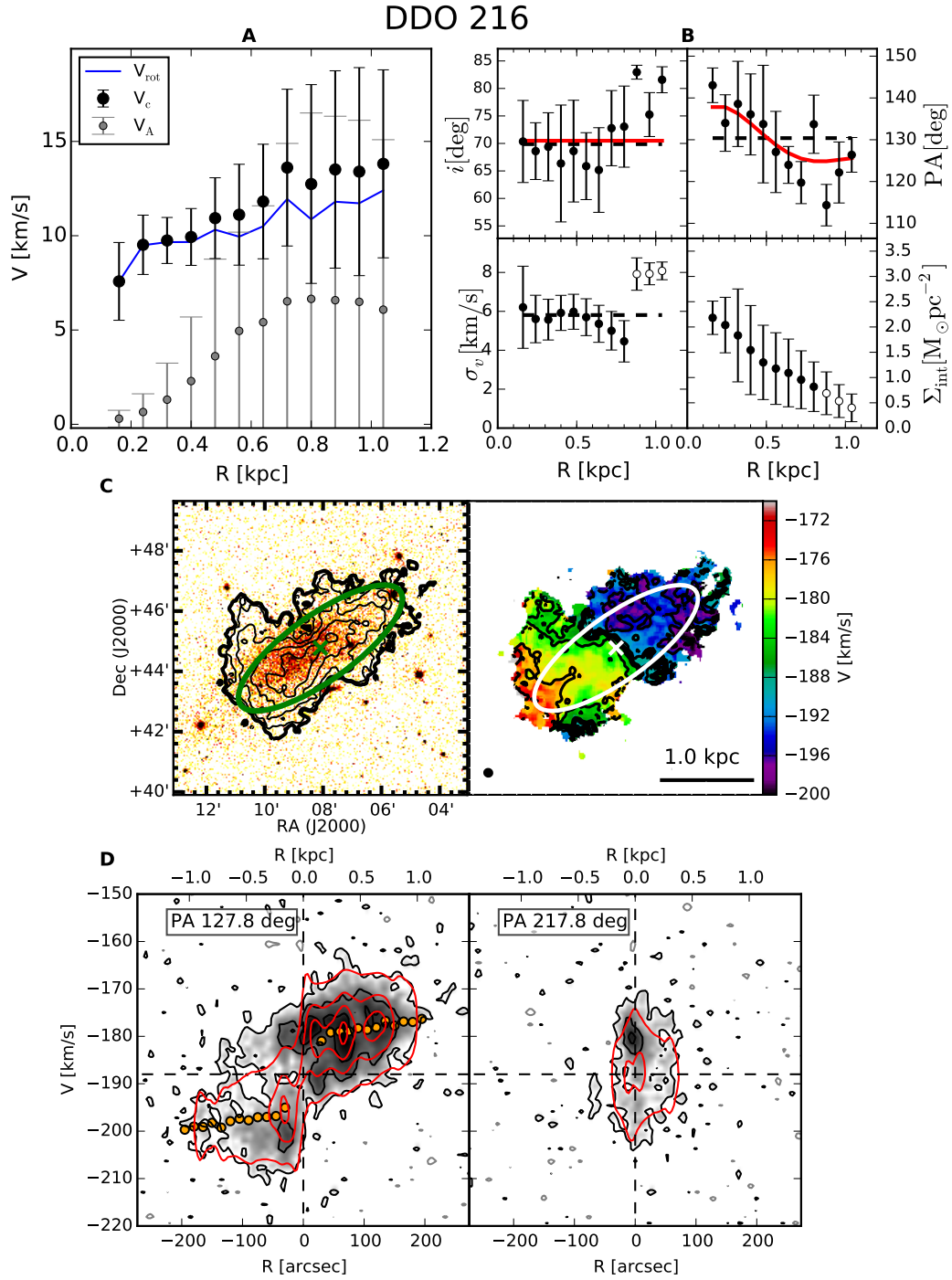


**Figure 3.22:** Notes. **C (left-hand panel):** Contours at  $2^n \sigma_{3T}$  and  $\sigma_{3T} = 0.40 M_{\odot} \text{pc}^{-2}$  (thick contour), stellar map in SDSS r band (Knapen et al., 2014); **C (right-hand panel):** Contours at  $V_{\text{sys}} \pm \Delta V$  where  $\Delta V = 5.0 \text{ km s}^{-1}$  and  $V_{\text{sys}} = -188.0 \text{ km s}^{-1}$  (thick contour). **D:** Contours at  $(2 + 6n) \sigma_{\text{ch}}$ , where  $\sigma_{\text{ch}} = 0.91 \text{ mJy beam}^{-1}$ , the grey contours are at  $-2\sigma_{\text{ch}}$ .

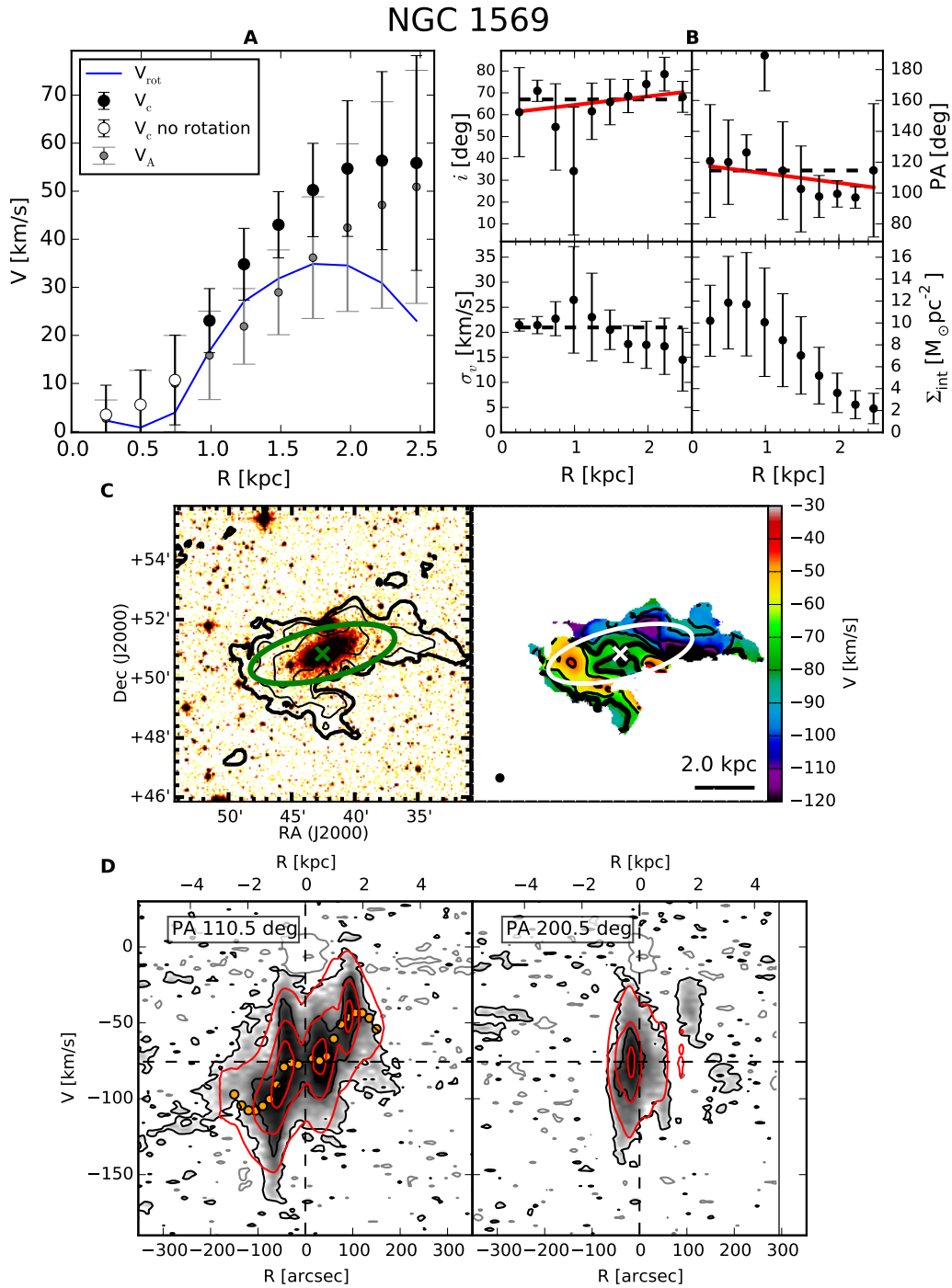


**Figure 3.23:** Notes. **A:** The empty circles indicate the region in which there are no significant signs of gas rotation; **C (left-hand panel):** Contours at  $4^n \sigma_{3T}$  and  $\sigma_{3T} = 1.10 M_{\odot} \text{pc}^{-2}$  (thick contour), stellar map in J band from (Jarrett et al., 2003); **C (right-hand panel):** Contours at  $V_{\text{sys}} \pm \Delta V$  where  $\Delta V = 15.0 \text{ km s}^{-1}$  and  $V_{\text{sys}} = -75.6 \text{ km s}^{-1}$  (thick contour). **D:** Contours at  $(2 + 8n)\sigma_{\text{ch}}$ , where  $\sigma_{\text{ch}} = 0.77 \text{ mJy beam}^{-1}$ , the grey contours are at  $-2\sigma_{\text{ch}}$ .

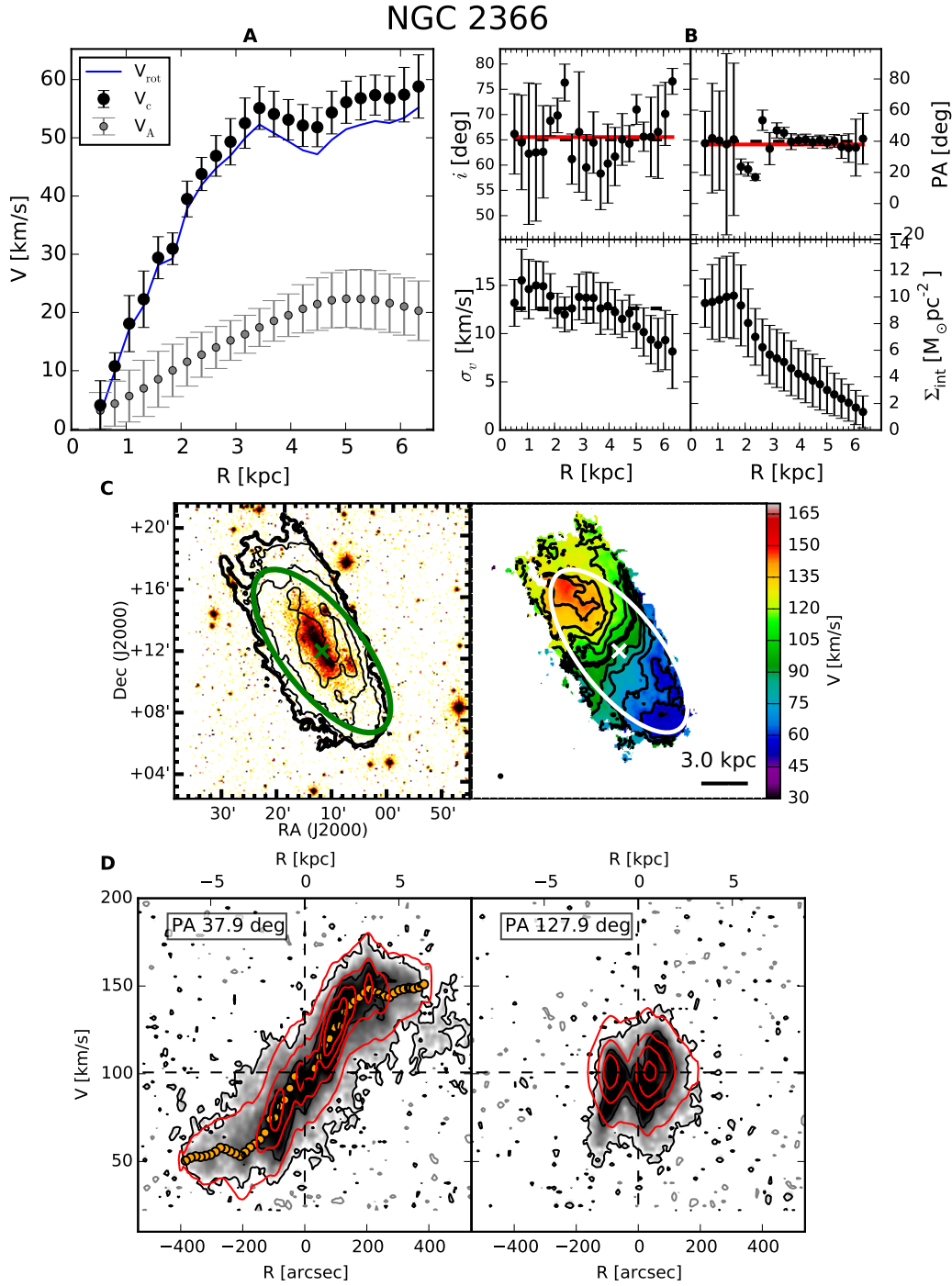


**Figure 3.24:** Notes. **C (left-hand panel):** Contours at  $3^n \sigma_{3T}$  and  $\sigma_{3T} = 0.59 M_{\odot} \text{pc}^{-2}$  (thick contour), stellar map in R band from Cook et al. (2014); **C (right-hand panel):** Contours at  $V_{\text{sys}} \pm \Delta V$  where  $\Delta V = 10.0 \text{ km s}^{-1}$  and  $V_{\text{sys}} = 100.8 \text{ km s}^{-1}$  (thick contour). **D:** Contours at  $(2+10n)\sigma_{\text{ch}}$ , where  $\sigma_{\text{ch}} = 0.52 \text{ mJy beam}^{-1}$ , the grey contours are at  $-\sigma_{\text{ch}}$ .

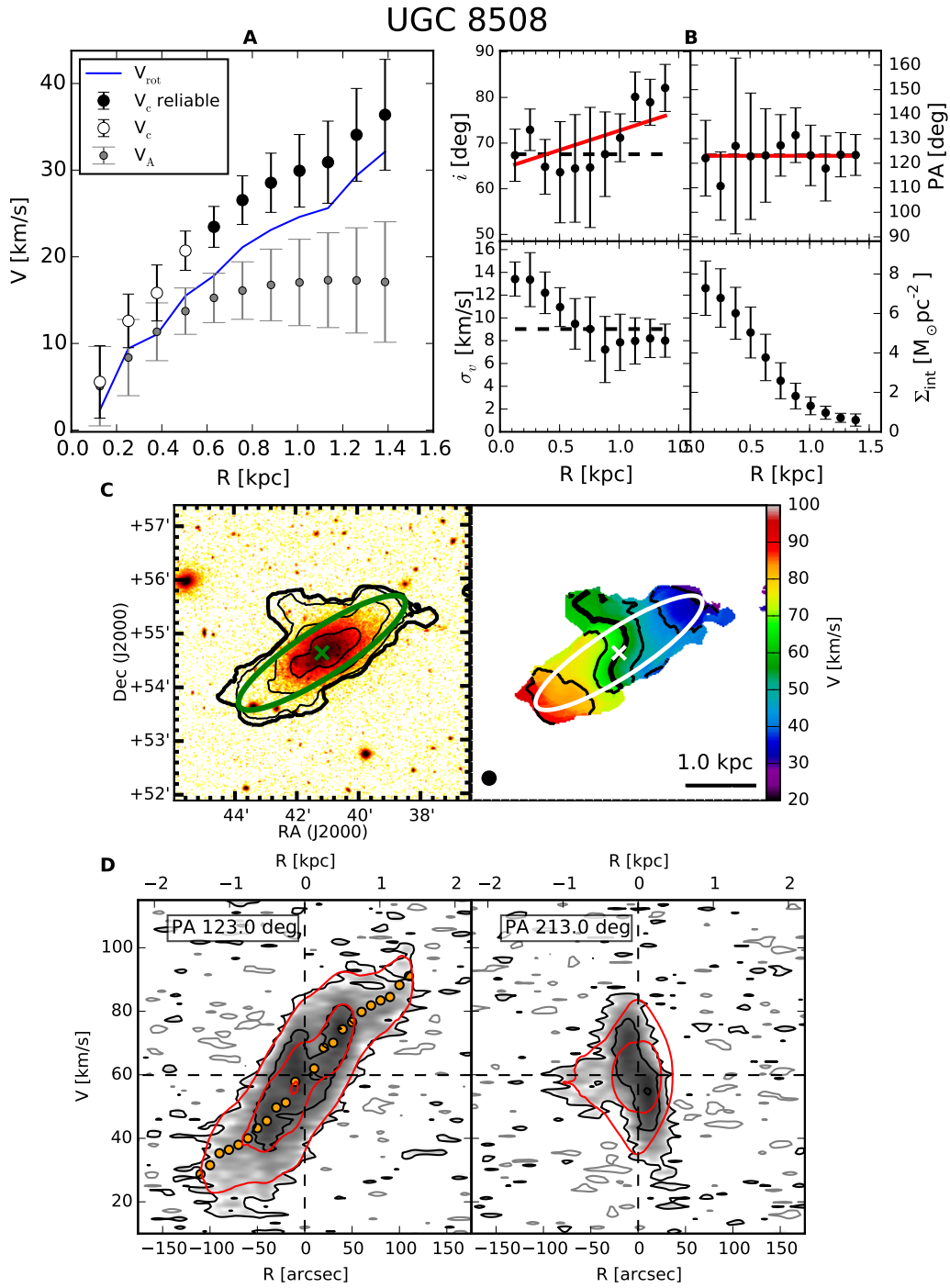


**Figure 3.25:** Notes. **A:** The empty circles indicate the region of the galaxy with peculiar kinematics (see the text); **C (left-hand panel):** Contours at  $3^n \sigma_{3T}$  and  $\sigma_{3T} = 0.54 M_{\odot} \text{pc}^{-2}$  (thick contour), stellar map in R band from Cook et al. (2014); **C (right-hand panel):** Contours at  $V_{\text{sys}} \pm \Delta V$  where  $\Delta V = 10.0 \text{ km s}^{-1}$  and  $V_{\text{sys}} = 59.9 \text{ km s}^{-1}$  (thick contour). **D:** Contours at  $(2 + 6n)\sigma_{\text{ch}}$ , where  $\sigma_{\text{ch}} = 1.31 \text{ mJy beam}^{-1}$ , the grey contours are at  $-2\sigma_{\text{ch}}$ .

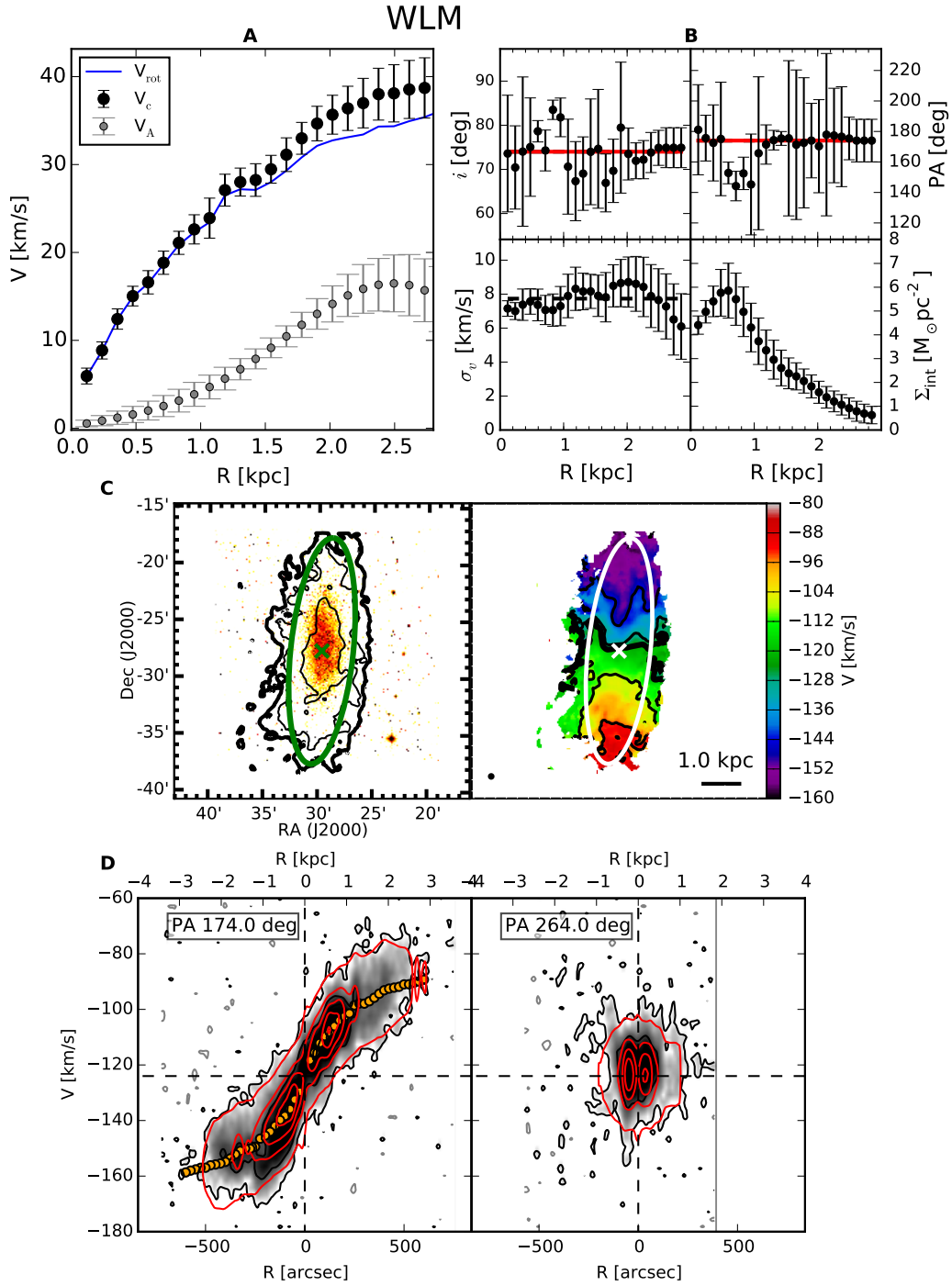


**Figure 3.26:** Notes. **C (left-hand panel):** Contours at  $2^n \sigma_{3T}$  and  $\sigma_{3T} = 0.58 M_{\odot} \text{pc}^{-2}$  (thick contour), stellar map in R band from Cook et al. (2014); **C (right-hand panel):** Contours at  $V_{\text{sys}} \pm \Delta V$  where  $\Delta V = 20.0 \text{ km s}^{-1}$  and  $V_{\text{sys}} = -124.0 \text{ km s}^{-1}$  (thick contour). **D:** Contours at  $(2 + 4n)\sigma_{\text{ch}}$ , where  $\sigma_{\text{ch}} = 2.00 \text{ mJy beam}^{-1}$ , the grey contours are at  $-2\sigma_{\text{ch}}$ .

### 3.A.2 Data

In the following Tables, one for each dIrr in our sample, we report all the kinematic and structural properties of the HI discs obtained in this Chapter. The Tables can be downloaded from the online version of Iorio et al. (2017b)<sup>5</sup>.

CVn I dwA						
R	R	$V_{\text{rot}}$	$V_A$	$V_c$	$\sigma_v$	$\Sigma_{\text{int}}$
(arcsec)	(kpc)	( $\text{km s}^{-1}$ )	( $M_{\odot} \text{pc}^{-2}$ )			
(1)	(2)	(3)	(4)	(5)	(6)	(7)
10.00	0.17	$4.80 \pm 0.91$	$4.18 \pm 2.30$	$6.37 \pm 1.66$	$9.58 \pm 0.47$	$12.33 \pm 2.74$
20.00	0.35	$6.04 \pm 1.54$	$6.40 \pm 2.10$	$8.80 \pm 1.86$	$9.09 \pm 0.82$	$12.55 \pm 3.99$
30.00	0.52	$7.50 \pm 1.93$	$8.15 \pm 1.41$	$11.08 \pm 1.67$	$7.79 \pm 1.17$	$11.78 \pm 3.99$
40.00	0.70	$11.71 \pm 1.70$	$9.55 \pm 1.45$	$15.12 \pm 1.61$	$7.60 \pm 0.91$	$9.40 \pm 3.26$
50.00	0.87	$12.42 \pm 1.98$	$10.93 \pm 2.02$	$16.55 \pm 2.00$	$7.49 \pm 1.06$	$6.57 \pm 2.38$
60.00	1.05	$13.96 \pm 2.89$	$12.21 \pm 2.61$	$18.54 \pm 2.77$	$5.95 \pm 1.78$	$4.26 \pm 1.78$
70.00	1.22	$14.70 \pm 3.73$	$13.44 \pm 3.20$	$19.92 \pm 3.50$	$8.13 \pm 0.61$	$2.71 \pm 1.34$
80.00	1.40	$16.68 \pm 3.73$	$14.58 \pm 3.54$	$22.15 \pm 3.65$	$2.44 \pm 1.17$	$1.81 \pm 0.99$
90.00	1.57	$15.72 \pm 3.73$	$16.00 \pm 4.13$	$22.43 \pm 3.94$	$7.57 \pm 0.72$	$1.11 \pm 0.73$

**Table 3.27: Kinematics and structural properties obtained for CVn I dwA.** -**(1)(2)** Sampling radii; **(3)** rotational velocity; **(4)** pressure-support correction term (see Sec. 3.3.3); **(5)** circular velocity; **(6)** velocity dispersion; **(7)** intrinsic HI surface density.

<sup>5</sup>The data tables can be downloaded also from <http://www.filippofraternali.com/resources/finalrot.zip>

DDO 47						
R (arcsec)	R (kpc)	$V_{\text{rot}}$ ( $\text{km s}^{-1}$ )	$V_{\text{A}}$ ( $\text{km s}^{-1}$ )	$V_{\text{c}}$ ( $\text{km s}^{-1}$ )	$\sigma_v$ ( $\text{km s}^{-1}$ )	$\Sigma_{\text{int}}$ ( $M_{\odot} \text{ pc}^{-2}$ )
(1)	(2)	(3)	(4)	(5)	(6)	(7)
15.00	0.38	$18.23 \pm 3.23$	$0.53 \pm 0.79$	$18.24 \pm 3.22$	$9.90 \pm 1.30$	$4.29 \pm 1.12$
30.00	0.76	$26.91 \pm 2.61$	$0.90 \pm 1.34$	$26.92 \pm 2.61$	$7.88 \pm 1.98$	$3.80 \pm 1.18$
45.00	1.13	$25.72 \pm 3.79$	$1.31 \pm 1.94$	$25.75 \pm 3.79$	$8.38 \pm 1.78$	$3.66 \pm 1.22$
60.00	1.51	$29.66 \pm 2.61$	$1.81 \pm 2.68$	$29.71 \pm 2.61$	$8.70 \pm 1.78$	$3.80 \pm 1.58$
75.00	1.89	$27.33 \pm 2.49$	$2.48 \pm 3.67$	$27.45 \pm 2.50$	$7.95 \pm 1.36$	$3.90 \pm 1.74$
90.00	2.27	$28.88 \pm 2.76$	$3.20 \pm 4.11$	$29.06 \pm 2.78$	$7.81 \pm 1.29$	$3.77 \pm 1.32$
105.00	2.65	$34.73 \pm 2.30$	$4.07 \pm 3.96$	$34.97 \pm 2.33$	$7.74 \pm 1.24$	$3.98 \pm 1.07$
120.00	3.03	$39.85 \pm 2.37$	$5.05 \pm 3.48$	$40.17 \pm 2.39$	$7.89 \pm 0.80$	$3.87 \pm 1.34$
135.00	3.40	$46.64 \pm 2.35$	$5.92 \pm 3.35$	$47.02 \pm 2.37$	$8.10 \pm 1.20$	$3.44 \pm 1.30$
150.00	3.78	$53.45 \pm 3.15$	$6.79 \pm 3.63$	$53.88 \pm 3.16$	$7.87 \pm 1.17$	$2.98 \pm 1.07$
165.00	4.16	$57.87 \pm 3.27$	$7.42 \pm 4.21$	$58.35 \pm 3.28$	$7.40 \pm 1.36$	$2.74 \pm 1.04$
180.00	4.54	$60.23 \pm 2.97$	$8.02 \pm 5.33$	$60.76 \pm 3.03$	$8.14 \pm 1.27$	$2.49 \pm 1.31$
195.00	4.92	$62.27 \pm 3.45$	$9.10 \pm 6.36$	$62.93 \pm 3.54$	$8.01 \pm 1.66$	$2.11 \pm 1.31$
210.00	5.29	$63.20 \pm 5.08$	$10.03 \pm 7.91$	$63.99 \pm 5.17$	$8.00 \pm 0.80$	$1.66 \pm 1.16$

**Table 3.28:** Same as Tab. 3.27 but for DDO 47

DDO 50						
R (arcsec) (1)	R (kpc) (2)	$V_{\text{rot}}$ ( $\text{km s}^{-1}$ ) (3)	$V_{\text{A}}$ ( $\text{km s}^{-1}$ ) (4)	$V_{\text{c}}$ ( $\text{km s}^{-1}$ ) (5)	$\sigma_v$ ( $\text{km s}^{-1}$ ) (6)	$\Sigma_{\text{int}}$ ( $M_{\odot} \text{ pc}^{-2}$ ) (7)
15.00	0.25	$5.79 \pm 10.14$	$0.75 \pm 1.11$	$5.83 \pm 10.06$	$11.42 \pm 1.70$	$9.43 \pm 1.68$
30.00	0.49	$13.03 \pm 2.76$	$1.23 \pm 1.82$	$13.08 \pm 2.75$	$12.62 \pm 2.42$	$8.16 \pm 2.66$
45.00	0.74	$29.18 \pm 4.58$	$1.80 \pm 2.67$	$29.23 \pm 4.57$	$10.88 \pm 2.41$	$7.50 \pm 3.18$
60.00	0.99	$34.67 \pm 4.80$	$2.45 \pm 3.64$	$34.75 \pm 4.79$	$9.19 \pm 2.50$	$7.38 \pm 3.62$
75.00	1.24	$39.88 \pm 5.02$	$3.21 \pm 4.75$	$40.01 \pm 5.02$	$7.99 \pm 2.34$	$6.76 \pm 3.83$
90.00	1.48	$40.08 \pm 7.46$	$4.07 \pm 6.04$	$40.29 \pm 7.45$	$10.57 \pm 2.19$	$6.81 \pm 4.43$
105.00	1.73	$43.17 \pm 5.62$	$5.04 \pm 6.67$	$43.47 \pm 5.64$	$9.63 \pm 2.06$	$6.86 \pm 4.26$
120.00	1.98	$41.72 \pm 5.54$	$5.83 \pm 6.37$	$42.13 \pm 5.56$	$9.57 \pm 1.82$	$7.11 \pm 4.14$
135.00	2.23	$41.60 \pm 5.64$	$6.69 \pm 5.71$	$42.13 \pm 5.65$	$9.43 \pm 1.79$	$7.42 \pm 4.11$
150.00	2.47	$40.27 \pm 6.61$	$7.35 \pm 5.15$	$40.94 \pm 6.56$	$9.57 \pm 2.09$	$7.64 \pm 4.04$
165.00	2.72	$40.81 \pm 6.02$	$7.95 \pm 4.68$	$41.57 \pm 5.98$	$10.12 \pm 2.10$	$7.00 \pm 3.32$
180.00	2.97	$40.85 \pm 4.39$	$8.36 \pm 4.57$	$41.69 \pm 4.40$	$9.00 \pm 2.29$	$6.57 \pm 2.56$
195.00	3.21	$38.98 \pm 3.92$	$8.77 \pm 4.18$	$39.96 \pm 3.93$	$8.80 \pm 2.11$	$6.64 \pm 2.61$
210.00	3.46	$38.18 \pm 4.01$	$9.44 \pm 4.42$	$39.33 \pm 4.04$	$8.83 \pm 1.96$	$6.33 \pm 3.03$
225.00	3.71	$37.23 \pm 3.90$	$10.13 \pm 4.91$	$38.59 \pm 3.98$	$8.88 \pm 1.69$	$5.41 \pm 2.75$
240.00	3.96	$38.62 \pm 4.10$	$10.91 \pm 5.99$	$40.13 \pm 4.27$	$7.74 \pm 1.60$	$4.58 \pm 2.40$
255.00	4.20	$42.37 \pm 3.61$	$11.19 \pm 7.22$	$43.82 \pm 3.94$	$6.71 \pm 1.48$	$3.94 \pm 2.29$
270.00	4.45	$44.13 \pm 3.62$	$11.45 \pm 8.11$	$45.59 \pm 4.05$	$8.04 \pm 2.70$	$3.46 \pm 2.10$
285.00	4.70	$43.15 \pm 3.75$	$11.49 \pm 8.98$	$44.66 \pm 4.30$	$6.26 \pm 1.18$	$3.09 \pm 1.67$
300.00	4.95	$43.90 \pm 3.72$	$11.36 \pm 9.20$	$45.34 \pm 4.28$	$8.01 \pm 3.90$	$2.86 \pm 1.27$
315.00	5.19	$41.74 \pm 4.26$	$11.22 \pm 9.59$	$43.22 \pm 4.81$	$8.00 \pm 4.67$	$2.82 \pm 1.27$
330.00	5.44	$38.88 \pm 5.12$	$10.95 \pm 9.86$	$40.39 \pm 5.60$	$7.97 \pm 2.94$	$2.75 \pm 1.30$
345.00	5.69	$37.47 \pm 6.25$	$10.84 \pm 9.72$	$39.00 \pm 6.58$	$8.01 \pm 1.40$	$2.46 \pm 1.21$
360.00	5.93	$36.81 \pm 7.47$	$10.54 \pm 9.65$	$38.29 \pm 7.66$	$8.03 \pm 0.76$	$2.02 \pm 1.08$
375.00	6.18	$38.73 \pm 9.62$	$10.20 \pm 9.87$	$40.04 \pm 9.63$	$8.03 \pm 0.74$	$1.50 \pm 0.94$
390.00	6.43	$36.33 \pm 10.14$	$9.80 \pm 10.00$	$37.63 \pm 10.13$	$1.64 \pm 1.64$	$1.02 \pm 0.85$

Table 3.29: Same as Tab. 3.27 but for DDO 50

DDO 52						
R (arcsec) (1)	R (kpc) (2)	$V_{\text{rot}}$ ( $\text{km s}^{-1}$ ) (3)	$V_{\text{A}}$ ( $\text{km s}^{-1}$ ) (4)	$V_{\text{c}}$ ( $\text{km s}^{-1}$ ) (5)	$\sigma_v$ ( $\text{km s}^{-1}$ ) (6)	$\Sigma_{\text{int}}$ ( $M_{\odot} \text{ pc}^{-2}$ ) (7)
9.00	0.45	$11.76 \pm 3.14$	$0.02 \pm 0.09$	$11.76 \pm 3.14$	$6.88 \pm 1.91$	$3.18 \pm 0.52$
18.00	0.90	$19.91 \pm 4.33$	$0.06 \pm 0.18$	$19.91 \pm 4.33$	$5.80 \pm 2.63$	$3.23 \pm 0.48$
27.00	1.35	$28.53 \pm 3.02$	$0.12 \pm 0.28$	$28.53 \pm 3.02$	$5.87 \pm 1.80$	$2.89 \pm 0.67$
36.00	1.80	$34.82 \pm 2.73$	$0.22 \pm 0.37$	$34.82 \pm 2.73$	$8.04 \pm 0.50$	$2.39 \pm 0.69$
45.00	2.25	$37.06 \pm 3.47$	$0.41 \pm 0.60$	$37.07 \pm 3.47$	$8.01 \pm 0.57$	$2.19 \pm 0.59$
54.00	2.70	$39.59 \pm 3.68$	$0.74 \pm 1.10$	$39.60 \pm 3.68$	$7.64 \pm 0.48$	$2.03 \pm 0.73$
63.00	3.15	$43.36 \pm 3.26$	$1.37 \pm 2.03$	$43.39 \pm 3.26$	$8.00 \pm 0.54$	$2.09 \pm 0.69$
72.00	3.60	$43.76 \pm 4.36$	$2.26 \pm 3.34$	$43.82 \pm 4.36$	$7.89 \pm 0.54$	$2.14 \pm 0.65$
81.00	4.04	$47.29 \pm 4.39$	$3.64 \pm 4.66$	$47.43 \pm 4.40$	$8.09 \pm 0.64$	$2.04 \pm 0.68$
90.00	4.49	$48.74 \pm 4.89$	$5.66 \pm 5.35$	$49.06 \pm 4.90$	$8.08 \pm 0.70$	$1.83 \pm 0.63$
99.00	4.94	$50.28 \pm 6.32$	$7.95 \pm 7.12$	$50.91 \pm 6.34$	$8.03 \pm 0.62$	$1.56 \pm 0.59$
108.00	5.39	$52.01 \pm 3.91$	$11.20 \pm 10.90$	$53.20 \pm 4.46$	$8.04 \pm 0.93$	$1.21 \pm 0.51$

Table 3.30: Same as Tab. 3.27 but for DDO 52

DDO 53						
R (arcsec) (1)	R (kpc) (2)	$V_{\text{rot}}$ ( $\text{km s}^{-1}$ ) (3)	$V_{\text{A}}$ ( $\text{km s}^{-1}$ ) (4)	$V_{\text{c}}$ ( $\text{km s}^{-1}$ ) (5)	$\sigma_v$ ( $\text{km s}^{-1}$ ) (6)	$\Sigma_{\text{int}}$ ( $M_{\odot} \text{ pc}^{-2}$ ) (7)
12.00	0.21	$3.14 \pm 4.92$	$0.12 \pm 0.37$	$3.14 \pm 4.92$	$7.81 \pm 1.45$	$9.22 \pm 2.93$
18.00	0.31	$5.80 \pm 4.92$	$0.28 \pm 0.60$	$5.81 \pm 4.92$	$7.74 \pm 1.08$	$10.77 \pm 3.83$
24.00	0.42	$7.09 \pm 1.82$	$0.60 \pm 0.95$	$7.11 \pm 1.82$	$6.64 \pm 1.17$	$12.49 \pm 4.48$
30.00	0.52	$11.14 \pm 4.92$	$1.16 \pm 1.72$	$11.20 \pm 4.90$	$7.99 \pm 0.86$	$12.04 \pm 3.95$
36.00	0.63	$12.85 \pm 4.14$	$2.12 \pm 3.15$	$13.02 \pm 4.11$	$7.98 \pm 1.84$	$10.39 \pm 3.33$
42.00	0.73	$14.10 \pm 3.91$	$3.65 \pm 5.42$	$14.56 \pm 4.02$	$7.96 \pm 0.62$	$8.62 \pm 2.91$
48.00	0.84	$17.11 \pm 4.92$	$5.89 \pm 7.19$	$18.10 \pm 5.21$	$8.00 \pm 0.58$	$7.40 \pm 2.63$
54.00	0.94	$17.97 \pm 4.92$	$7.79 \pm 11.56$	$19.59 \pm 6.44$	$7.99 \pm 0.69$	$5.94 \pm 2.77$
60.00	1.05	$21.58 \pm 4.92$	$8.59 \pm 12.73$	$23.23 \pm 6.56$	$7.93 \pm 0.72$	$4.65 \pm 2.80$

Table 3.31: Same as Tab. 3.27 but for DDO 53

DDO 87						
R (arcsec)	R (kpc)	$V_{\text{rot}}$ ( $\text{km s}^{-1}$ )	$V_A$ ( $\text{km s}^{-1}$ )	$V_c$ ( $\text{km s}^{-1}$ )	$\sigma_v$ ( $\text{km s}^{-1}$ )	$\Sigma_{\text{int}}$ ( $M_{\odot} \text{ pc}^{-2}$ )
(1)	(2)	(3)	(4)	(5)	(6)	(7)
12.00	0.43	$13.11 \pm 3.43$	$1.30 \pm 1.33$	$13.17 \pm 3.41$	$7.29 \pm 1.46$	$2.64 \pm 0.54$
24.00	0.86	$21.23 \pm 2.62$	$1.94 \pm 1.66$	$21.32 \pm 2.61$	$6.42 \pm 1.14$	$2.66 \pm 0.76$
36.00	1.29	$25.92 \pm 2.95$	$2.47 \pm 1.69$	$26.04 \pm 2.94$	$6.26 \pm 1.22$	$2.44 \pm 0.81$
48.00	1.72	$34.06 \pm 3.06$	$2.97 \pm 1.60$	$34.19 \pm 3.05$	$6.65 \pm 1.29$	$2.79 \pm 1.36$
60.00	2.15	$37.68 \pm 2.48$	$3.38 \pm 1.56$	$37.83 \pm 2.47$	$6.04 \pm 1.28$	$2.56 \pm 1.06$
72.00	2.58	$38.68 \pm 2.94$	$3.81 \pm 1.53$	$38.87 \pm 2.93$	$4.81 \pm 1.42$	$1.92 \pm 0.88$
84.00	3.01	$40.32 \pm 4.67$	$4.27 \pm 1.57$	$40.54 \pm 4.64$	$7.98 \pm 0.57$	$1.60 \pm 0.88$
96.00	3.44	$43.67 \pm 3.52$	$4.74 \pm 1.82$	$43.93 \pm 3.50$	$4.67 \pm 1.62$	$1.68 \pm 0.87$
108.00	3.87	$44.94 \pm 2.87$	$5.23 \pm 2.08$	$45.24 \pm 2.86$	$4.67 \pm 1.37$	$1.89 \pm 0.73$
120.00	4.31	$48.12 \pm 4.11$	$5.94 \pm 2.56$	$48.49 \pm 4.09$	$8.05 \pm 0.57$	$1.75 \pm 0.51$
132.00	4.74	$49.83 \pm 3.36$	$6.86 \pm 3.68$	$50.30 \pm 3.37$	$1.70 \pm 1.67$	$1.37 \pm 0.47$
144.00	5.17	$51.43 \pm 9.16$	$7.38 \pm 4.40$	$51.96 \pm 9.08$	$8.03 \pm 0.52$	$0.97 \pm 0.48$

Table 3.32: Same as Tab. 3.27 but for DDO 87

DDO 101						
R (arcsec)	R (kpc)	$V_{\text{rot}}$ ( $\text{km s}^{-1}$ )	$V_A$ ( $\text{km s}^{-1}$ )	$V_c$ ( $\text{km s}^{-1}$ )	$\sigma_v$ ( $\text{km s}^{-1}$ )	$\Sigma_{\text{int}}$ ( $M_{\odot} \text{ pc}^{-2}$ )
(1)	(2)	(3)	(4)	(5)	(6)	(7)
6.00	0.19	$19.42 \pm 4.12$	$0.00 \pm 0.04$	$19.42 \pm 4.12$	$3.58 \pm 3.69$	$1.22 \pm 0.46$
12.00	0.37	$29.47 \pm 4.90$	$0.01 \pm 0.07$	$29.47 \pm 4.90$	$6.36 \pm 2.38$	$1.44 \pm 0.51$
18.00	0.56	$37.92 \pm 3.67$	$0.03 \pm 0.11$	$37.92 \pm 3.67$	$6.74 \pm 1.95$	$1.67 \pm 0.64$
24.00	0.74	$43.59 \pm 3.08$	$0.13 \pm 0.21$	$43.59 \pm 3.07$	$6.12 \pm 1.74$	$1.91 \pm 0.67$
30.00	0.93	$49.90 \pm 3.22$	$0.44 \pm 0.66$	$49.90 \pm 3.22$	$5.69 \pm 1.81$	$1.89 \pm 0.56$
36.00	1.12	$54.73 \pm 2.66$	$1.34 \pm 1.98$	$54.75 \pm 2.66$	$4.65 \pm 1.84$	$1.88 \pm 0.67$
42.00	1.30	$56.47 \pm 2.41$	$3.24 \pm 4.80$	$56.56 \pm 2.42$	$4.84 \pm 1.42$	$1.74 \pm 0.66$
48.00	1.49	$58.14 \pm 2.42$	$4.81 \pm 7.13$	$58.34 \pm 2.48$	$4.12 \pm 1.71$	$1.41 \pm 0.64$
54.00	1.68	$59.52 \pm 2.46$	$5.11 \pm 7.57$	$59.74 \pm 2.54$	$3.69 \pm 1.59$	$0.98 \pm 0.63$
60.00	1.86	$59.76 \pm 3.55$	$4.43 \pm 6.57$	$59.93 \pm 3.57$	$3.01 \pm 1.94$	$0.53 \pm 0.56$

Table 3.33: Same as Tab. 3.27 but for DDO 101

DDO 126						
R (arcsec)	R (kpc)	$V_{\text{rot}}$ ( $\text{km s}^{-1}$ )	$V_{\text{A}}$ ( $\text{km s}^{-1}$ )	$V_{\text{c}}$ ( $\text{km s}^{-1}$ )	$\sigma_v$ ( $\text{km s}^{-1}$ )	$\Sigma_{\text{int}}$ ( $M_{\odot} \text{ pc}^{-2}$ )
(1)	(2)	(3)	(4)	(5)	(6)	(7)
20.00	0.48	$6.01 \pm 2.48$	$4.90 \pm 2.05$	$7.75 \pm 2.32$	$11.96 \pm 0.60$	$5.06 \pm 1.01$
30.00	0.71	$9.65 \pm 4.48$	$6.31 \pm 2.01$	$11.53 \pm 3.91$	$10.86 \pm 1.18$	$5.04 \pm 1.07$
40.00	0.95	$14.57 \pm 4.66$	$7.63 \pm 1.73$	$16.44 \pm 4.20$	$10.70 \pm 1.37$	$4.76 \pm 1.44$
50.00	1.19	$19.94 \pm 4.55$	$8.72 \pm 1.28$	$21.77 \pm 4.20$	$10.46 \pm 1.10$	$4.26 \pm 1.17$
60.00	1.43	$23.13 \pm 3.80$	$9.60 \pm 1.26$	$25.05 \pm 3.54$	$10.15 \pm 1.10$	$3.91 \pm 1.03$
70.00	1.66	$28.03 \pm 2.60$	$10.49 \pm 1.42$	$29.93 \pm 2.49$	$10.19 \pm 0.97$	$3.70 \pm 1.12$
80.00	1.90	$29.07 \pm 1.95$	$11.36 \pm 1.72$	$31.21 \pm 1.92$	$9.10 \pm 1.26$	$3.66 \pm 1.10$
90.00	2.14	$31.84 \pm 1.31$	$12.12 \pm 2.06$	$34.07 \pm 1.43$	$8.27 \pm 1.04$	$3.63 \pm 1.39$
100.00	2.38	$32.61 \pm 1.68$	$12.73 \pm 2.56$	$35.00 \pm 1.82$	$7.79 \pm 0.62$	$3.36 \pm 1.39$
110.00	2.61	$33.59 \pm 1.58$	$13.08 \pm 2.97$	$36.05 \pm 1.82$	$8.02 \pm 1.01$	$2.84 \pm 1.11$
120.00	2.85	$35.31 \pm 1.57$	$13.40 \pm 3.20$	$37.77 \pm 1.85$	$7.56 \pm 1.05$	$2.25 \pm 1.02$
130.00	3.09	$36.37 \pm 2.31$	$13.51 \pm 3.46$	$38.79 \pm 2.47$	$8.05 \pm 4.00$	$1.74 \pm 1.01$
140.00	3.33	$36.82 \pm 2.99$	$13.49 \pm 3.51$	$39.22 \pm 3.06$	$8.05 \pm 0.78$	$1.29 \pm 0.86$

**Table 3.34:** Same as Tab. 3.27 but for DDO 126

DDO 133						
R (arcsec)	R (kpc)	$V_{\text{rot}}$ ( $\text{km s}^{-1}$ )	$V_{\text{A}}$ ( $\text{km s}^{-1}$ )	$V_{\text{c}}$ ( $\text{km s}^{-1}$ )	$\sigma_v$ ( $\text{km s}^{-1}$ )	$\Sigma_{\text{int}}$ ( $M_{\odot} \text{ pc}^{-2}$ )
(1)	(2)	(3)	(4)	(5)	(6)	(7)
11.00	0.19	$9.93 \pm 2.00$	$2.26 \pm 1.98$	$10.19 \pm 2.00$	$10.20 \pm 1.06$	$4.96 \pm 1.18$
22.00	0.37	$16.77 \pm 3.21$	$3.54 \pm 2.48$	$17.14 \pm 3.19$	$9.64 \pm 1.35$	$6.01 \pm 1.44$
33.00	0.56	$20.30 \pm 2.70$	$4.72 \pm 2.52$	$20.84 \pm 2.69$	$8.92 \pm 1.27$	$5.93 \pm 1.81$
44.00	0.75	$24.39 \pm 2.87$	$5.80 \pm 2.32$	$25.07 \pm 2.84$	$8.82 \pm 1.30$	$5.37 \pm 1.74$
55.00	0.93	$28.15 \pm 2.70$	$6.84 \pm 1.96$	$28.97 \pm 2.66$	$9.09 \pm 1.18$	$5.02 \pm 1.84$
66.00	1.12	$31.74 \pm 2.44$	$7.72 \pm 1.63$	$32.66 \pm 2.40$	$8.55 \pm 1.30$	$5.21 \pm 2.27$
77.00	1.31	$33.89 \pm 2.56$	$8.53 \pm 1.66$	$34.94 \pm 2.52$	$8.07 \pm 1.34$	$5.15 \pm 2.54$
88.00	1.49	$36.51 \pm 2.99$	$9.41 \pm 1.98$	$37.70 \pm 2.94$	$7.80 \pm 0.79$	$4.58 \pm 2.41$
99.00	1.68	$38.62 \pm 2.84$	$10.34 \pm 2.25$	$39.98 \pm 2.81$	$6.93 \pm 1.23$	$4.14 \pm 2.16$
110.00	1.87	$40.50 \pm 2.90$	$11.27 \pm 2.87$	$42.04 \pm 2.90$	$7.87 \pm 1.56$	$3.65 \pm 1.93$
121.00	2.05	$43.19 \pm 3.14$	$12.04 \pm 3.46$	$44.84 \pm 3.17$	$8.02 \pm 1.84$	$3.23 \pm 1.60$
132.00	2.24	$44.19 \pm 3.49$	$12.87 \pm 4.14$	$46.02 \pm 3.54$	$8.02 \pm 1.37$	$2.86 \pm 1.26$
143.00	2.43	$44.39 \pm 3.29$	$13.51 \pm 4.69$	$46.40 \pm 3.43$	$8.06 \pm 4.71$	$2.55 \pm 1.03$
154.00	2.61	$44.13 \pm 3.40$	$14.04 \pm 5.12$	$46.31 \pm 3.59$	$5.56 \pm 1.55$	$1.89 \pm 0.98$
165.00	2.80	$46.75 \pm 5.09$	$14.42 \pm 5.46$	$48.92 \pm 5.12$	$8.06 \pm 0.48$	$1.25 \pm 0.77$

**Table 3.35:** Same as Tab. 3.27 but for DDO 133

DDO 154						
R (arcsec)	R (kpc)	$V_{\text{rot}}$ ( $\text{km s}^{-1}$ )	$V_{\text{A}}$ ( $\text{km s}^{-1}$ )	$V_{\text{c}}$ ( $\text{km s}^{-1}$ )	$\sigma_v$ ( $\text{km s}^{-1}$ )	$\Sigma_{\text{int}}$ ( $M_{\odot} \text{ pc}^{-2}$ )
(1)	(2)	(3)	(4)	(5)	(6)	(7)
15.00	0.27	$10.29 \pm 2.27$	$2.69 \pm 1.26$	$10.64 \pm 2.22$	$10.90 \pm 1.16$	$2.78 \pm 0.67$
30.00	0.54	$13.89 \pm 2.01$	$3.77 \pm 1.51$	$14.39 \pm 1.98$	$10.61 \pm 1.01$	$2.97 \pm 0.94$
45.00	0.81	$19.18 \pm 1.52$	$4.59 \pm 1.57$	$19.72 \pm 1.52$	$10.50 \pm 0.93$	$3.24 \pm 1.16$
60.00	1.08	$24.36 \pm 1.21$	$5.28 \pm 1.53$	$24.92 \pm 1.22$	$10.08 \pm 1.15$	$3.50 \pm 1.15$
75.00	1.35	$27.27 \pm 1.75$	$5.91 \pm 1.45$	$27.90 \pm 1.74$	$9.74 \pm 1.03$	$3.39 \pm 0.92$
90.00	1.61	$29.57 \pm 1.52$	$6.51 \pm 1.29$	$30.28 \pm 1.51$	$9.21 \pm 0.98$	$3.27 \pm 0.94$
105.00	1.88	$31.44 \pm 1.60$	$7.07 \pm 1.14$	$32.23 \pm 1.58$	$8.69 \pm 1.00$	$3.10 \pm 0.87$
120.00	2.15	$33.92 \pm 1.58$	$7.68 \pm 1.00$	$34.78 \pm 1.56$	$8.38 \pm 1.07$	$2.79 \pm 0.83$
135.00	2.42	$36.06 \pm 1.45$	$8.30 \pm 0.97$	$37.00 \pm 1.43$	$7.97 \pm 0.83$	$2.53 \pm 0.84$
150.00	2.69	$38.35 \pm 1.62$	$8.96 \pm 0.98$	$39.38 \pm 1.59$	$7.88 \pm 1.02$	$2.29 \pm 0.84$
165.00	2.96	$41.11 \pm 1.38$	$9.61 \pm 1.06$	$42.22 \pm 1.37$	$7.98 \pm 0.96$	$2.12 \pm 0.82$
180.00	3.23	$43.02 \pm 1.37$	$10.36 \pm 1.14$	$44.25 \pm 1.36$	$8.31 \pm 0.96$	$2.00 \pm 0.77$
195.00	3.50	$44.51 \pm 1.35$	$11.11 \pm 1.29$	$45.87 \pm 1.34$	$8.05 \pm 0.78$	$1.90 \pm 0.74$
210.00	3.77	$44.89 \pm 1.35$	$11.87 \pm 1.54$	$46.44 \pm 1.37$	$8.51 \pm 0.96$	$1.81 \pm 0.73$
225.00	4.04	$45.71 \pm 1.41$	$12.61 \pm 1.71$	$47.41 \pm 1.43$	$8.58 \pm 0.98$	$1.60 \pm 0.71$
240.00	4.31	$46.08 \pm 2.24$	$13.25 \pm 1.93$	$47.95 \pm 2.22$	$9.12 \pm 1.14$	$1.34 \pm 0.67$
255.00	4.57	$46.66 \pm 1.96$	$13.81 \pm 2.03$	$48.66 \pm 1.97$	$8.76 \pm 1.48$	$1.12 \pm 0.61$
270.00	4.84	$45.96 \pm 2.44$	$14.25 \pm 2.14$	$48.12 \pm 2.41$	$9.10 \pm 1.32$	$0.94 \pm 0.56$
285.00	5.11	$45.88 \pm 2.50$	$14.46 \pm 2.12$	$48.11 \pm 2.47$	$8.52 \pm 1.46$	$0.82 \pm 0.50$
300.00	5.38	$45.26 \pm 2.35$	$14.62 \pm 2.12$	$47.56 \pm 2.33$	$8.22 \pm 1.34$	$0.76 \pm 0.44$
315.00	5.65	$44.96 \pm 2.24$	$14.49 \pm 2.19$	$47.24 \pm 2.24$	$7.77 \pm 1.22$	$0.70 \pm 0.39$
330.00	5.92	$45.24 \pm 2.35$	$14.05 \pm 2.36$	$47.37 \pm 2.35$	$7.02 \pm 1.65$	$0.64 \pm 0.34$
345.00	6.19	$45.24 \pm 2.17$	$13.47 \pm 2.61$	$47.20 \pm 2.21$	$6.03 \pm 1.76$	$0.58 \pm 0.30$
360.00	6.46	$45.30 \pm 3.39$	$12.42 \pm 3.14$	$46.97 \pm 3.37$	$8.07 \pm 0.97$	$0.50 \pm 0.25$
375.00	6.73	$46.50 \pm 3.64$	$10.72 \pm 4.04$	$47.72 \pm 3.66$	$8.21 \pm 0.70$	$0.42 \pm 0.21$
390.00	7.00	$45.86 \pm 5.08$	$9.00 \pm 5.28$	$46.74 \pm 5.09$	$8.12 \pm 0.64$	$0.37 \pm 0.19$

**Table 3.36:** Same as Tab. 3.27 but for DDO 154

DDO 168						
R (arcsec)	R (kpc)	$V_{\text{rot}}$ ( $\text{km s}^{-1}$ )	$V_{\text{A}}$ ( $\text{km s}^{-1}$ )	$V_{\text{c}}$ ( $\text{km s}^{-1}$ )	$\sigma_v$ ( $\text{km s}^{-1}$ )	$\Sigma_{\text{int}}$ ( $M_{\odot} \text{ pc}^{-2}$ )
(1)	(2)	(3)	(4)	(5)	(6)	(7)
15.00	0.31	$9.18 \pm 2.06$	$6.88 \pm 6.80$	$11.47 \pm 4.40$	$13.52 \pm 0.92$	$16.43 \pm 2.87$
30.00	0.63	$15.02 \pm 2.42$	$10.03 \pm 4.49$	$18.06 \pm 3.21$	$12.40 \pm 1.59$	$12.12 \pm 4.26$
45.00	0.94	$16.66 \pm 3.25$	$12.03 \pm 3.22$	$20.55 \pm 3.24$	$12.96 \pm 1.57$	$9.26 \pm 4.49$
60.00	1.25	$24.52 \pm 2.67$	$13.24 \pm 3.17$	$27.86 \pm 2.79$	$12.14 \pm 1.75$	$6.94 \pm 4.18$
75.00	1.56	$32.22 \pm 2.98$	$13.98 \pm 4.09$	$35.12 \pm 3.18$	$10.00 \pm 2.44$	$5.23 \pm 3.66$
90.00	1.88	$38.70 \pm 2.62$	$14.42 \pm 5.11$	$41.30 \pm 3.03$	$10.53 \pm 1.35$	$4.29 \pm 3.46$
105.00	2.19	$44.59 \pm 3.20$	$14.73 \pm 6.09$	$46.96 \pm 3.59$	$8.89 \pm 1.75$	$3.65 \pm 3.01$
120.00	2.50	$48.30 \pm 3.38$	$14.86 \pm 6.89$	$50.53 \pm 3.81$	$8.74 \pm 1.70$	$3.30 \pm 2.60$
135.00	2.81	$50.71 \pm 3.11$	$14.93 \pm 7.40$	$52.86 \pm 3.64$	$8.82 \pm 1.59$	$2.81 \pm 2.17$
150.00	3.13	$51.66 \pm 3.45$	$15.01 \pm 7.68$	$53.80 \pm 3.95$	$8.44 \pm 1.60$	$2.37 \pm 1.91$
165.00	3.44	$52.41 \pm 3.91$	$15.04 \pm 8.16$	$54.53 \pm 4.38$	$7.73 \pm 1.87$	$1.98 \pm 1.80$
180.00	3.75	$53.31 \pm 5.10$	$15.05 \pm 8.36$	$55.39 \pm 5.41$	$8.05 \pm 1.60$	$1.62 \pm 1.74$
195.00	4.07	$55.88 \pm 5.05$	$15.00 \pm 8.51$	$57.85 \pm 5.36$	$7.97 \pm 4.54$	$1.37 \pm 1.60$
210.00	4.38	$53.24 \pm 6.75$	$14.96 \pm 8.52$	$55.30 \pm 6.90$	$8.13 \pm 1.60$	$1.10 \pm 1.37$
225.00	4.69	$53.25 \pm 6.45$	$14.92 \pm 8.67$	$55.30 \pm 6.64$	$8.04 \pm 0.76$	$0.86 \pm 1.07$

**Table 3.37:** Same as Tab. 3.27 but for DDO 168

DDO 210						
R (arcsec)	R (kpc)	$V_{\text{rot}}$ ( $\text{km s}^{-1}$ )	$V_{\text{A}}$ ( $\text{km s}^{-1}$ )	$V_{\text{c}}$ ( $\text{km s}^{-1}$ )	$\sigma_v$ ( $\text{km s}^{-1}$ )	$\Sigma_{\text{int}}$ ( $M_{\odot} \text{ pc}^{-2}$ )
(1)	(2)	(3)	(4)	(5)	(6)	(7)
30.00	0.13	$3.31 \pm 1.68$	$1.42 \pm 2.08$	$3.60 \pm 1.75$	$6.42 \pm 0.46$	$3.54 \pm 0.54$
40.00	0.17	$3.47 \pm 1.83$	$2.84 \pm 3.25$	$4.48 \pm 2.50$	$6.29 \pm 0.62$	$3.17 \pm 0.56$
50.00	0.22	$3.90 \pm 1.08$	$4.87 \pm 3.36$	$6.24 \pm 2.70$	$6.65 \pm 0.66$	$2.80 \pm 0.57$
60.00	0.26	$4.40 \pm 1.17$	$7.51 \pm 3.25$	$8.70 \pm 2.86$	$6.71 \pm 0.91$	$2.36 \pm 0.65$
70.00	0.31	$4.82 \pm 1.44$	$10.63 \pm 4.70$	$11.67 \pm 4.33$	$5.78 \pm 1.23$	$1.92 \pm 0.70$
80.00	0.35	$4.53 \pm 1.40$	$13.76 \pm 6.76$	$14.49 \pm 6.44$	$5.71 \pm 1.87$	$1.51 \pm 0.73$
90.00	0.39	$5.56 \pm 1.56$	$15.86 \pm 8.81$	$16.80 \pm 8.22$	$4.71 \pm 1.25$	$1.15 \pm 0.74$
100.00	0.44	$3.87 \pm 1.83$	$17.37 \pm 9.74$	$17.80 \pm 9.52$	$7.95 \pm 0.42$	$0.86 \pm 0.70$

**Table 3.38:** Same as Tab. 3.27 but for DDO 210

DDO 216						
R (arcsec)	R (kpc)	$V_{\text{rot}}$ ( $\text{km s}^{-1}$ )	$V_{\text{A}}$ ( $\text{km s}^{-1}$ )	$V_{\text{c}}$ ( $\text{km s}^{-1}$ )	$\sigma_v$ ( $\text{km s}^{-1}$ )	$\Sigma_{\text{int}}$ ( $M_{\odot} \text{ pc}^{-2}$ )
(1)	(2)	(3)	(4)	(5)	(6)	(7)
30.00	0.16	$7.57 \pm 2.06$	$0.30 \pm 0.44$	$7.58 \pm 2.06$	$6.21 \pm 2.11$	$2.18 \pm 0.33$
45.00	0.24	$9.50 \pm 1.57$	$0.65 \pm 0.97$	$9.52 \pm 1.57$	$5.61 \pm 1.22$	$2.04 \pm 0.55$
60.00	0.32	$9.66 \pm 1.20$	$1.31 \pm 1.94$	$9.75 \pm 1.22$	$5.57 \pm 1.05$	$1.83 \pm 0.92$
75.00	0.40	$9.67 \pm 1.32$	$2.29 \pm 3.40$	$9.93 \pm 1.51$	$5.92 \pm 0.90$	$1.54 \pm 0.88$
90.00	0.48	$10.32 \pm 1.38$	$3.61 \pm 5.15$	$10.93 \pm 2.14$	$5.98 \pm 0.90$	$1.30 \pm 0.74$
105.00	0.56	$9.95 \pm 1.46$	$4.95 \pm 5.24$	$11.11 \pm 2.67$	$5.70 \pm 0.95$	$1.18 \pm 0.71$
120.00	0.64	$10.50 \pm 1.25$	$5.41 \pm 6.17$	$11.81 \pm 3.04$	$5.36 \pm 0.95$	$1.09 \pm 0.67$
135.00	0.72	$11.95 \pm 1.24$	$6.52 \pm 8.37$	$13.61 \pm 4.16$	$5.00 \pm 0.99$	$0.96 \pm 0.57$
150.00	0.80	$10.87 \pm 1.34$	$6.65 \pm 9.86$	$12.74 \pm 5.27$	$4.46 \pm 1.06$	$0.82 \pm 0.49$
165.00	0.88	$11.80 \pm 2.51$	$6.58 \pm 9.76$	$13.51 \pm 5.23$	$7.92 \pm 0.83$	$0.69 \pm 0.42$
180.00	0.96	$11.72 \pm 3.36$	$6.49 \pm 9.63$	$13.40 \pm 5.52$	$7.93 \pm 0.56$	$0.53 \pm 0.33$
195.00	1.04	$12.40 \pm 3.36$	$6.08 \pm 9.01$	$13.81 \pm 4.98$	$8.08 \pm 0.46$	$0.40 \pm 0.27$

Table 3.39: Same as Tab. 3.27 but for DDO 216

NGC 1569						
R (arcsec)	R (kpc)	$V_{\text{rot}}$ ( $\text{km s}^{-1}$ )	$V_{\text{A}}$ ( $\text{km s}^{-1}$ )	$V_{\text{c}}$ ( $\text{km s}^{-1}$ )	$\sigma_v$ ( $\text{km s}^{-1}$ )	$\Sigma_{\text{int}}$ ( $M_{\odot} \text{ pc}^{-2}$ )
(1)	(2)	(3)	(4)	(5)	(6)	(7)
15.00	0.25	$2.27 \pm 8.27$	$2.67 \pm 3.89$	$3.51 \pm 6.12$	$21.45 \pm 1.22$	$10.20 \pm 3.24$
30.00	0.49	$0.81 \pm 8.27$	$5.53 \pm 7.18$	$5.59 \pm 7.21$	$21.43 \pm 1.72$	$11.85 \pm 4.23$
45.00	0.74	$3.94 \pm 1.25$	$9.96 \pm 10.02$	$10.71 \pm 9.33$	$22.72 \pm 3.40$	$11.71 \pm 4.72$
60.00	0.99	$16.76 \pm 2.92$	$15.84 \pm 9.20$	$23.06 \pm 6.67$	$26.47 \pm 10.63$	$10.06 \pm 4.95$
75.00	1.24	$27.07 \pm 7.20$	$21.87 \pm 7.86$	$34.80 \pm 7.47$	$23.03 \pm 8.77$	$8.43 \pm 4.24$
90.00	1.48	$31.81 \pm 4.73$	$28.96 \pm 8.82$	$43.02 \pm 6.89$	$20.50 \pm 3.94$	$7.03 \pm 3.53$
105.00	1.73	$34.87 \pm 4.86$	$36.17 \pm 12.66$	$50.25 \pm 9.72$	$17.65 \pm 3.69$	$5.19 \pm 2.59$
120.00	1.98	$34.55 \pm 6.43$	$42.41 \pm 17.44$	$54.71 \pm 14.12$	$17.50 \pm 4.71$	$3.61 \pm 1.80$
135.00	2.23	$30.89 \pm 8.27$	$47.13 \pm 21.48$	$56.35 \pm 18.53$	$17.21 \pm 5.62$	$2.54 \pm 1.28$
150.00	2.47	$23.04 \pm 8.27$	$50.90 \pm 24.25$	$55.87 \pm 22.35$	$14.53 \pm 6.25$	$2.18 \pm 1.38$

Table 3.40: Same as Tab. 3.27 but for NGC 1569

NGC 2366						
R (arcsec)	R (kpc)	$V_{\text{rot}}$ ( $\text{km s}^{-1}$ )	$V_{\text{A}}$ ( $\text{km s}^{-1}$ )	$V_{\text{c}}$ ( $\text{km s}^{-1}$ )	$\sigma_v$ ( $\text{km s}^{-1}$ )	$\Sigma_{\text{int}}$ ( $M_{\odot} \text{ pc}^{-2}$ )
(1)	(2)	(3)	(4)	(5)	(6)	(7)
32.00	0.53	$2.57 \pm 5.48$	$3.16 \pm 3.09$	$4.07 \pm 4.21$	$13.18 \pm 2.42$	$9.54 \pm 1.81$
48.00	0.79	$9.85 \pm 1.87$	$4.34 \pm 3.86$	$10.77 \pm 2.31$	$15.52 \pm 3.23$	$9.63 \pm 2.80$
64.00	1.05	$17.18 \pm 4.86$	$5.65 \pm 4.45$	$18.09 \pm 4.82$	$14.62 \pm 3.08$	$9.79 \pm 3.14$
80.00	1.32	$21.15 \pm 4.84$	$6.96 \pm 4.82$	$22.27 \pm 4.84$	$14.99 \pm 2.52$	$10.01 \pm 3.05$
96.00	1.58	$28.14 \pm 3.48$	$8.53 \pm 4.80$	$29.41 \pm 3.61$	$14.91 \pm 2.54$	$10.10 \pm 3.22$
112.00	1.85	$29.27 \pm 2.43$	$10.05 \pm 4.50$	$30.95 \pm 2.72$	$13.89 \pm 2.31$	$9.36 \pm 3.04$
128.00	2.11	$37.77 \pm 2.95$	$11.53 \pm 4.17$	$39.49 \pm 3.07$	$12.39 \pm 1.78$	$8.05 \pm 2.55$
144.00	2.37	$41.89 \pm 2.73$	$12.74 \pm 3.86$	$43.78 \pm 2.84$	$11.98 \pm 1.80$	$7.00 \pm 2.13$
160.00	2.64	$44.76 \pm 3.48$	$13.99 \pm 3.61$	$46.89 \pm 3.49$	$12.61 \pm 2.25$	$6.22 \pm 2.12$
176.00	2.90	$46.92 \pm 4.04$	$15.19 \pm 3.42$	$49.32 \pm 3.98$	$13.80 \pm 2.37$	$5.67 \pm 2.19$
192.00	3.16	$49.94 \pm 4.42$	$16.26 \pm 3.26$	$52.52 \pm 4.32$	$13.72 \pm 2.67$	$5.39 \pm 2.18$
208.00	3.43	$52.28 \pm 3.70$	$17.42 \pm 3.26$	$55.10 \pm 3.66$	$13.69 \pm 2.61$	$5.12 \pm 2.18$
224.00	3.69	$50.80 \pm 3.97$	$18.55 \pm 3.48$	$54.09 \pm 3.92$	$12.62 \pm 2.70$	$4.65 \pm 2.06$
240.00	3.96	$49.38 \pm 3.43$	$19.52 \pm 3.66$	$53.10 \pm 3.47$	$12.86 \pm 2.43$	$4.23 \pm 1.90$
256.00	4.22	$47.86 \pm 3.50$	$20.63 \pm 4.14$	$52.11 \pm 3.61$	$12.24 \pm 2.31$	$4.01 \pm 1.96$
272.00	4.48	$47.17 \pm 3.05$	$21.44 \pm 4.51$	$51.81 \pm 3.35$	$11.52 \pm 1.93$	$3.72 \pm 1.97$
288.00	4.75	$49.64 \pm 3.42$	$22.10 \pm 4.74$	$54.34 \pm 3.67$	$12.10 \pm 1.91$	$3.44 \pm 1.93$
304.00	5.01	$51.47 \pm 3.32$	$22.35 \pm 4.92$	$56.11 \pm 3.62$	$10.74 \pm 2.25$	$3.01 \pm 1.77$
320.00	5.27	$52.23 \pm 3.44$	$22.31 \pm 5.07$	$56.80 \pm 3.74$	$10.16 \pm 2.50$	$2.68 \pm 1.60$
336.00	5.54	$52.88 \pm 3.06$	$22.15 \pm 5.06$	$57.33 \pm 3.43$	$9.37 \pm 2.50$	$2.36 \pm 1.48$
352.00	5.80	$52.53 \pm 3.52$	$21.60 \pm 5.02$	$56.80 \pm 3.78$	$8.83 \pm 2.76$	$2.06 \pm 1.38$
368.00	6.07	$53.41 \pm 4.64$	$21.02 \pm 4.92$	$57.40 \pm 4.68$	$9.32 \pm 3.07$	$1.69 \pm 1.28$
384.00	6.33	$55.20 \pm 5.48$	$20.29 \pm 5.11$	$58.82 \pm 5.44$	$8.15 \pm 3.84$	$1.37 \pm 1.20$

Table 3.41: Same as Tab. 3.27 but for NGC 2366

UGC 8508						
R (arcsec)	R (kpc)	$V_{\text{rot}}$ ( $\text{km s}^{-1}$ )	$V_A$ ( $\text{km s}^{-1}$ )	$V_c$ ( $\text{km s}^{-1}$ )	$\sigma_v$ ( $\text{km s}^{-1}$ )	$\Sigma_{\text{int}}$ ( $M_{\odot} \text{ pc}^{-2}$ )
(1)	(2)	(3)	(4)	(5)	(6)	(7)
10.00	0.13	$2.30 \pm 0.71$	$5.07 \pm 4.58$	$5.56 \pm 4.18$	$13.41 \pm 1.50$	$7.28 \pm 1.38$
20.00	0.25	$9.42 \pm 1.36$	$8.37 \pm 4.40$	$12.60 \pm 3.09$	$13.36 \pm 2.37$	$6.78 \pm 1.48$
30.00	0.38	$11.04 \pm 3.11$	$11.35 \pm 3.34$	$15.83 \pm 3.23$	$12.21 \pm 1.83$	$6.01 \pm 1.31$
40.00	0.50	$15.50 \pm 1.88$	$13.73 \pm 2.68$	$20.70 \pm 2.27$	$10.95 \pm 1.71$	$5.03 \pm 1.29$
50.00	0.63	$17.82 \pm 1.92$	$15.25 \pm 2.85$	$23.45 \pm 2.36$	$9.48 \pm 2.22$	$3.77 \pm 1.18$
60.00	0.76	$21.10 \pm 2.46$	$16.10 \pm 3.32$	$26.54 \pm 2.81$	$9.02 \pm 2.79$	$2.59 \pm 0.91$
70.00	0.88	$23.11 \pm 2.97$	$16.75 \pm 4.13$	$28.54 \pm 3.42$	$7.23 \pm 2.90$	$1.82 \pm 0.65$
80.00	1.01	$24.60 \pm 3.74$	$17.04 \pm 4.98$	$29.93 \pm 4.18$	$7.85 \pm 2.47$	$1.32 \pm 0.45$
90.00	1.13	$25.62 \pm 4.36$	$17.30 \pm 5.47$	$30.91 \pm 4.74$	$7.98 \pm 2.03$	$0.97 \pm 0.33$
100.00	1.26	$29.37 \pm 5.08$	$17.27 \pm 6.07$	$34.07 \pm 5.35$	$8.20 \pm 1.68$	$0.71 \pm 0.23$
110.00	1.39	$32.13 \pm 6.23$	$17.09 \pm 6.95$	$36.39 \pm 6.39$	$8.01 \pm 1.46$	$0.60 \pm 0.31$

**Table 3.42:** Same as Tab. 3.27 but for UGC 8508

WLM						
R (arcsec)	R (kpc)	$V_{\text{rot}}$ ( $\text{km s}^{-1}$ )	$V_{\text{A}}$ ( $\text{km s}^{-1}$ )	$V_{\text{c}}$ ( $\text{km s}^{-1}$ )	$\sigma_v$ ( $\text{km s}^{-1}$ )	$\Sigma_{\text{int}}$ ( $M_{\odot} \text{ pc}^{-2}$ )
(1)	(2)	(3)	(4)	(5)	(6)	(7)
25.00	0.12	$5.92 \pm 0.90$	$0.54 \pm 0.38$	$5.94 \pm 0.90$	$7.15 \pm 0.46$	$4.41 \pm 0.38$
50.00	0.24	$8.81 \pm 0.98$	$0.86 \pm 0.58$	$8.86 \pm 0.97$	$7.00 \pm 0.50$	$4.97 \pm 0.47$
75.00	0.36	$12.37 \pm 1.16$	$1.20 \pm 0.75$	$12.43 \pm 1.16$	$7.38 \pm 0.92$	$5.40 \pm 0.64$
100.00	0.48	$14.95 \pm 1.12$	$1.57 \pm 0.92$	$15.04 \pm 1.12$	$7.57 \pm 0.75$	$5.77 \pm 0.98$
125.00	0.60	$16.48 \pm 1.33$	$2.10 \pm 1.07$	$16.61 \pm 1.33$	$7.36 \pm 0.93$	$5.86 \pm 1.15$
150.00	0.72	$18.66 \pm 1.32$	$2.53 \pm 1.20$	$18.83 \pm 1.32$	$7.07 \pm 0.86$	$5.50 \pm 1.10$
175.00	0.84	$20.86 \pm 1.31$	$3.14 \pm 1.29$	$21.10 \pm 1.31$	$7.06 \pm 0.95$	$4.97 \pm 1.04$
200.00	0.96	$22.30 \pm 1.67$	$3.86 \pm 1.36$	$22.63 \pm 1.66$	$7.29 \pm 1.16$	$4.31 \pm 1.02$
225.00	1.07	$23.44 \pm 2.31$	$4.69 \pm 1.35$	$23.90 \pm 2.28$	$7.89 \pm 1.28$	$3.73 \pm 0.98$
250.00	1.19	$26.49 \pm 1.83$	$5.65 \pm 1.29$	$27.09 \pm 1.81$	$8.31 \pm 1.27$	$3.35 \pm 0.85$
275.00	1.31	$27.19 \pm 1.61$	$6.72 \pm 1.20$	$28.01 \pm 1.59$	$8.16 \pm 1.08$	$2.95 \pm 0.82$
300.00	1.43	$27.11 \pm 1.90$	$7.89 \pm 1.14$	$28.24 \pm 1.86$	$8.16 \pm 1.00$	$2.61 \pm 0.75$
325.00	1.55	$28.01 \pm 1.62$	$9.15 \pm 1.13$	$29.47 \pm 1.58$	$7.90 \pm 1.22$	$2.38 \pm 0.65$
350.00	1.67	$29.31 \pm 1.98$	$10.46 \pm 1.19$	$31.12 \pm 1.92$	$7.82 \pm 1.45$	$2.25 \pm 0.57$
375.00	1.79	$30.82 \pm 1.86$	$11.76 \pm 1.43$	$32.98 \pm 1.81$	$8.49 \pm 1.24$	$2.06 \pm 0.51$
400.00	1.91	$32.13 \pm 2.00$	$13.01 \pm 1.74$	$34.66 \pm 1.97$	$8.65 \pm 1.39$	$1.83 \pm 0.48$
425.00	2.03	$32.74 \pm 2.24$	$14.14 \pm 2.06$	$35.67 \pm 2.21$	$8.71 \pm 1.48$	$1.59 \pm 0.46$
450.00	2.15	$33.11 \pm 2.54$	$15.11 \pm 2.40$	$36.39 \pm 2.51$	$8.60 \pm 1.61$	$1.38 \pm 0.45$
475.00	2.27	$33.42 \pm 2.83$	$15.85 \pm 2.77$	$36.99 \pm 2.82$	$8.42 \pm 1.75$	$1.20 \pm 0.44$
500.00	2.39	$34.32 \pm 2.94$	$16.32 \pm 2.99$	$38.01 \pm 2.95$	$7.88 \pm 1.85$	$1.06 \pm 0.43$
525.00	2.51	$34.35 \pm 3.26$	$16.48 \pm 3.23$	$38.10 \pm 3.26$	$7.65 \pm 1.84$	$0.92 \pm 0.43$
550.00	2.63	$34.94 \pm 3.25$	$16.28 \pm 3.48$	$38.54 \pm 3.30$	$7.28 \pm 1.92$	$0.79 \pm 0.42$
575.00	2.75	$35.39 \pm 3.38$	$15.70 \pm 3.58$	$38.72 \pm 3.43$	$6.51 \pm 2.10$	$0.69 \pm 0.40$
600.00	2.87	$36.08 \pm 3.03$	$14.70 \pm 3.70$	$38.96 \pm 3.20$	$6.10 \pm 1.93$	$0.63 \pm 0.37$

Table 3.43: Same as Tab. 3.27 but for WLM

### 3.B An alternative scenario for DDO 216

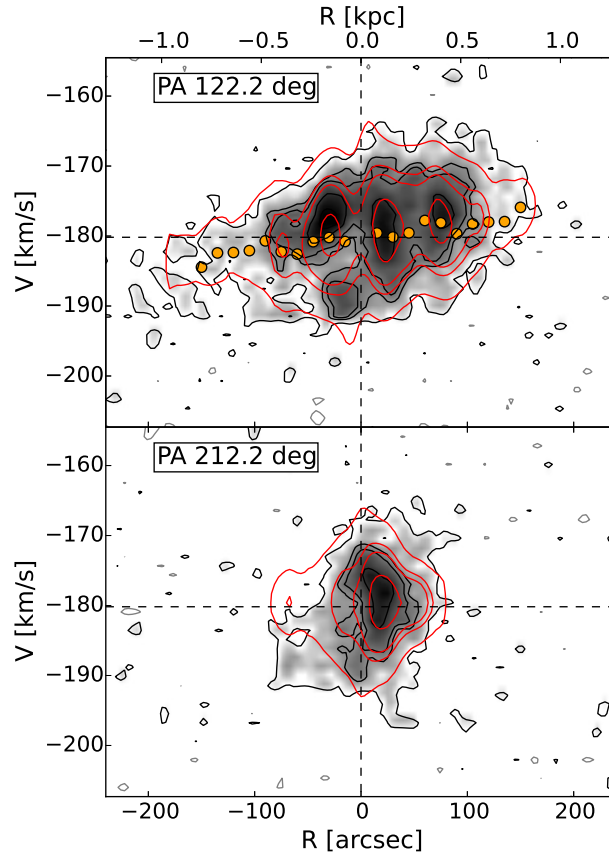


**Figure 3.44:** PV along the major axis (**upper panel**) and the minor axis (**bottom panel**) for the scenario2 of the galaxy DDO 216 (see text). The black contours indicate the datacube while the red contours show the best-fit model found with 3DB. Contours at  $(2 + 6n)\sigma_{\text{ch}}$ , where  $\sigma_{\text{ch}} = 0.91 \text{ mJy beam}^{-1}$ , the grey contours are at  $-2\sigma_{\text{ch}}$ . The yellow points indicate the rotational velocity found with 3DB.

DDO 216 shows a peculiar kinematics: a velocity gradient of about  $10 \text{ km s}^{-1}$  appears clearly in the velocity field (right-hand panel in Box C in Fig. 3.22) and in the channel maps, but it could be entirely due to a single ‘cloud’ at a discrepant velocity in the approaching side of the galaxy (Stil & Israel, 2002b). The analysis of the channel maps partially supports this hypothesis: the receding and the approaching sides of the galaxy seem to have a slightly distinct kinematics and the emission of the two halves overlaps between  $-186 \text{ km s}^{-1}$  and  $-190 \text{ km s}^{-1}$ , while the  $V_{\text{sys}}$  found with 3DB is around  $-180 \text{ km s}^{-1}$ . At the same time, the total HI map does not show the clear presence of a separate component at the supposed position of the cloud (left-hand panel in Box C in Fig. 3.22). In conclusion we did not have sufficient elements to confirm or exclude the existence of a HI component other than the disc

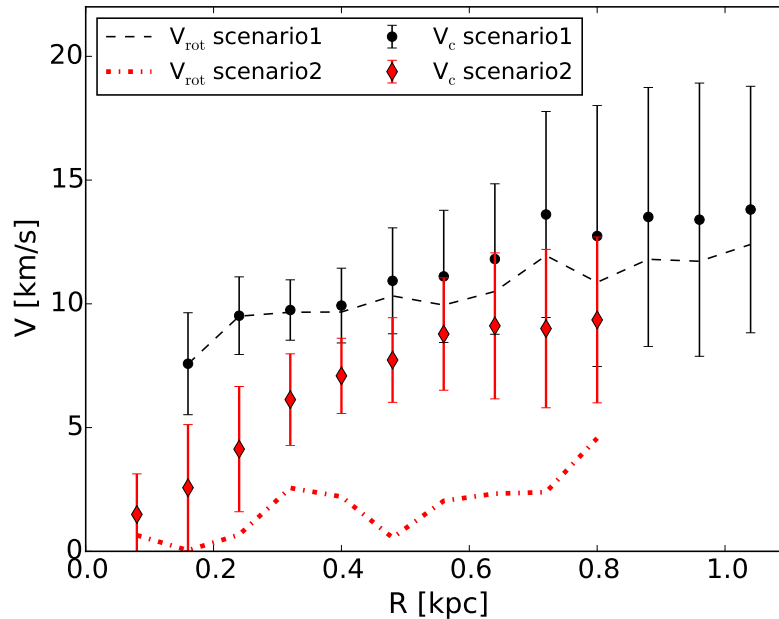


**Figure 3.45:** Rotational velocities (red dashed line) and circular velocities (red points) found for the scenario2 of DDO 216 (see text). The rotation curves of the scenario1 are also shown for comparison.

of DDO 216. We can summarise the two hypotheses as:

- *scenario1*: The main velocity gradient is genuine and totally due to the rotation of the HI disc.
- *scenario2*: The main velocity gradient is due to an HI substructure with a systemic velocity that differs by about  $20 \text{ km s}^{-1}$  from that of the HI disc.

The scenario1 is analysed in Sec. 3.4 while in this Appendix we describe the analysis of the scenario2. First of all we masked the region of the datacube containing the emission of the supposed HI cloud. The mask has been built by inspecting the channel maps using the task PYBLOT of GIPSY. Then we performed the kinematic fit of the ‘clean’ datacube with 3DB. We set  $i_{\text{ini}}$ ,  $\text{PA}_{\text{ini}}$  and the galactic centre to the values obtained from the stellar disc (Hunter & Elmegreen, 2006). Contrarily to the scenario1 (Sec. 3.4) we used the  $V_{\text{sys}}$  estimated with 3DB, the two estimates differ by about  $8 \text{ km s}^{-1}$ , while the final best-fit PA ( $120^\circ$ ) is tilted of about  $10^\circ$ - $15^\circ$  with respect to the values found in the scenario1 (Box B in Fig. 3.22).

Without the ‘cloud’ the velocity gradient almost disappears and the kinematics is dominated by the chaotic motion of the gas as it is clearly visible in the PVs in Fig. 3.44. As a consequence, the final rotation curve is “shaped” by the asymmetric-drift correction. Fig. 3.45 compares the rotation curve found for the scenario1 and for

the scenario2: the velocities are compatible within the errors, but in scenario1 the  $V_c$  is systematically higher by about  $4 \text{ km s}^{-1}$  and it extends to larger radii.

Kirby et al. (2014) found that the stellar component of DDO 216 is rotating in the same direction as the gas with a  $V_{\text{rot}}$  of about  $10 \text{ km s}^{-1}$ , perfectly compatible with scenario1 (see Fig. 3.45). This velocity gradient is observed also in red giant stars, so the rotation is genuine and it is not caused by short-term hydrodynamical events (e.g. bubbles), which would influence the gas kinematics but not the kinematics of the old stellar populations. However the centre of the rotation and  $V_{\text{sys}}$  are quite different from what we found for scenario1 and they are instead compatible with scenario2. Further studies are needed to understand if the gas in this peculiar galaxy is rotating, which is crucial to accurately estimate its dynamical mass.

### 3.C Typical setup for $3^D$ BAROLO

In this Appendix we report the keywords and their values for our typical parameter file input of 3DB. For a detailed description of the keywords see the documentation of 3DB<sup>6</sup> ('...' means that the values depends on the analysed galaxy).

- FITSFILE ...; name of the datacube to fit.
- GALFIT TRUE; enable the 3D fitting of the datacube.
- NRADII ...; number of rings to be used in the fit.
- RADSEP ...; separation between rings in arcsec.
- VROT 30; initial guess for the rotation velocity in  $\text{km s}^{-1}$ .
- VDISP 8; initial guess for the velocity dispersion in  $\text{km s}^{-1}$ .
- INC ...; initial guess for  $i$  in degrees ( $i_{\text{ini}}$ , see Tab. 3.8).
- PA ...; initial guess for the PA in degrees ( $\text{PA}_{\text{ini}}$ , see Tab. 3.8).
- VSYS ...; initial guess for the systemic velocity in  $\text{km s}^{-1}$ .
- XPOS ...; initial guess for the  $x$  coordinate of the centre in pixel.
- YPOS ...; initial guess for the  $y$  coordinate of the centre in pixel.
- Z0 100/ $f_c$ ; initial guess for the scale height in arcsec,  $f_c$  is the conversion factor from arcsec to pc and it is listed in Tab. 3.2 for each galaxy.
- LTYPE 1; use a Gaussian profile for the HI vertical distribution.
- FREE VROT VDISP INC PA; parameters to fit with 3DB.
- FTYPE 2; use the absolute differences between models and datacube as residuals.
- WFUNC 1; use the cosine of the azimuthal angle as weighting function for the fit (see Sec. 3.3.2).
- CDENS 10; this parameter sets (in a non-trivial way) the number of 'clouds' to be used in the building of the ring models (see the GALMOD documentation<sup>7</sup>).
- NV 200; number of sub-clouds in which each cloud (see above) is divided to populate the spectral axis of the ring models.

<sup>6</sup><http://editeodoro.github.io/Bbarolo/documentation/>

<sup>7</sup><https://www.astro.rug.nl/~gipsy/tsk/galmod.dcl>

- TOL 1E-3; tolerance condition to stop the fit.
- MASK Smooth; create a mask for the fit smoothing the datacube.
- FACTOR 2; set the the smooth level of the mask (see above), the original datacube is smoothed with a beam larger FACTOR times the original beam.
- BLANKCUT 2.5; include in the mask (see above) only the pixels with S/N > 2.5 in the smoothed cube.
- SIDE B; fit the whole galaxy (B=both).
- TWOSTAGE TRUE; enable the two-stage method described in Sec. 3.3.2.
- BWEIGHT 1; set the weight of the blank pixels in the fit: the final sum of residuals between data and model is multiplied by the factor  $(1 + n_b)^{\text{BWEIGHT}}$ , where  $n_b$  is the number of pixels having the model but not the observation (see Di Teodoro & Fraternali 2015 for details).
- DELTAINC 40;  $i$  can assume values only between INC-DELTAINC and INC+DELTAINC. The used value is large enough to let the code to trace possible warps.
- DELTAPA 40; same as above, but for the PA.
- FLAGERRORS TRUE; enable the estimate of the errors on the fitted parameters.
- STARTRAD 1; avoid the fit of the first ring placed by default at RADSEP/2.
- LINEAR 0.424; instrumental resolution ( $\sigma_{\text{inst}}$ ) in unity of channel width. In all our galaxies the instrumental FWHM is equal to the channel separation, so  $\sigma_{\text{inst}} = 1/2.355 = 0.424$ .

If the parameters XPOS,YPOS,VSYS,PA,INC are omitted, 3DB estimates them as described in Appendix 3.3.2.

## Beyond Flatland: the thickness of the HI disc in dwarf irregulars

The vertical profile of the HI layer in disc galaxies is one of the most difficult parameters to estimate from observations: we can infer it directly only in discs seen edge-on and close enough to us to sample the vertical profile with more than one resolution element (see e.g. van der Kruit 1981). However, there are serious limitations due to the fact that edge-on galaxies can have warps along the line of sight (e.g. Zschaechner et al. 2011) that can introduce severe biases in the study of the HI vertical profile. In the literature, there are only a few attempts to derive information on the HI scale height indirectly from other observables in non-edge galaxies. Sicking (1997) tried to estimate the HI scale height in discs analysing the increase of the velocity dispersion that a HI thick layer produces along the line of sight. He applied his method to NGC 2403 and NGC 3198, but the estimate of the HI thickness results poorly constrained. Olling (1995) stated that it should be possible to infer the gas vertical profile from the analysis of the emission contours in individual channel maps of the HI datacubes, nevertheless he never designed this kind of method. Finally, in my Master thesis<sup>1</sup>, I tried to measure the HI thickness from the azimuthal periodic patterns it causes on the HI total emission map. I found that the expected azimuthal oscillations are too small and, in real galaxies, they are lost in the noise and in the intrinsic azimuthal inhomogeneities.

As a consequence, to date there are estimates for the HI vertical profile only for a small number of edge-on galaxies (e.g. Olling 1996; Kamphuis 2008; O'Brien, Freeman & van der Kruit 2010; Peters et al. 2017) and the Milky Way (e.g. Kalberla et al. 2007). Moreover, there are studies on the estimate of the HI disc thickness applying statistical methods to the observed axial ratio distribution of HI discs (e.g. Roychowdhury et al. 2010). All these studies conclude that the dIrrs have HI

---

<sup>1</sup>Iorio (2014), <http://amslaurea.unibo.it/7411>

discs that are significantly thicker than the HI discs in large spirals, like the Milky Way, both in absolute term and with respect to the radial extension, especially in the inner regions. This result is expected also from a theoretical point of view: assuming that the gas is in vertical hydrostatic equilibrium, the thickness of the HI disc depends on the vertical component of the gradient of the galactic potential (Olling, 1995; Elmegreen & Hunter, 2015). dIrrs are dynamically dominated by the DM halo that has a spheroidal distribution producing a vertical force that is relatively weaker with respect to that of spirals with heavy stellar discs. Moreover, since the vertical force tends to decrease with radius we expect that the HI layers “flare” becoming thicker in the outer parts of the discs (Olling, 1995).

Given the difficulties and the uncertainties discussed above, the HI vertical profile is rarely exploited for dynamical studies (see e.g. Olling 1996 for an application to the study of the DM halo shape in NGC 4244) and usually it is not even taken into account properly in the study of the kinematics and dynamics of disc galaxies. As done in [Chapter 3](#), the classical way to deal with the HI vertical profile is to assume a thin disc with constant scale height or even a razor-thin disc whose the vertical profile is a Dirac delta (e.g. de Blok et al. 2008; Oh et al. 2015). As discussed above, this simplistic approach can be justified in large spirals (e.g. Brinks & Burton 1984) but it is not clear what kind of biases these assumptions can introduce in the study of dIrrs. Indeed, this has not extensively studied in literature except for the work of Sicking (1997) concerning spiral galaxies.

In this Chapter, we aim to fill this gap, studying the effect that the presence of thick HI layers can have on the observed properties of HI discs, focusing on models that have properties typical of dIrrs (Sec. 4.1). Then in Sec. 4.2 we present, for the first time, a method to derive the kinematics and dynamics of galaxies taking into account the HI vertical profile in a dynamically self-consistent way. In order to test whether the results obtained in [Chapter 3](#) and used in [Chapter 5](#) are biased by the presence of thick HI discs, in Sec. 4.3 we exploit our original method to re-derive the intrinsic properties for three galaxies analysed in [Chapter 3](#). Finally, in Sec. 4.4 we draw our conclusions.

In this Chapter, we make use of the datacube analysis package GIPSY (van der Hulst et al., 1992), through the Chapter every name written in capital letters refers to a GIPSY task<sup>2</sup>. As in [Chapter 3](#), 3DB refers to <sup>3D</sup>BAROLO (Di Teodoro & Fraternali 2015, see Sec. 3.2).

---

<sup>2</sup>see <https://www.astro.rug.nl/~gipsy/dc123doc/alltasks.html> for GIPSY tasks documentation.

## 4.1 Effect of the HI thickness on observables

In the presence of a thin disc the observed HI emission can be easily related to the intrinsic properties of the galaxy: the observed velocity is a measure of the gas rotation in the equatorial plane, the observed velocity dispersion is an unbiased measure of the chaotic motion of the gas and the intrinsic profile of the HI surface density can be obtained by simply correcting the observed profile for the disc inclination. In the presence of a thick gaseous layer, the line of sight (los) intercepts the emission coming from different radial and vertical positions. In particular, assuming that the HI disc is inclined with an angle  $i$ , a given position along the los,  $s$ , and a given azimuthal angle,  $\theta$ , the intercepted emission comes from a generic emitting cloud with coordinates

$$\begin{cases} z = s \cos i \\ R = \sqrt{R_0^2 + z^2 \tan^2 i + 2zR_0 \sin \theta \tan i}, \end{cases} \quad (4.1)$$

where  $z$  and  $R$  refer to a cylindrical frame of reference aligned with the equatorial plane of the galactic disc and centred in the galactic centre;  $R_0$  is the “elliptical” radius<sup>3</sup> of the point intercepted by the los on the disc equatorial plane<sup>4</sup>. From Eq. 4.1, it is apparent that, in the presence of a significant disc thickness, the intrinsic structural and kinematics properties of the HI disc cannot be obtained with the simple deprojection factors  $\sin i$  (Eq. 1.6) and  $\cos i$  (Eq. 3.3).

### 4.1.1 Datacube models

In order to study the difference between thin and thick disc models, we decided to compare mock datacubes of the HI emission. The model datacubes have been made using GALMOD (Sicking, 1997). Notice that, in this Chapter, the term pixel refers both to the 3D (two spatial dimensions and one spectral dimension) cells of the datacubes (sometimes called voxel) and to the 2D (two spatial dimensions) cells of the derived 2D maps (see Sec. 1.3.1). This software creates a HI disc model using the concept of tilted rings (see Sec. 1.3.3): the disc is divided in a series of circular rings and each of them is filled with discrete “clouds” to reproduce the density distribution of the gas considering the intrinsic surface density and the vertical density profile given in input. The inclination, the position angle and the vertical scale height of the rings are allowed to vary with radius. In order to complete the model, GALMOD also needs the kinematic information, such as the rotation curve of the HI disc and the radial profile of the velocity dispersion. The velocity dispersion given in input

<sup>3</sup> $R_0^2 = x^2 + y^2 \cos^{-2} i$ , where  $x$  and  $y$  are the coordinates in the plane of the sky and  $i$  is the inclination angle of the disc.

<sup>4</sup>see Iorio (2014) (<http://amslaurea.unibo.it/7411>) for a complete geometrical description of a thick disc.

is

$$\sigma_{\text{input}}(\text{R}) = \sqrt{\sigma_v^2(\text{R}) + \sigma_{\text{instr}}^2}, \quad (4.2)$$

where  $\sigma_v^2$  is the intrinsic velocity dispersion of the gas and  $\sigma_{\text{instr}}^2$  takes into account the instrumental resolution. In order to simulate Hanning-smoothed datacubes (see Sec. 3.3), we consider the instrumental resolution as a Gaussian with  $\text{FWHM} = 2\Delta V_{\text{ch}}$ , where  $\Delta V_{\text{ch}}$  is the channel separation of the datacube; therefore, the instrumental broadening is  $\sigma_{\text{instr}} = \Delta V_{\text{ch}} (2 \ln 2)^{-0.5}$ .

The clouds are distributed using a Monte Carlo method, both in the azimuthal and in the vertical direction. Each cloud generated by GALMOD has a velocity that is the sum of the systemic velocity of the galaxy and the rotation velocity corrected for the azimuthal angle of the ring (Eq. 1.6). In order to create the profile of the HI emission, the clouds are further divided into subclouds to which the code assigns a velocity equal to the velocity of the parent cloud plus a random contribution drawn from a Gaussian distribution with dispersion equal to  $\sigma_{\text{input}}$  (Eq. 4.2). Once each ring has been constructed, GALMOD produces a final ‘‘observed’’ cube in which the HI flux in each pixel is the sum of the signal of every subcloud there located.

In order to be directly comparable with real datacubes, the mock datacubes are then smoothed spatially to simulate the instrumental resolution; before the smoothing, the datacube can also be contaminated with a random signal with dispersion  $\sigma_{\text{noise}}$  to simulate the observational noise.

### 4.1.2 Comparing thick and thin disc models

In order to analyse the biases that a thick HI disc can cause, if the thickness is not taken into account, we build a series of datacube models. The intrinsic properties have been chosen to mimic the ones obtained for a sample of dIrrs in Chapter 3. For each disc model, we use GALMOD to make a thin (TN) datacube model considering a Dirac delta distribution for the vertical profile of the gas and a thick (TK) datacube model with a constant scale height,  $z_d$ , comparable to or larger than the radial scale length  $R_d$ . In Sec. 4.3 we will see that the scale height of dIrrs is expected to increase with radius and reaches  $z_d \sim R_d$  only in the very outer parts of the discs. However, the choice of maximizing the HI thickness over the whole disc is done deliberately to make more evident its effects on observable properties. In the following, we focus in detail on the TK-TN comparison of disc models with properties similar to the dIrr WLM (Fig. 3.26).

The input properties of the HI disc models are shown in Fig. 4.1: the intrinsic surface density follows a radial profile with an inner depression and an exponential fall-off in the outer parts; the rotation curve is slowly rising and reaches about  $40 \text{ km s}^{-1}$  in the outer disc, the velocity dispersion is fixed at  $8 \text{ km s}^{-1}$ . We assume that the rotation velocity is cylindrical, i.e. it depends only on the radius  $R$  and

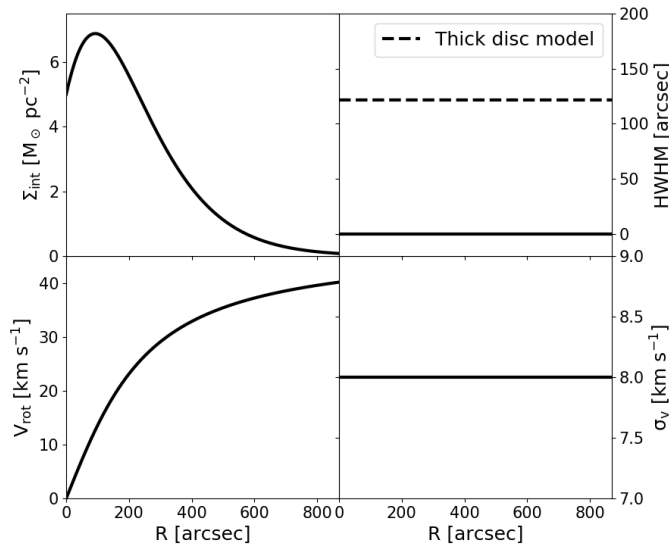


**Figure 4.1:** Input properties for a thin and a thick HI disc models (the properties are the same except for the HI disc thickness). Clockwise from the upper-left panel to the bottom-right panel: intrinsic surface density; half width half maximum of the vertical profile of the gas (assumed Gaussian); rotational velocity of the gas (assumed cylindrical, see text); intrinsic velocity dispersion of the gas.

does not have vertical gradient (see Sec. 4.2.1). The TK disc model has a Gaussian vertical profile and a constant scale height of  $\sim 100''$ , comparable with the radial scale length ( $R_d = 120''$ ). We assume a constant inclination angle of  $65^\circ$ , a PA of  $0^\circ$  and a null systemic velocity. The resultant datacubes have  $177 \times 177$  pixels with dimension  $9.4''$ , a channel separation of  $2.5 \text{ km s}^{-1}$  and 81 channels. The models have been spatially smoothed with a Gaussian with  $\text{FWHM} = 25'' \times 25''$  mimicking the instrumental beam and the velocity dispersion in input has been increased to  $\sigma_{\text{input}} = 8.27 \text{ km s}^{-1}$  to simulate the Hanning-smoothing (Eq. 4.2).

Mimicking a classical 2D analysis of the HI datacubes (e.g. Oh et al. 2015), we build the total HI map summing all the signal in the channels, then we fit a Gaussian to the HI profile in each pixel using the task GAUFIT. The best-fit centroids and standard deviations are used to build the velocity fields and the velocity dispersion maps. The maps are shown in Fig. 4.2 together with the residual maps between the TK and TN disc models. The HI total maps are significantly different: the TN map reflects immediately the profile of the surface density given in input including the central HI hole (Fig. 4.1), while the gas distribution in the TK is more diffuse and the presence of the inner deficit of HI has been smoothed out. These differences are more evident in the residual map: in the very inner part the TK model has a deficit of about  $4 M_\odot \text{ pc}^{-2}$ , while in the outer disc, the TK models contains more gas than the TN model especially near the minor axis where we accumulate flux coming from

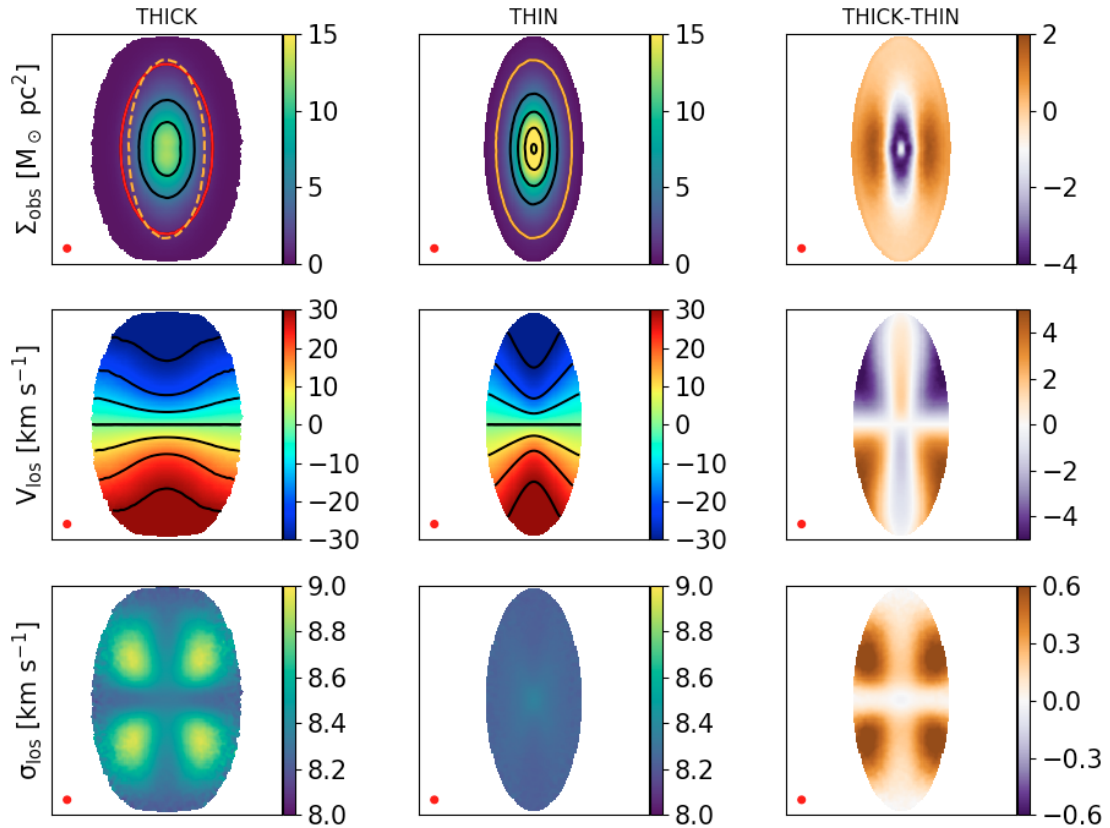


**Figure 4.2:** “Observed” maps of the HI disc models made with GALMOD given the input properties shown in Fig. 4.1 (see text). The first two columns show the maps obtained for the thick and thin disc model, while the third column shows the differences between them. The first row shows the observed surface density maps integrated across the cube channels, the black iso-density contours indicate the levels 5, 10, 15  $M_{\odot} \text{pc}^{-2}$ , the red and orange (solid and dashed) contours show the level 1  $M_{\odot} \text{pc}^{-2}$  for the thick and thin model, respectively; the second row shows the velocity fields, the iso-velocity contours span from  $-30 \text{ km s}^{-1}$  to  $30 \text{ km s}^{-1}$  with step of  $10 \text{ km s}^{-1}$ ; the third row shows the velocity dispersion maps. In order to make the plot clearer, we blanked from the maps all the pixels where  $\Sigma_{\text{obs}} < 0.01 M_{\odot} \text{pc}^{-2}$ . The red circle in the bottom left corner of the panels show the assumed instrumental beam. The Field of View is  $14' \times 14'$ .

the HI layers above and below the equatorial plane. Therefore, the presence in the real datacube of a consistent excess of emission near the disc minor axis could be an hint of the existence of a thick HI disc (see e.g. UGC 8508 in Fig. 3.25 or WLM in Fig. 3.26, see also Fig. 4.14).

The velocity fields show differences not only in the very outer disc, where the observed velocities depends only on the kinematics of the gas above and below the equatorial plane, but also in the inner parts. The iso-velocity contours of the TK model are “stretched” with respect to the TN case, hence just looking at the velocity field the radial gradient of the gas rotation can be misinterpreted to be steeper than

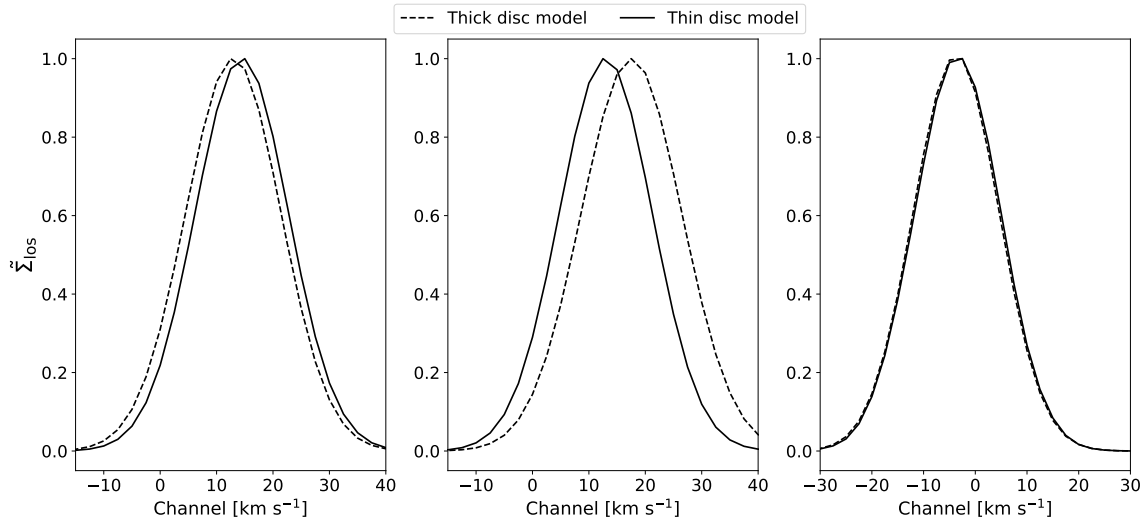


**Figure 4.3:** HI line profiles from the thick (dashed) and thin (solid) datacube models shown in Fig. 4.2. The profiles are from three different pixels: one located on the major axis (**left-hand panel**), one located at an azimuthal angle of  $45^\circ$  (**middle panel**) and the last located on the minor axis (**right-hand panel**). The profiles have been normalised to the peak value.

it actually is<sup>5</sup>. More quantitative information on the differences can be obtained focusing on the “cross-shape” pattern in the residual map: along the major axis the TK velocities underestimate (in terms of absolute values) the real gas rotation in the equatorial plane of  $2 \text{ km s}^{-1}$  at most, while at intermediate azimuthal angles the effect is reversed and the in TK velocities overestimate the intrinsic velocities up to  $5 \text{ km s}^{-1}$ . Notice, however, that the information at these angles have usually a lower weight in the fitting of the observed velocities (see Sec. 3.3.2). Along the minor axis and in a small region around the major axis the two velocity fields show no differences. The reason behind these differences is shown in Fig. 4.3: in the presence of a thick disc the final HI line profile observed in a certain pixel is the resultant of the convolution of all the HI profiles intercepted along the los, each with its own value of  $V_{\text{los}}$  that depends on the radius and on the azimuthal angle (Eq. 1.6). In some regions this causes the shift of the line centroids and the broadening of the lines (see below). All the los passing for the minor axis intercept HI layers with  $V_{\text{los}} = V_{\text{sys}}$ , hence there is no shift of the centroids (see right-hand panel in Fig. 4.3) as shown in the residual map in Fig. 4.2.

The TN velocity dispersion map clearly shows the constant value of the velocity dispersion given in input ( $\sigma_v \sim 8.3 \text{ km s}^{-1}$ , including also the instrumental resolution, see Eq. 4.2), while the TK map shows a X-shape pattern of inflated dispersion

<sup>5</sup>The “opening angle” of the iso-velocity contours is related to the shape of the rotation curve: the larger is the angle the steeper is the rising of the rotation curve.

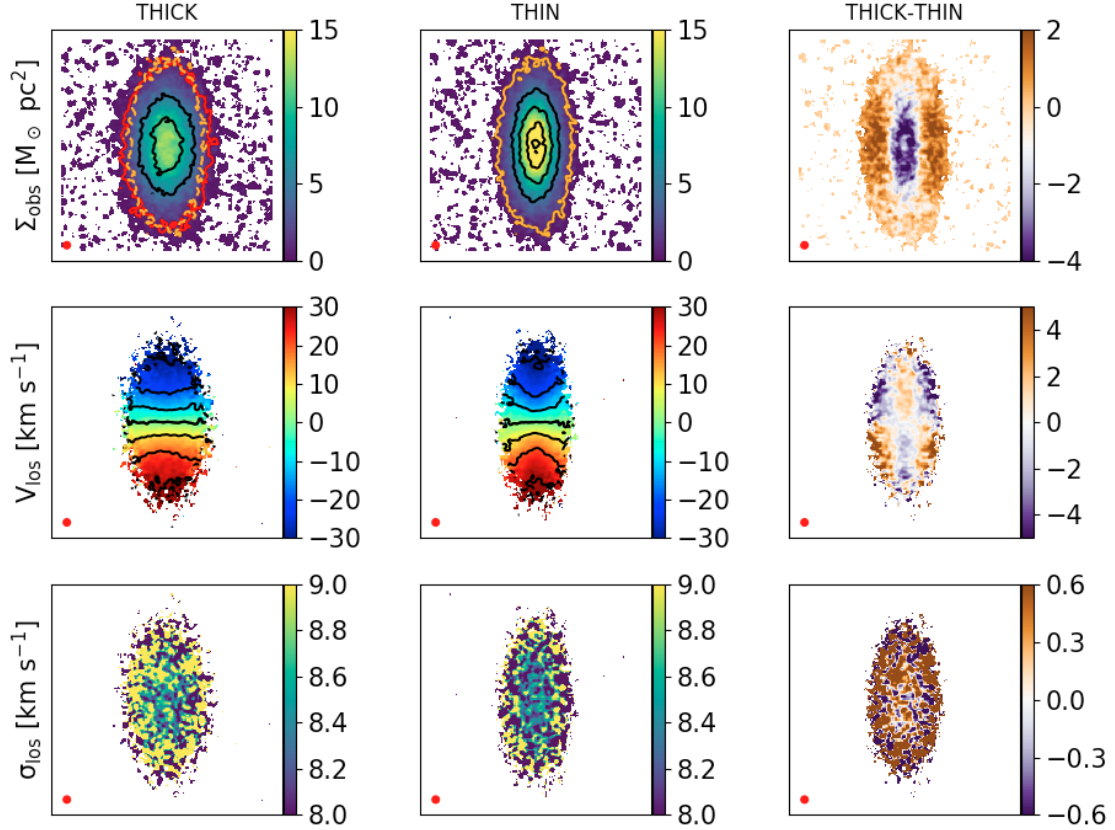


**Figure 4.4:** Same as Fig. 4.2, but we added Gaussian noise in the datacube models (noise-per-channel  $\sigma_{\text{ch}} = 0.06 M_{\odot} \text{ pc}^{-2}$ ). The maps have been obtained after that the datacubes have been cleaned applying a noise mask (see text).

that is clearly shown also in the residual map. The X-shape is not typical only of thick discs (Sicking, 1997), but it is a general pattern due to the mixing of HI line profile with different  $V_{\text{los}}$ . At intermediate azimuthal angles, the velocities in nearby pixels show large differences and this effect is maximized. Actually, the TN dispersion velocity map exhibits this pattern, but it is not appreciable in Fig. 4.4 because the increase of the observed dispersion is lower than  $0.1 \text{ km s}^{-1}$ .

The two models discussed above represent an idealized situation in which the datacubes have no noise. In order to present a more realistic analysis, we add artificial noise to the mock datacubes as follows. We take the datacubes created by GALMOD and we add in each pixel a flux taken from a Gaussian centered on 0 and with a standard deviation  $\sigma_{\text{noise}}$ , finally we apply the spatial smoothing as described at the beginning of this Section. The standard deviation of the Gaussian has been tuned to have in the final smoothed data cube a noise-per-channel  $\sigma_{\text{ch}} \sim 1 \text{ mJy beam}^{-1} = 0.06 M_{\odot} \text{ pc}^{-2}$  similar to the level of noise found in the datacubes analysed in Chapter 3 (see Tab. 3.2). We have cleaned the noisy datacubes as follows.

- We smooth the original datacube with a Gaussian that has a FWHM two times larger than the beam dimension;
- we estimate the noise in the smoothed cube,  $\sigma_{\text{ch}}^{\text{sm}}$ , calculating the standard deviation of the flux in channels free from the HI emission of the source;
- we blank all the pixels of the smoothed cubes with signal below  $3\sigma_{\text{ch}}^{\text{sm}}$  and we set the value of the remnant pixels to 1 obtaining a boolean mask;
- each pixel of the original datacube is multiplied by the correspondent pixel of the masks so that in the cleaned datacube all the pixels containing only noise are blanked.

Using the cleaned datacubes, we repeat the same analysis described for the “idealized” datacubes, but given the presence of the noise we use some more stringent conditions in GAUFIT: the fitted amplitude of the Gaussian needs to be larger than  $3\sigma_{\text{ch}}$ ; the fitted dispersion needs to be larger than the velocity resolution of the datacubes ( $\sigma_v > 1.8 \text{ km s}^{-1}$ ); the fitted velocity centroid needs to be between  $-60 \text{ km s}^{-1}$  and  $60 \text{ km s}^{-1}$ , i.e., it needs to be in the velocity range of the datacube in which the emission from HI source starts to be evident against the noise. The pixels in which at least one of the above conditions is not satisfied are blanked. The results are shown in Fig. 4.4. The differences shown in Fig. 4.2 are still present but now they are less evident, especially in the outer regions of the disc where they are lost in the noise. In particular the two velocity dispersion maps and their residual map are now very noisy and the X-shape pattern disappears, however the systematic increase of  $\sigma_v$  is still visible across all the disc.

Fig. 4.2 and Fig. 4.4 clearly show that the presence of a thick disc produces final maps that appear more “face-on” with respect to the thin disc case. In this context, it is interesting to note that the  $1 \text{ M}_{\odot} \text{ pc}^{-2}$  contour of the TN disc model overplotted to the TK HI total map (dashed-orange) in Fig. 4.4 highlights the excess of emission along the minor axis. This feature is similar to the ones observed in some HI map of the dIrrs analysed in Chapter 3 (e.g. WLM, see Box C in Fig. 3.26). Therefore, in the case of thick discs, it is possible to obtain a wrong estimate of the disc inclination and, as a consequence, we introduce further errors on the estimate of the gas rotational velocity (Eq. 1.6). In order to have an estimate of the magnitude of this effect, we made new thick and thin disc models with the same intrinsic properties shown in Fig. 4.1, but projecting the disc with different inclinations,  $i_{\text{true}}$  ranging from  $20^{\circ}$  to  $80^{\circ}$  with steps of  $10^{\circ}$ . We add noise ( $\sigma_{\text{ch}} \sim 0.06 \text{ M}_{\odot} \text{ pc}^{-2}$ ) to the datacubes and then we highlight the HI emission from the source as described above for the models shown in Fig. 4.4. For each disc model we fit ellipses to the the iso-density contours of the HI total map using the code RingFit described in Sec. 3.3.2, then the final inclination of the HI disc,  $i_{\text{obs}}$ , is estimated as the mean of the axial ratios

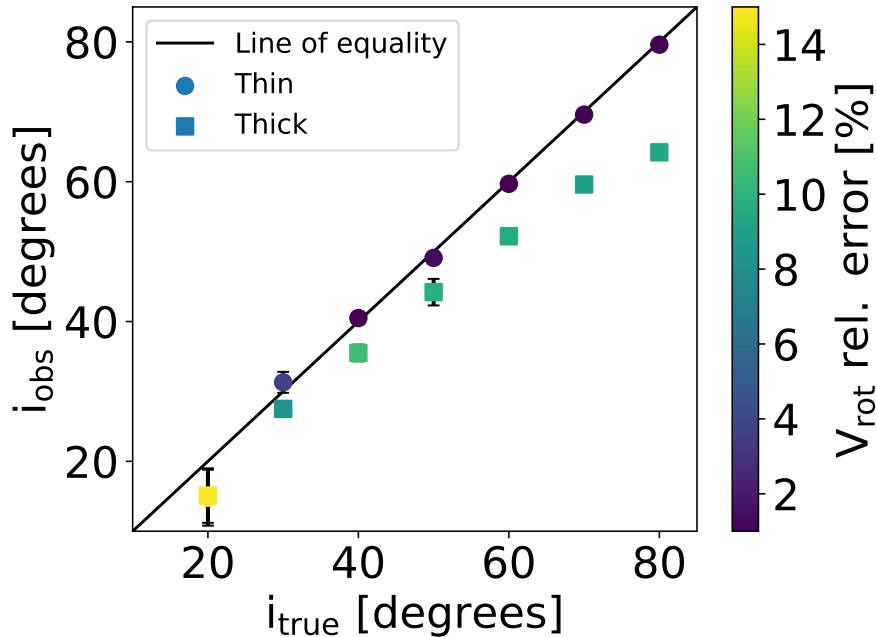


**Figure 4.5:** “Observed” inclinations recovered fitting the iso-density contours of the HI total maps (see text) versus the true inclinations of thin (circles) and thick (squares) galactic disc models. The color of the points indicates  $|\sin^{-1} i_{\text{obs}} - \sin^{-1} i_{\text{true}}| \times \sin i_{\text{true}}$ , i.e. the relative error that is produced on the estimate of the rotational velocity using the observed value of the inclination (see Eq. 1.6). Notice that the thin and thick estimates of  $i_{\text{obs}}$  for  $i_{\text{true}} = 20^\circ$  are practically coincident.

of the fitted ellipses. Fig. 4.5 shows the final results of this analysis. At very low inclination angles  $i_{\text{true}} < 30^\circ$ , the inclination is difficult to recover both for thick and thin disc models (see our analysis in Read et al. 2016), but for larger  $i_{\text{true}}$  the differences are evident: in the case of thin disc the axial ratio of the HI iso-density contours is a very robust proxy of the intrinsic inclination angle, while in the case of thick disc,  $i_{\text{true}}$  is systematically underestimated. This effect is more severe going toward higher intrinsic inclination angles: in these cases the los intercepts more and more HI layers above the galaxy midplane, increasing the observed HI emission along the minor axis. As a consequence, the final map looks more face-on than it actually is. However, the color scheme in Fig. 4.5 shows us that the mistake one makes in the inclination angle causes errors on the estimate of the intrinsic gas rotational velocity ( $V_{\text{rot}} \propto V_{\text{obs}} \sin^{-1} i$ , see Eq. 1.6) that are almost constant and not larger than 10%, except at very low inclinations. This is due to the fact that at large inclination angles, where the  $i_{\text{true}} - i_{\text{obs}}$  discrepancy is more significant, the sin function varies much more slowly with the angle.

Based on the above analysis and further analysing different disc models with different properties, we conclude that the assumption of a thin disc, when a thick

disc is present, biases the results as follows:

- (i) the surface density profile tends to be shallower than the real profile;
- (ii) the measured broadening of the HI line profiles is larger than the intrinsic velocity dispersion of the gas ( $\sigma_v$  is overestimated);
- (iii) the representative velocity estimated from the HI line profiles may not trace the gas rotation velocity at certain locations;
- (iv) the observed HI total map looks more face-on than it actually is.

Notice that the surface density is the observable that shows the largest relative differences (Fig. 4.2 and Fig. 4.4). Obviously, these effects influence the estimate of the final rotation curve: due to (iii) the observed velocities are no longer tracing the rotation on the equatorial plane, due to (iv) the intrinsic inclination can be underestimated and the rotation wrongly deprojected (Eq. 1.6), while (i) and (ii) bias the calculation of the asymmetric-drift correction (see Sec. 3.3.3). Geometrical properties as the galactic centre and the PA as well as the systemic velocity are not influenced by the presence of a thick disc.

In the presence of very thick disc, the combination of above effects causes the circular velocities, obtained with both 2D and 3D methods assuming a thin disc, to be lower than the intrinsic velocities at smaller radii (similar to the beam smearing) and higher in the outermost disc. The magnitude of these differences depends mainly on the thickness of the HI discs, but the  $i$  of the disc, the shape of the rotation curve and the instrumental properties (beam dimension) are also important parameters. In particular a rising rotation curve, typical of dIrrs, amplifies the errors.

In the next Section we will present a new original method to retrieve the HI disc properties (circular velocity, velocity dispersion, surface density) taking into account the biases introduced by the HI thickness.

## 4.2 An original method to account for gas thickness

### 4.2.1 Theoretical background

We assume that the gas in the HI disc can be treated as a fluid with an axisymmetric distribution, hence its intrinsic properties depend only on the cylindrical coordinates  $(R, z)$  in which  $R$  lies on the disc equatorial plane and  $z$  is normal to the disc plane. We further assume that the gas rotates around the  $z$ -axis with angular velocity  $\Omega$  and rotational velocity  $V_{\text{rot}} = \Omega R$ . Finally, we assume that there are not streaming motions along either the vertical direction ( $V_z = 0$ , hydrostatic equilibrium) or the

radial direction ( $V_R = 0$ , centrifugal equilibrium). Using the above assumptions the cylindrical components of the Euler equation can be expressed as

$$\begin{cases} \frac{1}{\rho} \frac{\partial P}{\partial z} = -\frac{\partial \Phi_{\text{tot}}}{\partial z} \\ \frac{1}{\rho} \frac{\partial P}{\partial R} = -\frac{\partial \Phi_{\text{tot}}}{\partial R} + \Omega^2 R \end{cases}, \quad (4.3)$$

where  $\rho$  is the 3D density of the HI and  $P$  its pressure. Assuming that the thermal pressure is negligible and that the gas is isotropic, the pressure and the density are related by the equation of state

$$P(R, z) = \sigma_v^2(R) \rho(R, z), \quad (4.4)$$

where  $\sigma_v$  is the HI velocity dispersion that is due mainly to the turbulent chaotic motions of the gas (see Sec. 5.3). Therefore, in Eq. 4.4,  $P$  refers to a turbulent pressure. A fluid with the above equation of state is isothermal in the vertical direction since  $\sigma_v$  is independent of  $z$ , but it is not isothermal in the radial direction since  $\sigma_v$  can vary with the radius. Therefore, it is not guaranteed that the isopycnic surfaces (equal density) and the isobaric surfaces (equal pressure) are coincident and the fluid cannot be considered barotropic. The assumption of a radially varying  $\sigma_v$  is justified by the observations (see e.g. Figs 3.10-3.26 or Tamburro et al. 2009), while the constant value assumed along the vertical direction is an assumption we make for simplicity. However, we note that  $\sigma_v = f(R)$  is also adopted in the study of edge-on galaxies where in principle a vertical variation of  $\sigma_v$  can be measured from the data (e.g. O'Brien, Freeman & van der Kruit 2010).

If the fluid is not barotropic, from the Poincaré Theorem (e.g. Tassoul 1980 and Barnabè et al. 2006) it follows that the angular velocity in Eq. 4.3 depends both on the radial and vertical coordinates ( $\Omega = \Omega(R, z)$ ). Therefore, the assumed equation of state (Eq. 4.4) predicts the existence of a vertical gradient in the gas rotational velocity. However, the assumption of cylindrical rotation ( $V_{\text{rot}} = V_{\text{rot}}(R)$ ) may be not so far from the reality. In order to justify this statement, we start using Eq. 4.4 to write the pressure gradient as

$$\vec{\nabla} P(R, z) = \left[ \sigma_v^2(R) \frac{\partial \rho(R, z)}{\partial R} + 2\sigma_v(R) \rho(R, z) \frac{\partial \sigma_v(R)}{\partial R} \right] \hat{R} + \left[ \sigma_v^2(R) \frac{\partial \rho(R, z)}{\partial z} \right] \hat{z}. \quad (4.5)$$

In disc galaxies, except for the very inner part, the HI velocity dispersion profiles ( $\sigma_v(R)$ ) show an almost constant or slightly decreasing, radial trend (see Appendix 3.A for the dIrrs in our sample or Tamburro et al. 2009 for larger spirals). In these conditions, the radial variation of the density is much larger than the one of

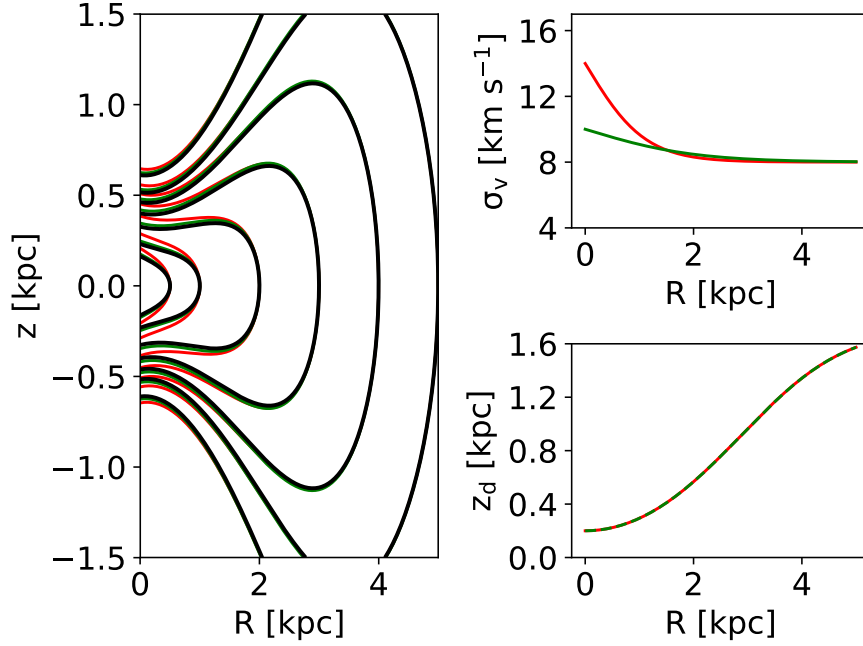


**Figure 4.6:** Comparison between the iso-density (black curves) and iso-pressure (red and green curves) contours for two disc models (**left-hand panel**). The two models have the same density  $\rho \propto \exp\left[-\frac{R}{R_d}\right] \exp\left[-0.5\frac{z}{z_d(R)}\right]$  where  $R_d = 1.5$  kpc and  $z_d(R)$  is shown in the **bottom-right panel**. The gas pressure is calculated using Eq. 4.4; the velocity dispersion profiles of the two models are shown in the **top-right panel**.

the velocity dispersion and the second term of the radial component of the pressure gradient in Eq. 4.5 is negligible, hence from Eq. 4.5 it follows

$$\vec{\nabla}P \simeq \sigma_v^2 \vec{\nabla}\rho. \quad (4.6)$$

Eq. 4.6 implies that, locally, the vectors normal to the the iso-density and iso-pressure surfaces have the same direction, hence these two surfaces can be considered coincident as it is the case of barotropic fluids. This concept is illustrated in Fig. 4.6 where we compare the iso-density and iso-pressure contours in the  $R - z$  plane for two disc models. The two models have the same density,  $\rho$ , but different velocity dispersion profiles, hence different turbulent pressures.  $\rho$  is exponential along the radial direction with scale length  $R_d = 1.5$  kpc, while in the vertical direction the gas is distributed following a Gaussian. The vertical scale height  $z_d(R)$  flares from about 0.2 kpc in the inner part to about 1.6 kpc at  $R = 5$  kpc as shown in the bottom-right panel of Fig. 4.6. The velocity dispersion profiles (top-right panel of Fig. 4.6) have been set to reproduce the cases of non-constant  $\sigma_v$  profiles observed for some galaxies in Chapter 3. The first model decreases from about 14 km s<sup>-1</sup> to 8 km s<sup>-1</sup> within  $R \sim 2$  kpc and then remains constant, similar to what we observe

for DDO 168 (Fig. 3.20); in the second model the decrease is shallow as we observe in DDO 133 (Fig. 3.18) or in DDO 126 (Fig. 3.17). The comparison between the isopressure contours (calculated using Eq. 4.4) and the iso-density contours (equal for the two models), shown in the left-hand panel of Fig. 4.6, confirms our prediction: for most of the disc the isopycnic and the isobaric surfaces are coincident and the largest discrepancies are found in the innermost regions where the gradient of  $\sigma_v$  is significant. We also found that the radial profile of the vertical scale height does not influence significantly the magnitude of this effect. In conclusion, given the conditions observed in the ISM, the HI discs can be considered reasonably barotropic with a cylindrical rotation. Moreover, the regions where these assumptions are less justified are in the innermost parts, where we expect that the disc is thin (see Sec. 4.3). Therefore, even if a vertical gradient of the rotation speed is present, it is expected to affect only an almost irrelevant (in term of density) portion of the gas. For these reasons, in the rest of the Chapter, we implicitly assume that the HI rotation is cylindrical.

Using Eq. 4.4 in Eq. 4.3 we obtain

$$\begin{cases} \sigma_v^2 \frac{\partial \ln \rho}{\partial z} = -\frac{\partial \Phi_{\text{tot}}}{\partial z} \\ \sigma_v^2 \frac{\partial \ln \rho}{\partial R} = -\frac{\partial \Phi_{\text{tot}}}{\partial R} + \omega^2 R, \end{cases} \quad (4.7)$$

where

$$\omega^2 = \Omega^2 - \frac{\partial \sigma_v^2(R)}{R \partial R} \quad (4.8)$$

Dynamical studies based on HI data usually focus on the radial part of Eq. 4.7: the total potential is retrieved fitting the observed rotation curve of the gas  $V_{\text{rot}} = \Omega R$  sometimes taking into account the pressure support terms (see Sec. 3.3.3). These results are obtained assuming that the HI disc is thin and the scale height equal to some arbitrary constant value, for example we assumed  $z_d = 100$  pc in the study of dIrrs in Chapter 3 (see Sec. 3.3.2). However, these assumptions are not compatible with the vertical component of Eq. 4.7 that, for a typical potential of dIrrs and spirals, predicts the presence of thick and flaring HI discs (see Sec. 4.3 and Fig. 4.15). The requirement that both the equilibrium equations are satisfied is not only for formal theoretical consistency because, as we have shown in Sec. 4.1, if not taken into account the presence of a thick HI disc can influence the observed properties introducing biases also in the dynamical analysis. In the following Section, we present a new original method in which the final kinematic and dynamic results are both consistent with the equilibrium conditions in Eq. 4.4 and corrected for the HI disc thickness.

### 4.2.2 The method

Our technique focuses on the 3D density distribution of gas,  $\rho$  and it takes advantage both of methods borrowed from the 2D analysis (e.g. ROTCUR) and of the exploitation of the the whole 3D datacube information as made in 3DB (Sec. 3.2). We define the HI 3D density as

$$\rho(\mathbf{R}, z) = \Sigma_{\text{int}}(\mathbf{R}) \frac{\zeta(z, z_d(\mathbf{R}))}{z_d(\mathbf{R})k}, \quad (4.9)$$

where  $\Sigma_{\text{int}}$  is the intrinsic surface density profile,  $\zeta$  is the functional form depending on the scale height  $z_d$  describing the HI vertical profile,  $k$  is a constant such that the integral of  $\rho$  along the vertical layer is exactly  $\Sigma_{\text{int}}$ , for example  $k = 2$  when  $\zeta$  is an exponential or a squared hyperbolic secant and  $k = \sqrt{2\pi}$  if  $\zeta$  is a Gaussian. Our method consists of an iterative process in which at each step we improve the estimate of the HI density profile (Eq. 4.9), using the observed information corrected for the HI thickness, and the total galactic potential obtained by the fit of the rotation curve. At the end of the iterations, the code returns the 3D density profile of the HI ( $\Sigma_{\text{int}}$  and  $z_d$ ), the unbiased estimate of the HI circular velocity and of the total galactic potential. The final results are totally compatible with the set of Euler equation in 4.3. The code is written as a Python extension of GIPSY. It recursively calls the tasks ELLINT, GAUFIT and ROTCUR to analyse the data and GALMOD to build disc models (see Sec. 4.1.1), while the parts of the code involving the dynamics (potentials, rotation curves, estimate of the scale height) make use of our Python module `galpynamics`<sup>6</sup>. A single code iteration consists in 5 sequential steps: each step is an independent part of the code that takes some data in input and returns new data or improve the data in input. These steps are briefly summarised below, while the detailed descriptions can be found in the next subsections. A  $\odot$  indicates a step with a proper sub-iterative process: in this case, the main iteration is “frozen” until the sub-iteration is concluded.

- 1 **Intrinsic surface density profile** ( $\odot$ ): taking into account the spatial instrumental resolution and the current model for the vertical profile of the HI disc, we deproject the observed surface density of the gas,  $\Sigma_{\text{obs}}$ , to obtain the intrinsic surface density  $\Sigma_{\text{int}}$  and the 3D density,  $\rho$ , using Eq. 4.9.
- 2 **Disc kinematics**: taking into account the current model for the 3D density profile of the HI disc and the current estimate of the rotational velocity  $V_{\text{rot}}$  and of the velocity dispersion  $\sigma_v$ , we correct the “observed” velocity field and the velocity dispersion maps to obtain improved maps of the kinematic properties in the disc equatorial plane. Then we use them to update the HI rotation

<sup>6</sup><https://github.com/iogiul/galpynamics>

curve and the HI velocity dispersion profile.

- 3 **Pressure support correction:** given the current model of the 3D HI density and the velocity dispersion profile, we correct the observed rotation curve obtaining the circular velocities that are tracers of the total galactic potential (see Sec. 3.3.3).
- 4 **Estimate of the DM density:** we find the best DM halo parameters fitting the circular velocity rotation curve.
- 5 **Estimate of the HI scale height ( $\odot$ ):** Given the current dynamical model (DM halo + stellar disc + HI disc) we estimate the HI vertical profile solving the vertical equilibrium conditions in Eq. 4.7.

The steps above are iterated until a converge on the HI properties (3D density, circular velocity and velocity dispersion) is reached. In each iteration we assume the knowledge of the geometrical properties of the galaxy (inclination angle, position angle and the coordinates of the centre). The position angle and the position of the centre is not affected by the presence of a thick disc (Sec. 4.1) and they can be found with the classical 2D (e.g. Oh et al. 2015) or 3D methods (see Sec. 3.3.2). The inclination angle could be influenced by the presence of a thick disc because the HI layers, above and below the equatorial plane, can produce an excess of emission near the minor axis that can artificially inflate the disc axial ratio (Sec. 4.1). Our method can be applied assuming a range of inclination angles comparing the final 3D datacube models with the observations to select the inclination angle that give the best representation of the data (see e.g. Fig. 4.14). Below we describe all the steps in detail.

### Preliminary steps

Before starting our iterative process, we need to produce preliminary data from the observed quantities. First of all, we separate the HI emission from the noise using a mask as described in Sec. 4.1.2. We use this “clean” datacube to make the HI total map (0th moment of the datacube) summing the emission through all the channels (see Sec. 3.3.1). The observed surface density profile,  $\Sigma_{\text{obs}}$ , and the related errors,  $\delta\Sigma_{\text{obs}}$ , are obtained calculating the mean and the standard deviation in the HI total map along elliptical rings defined by the disc geometrical parameters using the task ELLINT (see Sec. 3.3.1). The velocity field and the velocity dispersion map are obtained fitting the HI line profile in each pixel of the datacube with a Gaussian using the task GAUFIT. For each pixel, GAUFIT fits the HI line velocity profile and it returns an estimate of the best-fit Gaussian parameters: the amplitude  $A$ , the velocity centroid  $V_{\text{obs}}$  and the velocity dispersion  $\sigma_{\text{obs}}$ . Then, we blanked all the pixels that do not meet the following conditions.

- $A > n\sigma_{\text{ch}}$ , where  $\sigma_{\text{ch}}$  is the noise per channel and  $n$  is typically set to 3;
- $V_{\text{max}} > V_{\text{obs}} > V_{\text{min}}$ , where  $V_{\text{min}}$  and  $V_{\text{max}}$  are the values of the velocity in the first and last channels of the datacube that contain the source emission.
- $(V_{\text{max}} - V_{\text{min}}) > \sigma_{\text{obs}} > \sigma_{\text{inst}}$ , where  $\sigma_{\text{inst}}$  is the instrumental resolution.

Finally, as initial guess, we assume that the HI emission lies in a razor-thin disc, i.e. the vertical profile  $\zeta$  in Eq. 4.9 is a Dirac delta.

### Intrinsic surface density profile (step 1)

In this step we estimate the intrinsic surface density,  $\Sigma_{\text{int}}$ , needed to reproduce the observed radial surface density profile  $\Sigma_{\text{obs}}$  after the convolution with the instrumental beam. The initial guess for  $\Sigma_{\text{int}}$  is obtained simply correcting the observed surface density for the deprojection factor  $\cos i$  (Eq. 3.3). This first guess of  $\Sigma_{\text{int}}$  is then inserted in Eq. 4.9 to obtain a new estimate for the HI 3D density which is employed to make a HI datacube model using the task GALMOD (see Sec. 4.1). Once the datacube has been convolved with the instrumental beam, a model surface density,  $\Sigma_{\text{mod}}$ , is obtained using ELLINT in the same way we estimate  $\Sigma_{\text{obs}}$ .  $\Sigma_{\text{mod}}$  and  $\Sigma_{\text{obs}}$  are compared radius-by-radius and a new variable is defined as

$$\delta_{\Sigma}(\mathbf{R}) = \Sigma_{\text{mod}}^i(\mathbf{R}) - \Sigma_{\text{obs}}(\mathbf{R}), \quad (4.10)$$

then the new guess for the intrinsic surface density is

$$\Sigma_{\text{int}}^{i+1}(\mathbf{R}) = \Sigma_{\text{int}}^i(\mathbf{R}) + \delta_{\Sigma}^i(\mathbf{R}). \quad (4.11)$$

This process is iterated until the maximum difference between two successive estimates of the intrinsic surface density,  $\delta_{\text{max}} = \max(\delta_{\Sigma}^i(\mathbf{R})/h)$ , is lower than a certain threshold. Different values of  $h$  leads to use different types of residual: if  $h = 1$ ,  $\delta_{\text{max}}$  represents the maximum absolute difference between the observation and the projected model; if  $h = \Sigma_{\text{obs}}(\mathbf{R})$  or  $h = \delta_{\Sigma_{\text{obs}}}(\mathbf{R})$ ,  $\delta_{\text{max}}$  is the maximum relative residual with respect to the observational values or with respect to their  $1\sigma$  errors. Fig. 4.7 shows the result of this iterative method compared with the simple deprojection approach (Eq. 3.3) in the case of a HI disc model with a scale height flaring from  $50''$  in the centre to  $120''$  at last radius. Notice that to make the plot we assume to know the HI scale height at each radius, but in our code this information is improved at each step of the main iterative cycle. The final errors on  $\Sigma_{\text{int}}$  are estimated as  $\delta_{\Sigma_{\text{int}}} = \delta_{\Sigma_{\text{obs}}} \cos i$ .

Some steps of the main iterative cycle involve the calculations of integrals in which the density of the gas appears in the integrand functions (Eq. 4.22 and Eq. 4.33). In order to avoid that scatter noise in the intrinsic surface density adds

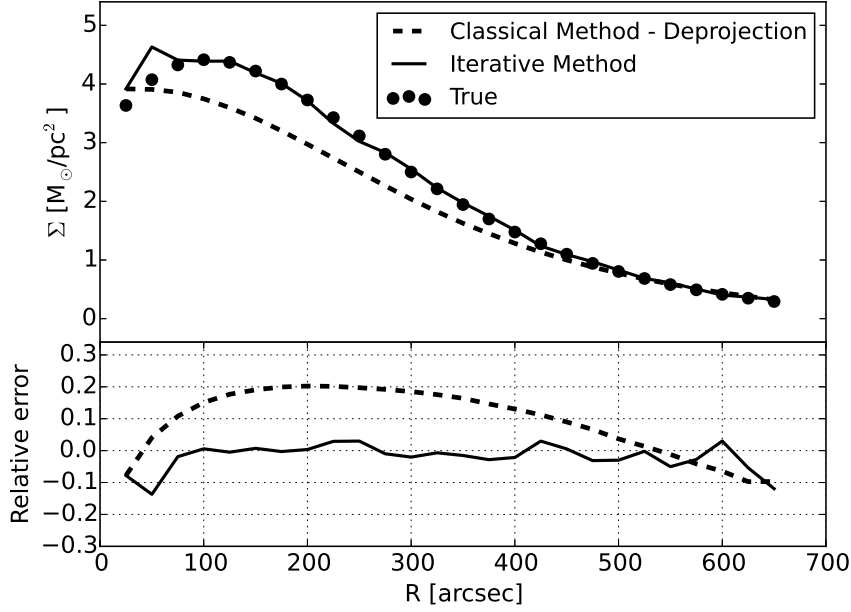


**Figure 4.7:** Performances of the classical deprojection method ( $\Sigma_{\text{int}} = \Sigma_{\text{obs}} \cos i$ ) and of our iterative method in retrieving the intrinsic surface density of a HI disc model. The scale height of the model flares from  $50''$  in the centre to  $120''$  at last radius, the instrumental beam resolution is  $25''$  and the disc is tilted  $65^\circ$  with respect to the los. **Top panel:** the points show the intrinsic surface density given in input, the dashed line indicates the estimate obtained with the classical deprojection method (Eq. 3.3), while the solid line shows the result obtained with our iterative method (see text). **Bottom panel:** relative errors (estimate-intrinsic/intrinsic) for the classical method (dashed line) and for our method (solid line).

“unrealistic” numerical scatters in the integral estimates, this step returns also a smooth functional form for the intrinsic surface density obtained fitting the final estimate of  $\Sigma_{\text{int}}$ . Currently the code supports the following fitting functions:

$$\Sigma_{\text{int}} R = \Sigma_0 \exp \left[ -\frac{R}{R_d} \right], \quad (4.12)$$

$$\Sigma_{\text{int}} R = \Sigma_0 \left( 1 + \frac{R}{R_d} \right)^\alpha \exp \left[ -\frac{R}{R_d} \right], \quad (4.13)$$

$$\Sigma_{\text{int}} R = \Sigma_0 \exp \left[ -0.5 \frac{(R - R_c)^2}{R_d^2} \right] \quad (4.14)$$

and

$$\Sigma_{\text{int}} R = \Sigma_0 \left( 1 + \sum_{i=1}^n a_i R^i \right) \exp \left[ -\frac{R}{R_d} \right]. \quad (4.15)$$

Eq. 4.12 is a simple exponential profile, Eq. 4.13 and Eq. 4.14 are useful to describe profiles that show an inner depression (e.g. WLM, Fig. 3.26), while Eq. 4.15 tuning the degree of the polynomials,  $n$ , can be adapted to a large variety of observed profiles. In particular, if  $n$  is large Eq. 4.15 is a sort of interpolating function that maintains the property to have an exponential decreases beyond a given radius.

### Disc kinematics (step 2)

In the presence of a thick HI disc the observed velocity field and velocity dispersion map ( $V_{\text{obs}}$ ,  $\sigma_{\text{obs}}$ ) are not tracing directly the kinematic properties of the gas in the equatorial plane of the disc (Sec. 4.1). In order to correct for this effect, we use the current estimate of  $V_{\text{rot}}$ ,  $\sigma_v$ ,  $\Sigma_{\text{int}}$  and  $z_d$  to build two models using GALMOD (Sec. 4.1.1): a thin-model assuming  $\zeta$  as a Dirac delta in Eq. 4.9 and a thick-model using the current estimate of the 3D HI density (Eq. 4.9). Using GAUFIT (see Sec. 4.1) we extract the velocity fields ( $V_{\text{thin}}$ ,  $V_{\text{thick}}$ ) and the velocity dispersion maps ( $\sigma_{\text{thin}}$ ,  $\sigma_{\text{thick}}$ ) from the two datacube models. Then we compare the thin and thick maps and we define two new maps in which each pixel, with coordinates  $(x, y)$ , contains the quantities

$$\begin{cases} \delta_V(x, y) &= V_{\text{thick}}(x, y) - V_{\text{thin}}(x, y) \\ \delta_\sigma(x, y) &= \sigma_{\text{thick}}(x, y) - \sigma_{\text{thin}}(x, y) \end{cases} \quad (4.16)$$

An example of residual maps  $\delta_V$  and  $\delta_\sigma$  is shown in Fig. 4.2.

The “improved” kinematic maps on the equatorial plane ( $V_{\text{eq}}$ ,  $\sigma_{\text{eq}}$ ) are obtained as

$$\begin{cases} V_{\text{eq}}(x, y) &= V_{\text{obs}}(x, y) - \delta_V(x, y) \\ \sigma_{\text{eq}}(x, y) &= \sigma_{\text{obs}}(x, y) - \delta_\sigma(x, y). \end{cases} \quad (4.17)$$

Each pixel of the velocity dispersion map is corrected for the instrumental resolution as  $\hat{\sigma}_{\text{eq}}(x, y) = \sqrt{\sigma_{\text{eq}}^2(x, y) - \sigma_{\text{inst}}^2}$  assuming that the instrumental broadening is a Gaussian with FWHM equal to two times the channel separation of the datacube. Finally the rotation curve and the velocity dispersion are estimated, as usual in 2D methods (e.g. Oh et al. 2015), from the “improved” maps. The HI rotation curve is obtained by fitting Eq. 1.6 ring-by-ring to the unbiased velocity field using ROTCUR in which we kept fixed all the geometrical parameters (inclination, PA, centre) and we fit only for  $V_{\text{rot}}$ . As done in Chapter 3 (Sec. 3.3.2), we give different weights,  $w$ , to the observed velocities across the disc using  $w = \cos \theta$ , where  $\theta$  is the azimuthal angle. This step is repeated two times considering separately the approaching ( $V_{\text{rot}}^{\text{app}}$ ) and the receding ( $V_{\text{rot}}^{\text{rec}}$ ) halves of the disc, the final  $V_{\text{rot}}$  and the related error are calculated as the mean and the standard deviation of  $V_{\text{rot}}^{\text{app}}$  and  $V_{\text{rot}}^{\text{rec}}$  at each radius. The velocity dispersion profile,  $\sigma_v$ , and the related errors,  $\delta_{\sigma_v}$ , are obtained taking

the average and the standard deviation of the observed values in  $\hat{\sigma}_{\text{eq}}$  along elliptical annuli using ELLINT as done for the observed surface density profile.

### Pressure support correction (step 3)

The HI circular velocities,  $V_c$ , are now obtained correcting the  $V_{\text{rot}}$  estimated in the previous step for the gas pressure support using the current estimate of  $\sigma_v$ ,  $\Sigma_{\text{int}}$  and  $z_d$ . Essentially, we use the method described in Sec. 3.3.3, but we take into account also the radial variation of the scale height. In this case, using Eq. 3.7, the asymmetric-drift correction term (Eq. 3.8) becomes

$$V_A^2(\text{R})|_{z=0} = -\text{R}\sigma_v^2(\text{R})\frac{\partial \ln(\sigma_v^2(\text{R})\Sigma_{\text{int}}(\text{R})z_d^{-1}(\text{R}))}{\partial \text{R}}. \quad (4.18)$$

The errors on  $V_A$  and on  $V_c$  are calculated with the same procedure described in Sec. 3.3.3.

### Estimate of the DM density (step 4)

In this step, we improve the dynamical model of the galaxy by fitting a DM halo model to the DM velocity defined as

$$V_{\text{DM}} = \sqrt{V_c^2 - V_*^2 - f_{\text{He}}|V_{\text{HI}}|V_{\text{HI}}}, \quad (4.19)$$

where  $V_c$  is the current circular velocity,  $V_*$  and  $V_{\text{HI}}$  are the rotational components due to the radial acceleration produced by the stellar disc and the HI disc, respectively (see Appendix 5.A). The factor  $f_{\text{He}}$  takes into account the presence of the Helium (we assume  $f_{\text{He}} = 1.33$  in this work, see e.g. Begum et al. 2008a; Lelli, McGaugh & Schombert 2016b). The  $V_{\text{HI}}$  term is not squared because in some cases the HI distribution has an inner depression that causes a radial force directed outward in the opposite direction with respect to the centripetal acceleration required to sustain the observed  $V_c$  (see Appendix 5.A). The uncertainties on  $V_{\text{DM}}$  are calculated applying the errors propagation to Eq. 4.19:

$$\delta_{V_{\text{DM}}} = \frac{\sqrt{V_c^2 \delta_{V_c}^2 + V_*^2 \delta_{V_*}^2 + f_{\text{He}}^2 V_{\text{HI}}^2 \delta_{V_{\text{HI}}}^2}}{V_{\text{DM}}}. \quad (4.20)$$

The rotation curves of the disc components are calculated from the matter distribution  $\rho_*$  for the star and  $\rho_{\text{HI}}$  for the gas as

$$V(\text{R}) = \sqrt{-\text{R}g(\text{R}, z = 0)} \quad (4.21)$$

where  $g$  is the radial component of the gravitational acceleration.  $g$  is estimated

calculating the integral (Casertano, 1983)

$$g(R, z = 0) = 4 G \int_0^\infty dR' \int_0^\infty dz' \frac{2\sqrt{R'}}{\sqrt{R'p}} [K(p) - E(p)] \frac{\partial \rho(R', z')}{\partial R'}, \quad (4.22)$$

where  $K$  and  $E$  are the complete elliptical integrals of the first and second kind as defined in Abramowitz & Stegun (1972),  $p = \epsilon - \sqrt{\epsilon^2 - 1}$  and

$$\epsilon = \frac{R^2 + R'^2 + (z' - z)^2}{2RR'}. \quad (4.23)$$

Concerning the stellar disc, the  $\rho$  inside the integral in Eq. 4.22 is usually expressed as a double exponential with a constant scale length, while for the HI disc the  $\rho$  comes from Eq. 4.9, where we use the current estimate of  $\Sigma_{\text{int}}$  and  $z_d$ . The errors on  $V_*$  and  $V_{\text{HI}}$  can be derived from the uncertainties of the observed surface density profiles using the method described in Appendix 5.A. However, when the DM matter is dominant, as it is the case for dIrrs,  $V_c$  is much larger than  $V_*$  and  $V_{\text{HI}}$ , hence Eq. 4.20 becomes

$$\delta_{V_{\text{DM}}} \approx \frac{V_c}{V_{\text{DM}}} \delta_{V_c}. \quad (4.24)$$

In the analysis of the dIrrs in Sec. 4.3, we calculate the errors on  $V_{\text{DM}}$  using Eq. 4.24.

Following Binney & Tremaine (2008), we assume that the DM halo is an oblate spheroid with axial ratio  $q$  and density  $\rho_h(m; \vec{\Theta})$ , where  $m$  is the elliptical radius defined as  $m^2 = R^2 + z^2 q^{-2}$  and  $\vec{\Theta}$  contains all the model parameters (e.g. central density and core radius for an isothermal halo, see Eq. 4.26 and Eq. 4.27). The circular velocity for a given halo model is

$$V_h^2(R; \vec{\Theta}) = 4\pi G q \int_0^R dm \frac{m^2 \rho_h(m; \vec{\Theta})}{\sqrt{R^2 - m^2(1 - q^2)}}. \quad (4.25)$$

Currently our code implement the possibility to use an isothermal halo with density

$$\rho_h(m; \rho_0, r_c) = \rho_0 \left(1 + \frac{m^2}{r_c^2}\right)^{-1}, \quad (4.26)$$

or a NFW halo with density

$$\rho_h(m; \rho_s, r_s) = \rho_s \left(\frac{m}{r_s}\right)^{-1} \left(1 + \frac{m}{r_s}\right)^{-2}; \quad (4.27)$$

the axial ratio  $q$  of the halo can be set between 0.01 (disc-like) and 1 (spherical).

Finally, the best set of halo parameters  $\vec{\Theta}_{\text{best}}$  are obtained maximizing the loga-

rithmic likelihood

$$\ln \mathcal{L} = - \sum_{\mathbf{R}} \frac{[V_{\text{h}}(\mathbf{R}; \vec{\Theta}) - V_{\text{DM}}(\mathbf{R})]^2}{\delta_{V_{\text{DM}}}^2(\mathbf{R})}. \quad (4.28)$$

### Estimate of the HI scale height (step 5)

Integrating the vertical component of Eq. 4.7 we obtain

$$\tilde{\rho}(\mathbf{R}, z) = \frac{\rho(\mathbf{R}, z)}{\rho(\mathbf{R}, 0)} = \exp \left[ - \frac{\Phi_{\text{tot}}(\mathbf{R}, z) - \Phi_{\text{tot}}(\mathbf{R}, 0)}{\sigma_v^2(\mathbf{R})} \right], \quad (4.29)$$

where the total potential  $\Phi_{\text{tot}}$  is the sum of the potentials due to the DM halo ( $\Phi_{\text{h}}$ ), the stellar disc ( $\Phi_{\text{*}}$ ) and the gaseous disc ( $\Phi_{\text{gas}} = f_{\text{He}} \Phi_{\text{HI}}$ ). Through Eq. 4.29, at each  $\mathbf{R}$ , we obtain the normalised vertical profile of the HI, from which we can estimate the vertical scale height  $z_{\text{d}}(\mathbf{R})$ .

The potential of the spheroidal halo is calculated through (Binney & Tremaine, 2008)

$$\Phi_{\text{h}}(\mathbf{R}, z) = -2\pi G \frac{q}{\sqrt{1-q^2}} \left( 2 \frac{\psi(\infty)}{\sin(\sqrt{1-q^2})} - \sqrt{1-q^2} \int_0^\infty d\tau \frac{\psi(m_\tau(\mathbf{R}, z, \tau))}{(\tau+1)\sqrt{\tau+q^2}} \right), \quad (4.30)$$

where

$$\psi(m) = \int_0^m dm' m' \rho_{\text{h}}(m') \quad (4.31)$$

and

$$m_\tau = \frac{R^2}{\tau+1} + \frac{z^2}{\tau+q^2}. \quad (4.32)$$

Notice that  $\psi(\infty)$  can diverge for certain density halo models (e.g. isothermal halo, Eq. 4.26), however Eq. 4.29 depends only on the vertical gradient of the potential, hence the term that depends on  $\psi(\infty)$  in Eq. 4.30 vanishes in Eq. 4.29.

Following Cuddeford (1993), the potential for the disc components are evaluated as

$$\Phi(\mathbf{R}, z) = - \frac{2G}{\sqrt{R}} \int_{-\infty}^\infty dR' \int_0^\infty dz' \sqrt{R'} \mathcal{Q}_{-\frac{1}{2}}(\epsilon) \rho(R', z'), \quad (4.33)$$

where  $\mathcal{Q}$  is the Legendre function of the second kind and  $\epsilon$  is defined in Eq. 4.23.

From Eq. 4.33 it is clear that the both the right-hand and the left-hand terms in Eq. 4.29 depend on the HI gas density, actually Eq. 4.29 is a differential equation that must be solved numerically. For this purpose, we developed an iterative method in which at each step the vertical profile of the HI,  $\tilde{\rho}^i$ , is evaluated from Eq. 4.29 considering the potential of the gaseous disc ( $\Phi_{\text{gas}}^i$ ) obtained from the previous 3D HI density estimate  $\rho^{i-1}$ . For each sampling radius, we fit  $\tilde{\rho}^i(\mathbf{R})$  with the functional form  $\zeta$  (Gaussian, exponential or squared hyperbolic secant) obtaining a measure of

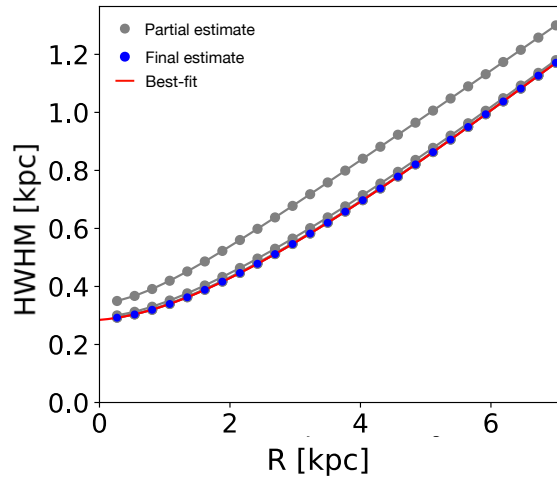


**Figure 4.8:** Step-by-step  $z_d$  estimate using the iterative method described in the text (“Estimate of the HI scale height” subsection). The grey points show the  $i$ -th partial estimates, in particular the upper-limit profile shows the first guess obtained considering only the potential due to the DM halo and the stellar disc. The blue points show the final estimate of the scale height and the red curve is the related best-fit functional form. In this particular case, the convergence is reached after 4 iterations, the last two are too similar to be appreciated in the Figure.

the scale height  $z_d$ . Finally, the radial trend of  $z_d$  is fitted with another functional form, typically a polynomial. In order to avoid strong unphysical discontinuities in the radial profile of  $z_d$ , we regularise the radial profile of the velocity dispersion with a smooth functional form as a low order polynomial. If a strong radial trend is not present, we assume a constant  $\sigma_v$  averaging the radial profile. The current estimate of  $\zeta(z, z_d)$  is used in Eq. 4.9 to define a new 3D density model and the cycle is repeated until the maximum difference between two successive estimates of  $z_d$  is less than a certain value, typically 1 pc. In the first iteration we consider only the DM halo and the stellar disc obtaining an upper limit for  $z_d$ . In order to have an estimate of the uncertainties in  $z_d$ , this step is repeated two times: one time considering an upper profile for the velocity dispersion as  $\sigma_v^{up}(R) = \sigma_v(R) + \delta_{\sigma_v}(R)$  and an other time considering a lower profile as  $\sigma_v^{low}(R) = \sigma_v(R) - \delta_{\sigma_v}(R)$ . The final values of  $z_d$  and the related errors are obtained taking the mean and the standard deviation of the two separated estimates of the scale height described above. Fig. 4.8 shows an example of how the convergence in the  $z_d$  profile is reached step-by-step. We stress that during the iterative estimate of  $z_d$ , the main iterative cycle is frozen.

After this last step, the code checks whether the convergence of the HI disc parameters ( $\Sigma_{int}$ ,  $z_d$ ,  $V_c$ ,  $\sigma_v$ ) is reached. If this is the case, the code stops the iterations and it makes a final disc model using GALMOD, otherwise a new iteration begins starting from the new estimate of the intrinsic surface density.

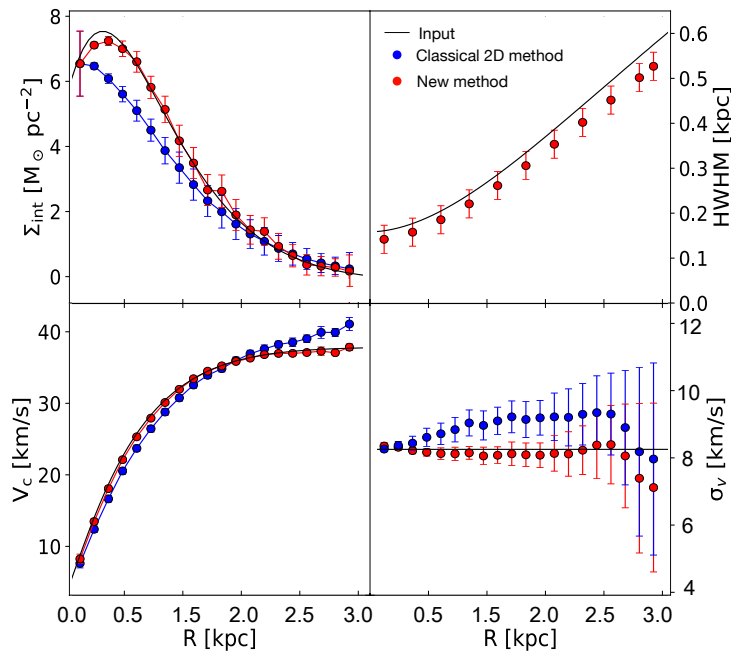


**Figure 4.9:** Comparison between the results obtained in the analysis of a HI disc model using a “classical” razor-thin 2D method (blue points) and our iterative method (red points) described in Sec. 4.2.2. The input properties of the HI disc are shown by the black curves.

### 4.2.3 Tests

We test our method with a series of dynamically self-consistent HI disc models made using GALMOD (Sec. 4.1.1): our method is able to nicely retrieve the intrinsic HI properties also in the presence of very thick discs.

As a comparison, we repeated these tests using the razor-thin 2D and 3D tilted ring approaches (see Sec. 1.3.3). 2D methods work on integrated maps (velocity fields) and they can not take into account the presence of a thick disc. 3DB is more promising since the scale height is one of the parameters needed in the datacube fitting (see Sec. 3.2 and Appendix 3.C), but we found that the fit is essentially insensitive of the HI thickness for small-medium values of the scale height and returns unacceptable results for very thick HI discs. The reason for this is that, even if 3DB works on the whole datacube, it fits one single ring at the time and it can not include the emission coming from the extended vertical layers of the other rings.

As an example, in Fig. 4.9, we show the results obtained for a WLM-like (Fig. 3.26) HI disc model: our method is able to retrieve the radial profile of the HI scale height, accordingly also the other estimated properties are totally compatible with the input profiles. Compared to our method, the classical 2D tilted-ring approach is obviously biased by the fact that the HI thickness is not taken into account: as expected (Sec. 4.1.2), it estimates a too shallow intrinsic surface density, larger velocity dis-

persions and the rotation curve tends to be artificially higher in the outer parts.

## 4.3 Application to real galaxies

### 4.3.1 The sample

In [Chapter 3](#), we have analysed a sample of dIrrs assuming for each of them a very thin HI disc with a Gaussian vertical profile and a constant scale height of 100 pc (see [Sec. 3.2.1](#)). However, in [Sec. 4.1](#), we have shown that, if not properly accounted for, the presence of a thick HI disc can bias the final results. In this Section, we applied the method presented in [Sec. 4.2.2](#) to estimate the thickness of the HI discs to a subsample of dIrrs from [Chapter 3](#) and we check whether the results obtained in that Chapter are significantly biased by the naive treatment of the HI disc thickness.

Among the 17 dIrrs ([Tab. 3.2](#)), we choose three galaxies: DDO 210, WLM and NGC 2366. DDO 210 ([Fig. 3.21](#)) is the smallest galaxy in our sample ( $R_{\max} = 0.4$  kpc) with a very low rotational velocity ( $\lesssim 5$  km s<sup>-1</sup>) and a final circular velocity, dominated by the asymmetric-drift corrections ([Sec. 3.3.3](#)), that reaches  $\sim 16$  km s<sup>-1</sup> in the outer disc. WLM ([Fig. 3.26](#)) is a galaxy with intermediate properties, a very regular kinematics and it reaches a circular velocity of about 40 km s<sup>-1</sup>. Finally, NGC 2366 is an “extended” dIrr ( $R_{\max} = 6.3$  kpc) with a rotation curve that becomes almost flat ( $V_c \sim 57$  km s<sup>-1</sup>) in the outer parts. These three galaxies are representative of all the different properties shown by dIrrs analysed in [Chapter 3](#): radial extent, dynamical mass and importance of the asymmetric-drift correction.

### 4.3.2 Results

The galaxies presented in [Sec. 4.3.1](#) have been analysed using our original method ([Sec. 4.2](#)): we assume a Gaussian vertical profile for the HI discs and we adopt the geometrical parameters ( $i$ , PA, centre) reported in [Tab. 3.8](#). The dynamical model for the galaxies has three components: a spherical isothermal spherical halo ([Eq. 4.26](#)), an exponential stellar disc (with a  $\text{sech}^2$  vertical profile) and a gaseous disc taking into account the Helium with a multiplicative factor  $f_{\text{He}} = 1.33$  (see [Eq. 4.19](#)). The smooth profiles of the HI surface density are obtained using [Eq. 4.13](#). In the analysis of the three galaxies, we assume that the velocity dispersion is constant across the disc and it is calculated as the mean of the  $\sigma_v(R)$  estimates. The iterative cycle is stopped when the maximum relative difference between two successive estimate of  $V_c$  and  $z_d$  is lower than 5%. Below we describe the results obtained.

- **DDO 210**, [Fig. 4.10](#): the HI disc of this galaxy is very thick compared to the radial dimension, we estimate an almost constant thickness of  $\sim 200$  pc, larger

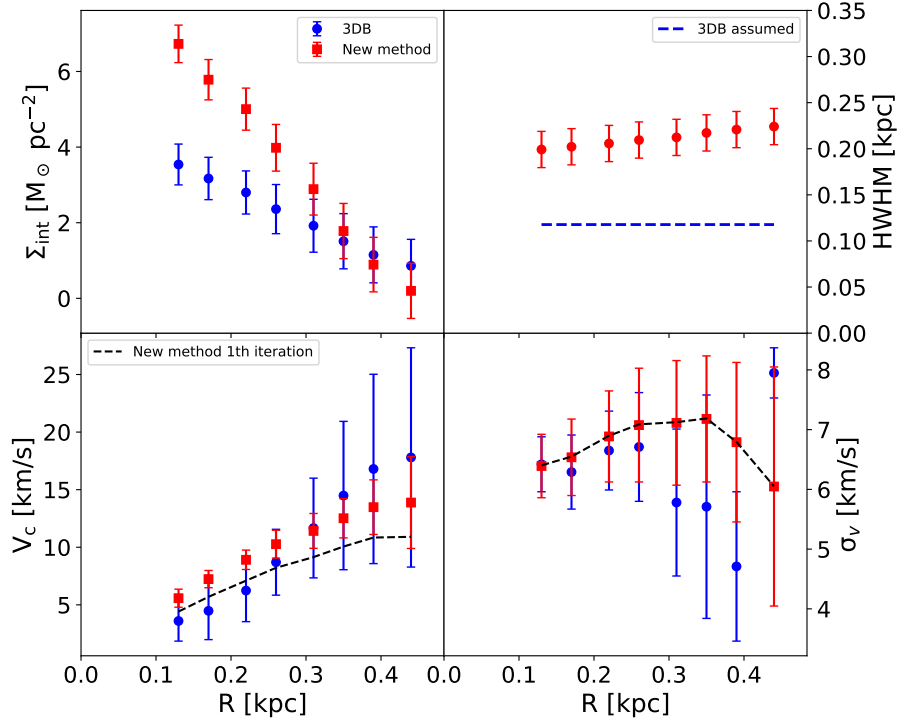


**Figure 4.10:** Comparison between the HI disc properties of DDO 210 (see Fig. 3.21) obtained with our method to take into account the HI thickness presented in Sec. 4.2.2 (red squares) and using 3DB in Chapter 3, assuming a thin disc (blue dots). The black-dashed lines indicate the kinematic results obtained at first step of our iterative method, i.e. assuming a razor-thin HI disc.

than the HI radial scale length ( $\sim 180$  pc) and about half of the observed radial extent. The presence of such thick disc combined with the large beam of  $\sim 70$  pc (Tab. 3.2) causes the observed surface density to be significantly smoothed. In fact, our unbiased estimated of the intrinsic radial profile,  $\Sigma_{\text{int}}$ , is much steeper with respect to the profile obtained with the classical deprojection method (Eq. 3.3). Since the circular velocity of this galaxy is totally dominated by the pressure support correction (Fig. 3.21), the steep radial profile of  $\Sigma_{\text{int}}$  increases the asymmetric-drift terms (Eq. 3.8) and the final circular velocity is systematically larger than the one estimated in the first iteration assuming a razor-thin disc.

Notice that our estimate of  $V_c$  at first iteration is different with respect to the  $V_c$  obtained with 3DB in Chapter 3. The differences are due to the fact that in our analysis we assume the velocity dispersion constant in the estimate of the asymmetric-drift correction (Sec. 3.3.3), while in Chapter 3 we follow its decreases in the outer part ( $R > 0.3$  kpc, see the bottom-right panel in Fig. 4.10).

As a results the  $V_c$  estimated with 3DB are higher beyond  $R = 0.3$  kpc. The different assumptions on the estimate of the asymmetric-drift correction are also at the base of the different magnitudes of the  $V_c$  errors. Given that the final  $V_c$  is dominated by the contribution of the pressure support, the final errors also are dominated by the uncertainties of the correction process (see Sec. 3.3.3) and the presence of a varying  $\sigma_v$  introduces an additional term in the error budget.

The best-fit parameters obtained for the DM halo are  $\rho_h = 0.07^{+0.02}_{-0.01} M_\odot \text{ pc}^{-3}$  and  $r_c = 0.55^{+0.52}_{-0.23}$  kpc (given the steep increase of the rotation curve and the small radial extent of the disc, the core radius is not well constrained). As comparison, (Oh et al., 2015) found  $\rho = 0.11 \pm 0.02 M_\odot \text{ pc}^{-3}$  and  $r_c = 0.20 \pm 0.05$  kpc. In this analysis, we have assumed a stellar disc with a central surface density  $\Sigma_0^* = 2.7 M_\odot \text{ pc}^{-2}$ , a radial scale length  $R_d^* = 200$  pc and vertical scale height  $z_d^* = 100$  pc. The vertical scale height is from Oh et al. (2015), while the central surface density and the radial scale length have been obtained fitting an exponential to the SED profile in Zhang et al. (2012). Given that we found  $z_d \sim 200$  pc for the HI disc, it is quite unlikely that the stars are settled on a thinner disc. However the contribution of the stellar disc to the global galactic potential is negligible, so the assumption of larger vertical scale height for the stellar disc has practically no impact on the final results.

Although the HI disc of DDO 210 is quite thick, the results on the kinematics obtained with our method and the ones estimated in Chapter 3 using 3DB are compatible within the errors. Moreover, the differences shown in Fig. 4.10 are mainly due to the different method used to estimate the kinematics (from 2D maps in our method and exploiting the whole datacube in 3DB) and on the assumption in the estimate of the asymmetric-drift, rather than to the different assumptions on the HI scale height.

- **WLM**, Fig. 4.11: this galaxy has a flaring thick HI disc in which the vertical scale height increases almost linearly from  $\sim 200$  pc in the centre to  $\sim 700$  pc in the outer part where it becomes larger than the HI radial scale length ( $R_d \sim 560$  pc). Including the HI thickness in the analysis, the intrinsic surface density shows a deeper depression in the inner part; the velocity dispersion in the last iteration is systematically lower by about  $0.6 \text{ km s}^{-1}$  in the inner disc and by  $0.3 \text{ km s}^{-1}$  in the outer disc with respect to the first iteration where we assumed a razor-thin disc; the circular velocities have a maximum difference of about  $5 \text{ km s}^{-1}$  that is compatible with the errors. The observed differences between the circular velocities are due to the naive treatment of the vertical profile employed in Chapter 3.

The best-fit parameters obtained for the DM halo are  $\rho_0 = 0.12 \pm 0.03 M_\odot \text{ pc}^{-3}$

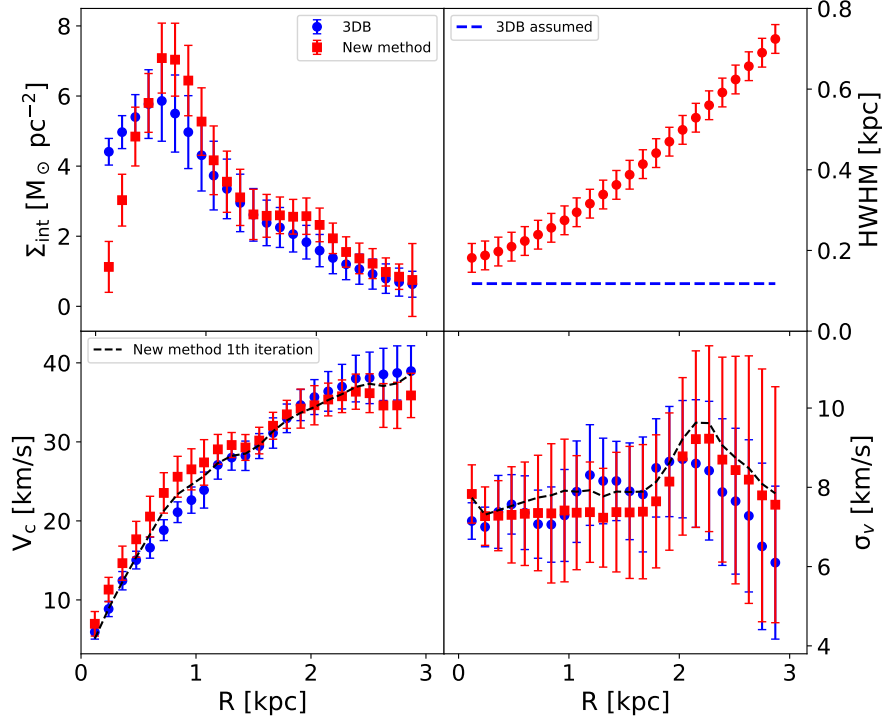


**Figure 4.11:** Same as Fig. 4.10 but for WLM (see Fig. 3.26).

and  $r_c = 0.44 \pm 0.06$  kpc, as comparison Oh et al. (2015) found  $\rho_0 = 0.06 \pm 0.01 M_\odot \text{pc}^{-3}$  and  $r_c = 0.74 \pm 0.01$  kpc. The stellar disc parameters used in this analysis have been taken from Leaman et al. (2012), who reported a total mass  $M_* = 1.1 \times 10^7 M_\odot$ , a radial scale length  $R_d^* = 0.99$  kpc and a constant vertical scale height  $z_d^* = 0.71$  kpc.

- **NGC 2366**, Fig. 4.12: the scale height of the HI disc in this galaxy is slightly lower than 500 pc in the inner part and then it flares linearly to  $\sim 1.30$  kpc at the last measured point. In absolute terms, the HI disc of NGC 2366 is the thickest among the three analysed galaxies: in the centre  $z_d$  is already two times larger than the one measured in DDO 210 and it is comparable with the maximum scale height reached in WLM. The main reason is that the velocity dispersion measured for this galaxy is quit high, especially in the inner part where it is almost two times larger than what it is observed in the other two galaxies. However, compared to the radial extent ( $R_{\text{max}} = 6.3$  kpc) and the radial scale length ( $R_d \sim 1.74$  kpc) of the HI disc, the vertical extent is not so relevant. As a consequence, the properties estimated with our method are largely compatible with the one obtained in Chapter 3 using 3DB.

The best-fit DM halo parameters obtained in our analysis are  $\rho_0 = 0.04 \pm$

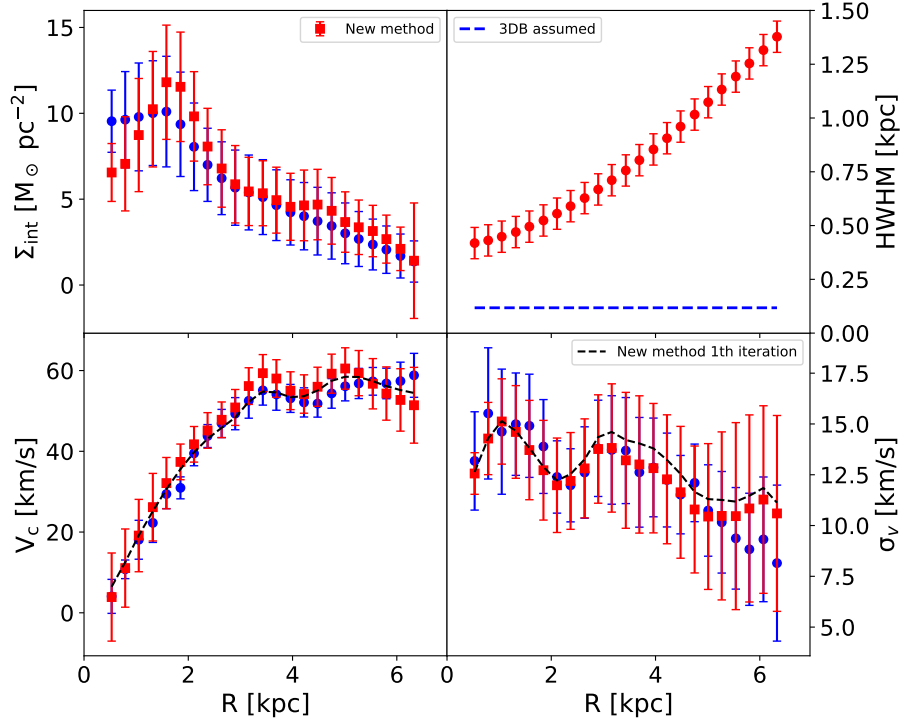


**Figure 4.12:** Same as Fig. 4.10 but for NGC 2366 (see Fig. 3.24).

$0.02 M_{\odot} \text{pc}^{-3}$  and  $r_c = 1.40 \pm 0.33$  kpc; they are compatible within the errors with  $\rho_0 = 0.04 \pm 0.01 M_{\odot} \text{pc}^{-3}$  and  $r_c = 1.21 \pm 0.04$  kpc obtained by Oh et al. (2015). We have assumed a stellar disc with a central surface density of  $\Sigma_0^* = 3.3 M_{\odot} \text{pc}^{-2}$ , a radial scale  $R_d^* = 1.6$  kpc and vertical scale height  $z_d^* = 260$  pc. As for WLM, the vertical scale height is from Oh et al. (2015), while the central surface density and the radial scale length have been obtained by fitting an exponential to the SED profile in Zhang et al. 2012 (private communication). As already discussed for DDO 210 (see above), it is unlikely that the stellar disc is so much thinner with respect to the HI disc. However, also in this case the assumption of thicker stellar disc does not change our results.

In conclusion, although we estimated a significant HI disc thickness for the three analysed galaxies, we also showed that it does not have a significant impact in the study of the kinematics and dynamics.

### 4.3.3 Testing working assumptions

The results of Sec. 4.3.2 have been obtained with the assumption that the DM halo is spherical and with an isothermal density law. Moreover, we used the inclination

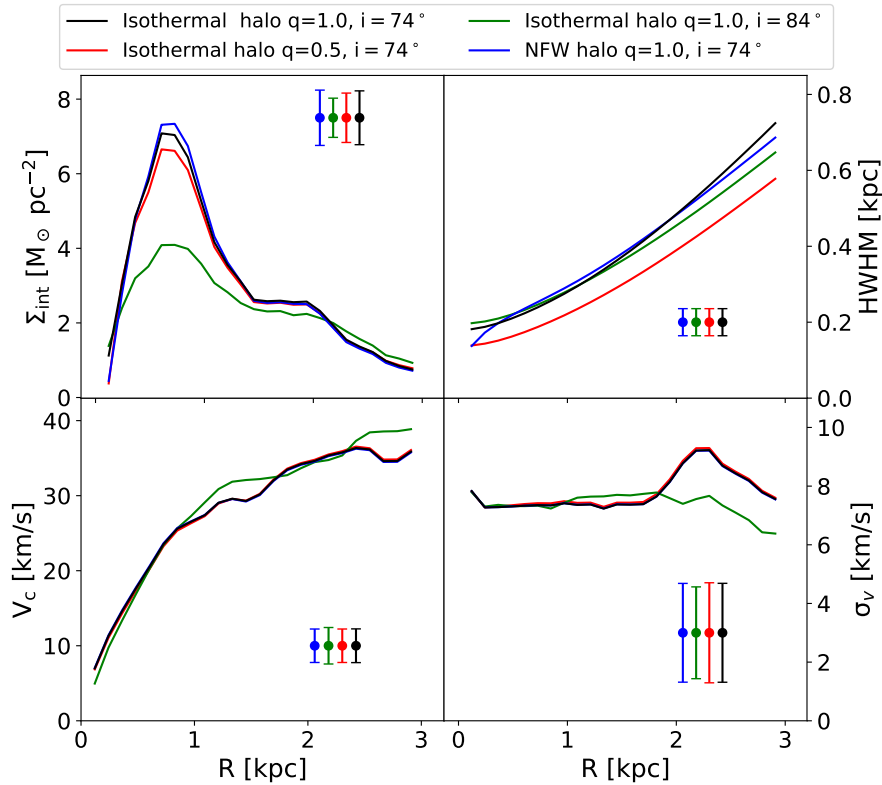


**Figure 4.13:** Results obtained applying the method described in Sec. 4.2.2 to WLM with different assumptions for the DM halo and the disc inclination  $i$ : spherical isothermal halo and  $i = 74^\circ$  (black curves); spherical isothermal halo and  $i = 84^\circ$  (green curves); flattened isothermal halo (axial ratio  $q = 0.5$ ) and  $i = 74^\circ$  (red curves); spherical NFW halo and  $i = 74^\circ$ . The points with errorbars indicate the mean errors of the different properties for the four cases.

angles estimated in Chapter 3 without considering the presence of a thick HI disc, but we have shown that in this case the true inclination angle can be underestimated (Fig. 4.5). In order to analyse how these assumptions influence the final results, we repeat the analysis of WLM (Sec. 4.3.2) making different assumptions on the DM halo properties and on the inclination angle:

- (i) spherical isothermal halo and disc inclination angle  $i = 74^\circ$ , this is the same case already analysed in this section and it is used as benchmark;
- (ii) spherical isothermal halo and disc inclination angle  $i = 84^\circ$ , in this case we highlight the differences introduced by a different inclination angle;
- (iii) flattened isothermal halo with axial ratio  $q = 0.5$  and disc inclination angle  $i = 74^\circ$ , with these assumptions we highlight the differences introduced by a non-spherical DM halo;

- (iv) spherical NFW halo and disc inclination angle  $i = 74^\circ$ , in this case, we analyse the differences introduced by a different density model (Eq. 4.27) for the DM halo.

The comparison of the final results is shown in Fig. 4.13. The assumptions (i) and (iv) give very similar results, all compatible within the errors. Therefore the assumption of isothermal or NFW DM halos does not have a large impact on the final outcomes. Using a (quite) flattened halo in (iii), we obtain that the HI disc is thinner; this is expected since in this case the DM halo is more concentrated in the equatorial plane and the vertical gradient of the potential is steeper (Eq. 4.29). Considering a thinner HI disc, the peak of the intrinsic surface density results less pronounced. Concerning the kinematics, the assumption of a flattened halo does not have any influence on the final results.

The largest differences are obtained using the assumption (ii), although the radial profile of the vertical scale height is compatible with the results obtained using (i) and (iv). The large discrepancy shown by the intrinsic surface density profiles is due mainly to the fact that the observed disc surfaces are “shrunk” by a factor  $\cos i$  and the difference between  $\cos(84^\circ)$  and  $\cos(74^\circ)$  is relevant. The differences on the results obtained for  $V_c$  and  $\sigma_v$  are due to the fact that changing the inclination the tilted-rings used in ROTCUR for  $V_c$  and in ELLINT for  $\sigma_v$  (see Sec. 4.2.2) encircle different disc regions with respect to the case of  $i = 74^\circ$ . In particular, between 2 kpc and 3 kpc, they do not “intercept” the regions of the disc with high velocity dispersion that cause the visible “bump” in the  $\sigma_v$  profiles. However, all the estimated  $V_c$  and  $\sigma_v$  are compatible within the errors with results obtained assuming (i), (iii) and (iv).

#### 4.3.4 Understanding the HI emission near the minor axis

In Sec. 4.1.2 we found, using disc models, that the presence of a thick disc is expected to produce an excess of HI emission near the minor axis. In particular, we argued that the features shown in Fig. 4.4 for the disc models are similar to the what see for WLM in Chapter 3 (Fig. 3.26) and also in other galaxies (e.g. UGC 8508, see Fig. 3.25). In this Section, we use the results obtained in Sec. 4.3.2 to investigate whether the excess of emission found in WLM can be explained with the emission from the HI layers above and below the equatorial plane. To this aim, we use GALMOD (Sec. 4.1.1) to make an HI disc model using as input the properties estimated taking into account the HI disc thickness (Fig. 4.11). Given that in the presence of a thick disc the intrinsic inclination of HI disc can be underestimated (see Fig. 4.5), as comparison, we build an other disc model using the HI intrinsic properties ( $\Sigma_{\text{int}}, V_c, \sigma_v, z_d$ ) estimated with our method (Sec. 4.2.2) assuming an inclination angle of  $84^\circ$  (see Sec. 4.3.3 and Fig. 4.13). Finally, we make a last model

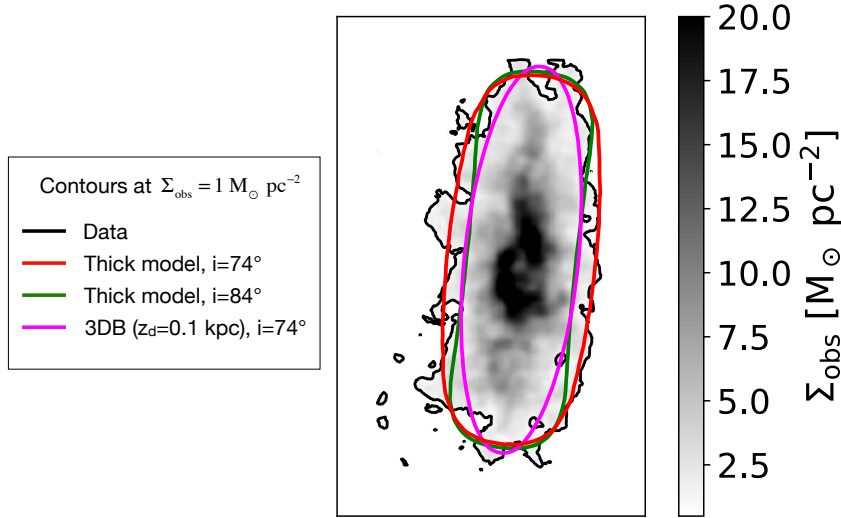


**Figure 4.14:** Comparison between the iso-density contours at  $1 M_{\odot} \text{ pc}^{-2}$  of the HI total map of WLM (black contour) and of the disc models obtained with GALMOD (Sec. 4.1.1) using the HI parameters obtained Sec. 4.3 (see Fig. 4.13) taking into account the HI thickness and assuming a disc inclination of  $74^{\circ}$  (red contour) and  $84^{\circ}$  (green contour). The magenta contour indicates the emission from the disc model obtained using the results found in Chapter 3 with 3DB and assuming a constant scale height  $z_d = 100 \text{ pc}$ . The image in background shows the integrated emission of WLM in units of  $M_{\odot} \text{ pc}^{-2}$ .

using the results obtained in Chapter 3 with 3DB and assuming a thin disc with  $z_d = 100 \text{ pc}$  (Fig. 3.26). In Fig. 4.14 we compare the performance of the three models to “populate” the regions around the minor axis overplotting the iso-density contours at  $1 M_{\odot} \text{ pc}^{-2}$  of the total maps of the three models with the one of the observed HI total map of WLM. As already discussed, the model obtained using the results of 3DB is not able to reproduce the excess of emission along the minor axis. The thick disc model with  $i = 84^{\circ}$  is able to account for the excess of the emission near the major axis but it is still not able to reproduce the emission near the minor axis. On the contrary, the thick disc model with the inclination  $i = 74^{\circ}$  gives a very good match to the data. Therefore, we can conclude that the excess of the emission near the minor axis observed in WLM, and likely also in other dIrrs (e.g. UGC 8508, Fig. 3.25), is produced by the thick HI layers intercepted along the los. This result introduces a further warning (see Sec. 3.4.2) in the study of the gas kinematics around the minor axis. In fact, in these regions the HI signal has poor information on the gas rotation, moreover it can be dominated by the noise and in the outer parts of the disc it can come from regions of the galaxy outside the disc equatorial plane. If these effects are not take into account, the final results can be

heavily biased.

## 4.4 Conclusions

In this Chapter we have demonstrated, using mock datacubes, that the presence of a thick disc can bias the estimate of intrinsic properties of the HI discs. If the HI thickness is not taken into account the recovered intrinsic surface density is shallower than the real one, the rotation curve tends to be artificially higher in the outer parts and the velocity dispersion is overestimated.

In order to take into account these biases, we have developed the first dynamical self-consistent method to recover the intrinsic properties of thick HI discs under the assumption of vertical hydrostatic equilibrium. We found that, even in the presence of a significant thick disc, as it is the case for dIrrs, the magnitude of the biases described before is not dramatic and surely the introduced errors represent a second-order effects with respect to uncertainties due to the correction for the pressure support (Sec. 3.3.3), the estimate of the inclination (Sec. 3.3.2) and the observational limitations (noise, instrumental resolution, datacube reduction systematics).

Concerning the study of dIrrs, given the above results, we are confident that the results obtained in Chapter 3 for a sample of 17 dIrrs are robust even if we did not take into account properly the HI disc thickness. We have confirmed quantitatively this result for three galaxies in the sample, the galaxies are representative of the different properties of the whole sample. The small differences that we found between the results obtained in this Chapter and the ones obtained in Chapter 3 are mainly due to the different techniques used to extract the rotation curve and the velocity dispersion from the datacube rather than in the assumptions made for the HI vertical profile.

Since our work focuses on dIrrs, we have not tested our method with larger spirals, however we expect that the deep potential of these objects produces HI discs that are both absolutely and relatively (with respect to the radial dimensions) thinner than the HI discs in dIrrs. As an example, in Fig. 4.15 we compare the radial trends of the HI thickness obtained for three dIrrs in Sec. 4.3 with the ones estimated for three spiral galaxies with different Hubble types: NGC 2403 (Sc), NGC 7331(Sb), NGC 2841 (Sa), the dynamical models used for the spirals are from Bacchini et al. (in prep.). In conclusion, the biases introduced by the HI thickness in the study of the kinematics and dynamics in spirals should be totally negligible.

In conclusion, we have demonstrated that the assumption of razor-thin disc usually used in the study of HI discs, even if conceptually wrong, is a reasonable simplification that does not introduce significant errors in the study of kinematics and dynamics also in the case of dIrrs. Notice, however, that we have also found that a thick HI disc has a non-negligible effect on the analysis of the intrinsic distribution

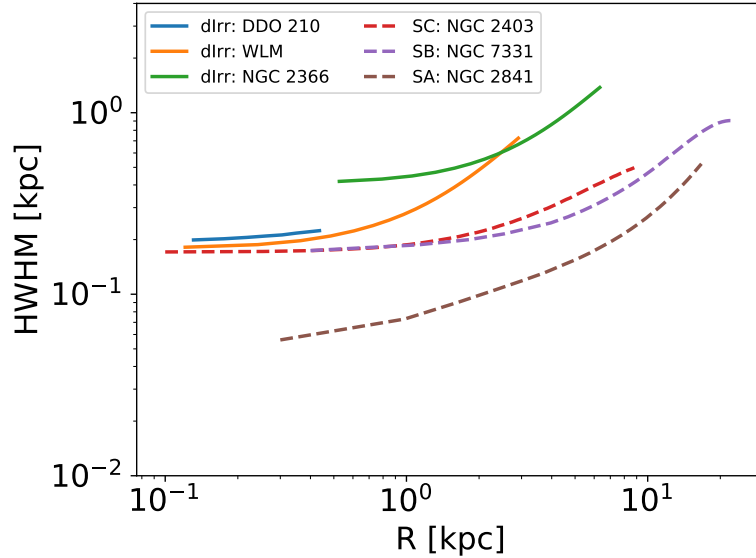


**Figure 4.15:** Radial profiles of the HI disc thickness (measured as the HWHM of the gas vertical distribution) for three dIrrs (DDO 210, WLM, NGC 2366) and three spirals of different Hubble types (NGC 2403, Sc; NGC 7331, Sb; NGC 2841, Sa). The profiles of the spirals have been obtained estimating the scale height with the method described in Sec. 4.2.2 adopting the dynamical models by Bacchini et al. (in prep.). The profiles of the dIrrs have been obtained in Sec. 4.3.2

of HI in galaxies. The combination of the wrong estimate of the surface density and arbitrary assumptions on the vertical profile makes the estimate of the 3D density of the HI in discs very uncertain and prone to biases. As a consequence studies that use these quantities (e.g. gas density-star formation relations) should carefully analyse the impact of such errors on their results. In this context, the original method that we present in this Chapter represents a very useful tool to obtain a robust and dynamically self-consistent estimate of the gas distribution in discs.

## Scaling relations of dwarf irregulars<sup>†</sup>

Scaling relations involving the kinematic properties of galaxies are very useful to investigate the elusive properties of the dark matter (DM) and its possible origin. It is well known that the visible matter is not enough to explain the global dynamics of disc galaxies (e.g. Bosma 1978, Rubin, Ford & Thonnard 1980). As a consequence, one could naively expect that the large-scale kinematics of these galaxies is fully dominated by their DM halos with no relation to baryons. Instead, there is clear evidence of strong connection between global kinematical properties of disc galaxies and their baryonic content (e.g. Sancisi 2004; Swaters et al. 2012, 2014). For example, the well known Tully-Fisher relation (Tully & Fisher, 1977; Combes, 2009) links the intrinsic luminosity of a spiral galaxy and its rotation velocity or emission line width that are tracers of the dynamical mass. A modern version of the Tully-Fisher relation is the so called baryonic Tully-Fisher relation in which the luminosity is replaced by the total baryonic mass of the galaxies (stars+gas) and the emission line width by the rotation speed in the flat part of the rotation curves. McGaugh et al. (2000) found that the relation between these two properties is very tight and extends over 6 orders of magnitude in baryonic mass. In Read et al. (2017), we fitted DM halo models to the rotation curves obtained in Chapter 3 finding a monotonic stellar mass-halo mass relation with little scatter.

Recently, McGaugh, Lelli & Schombert (2016) and Lelli et al. (2017) compared the observed “local” radial accelerations based on the visible rotation curves ( $g_{\text{obs}}(R) = V^2(R) R^{-1}$ ) and the acceleration expected from the baryonic matter ( $g_{\text{bar}}(R)$ ) for a large sample of discs and elliptical galaxies, finding that these two quantities are tightly correlated (this correlation is known as radial acceleration relation, RAR). In the region of high acceleration (inner parts of large galaxies) the potential is dominated by the baryonic matter and  $g_{\text{obs}} \simeq g_{\text{bar}}$  (see e.g. Sancisi 2004),

---

<sup>†</sup>This research made use of the LITTLE THINGS (Hunter et al., 2012) and the SPARC (Lelli, McGaugh & Schombert, 2016a) data sample.

while for  $g_{\text{bar}} \lesssim 10^{-13} \text{ km s}^{-2}$  the data deviate from the Newtonian linear relation following instead  $g_{\text{obs}} \propto \sqrt{g_{\text{bar}}}$ .

The above scaling relations are usually used to test and validate cosmological models. For example, in Read et al. (2017) we compared our stellar mass-halo mass relation with the results of the abundance matching analysis using the “field galaxy” stellar mass function from the Sloan Digital Sky Survey (Abazajian et al., 2009) and the halo mass function from  $\Lambda$ CDM simulations (Klypin, Trujillo-Gomez & Primack, 2011). We found that the distribution of our data is perfectly compatible with the theoretical expected relation. However, the local coupling as implied by the RAR could pose some challenges for  $\Lambda$ CDM and it could be at the basis of other  $\Lambda$ CDM tensions, such as the unexpected diversity of the rotation curves in dwarf galaxies (Oman et al. 2015, see also our work in Read et al. 2016). Keller & Wadsley (2017) and Navarro et al. (2017) found that the RAR is a natural product of the galaxy formation in a  $\Lambda$ CDM N-body simulations, none the less the physical motivation behind the existence of such relation is matter of debate and the RAR is often used to test alternative gravitational theories (see e.g. Lelli, McGaugh & Schombert 2017) or alternative DM models (see e.g. Cai, Liu & Wang 2017). In this context, dwarf galaxies are of great interest given that their baryonic content is essentially negligible in the total mass budget. Therefore, it is very important to assess whether the Baryonic Tully-Fisher relation and the RAR are still in place at this very small scales and if they have the same properties found using samples of more massive galaxies.

A study by Tamburro et al. (2009) revealed that in star-forming disc galaxies, the kinetic energy of the turbulent motions correlates with the star formation rate density. Based on this finding Tamburro et al. (2009) argued that the source of energy sustaining the ISM turbulence can be provided by the SN explosions in region with high star-formation rate density. However, there is evidence that the star formation cannot account for all the required energy, especially in the outer part of the discs where the star formation rate is low (e.g. Dib, Bell & Burkert 2006). Other proposed mechanisms are the rotational shear (e.g. Wada, Meurer & Norman 2002; Schaye 2004), the kinematic and dynamic influence of spiral arms (e.g. Elmegreen, Elmegreen & Leitner 2003; Elmegreen et al. 2003), gravitational instability due to gas accretion (e.g. Krumholz & Burkhardt 2016) and the thermal and magnetic instabilities (e.g. Sellwood & Balbus 1999; Piontek & Ostriker 2005; Hennebelle & Audit 2007; Hennebelle, Audit & Miville-Deschênes 2007). In this context, the dIrr galaxies are of great interest, because they are characterized by lack of spiral arms, low rotational velocities and shallow gravitational potentials. All these features suggest that in dIrrs the star formation activity is the main source of energy feeding the turbulence.

In this Chapter, we make use of circular velocity, velocity dispersion and the HI

density profiles obtained in [Chapter 3](#) for a sample of 17 dIrrs (see [Sec. 3.1](#), see also [Tab. 3.2](#) and [Tab. 3.8](#)) taken from the LITTLE THINGS survey ([Hunter et al., 2012](#)) to investigate scaling relations and their possible implications. In [Sec. 5.1](#), we use the HI circular velocities to build a low-mass baryonic Tully-Fisher, in [Sec. 5.2](#) we test the radial acceleration relation using the circular velocities and the HI surface density profiles. Finally, in [Sec. 5.3](#) we analyse the correlation between the turbulence in the HI and the star formation rate density. A summary is given in [Sec. 5.4](#).

## 5.1 Test of the baryonic Tully-Fisher relation

The baryonic Tully-Fisher relation (BTFR) links a characteristic circular velocity ( $V$ ) of a galaxy with its total baryonic mass ( $M_{\text{bar}}$ ). The relation, which can be written as

$$\log\left(\frac{M_{\text{bar}}}{M_{\odot}}\right) = s \log\left(\frac{V}{\text{km s}^{-1}}\right) + A, \quad (5.1)$$

is very tight and extends over 6 orders of magnitude in  $M_{\text{bar}}$  ([McGaugh, 2012](#); [Lelli, McGaugh & Schombert, 2016c](#)). The existence of this relation represents a fundamental benchmark for cosmological models and for galaxy formation theories ([Brook, Santos-Santos & Stinson, 2016](#); [Di Cintio & Lelli, 2016](#); [McGaugh et al., 2000](#)). In this context it is very important to extend the study of the BTFR down to extremely low-mass dwarf galaxies (e.g. [Begum et al. 2008a](#)).

In this section we present the BTFR for the galaxies analysed in [Chapter 3](#) ([Fig. 5.1](#)) and then we compare it with the results of [Lelli, McGaugh & Schombert \(2016c\)](#) ([Fig. 5.2](#)). The derivation of the baryonic mass and of the characteristic velocity is described in the following Section.

### 5.1.1 Estimate of the characteristic velocity and baryonic mass

#### Rotation velocity

The rotation velocities used in the Tully-Fisher relation (TFR) are  $W_{20}$  and  $V_{\text{flat}}$ :  $W_{20}$  is the velocity width of the global HI line profiles, while  $V_{\text{flat}}$  is the value of the flat portion of the rotation curve. [Verheijen \(2001\)](#) found that  $V_{\text{flat}}$  minimises the scatter in the TFR, so it is the best way to study the BTFR using high resolution HI data (see also [Brook, Santos-Santos & Stinson 2016](#)). However, several rotation curves of dIrrs do not reach the flat part (e.g. DDO 53, [Fig. 3.14](#)) or the flattening is entirely due to the asymmetric-drift correction (e.g. NGC 1569, [Fig. 3.23](#)). As indicator of the rotation velocity, we therefore used the velocity of the outer disc ( $V_o$ ) estimated in [Chapter 3](#) as the mean circular velocity of the last three fitted rings (see [Sec. 3.4](#)).  $V_o$  is a measure of  $V_{\text{flat}}$  for galaxies in which the flat part of the rotation curve is observed. For galaxies with a rising rotation curve  $V_o$  is an

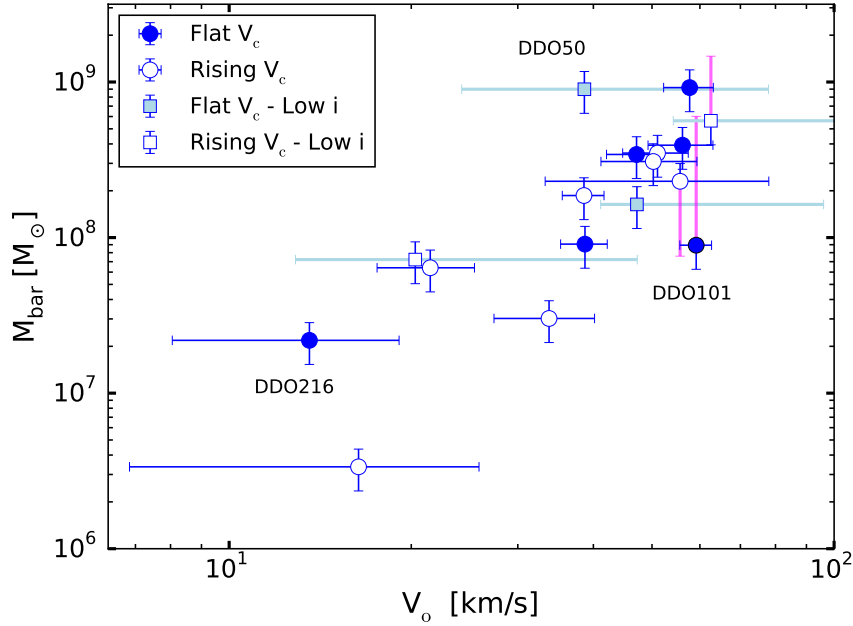


**Figure 5.1:** BTFR for the galaxies analysed in [Chapter 3](#) (see [Sec. 3.1](#)). The empty and the solid symbols indicate galaxies with rising or flat rotation curve, respectively. The squares indicate nearly face-on galaxies. The blue bars indicate  $1\sigma$  errors. The light-blue and the magenta bars indicate intervals of allowed values (see text).

estimate of the maximum circular velocity within the analysed radial range. The values of  $V_o$  and the related uncertainties for the galaxies in our sample are reported in [Tab. 3.8](#). Galaxies with rising rotation curves are indicated with empty markers in [Fig. 5.1](#) and [Fig. 5.2](#). For the five galaxies with low inclinations  $i$  (squares in [Fig. 5.1](#) and [Fig. 5.2](#)) the uncertainties on  $i$  and on the velocities can be largely underestimated, so we present these galaxies with a bar that indicates the interval between a minimum (assuming  $i = 40^\circ$ ) and a maximum (assuming  $i = 20^\circ$ ) value of  $V_o$  (see [Eq. 1.6](#)).

## Baryonic mass

The total baryonic mass of the galaxies has been calculated as

$$M_{\text{bar}} = M_* + 1.33M_{\text{HI}}, \quad (5.2)$$

where  $M_*$  is the stellar mass,  $M_{\text{HI}}$  is the mass of the atomic hydrogen and the factor 1.33 takes into account the the presence of Helium ([Begum et al., 2008a](#); [Lelli, McGaugh & Schombert, 2016c](#)). The molecular gas is likely irrelevant in the mass budget of dwarf galaxies ([Taylor, Kobulnicky & Skillman, 1998](#)). The mass of atomic gas is measured from the HI datacubes ([Sec. 3.3.1](#) and [Tab. 3.2](#)), while the stellar

masses are from Walter & Brinks (2001) for DDO 47 and from Zhang et al. (2012) for all the other galaxies. The estimate of the mass is proportional to the square of the galactic distance, therefore errors on the distance add further uncertainties on the final estimate of the baryonic mass. Unfortunately, the works from which we have taken the stellar masses (Walter & Brinks, 2001; Zhang et al., 2012) and the distances (Hunter et al., 2012) do not report the errors on their measures, so we assumed a conservative error of the 30% for  $M_{\text{bar}}$  motivated by the stellar population synthesis models (McGaugh & Schombert, 2014; Meidt et al., 2014; Schombert & McGaugh, 2014). We also performed a deeper analysis for the distance uncertainties. The relative difference between the masses estimated assuming two different distances is

$$\delta_D = \frac{M(D_1) - M(D_2)}{M(D_1)} = \frac{D_1^2 - D_2^2}{D_1^2}. \quad (5.3)$$

For each galaxy in our sample we choose the best distance estimator<sup>1</sup> available on NED (NASA/IPAC Extragalactic Database) and we considered the minimum ( $D_{\text{NED}}^{\text{min}}$ ) and the maximum ( $D_{\text{NED}}^{\text{max}}$ ) estimate of the distance. DDO 101 has only two distance estimates in NED: 5.9 Mpc from Tully (1988) and 16.6 Mpc from Karachentsev, Makarov & Kaisina (2013). Hence, we use these two values as  $D_{\text{NED}}^{\text{min}}$  and  $D_{\text{NED}}^{\text{max}}$ . Notice that Karachentsev, Makarov & Kaisina (2013) used the TFR to estimate the distance, thus  $D_{\text{NED}}^{\text{max}}$  is very uncertain and it is not surprising that using this distance the galaxy “moves” exactly on the BTFR (see Fig. 5.1 and Fig. 5.2). Using Eq. 5.3 we calculate

$$\delta_D^{\text{min/max}} = 1 - \left( \frac{\min [D, D_{\text{NED}}^{\text{min/max}}]}{\max [D, D_{\text{NED}}^{\text{min/max}}]} \right)^2, \quad (5.4)$$

where  $D$  is the distance assumed in this work (see Tab. 3.2). When  $\delta_D$  is large the error on the total mass is dominated by the uncertainty on the distance. Three galaxies have  $\delta_D$  larger than 60%: DDO 47 ( $\delta_D^{\text{max}} = 62\%$ ), DDO 101 ( $\delta_D^{\text{max}} = 85\%$ ) and NGC 1569 ( $\delta_D^{\text{min}} = 68\%$ ). For these galaxies we do not show the  $1\sigma$  error on the baryonic mass, but a magenta bar indicating the interval of mass found assuming the distance  $D$  or the distance  $D_{\text{ned}}^{\text{min/max}}$ .

### 5.1.2 Results

In Fig. 5.1 we show the distribution of the data for the dIrrs of our sample in the  $M_{\text{bar}} - V$  plane, while in Fig. 5.2 we compare our data with a recent fit to the BTFR (Lelli, McGaugh & Schombert, 2016c) using the galaxies in the SPARC sample (Lelli,

<sup>1</sup>The scale of distance estimators is, from the best to the worst: Cepheids, RGB-Tip, CMD, Brightest-Stars.

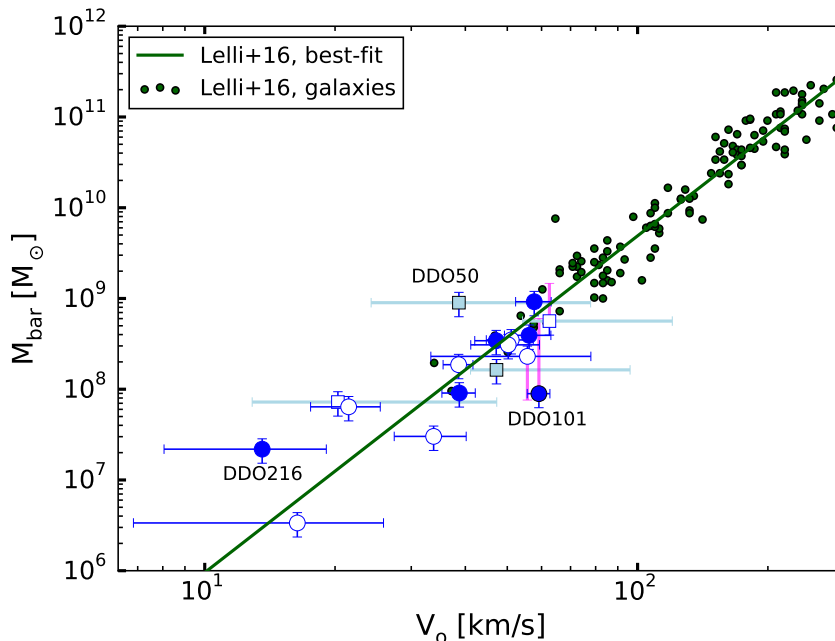


**Figure 5.2:** Same data as in Fig. 5.1 compared with the galaxies and the BTFR from Lelli, McGaugh & Schombert (2016c).

McGaugh & Schombert, 2016a). Interestingly the two datasets overlap between  $10^8 M_{\odot}$  and  $10^9 M_{\odot}$ . In this range our data are perfectly compatible with the parameters of the BTFR estimated in Lelli, McGaugh & Schombert (2016c) ( $s = 3.95$  and  $A = 1.86$  in Eq. 5.1); moreover, we have fitted our data with a linear relation leaving the intrinsic scatter ( $f$ ) as the only free parameter (the other parameters have been fixed to the values found by Lelli, McGaugh & Schombert 2016c). The best-fitting result is  $f = 0.1 \pm 0.1$ , so we also confirm the very small scatter around the relation in contrast to Begum et al. (2008a). This remains the case, even when including galaxies with rising rotation curves: the only two outliers are DDO 50 (a nearly face-on galaxy) and DDO 101 (for which the uncertainty on the distance is large; Sec. 3.4.1, see also Read et al. 2016). Below  $10^8 M_{\odot}$  the distribution of the galaxies looks again compatible with the relation of Lelli, McGaugh & Schombert (2016c). It appears more scattered, but this could owe entirely to the large error bars for these low-mass systems (that results from the increasingly important asymmetric-drift correction). Furthermore, there are only a few galaxies in this mass range and all of them have rising rotation curves (with the exception of DDO 216 that has rather peculiar kinematics; see Fig. 3.22, Sec. 3.4.1 and Appendix 3.B). In order to further investigate the positions of these galaxies, we exploited the rotation curve predicted by the best-fit Core-NFW DM profiles (Read, Agertz & Collins, 2016) obtained in Read et al. (2017). Using these theoretical rotation curves, we estimated the expected maximum velocity ( $V_{\max}$ ) for the five galaxies with  $M_{\text{bar}} < 10^8 M_{\odot}$

(CVnIdwA, DDO 53, DDO 210, DDO 216 and UGC 8508, see Figs in the Appendix 3.A.1). In case of dIrrs,  $V_{\max}$  is very similar to the velocity of the flat part of the rotation curve (Read et al., 2017). The obtained  $V_{\max}$  are all compatible, within the errors, with the  $V_o$  estimated in Sec. 3.4 (see Tab. 3.8). If we use the values of  $V_{\max}$ , the galaxy with the lowest baryonic mass (DDO 210) maintains the same position shown in Fig. 5.2, the three galaxies (DDO 53, DDO 216 and CVnIdwA) located to the left with respect to the best-fit green line move to the right by about 0.10/0.15 dex; finally, the last galaxy (UGC 8508) moves slightly to the right by about 0.07 dex. In conclusion, using  $V_{\max}$  for the galaxies with  $M_{\text{bar}} < 10^8 M_{\odot}$ , the main results of our analysis are still valid, moreover in this case the scatter at the low-mass end of the relation turns out to be even lower.

The presence of a small scatter is compatible with recent results from  $\Lambda$ CDM simulations (e.g. Brook, Santos-Santos & Stinson 2016; Sales et al. 2017), however these works also predict that the BTF should become increasingly steep at the low-mass end starting from  $M_{\text{bar}} \sim 10^8 M_{\odot}$ . This result is not supported by our data and by other similar works (e.g. Begum et al. 2008a; Adams et al. 2014; Papastergis et al. 2015). It is still debated whether this low-mass tension owes to some failure of the hydrodynamical simulations to catch properly the baryonic physics or to observational biases. A common argument supporting the latter hypothesis is that the observed rotation curves of low-mass dIrrs do not reach the flat part, as a consequence the final velocities used to build the BTF are systematically lower. In our view, it is quite unlikely that the systematic errors “conspire” to move the galaxies exactly on the relation found for more massive galaxies. Moreover, fitting the observed rotation curves with physical models (Cored NFW profile, see above), we found that the values of the flat part of the rotation curves are not significantly different with respect to the velocities estimated in the outer part of the discs (Read et al. 2017, see also Oman et al. 2016 for similar conclusions).

## 5.2 Test of the radial acceleration relation

The radial acceleration relation (RAR) is a relation found by McGaugh, Lelli & Schombert (2016) and Lelli et al. (2017) between the observed “local” radial accelerations based on the observed rotation curves ( $g_{\text{obs}}(R) = V^2(R) R^{-1}$ ) and the accelerations expected from the distribution of the baryonic matter ( $g_{\text{bar}}$ ). In order to simplify the notation, in the following Equations  $\log g_{\text{obs}}$  and  $\log g_{\text{bar}}$  are equivalent to  $\log \frac{g_{\text{obs}}}{\text{km s}^{-2}}$  and  $\log \frac{g_{\text{bar}}}{\text{km s}^{-2}}$ , respectively.

Concerning the RAR, dwarf galaxies are of great interest: their baryonic content is essentially negligible in the total mass budget and they probe the lowest acceleration regime ( $g_{\text{bar}} < 10^{-14} \text{ km s}^{-2}$ ). Lelli et al. (2017) found that dSphs are

compatible with the RAR in the range  $-15 \lesssim \log g_{\text{bar}} \lesssim -14$  while at very low acceleration the data seem to indicate a flattening of the RAR around  $\log g_{\text{obs}} \sim -14$ . Given that dSphs do not have rotating discs, their  $g_{\text{obs}}$  cannot be estimated at every radius and each galaxy adds only one point in the  $\log g_{\text{bar}} - \log g_{\text{obs}}$  plane. Moreover, all the known dSphs are satellites of more massive galaxies, hence their measure of  $g_{\text{obs}}$  can be biased by the influence of tidal fields as it is not guaranteed that they are in equilibrium (e.g. Roderick et al. 2016, 2015; Palma et al. 2003, see also Battaglia, Sollima & Nipoti 2015). Hence, the properties of the RAR estimated using such galaxies are uncertain: in particular, the low-acceleration end of the RAR is mainly due to a sample of recently discovered ultra-faint dSphs (e.g. Koposov et al. 2015; Willman et al. 2005) for which the estimates are even more uncertain. In this context, dIrrs can come to our rescue: they probe almost the same low acceleration regime as the dSphs, but their rotating HI discs allow us to populate the RAR plane in the same way as it has been done for larger galaxies. In this Section, we will use the circular velocities obtained in Chapter 3 for 17 dIrrs to test the low acceleration regime of the RAR and compare our results with the findings of Lelli et al. (2017).

### 5.2.1 Estimate of the observed and baryonic acceleration

The observed and baryonic accelerations have been estimated as follows.

#### Observed acceleration

Following Lelli et al. (2017) we define

$$g_{\text{obs}} = \frac{V_c^2(R)}{R}. \quad (5.5)$$

$g_{\text{obs}}$  traces the gravitational potential at every radius, so it is important to use the circular velocities  $V_c$  corrected for the asymmetric-drift (Eq. 3.6, see Sec. 3.3.3) instead of the observed rotational velocities  $V_{\text{rot}}$ , especially for the less massive galaxies (e.g. DDO 210, see Fig. 3.21 and Tab. 3.38). The error on  $g_{\text{obs}}$  ( $\delta_{g_{\text{obs}}}$ ) depends on the uncertainties,  $\delta_{V_c}$ , on  $V_c$  (Eq. 3.11, see Sec. 3.3.3) and on the uncertainties  $\delta_D$  on the distance estimate that it is needed to transform  $R$  from the angular scale to the physical one. The final value of the circular velocity depends also on the assumed value of the disc inclination (Eq. 1.6), hence the uncertainty on  $i$  must be added to the total error budget. In conclusion, using the error propagation theory, we obtain (Lelli et al., 2017):

$$\delta_{g_{\text{obs}}} = g_{\text{obs}} \sqrt{\left(\frac{2\delta_{V_c}}{V_c}\right)^2 + \left(\frac{2\delta_i}{\tan i}\right)^2 + \left(\frac{\delta_D}{D}\right)^2}. \quad (5.6)$$

The values and the errors of the circular velocity are reported for each radius and for each galaxy in the Tables 3.27-3.43 in the Atlas in Chapter 3 (Appendix 3.A.2), the used value for  $i$  and  $\delta_i$  can be found in Col. 10 of Tab. 3.8. Concerning the distances, we used the values reported in Col. 1 of Tab. 3.2 while the related errors have been estimated using the standard deviation of various flux measurements reported in NED.

### Baryonic acceleration

The radial acceleration due to the observed distribution of matter can be written as

$$g_{\text{bar}} = \frac{V_{\text{gas}}^2(R) + V_*^2(R)}{R}, \quad (5.7)$$

where  $V_{\text{gas}}$  and  $V_*$  are the rotation speeds expected considering the distribution of matter in the gaseous and stellar disc, respectively. Given that both the numerator and the denominator of Eq. 5.7 depend linearly on the distance  $D$ ,  $g_{\text{bar}}$  is distance independent. Therefore, to estimate the error on  $g_{\text{bar}}$  we ignore the contribution of the distance uncertainties in the estimates of the errors on  $V_{\text{gas}}$  and  $V_*$  (Eq. 5.10).

$V_*$  is taken from Oh et al. (2015) multiplying their estimates by the factor  $f = \cos i (\cos i_{\text{O15}})^{-1}$  that takes into account the possible mismatch between our best-fit inclinations,  $i$  (see Tab. 3.8), and ones assumed in Oh et al. (2015) ( $i_{\text{O15}}$ ). The estimate of the stellar rotation curve depends on the assumed inclination angle and on the assumed stellar mass-to-light ratio  $\Upsilon$ . These quantities are needed to obtain, from the observed surface brightness profile of the stellar disc, the intrinsic surface density profile,  $\Sigma_*$ , and  $V_* \propto \sqrt{\Sigma_*} \propto \sqrt{\cos i} \Upsilon$ . Propagating the errors, we get

$$\delta_{V_*} = \frac{V_*}{2} \sqrt{\left(\frac{\delta\Upsilon}{\Upsilon}\right)^2 + (\tan i \delta_i)^2}, \quad (5.8)$$

where, motivated by stellar population synthesis models (e.g. Meidt et al. 2014), we set  $\delta\Upsilon \Upsilon^{-1} = 0.30$  for all the galaxies in our sample. The assumed value of  $\Upsilon$  for each galaxy in our sample can be found in Oh et al. (2015).

The rotation curve due to the gaseous component is calculated as  $V_{\text{gas}} = \sqrt{1.33} V_{\text{HI}}$ , where 1.33 takes into account the presence of helium (see Sec. 5.1.1) and  $V_{\text{HI}}$  and the related errors  $\delta_{V_{\text{HI}}}$  are estimated as explained in Appendix 5.A. The final value of circular velocity also depends on the assumed inclination angle of the HI disc ( $V_{\text{gas}} \propto \sqrt{\cos i}$ ), therefore, propagating the uncertainties the final error is

$$\delta_{V_{\text{gas}}} = V_{\text{gas}} \sqrt{\left(\frac{\delta_{V_{\text{HI}}}}{V_{\text{HI}}}\right)^2 + \left(\frac{\tan i \delta_i}{2}\right)^2}. \quad (5.9)$$

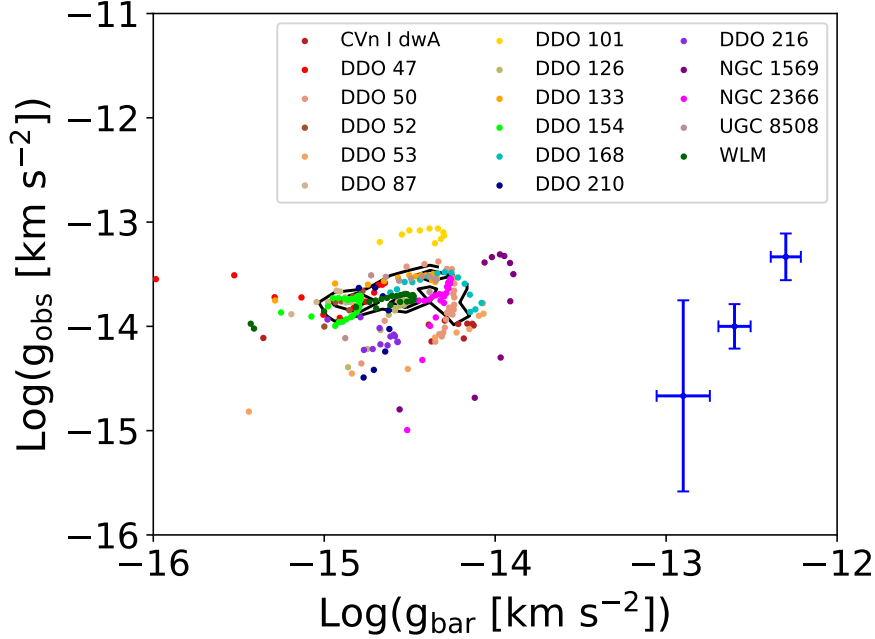


**Figure 5.3:** Distribution of the data for the dIrrs of our sample in the RAR plane ( $\log g_{\text{obs}} - \log g_{\text{bar}}$ ): each colour indicates a different galaxy as shown in the legend (see Sec. 3.4 for a detailed descriptions of each galaxy). The error bars on the right indicate the median  $\delta_{\log g_{\text{obs}}}$  and  $\delta_{\log g_{\text{bar}}}$  calculated in bins of  $\log g_{\text{obs}}$ : from the bottom to the top  $-15.0 < \log g_{\text{obs}} < -14.3$ ,  $-14.3 < \log g_{\text{obs}} < -13.7$  and  $-13.7 < \log g_{\text{obs}} < -13.0$ . The black contours indicate regions with 5, 10 and 15 counts for a 2D binned map built in the range  $\log g_{\text{obs}} = [-16, -13]$  and  $\log g_{\text{bar}} = [-16, -13]$  using 15x15 bins.

Applying the error propagations to Eq. 5.7 the final error on  $g_{\text{bar}}$  is

$$\delta_{g_{\text{bar}}} = 2g_{\text{bar}} \frac{\sqrt{V_{\text{gas}}^2 \delta_{V_{\text{gas}}}^2 + V_*^2 \delta_{V_*}^2}}{(V_{\text{gas}}^2 + V_*^2)}, \quad (5.10)$$

where  $\delta_{V_*}$  and  $\delta_{V_{\text{gas}}}$  are given by Eq. 5.8 and Eq. 5.9, respectively. Finally the errors on the related logarithmic quantities  $\log g_{\text{obs}}$  and  $\log g_{\text{bar}}$  (see Fig. 5.3) are  $\delta_{\log g_{\text{obs}}} = \delta_{g_{\text{obs}}} (g_{\text{obs}} \ln 10)^{-1}$  and  $\delta_{\log g_{\text{bar}}} = \delta_{g_{\text{bar}}} (g_{\text{bar}} \ln 10)^{-1}$ .

Fig. 5.10 in Appendix 5.A shows the  $V_{\text{HI}}$  and the  $V_*$  estimates for the dIrrs in our sample.

## 5.2.2 Results and discussions

In Fig. 5.3 we show the  $g_{\text{obs}} - g_{\text{bar}}$  estimates for the dIrrs in our sample, we exclude 2 points from DDO 101 and one point from WLM because they have negative values of  $V_{\text{gas}}$  (see Appendix 5.A for details). Most of the points are located around  $\log g_{\text{obs}} \sim -13.8$  as shown by the black contours. There are some outliers, especially

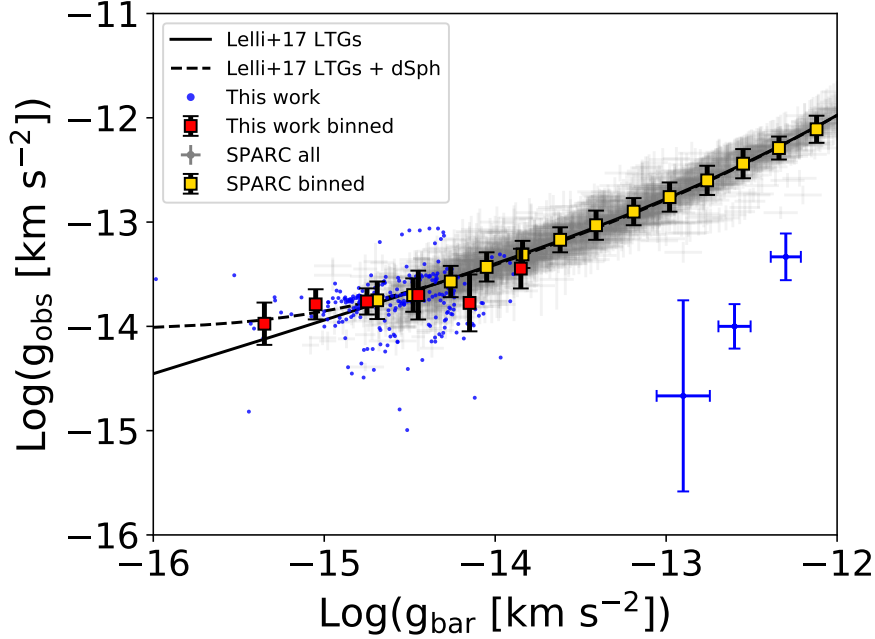


**Figure 5.4:** Same as Fig. 5.3, but with additional points (gray markers) taken from the SPARC data sample (Lelli, McGaugh & Schombert, 2016a) and the best-fit RAR obtained in Lelli et al. (2017) for the SPARC data (Eq. 5.11, solid line) and for the SPARC+dSphs data (Eq. 5.12, dashed line). The yellow squares and the red squares show the binned profile of the SPARC data (from Lelli et al. 2017) and of our data, respectively. Concerning our data, the estimated values and the errors of the binned profile have been obtained calculating the median and the MAD (see text) of the different  $g_{\text{obs}}$  estimates.

at lower  $g_{\text{obs}}$ , but most of them come from two galaxies: DDO 101 ( $\log g_{\text{obs}} \sim -13$ ) and DDO 216 ( $\log g_{\text{obs}} \lesssim -14.3$ ), both of which are peculiar galaxies. DDO 101 is an outlier in all the relations analysed in this Chapter (see Sec. 5.1.2 and Sec. 5.3.3): it has a very uncertain estimate of the distance (see Sec. 5.1) that afflicts  $g_{\text{obs}}$  and it is also the only galaxy in our sample for which  $g_{\text{bar}}$  is dominated by the stellar component (see Fig. 5.9), hence the error  $\delta g_{\text{bar}}$  is dominated by the large uncertainties in the mass-to-light ratio  $\Upsilon$ . Concerning DDO 216, the estimate of  $g_{\text{obs}}$  is highly uncertain due to a combination of effects: it has peculiar kinematics as discussed in Appendix 3.B and the error in distance is about 50% of the estimated distance. However, even the most distant outliers can be considered compatible with the position of the bulk of the other points within the errors. The overall distribution can be considered flat in  $g_{\text{obs}}$ , although the black contours show a shallow increase of  $g_{\text{obs}}$  as a function of  $g_{\text{bar}}$ .

In Fig. 5.4, we show the binned profile obtained calculating the median and the MAD (median absolute deviation, see Sec. 3.3.3 and Appendix 5.A for further details) of the points shown in Fig. 5.3. The obtained profile is compared with the

points and the best-fitting relations found in Lelli et al. (2017):

$$g_{\text{obs}} = g_{\text{bar}} \left( 1 + \exp \left[ -\sqrt{\frac{g_{\text{bar}}}{g_{\dagger}}} \right] \right)^{-1} \quad (5.11)$$

with  $g_{\dagger} = 1.2 \times 10^{-13} \text{ km s}^{-2}$ , considering the late-type galaxies (LTGs) in the SPARC data sample (Lelli, McGaugh & Schombert, 2016a), and

$$g_{\text{obs}} = g_{\text{bar}} \left( 1 + \exp \left[ -\sqrt{\frac{g_{\text{bar}}}{g_{\dagger}}} \right] \right)^{-1} + \hat{g} \exp \left[ -\sqrt{g_{\text{bar}} \frac{g_{\dagger}}{\hat{g}^2}} \right] \quad (5.12)$$

with  $g_{\dagger} = 1.1 \times 10^{-13} \text{ km s}^{-2}$  and  $\hat{g} = 9.2 \times 10^{-13} \text{ km s}^{-2}$ , adding also a sample of dSphs (see Lelli et al. 2017 for details).

Interestingly most of our points are around  $\log g_{\text{bar}} \sim -14.8$  where the statistic of the SPARC sample starts to be less significant. Consistently with the distribution of points shown in Fig. 5.3, our binned profile shows a flat distribution  $g_{\text{obs}} = \text{const}$  independent of  $g_{\text{bar}}$ ; however, within the errors, the profile is totally compatible with the binned profile and the best-fit relation obtained in Lelli et al. (2017) using the complete SPARC sample.

In the very low acceleration regime ( $\log g_{\text{bar}} \lesssim -15$ ), we do not have large statistics, but our data seems to deviate from the RAR (solid line) and approaches the acceleration floor at  $\log g_{\text{obs}} \sim -14$  as traced by dSphs in Lelli et al. (2017) (dashed line). As already discussed, we can further speculate that our data are compatible with a constant  $g_{\text{obs}}$  independently of the value of the  $g_{\text{bar}}$ , hence the presence of a “common” constant  $g_{\text{obs}}$  acceleration, can be a general property of dwarf galaxies, both dSphs and dIrrs. Following this idea, we fit our data with

$$g_{\text{obs}} = g_{\text{dyn}}, \quad (5.13)$$

where we use the term  $g_{\text{dyn}}$  to define the “common” observed acceleration. We find that the best-fit value is  $\log g_{\text{dyn}} = -13.75$  ( $g_{\text{dyn}} \simeq 1.8 \times 10^{-14} \text{ km s}^{-2}$ ). In order to compare how the three functional forms discussed above (RAR, Eq. 5.11; RAR + acceleration floor Eq. 5.12; and constant, Eq. 5.13) adapt to our data we calculate the  $\chi_{\nu}^2$  statistics as

$$\chi_{\nu}^2 = \nu^{-1} \sum_i^N \frac{[y_i - f(x_i)]^2}{\delta_{y_i}^2 + \delta_{x_i}^2 \left[ \frac{\partial f}{\partial x}(x_i) \right]^2} \quad (5.14)$$

where  $x = g_{\text{bar}}$ ,  $y = g_{\text{obs}}$  and  $f$  represent the theoretical function to test (Equations 5.11-5.13); the  $\nu$  term indicates the degrees of freedom and it is defined as the difference between the number of data  $N$  and the number of fitted parameters. We take into account the error on  $g_{\text{bar}}$  considering that locally  $f$  can be approximated with a linear relation with the slope equal to the partial derivative of  $f$  with respect

to  $g_{\text{bar}}$ . Notice that using Eq. 5.13, we are considering an actual fit to our data, while the parameters of Eq. 5.11 and Eq. 5.12 have been obtained by Lelli et al. (2017) fitting the whole SPARC data sample (including a sample of dSphs) over  $\sim 4$  (6 considering the dSphs) dex in  $g_{\text{bar}}$  as opposed to the  $\sim 2$  dex sampled with our data. Therefore, independently from the number of parameters, the degrees of freedom of Eq. 5.11 and Eq. 5.12 are equal to the total number of points ( $\nu = 248$ ). Our best-fit relation (Eq. 5.13) has been obtained fitting one parameter ( $g_{\text{dyn}}$ ), hence  $\nu = 247$ . The  $\chi^2_\nu$  obtained for the best-fit function to the SPARC data (Eq. 5.11) is 0.94, considering the best-fit function with the acceleration floor obtained for the SPARC+dSphs (Eq. 5.12) we find  $\chi^2 = 0.88$ , finally considering our best-fit constant acceleration,  $g_{\text{dyn}}$  (Eq. 5.13), we obtain  $\chi^2 = 0.72$ . We tested if these differences are significant exploiting the fact that the ratio between two reduced chi squares with degrees of freedom  $\nu_1, \nu_2$  follows the F-distribution  $F(\nu_1, \nu_2)$ . We found that the use of a constant acceleration represents, at the significance level of 5%, a significant improvement in the description of the data; while, the  $\chi^2$  obtained for Eq. 5.12 (acceleration floor at low  $g_{\text{bar}}$ ) and Eq. 5.13 (constant acceleration) are compatible at the same level of significance (5%).

In conclusion, using the galaxies analysed in Chapter 3 we have found that dIrrs are compatible with the RAR found by McGaugh, Lelli & Schombert (2016) and Lelli et al. (2017), while a statistical analysis reveals that our galaxies favour models that takes into account the presence of a floor in  $g_{\text{obs}}$  as already found by Lelli et al. (2017) using a sample of dSph.

### 5.3 What is feeding the turbulence?

The HI medium in galaxies consist of two stable co-existing phases: the cold neutral medium (CNM) and the warm neutral medium (WNM) (see Sec. 1.3.1). The expected thermal broadening of the HI line emission is  $\sim 1 \text{ km s}^{-1}$  for the CNM and  $\sim 6 - 8 \text{ km s}^{-1}$  for the WNM. The HI emission from the disc of spirals and dIrrs shows a continuous range of line widths (i.e. velocity dispersion,  $\sigma_v$ ), that can reach values up to  $20 \text{ km s}^{-1}$  in the inner part of the discs and rarely goes below  $\sim 6 - 8 \text{ km s}^{-1}$  in the outer parts (see e.g. Dickey & Lockman 1990; Kamphuis 1993; Boomsma et al. 2008; Tamburro et al. 2009, see also Tables 3.27-3.43 in Appendix 3.A.2 for the dIrrs analysed in Chapter 3 ). The values of the velocity dispersion found in the outer parts of the HI discs can be explained if most of the gas is in the warm phase, but the very high values of  $\sigma_v$  reached in the rest of the disc require an additional source of “chaotic” motion along the line of sight. The general consensus is that broadening of HI lines beyond larger than  $\sim 8 \text{ km s}^{-1}$  can be attributed to stochastic fluctuations of velocity and pressure driven by the turbulence (Elmegreen & Scalo, 2004; Scalo & Elmegreen, 2004). The decay time scale of the

turbulence is quite small ( $\sim 10$  Myr, Mac Low 1999), therefore the turbulence needs to be sustained by a continuous supply of energy. As discussed at the beginning of the Chapter, several mechanisms have been proposed as sources of the turbulent energy, including rotational shear (e.g. Wada, Meurer & Norman 2002; Schaye 2004), gravitational (e.g. Krumholz & Burkhardt 2016) and/or magnetic instabilities (e.g. Piontek & Ostriker 2005). However, in the case of dIrrs the predominant source of energy could be the kinetic energy injected in the ISM by the Supernova (SN) explosions. SNe are due to young and massive stars, therefore the rate of energy injected by SNe in the ISM correlates with the star formation rate.

In this Section, we analyse possible correlations between proxies of the turbulence (velocity dispersion and kinetic energy) and the star formation rate densities for 16 dIrrs analysed in Chapter 3 (we exclude DDO 210 because it does not have an estimate of the SFR, see Sec. 5.3.1).

### 5.3.1 Star formation rate data

The integrated star formation rates for the galaxies in our sample have been taken from the work of Hunter & Elmegreen (2004). They estimated the current star formation activity for a large sample of dIrrs using the  $H\alpha$  luminosity. The relevant quantities we use in this analysis are:

- $R_{H\alpha}$  : the largest radius that contains  $H\alpha$  emission;
- $R_d$  : the stellar disc scale length in the  $V$ -band reported in Hunter & Elmegreen (2004);
- SFR: the star formation rate estimated from the integrated  $H\alpha$  flux within  $R_{H\alpha}$ ;
- SFRD: the SFR normalised to a characteristic disc surface, we consider two definitions of SFRD:  $SFRD^\alpha$  when the surface is the area containing the  $H\alpha$  emission ( $\pi R_{H\alpha}^2$ ) and  $SFRD^d$  when the surface is calculated within the stellar scale length ( $\pi R_d^2$ ).

The  $SFRD^\alpha$  is a proper estimate of the mean SFR over the whole area in which the SFR has been measured, however  $R_{H\alpha}$  is an “observational” scale that could depend on the observational methods and instrumental properties. For example for a number of galaxies in Hunter & Elmegreen (2004), including two objects in our sample (DDO 50 and NGC 1569), the  $H\alpha$  emission exceeds the size of the imaged region. Moreover if the SFR shows a significant radial gradient, as it is the case for most of the galaxies in our sample (see Fig. 1 in Zhang et al. 2012), most of the SF takes place in an area much smaller than the area inside  $R_{H\alpha}$ . The  $SFRD^d$  can represent a more meaningful physical estimate of the characteristic SFRD, thus

the radial scale length in the  $V$ -band is more indicative of the older rather than the current star formation activity. However, Zhang et al. (2012) found that  $R_d$  in the  $V$ -band ( $R_d^V$ ) is roughly comparable to/or larger than the scale lengths of the emission at shorter wavelengths corresponding to younger stellar populations. Therefore, using  $R_d^V$  we are confident that we are not excessively overestimating the SFRD and consequently the rate of energy injected in the ISM (see Sec. 5.3.4).

In the following analysis, we divide our galaxies in two samples: the complete sample (labelled as “All” in Fig. 5.5, Fig. 5.6 and Tab. 5.7), which contains all the galaxies (except DDO 210 that has no detected  $H\alpha$  emission in Hunter & Elmegreen 2004), and a subsample (labelled as “subsample”) obtained excluding NGC 1569 (see Fig. 3.23) that shows a very intense star formation activity ( $\text{SFRD}^d \sim 1.3 \text{ M}_\odot \text{yr}^{-1} \text{kpc}^{-2}$ ) compared to the other galaxies (mean  $\text{SFRD}^d \sim 0.006 \text{ M}_\odot \text{yr}^{-1} \text{kpc}^{-2}$ ), and DDO 101 (see Fig. 3.16) that is an outlier in all the analysed relations (see Sec. 5.3.2 and Sec. 5.3.3). In the following Sections, when the units are not explicitly reported, we are giving  $\sigma_v$  in  $\text{km s}^{-1}$ , SFRD in  $\text{M}_\odot \text{yr}^{-1} \text{pc}^{-2}$  and kinetic energy per units area ( $E_{\text{kin}}$ ) in  $10^{43} \text{ erg pc}^{-2}$ .

### 5.3.2 Velocity dispersion

Being the velocity dispersion a direct proxy for the turbulence, we would expect to find a correlation with the SFRD. We calculate the characteristic velocity dispersion,  $\langle \sigma_v \rangle$  as the median of the velocity dispersion estimates (see Appendix 3.A) out to  $R_{H\alpha}$ , while the errors have been obtained using the MAD as done in Sec. 3.3.3. Fig. 5.5 shows the position of the galaxies in our sample in the logarithmic  $\sigma_v$ - $\text{SFRD}^\alpha$  plane (left-hand panel) and in the logarithmic  $\sigma_v$ - $\text{SFRD}^d$  plane (right-hand panel).

In both panels a linear relation appears: the properties of this relation have been obtained by fitting a linear functional form, including also an intrinsic scatter, through an MCMC posterior sampling method. The results are summarised in Tab. 5.7. Using the complete sample the best-fit slope is  $\sim 0.14$  considering the  $\text{SFRD}^d$  and  $\sim 0.16$  considering the  $\text{SFRD}^\alpha$ : the relation is shallow, but the posterior distributions of the slopes (shown by the red histogram in the small sub-panels in Fig. 5.5) are not compatible with 0, so a flat distribution is statistically excluded (as shown also by the grey bands). The only clear outlier in the relations is DDO 101, shown in Fig. 5.5 as the yellow circle at  $\log \text{SFRD}^\alpha \sim \log \text{SFRD}^d \sim -9$ . However given the large uncertain on  $\langle \sigma_v \rangle$  (see Fig. 3.16) and considering the intrinsic scatter, it is still compatible with the relations. Moreover, we note that a significant part of the visible gradient can be due to the presence of NGC 1569, the galaxy with the most extreme SFRD properties, therefore we repeated the fit considering only the galaxies in the subsample (square points in Fig. 5.5), i.e. excluding DDO 101 and NGC 1569. In this case the best-fit relations becomes flatter, but they are

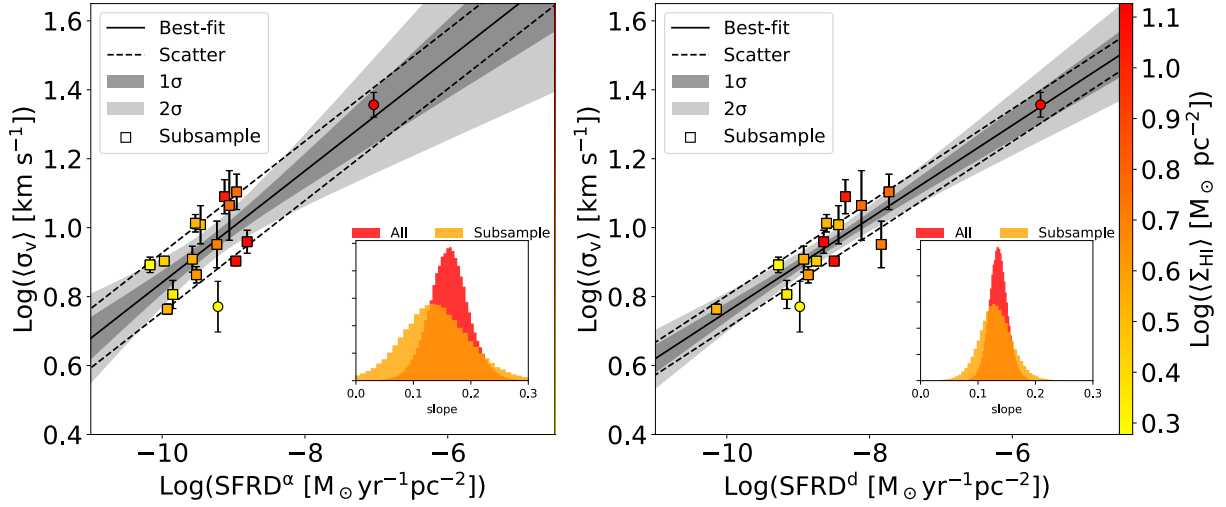


**Figure 5.5:** Median velocity dispersion  $\langle \sigma_v \rangle$  as a function of  $\text{SFRD}^\alpha$  (left-hand panel) and  $\text{SFRD}^d$  (right-hand panel) for the galaxies in our sample, see the text for details on these quantities. The squares indicate the galaxies included in the subsample (see text), the black lines show the best-fit linear relation (considering all galaxies), while the grey bands indicate the  $1\sigma$  and  $2\sigma$  uncertainties. The dashed lines show the best-fit relation  $\pm$  the best value found for the intrinsic scatter. The histograms in the insets show the posterior distributions of the relation slopes for both the whole sample (red) and the subsample excluding NGC 1569 and DDO 101 (orange). The colour code of the markers indicates the mean value of the HI surface density within  $R_{\text{H}\alpha}$ .

still compatible with the results obtained for the complete sample, as shown by the orange histograms. Removing NGC 1569, we have significantly reduced the dynamical range of the SFRD, as a consequence the uncertainties on the slope are doubled and the distribution of points in the left-hand panel becomes marginally compatible with a flat distribution. In both cases, the intrinsic scatter estimated for the relation is  $\lesssim 0.1$  dex, so most of the uncertainties are due to errors on the velocity dispersion estimates.

The colour code of the points indicate the mean surface density  $\langle \Sigma_{\text{HI}} \rangle$  estimated dividing the mass of HI disc inside  $R_{\text{H}\alpha}$  by the area of the disc within  $R_{\text{H}\alpha}$ : it is visible a trend of increasing surface density as function of the SFRD, this is expected since the SFRD correlates with  $\Sigma_{\text{HI}}$  (Kennicutt-Schmidt law, Kennicutt 1998).

### 5.3.3 Kinetic energy

The possible sources that feed the turbulence need to inject an amount of energy in the ISM comparable with the kinetic energy of the turbulent motions. Therefore, if the star formation activity is one of the main players in sustaining the turbulence, we expect that the kinetic energy per unit area correlates with the SFRD.

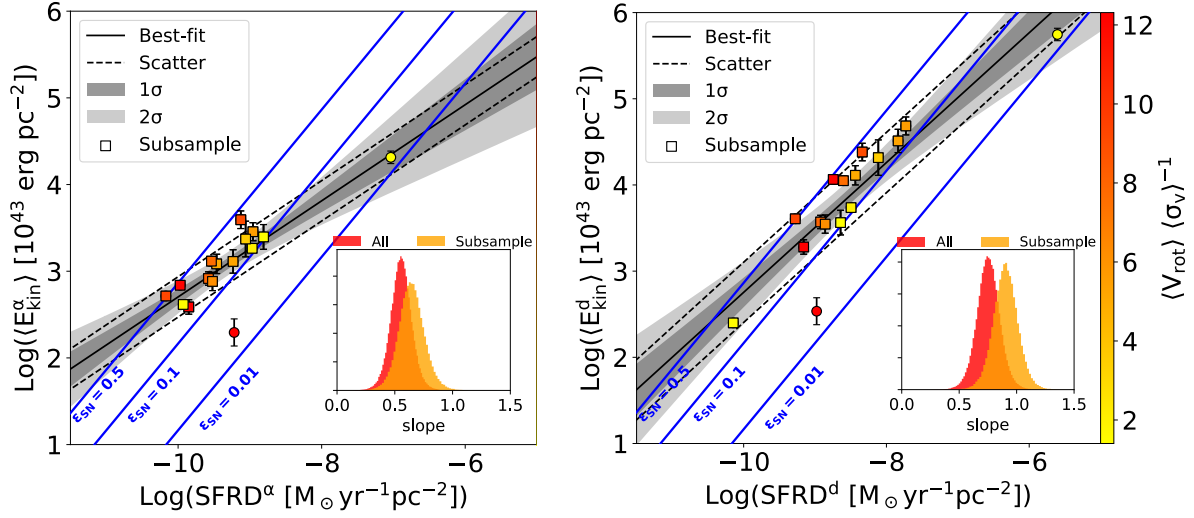


**Figure 5.6:** Same as Fig. 5.5 but for the relation between the kinetic energy per unit area and the SFRD. The values of  $\langle E_{\text{kin}}^\alpha \rangle$  and  $\langle E_{\text{kin}}^d \rangle$  have been calculated considering the velocity dispersion and HI mass estimated within  $R_{\text{H}\alpha}$  or  $R_d$  (further details in the text). The blue lines have a unity slope and represent the SN energy input in the ISM considering an efficiency  $\epsilon_{\text{SN}} = 0.5, 0.1, 0.01$ . The color code of the markers indicates the ratio between the mean value the three last points of the rotational velocities and the median of the velocity dispersion estimated across all the disc (see Tables 3.27-3.43 in Appendix 3.A.2).

The kinetic energy per unit area is defined as  $E_{\text{kin}} = (3/2)\Sigma_{\text{HI}}\sigma_v^2$ , where  $\sigma_v$  is the velocity dispersion measured along the line of sight and the factor 3 takes into account the three components of the velocity dispersion assumed isotropic. We use two estimators for the characteristic kinetic energy:  $\langle E_{\text{kin}}^\alpha \rangle = (3/2)\langle \Sigma_{\text{HI}}^\alpha \rangle \langle \sigma_v \rangle^2$  and  $\langle E_{\text{kin}}^d \rangle = (3/2)\langle \Sigma_{\text{HI}}^d \rangle \langle \sigma_v \rangle^2$ , where  $\langle \sigma_v \rangle$  is estimated as in the previous Section and the mean surface density is calculated dividing the mass of the galaxy within  $R_{\text{H}\alpha}$  by the disc surface inside  $R_{\text{H}\alpha}$  and  $R_d$  in the case of  $\langle \Sigma_{\text{HI}}^\alpha \rangle$  and  $\langle \Sigma_{\text{HI}}^d \rangle$ , respectively. Fig. 5.6 shows the distribution of the galaxies in our sample in the logarithmic  $\langle E_{\text{kin}}^\alpha \rangle$ -SFRD $^\alpha$  (left-hand panel) and  $\langle E_{\text{kin}}^d \rangle$ -SFRD $^d$  (right-hand panel) planes: considering the complete sample, the data follows a linear relation with a best-fit slope  $s \sim 0.6$  in the first case and  $s \sim 0.8$  in the second case (see Tab. 5.7 for further details). The two slopes are compatible within  $1\sigma$  and the existence of a flat relation is strongly unlikely as shown by the slope posteriors (red histograms in the small panels in Fig. 5.6).

As before, DDO 101 is an outlier in the relation as shown by the red dot with  $\log \text{SFRD}^\alpha \sim \log \text{SFRD}^d \sim -9$ ; in this case, DDO 101 is even more off set from the best-fit relation because it has not only a velocity dispersion lower than other galaxies with similar SFRD (as shown in Fig. 5.5), but also a lower mean value of the surface density inside  $R_{\text{H}\alpha}$  (see Fig. 3.16).

Excluding DDO 101 and NGC 1569 (the galaxy with the highest SFRD), our best-fit slopes increases to  $s \sim 0.7$  and  $s \sim 0.9$ , while the intrinsic scatter decreases of about 0.1 dex (see Tab. 5.7), hence a consistent part of the scatter is due to the position of these two galaxies. Interestingly, using the subsample, the slope of the relation in the  $\langle E_{\text{kin}}^\alpha \rangle$ -SFRD<sup>d</sup> is compatible with one within  $1\sigma$ , as also shown by the slope posterior distribution (the orange histogram in the small subplots); a linear scaling could be expected for the correlation between the rate energy injected in the ISM by the SNe and the SFRD (see below).

### 5.3.4 Kinetic energy from SN explosions

Most of the energy released by the star formation activity is through the explosion of young massive stars as core-collapse SNe. For a give initial mass function (IMF), the rate of these events is proportional to the rate of newborn stars, hence to the SFR. The total kinetic energy per unit area released by SN explosions is

$$E_{\text{kin}} = \eta E_{\text{SN}} \tau, \quad (5.15)$$

where  $\eta$  is the rate of SNe per unit area per unit time,  $E_{\text{SN}}$  is the mean total energy released in a single SN and  $\tau$  is the decay time of the turbulence. Following Tamburro et al. (2009) we make a series of assumptions:

- we consider only core-collapse SNe, so  $\eta \propto \text{SFRD}$ ;
- we assume a Kroupa IMF (Kroupa, 2001), considering stars in the mass range 0.1-120  $M_\odot$ ;
- only stars above 8  $M_\odot$  produce core-collapse SNe;
- the energy released per single SN event is  $10^{51}$  erg;
- we assume steady state equilibrium between the energy input rate and the energy loss rate of the turbulence. In this case,  $\tau$  represents the decay time of the turbulent energy that depends on the driving scale length  $\lambda$  and the velocity dispersion  $\sigma_v$ , we assume  $\lambda = 100$  pc (Joung & Mac Low, 2006; de Avillez & Breitschwerdt, 2007) and  $\sigma_v = 8.7$  km s<sup>-1</sup> calculated as the mean of all the median  $\sigma_v$  estimated for the galaxy in our sample (see Tab. 3.8), so  $\tau \simeq 11$  Myr. This last assumption is discussed in detail in the last part of this Section.

Using the above assumptions in Eq. 5.15, the kinetic energy per unit time injected in the ISM is

$$\frac{E_{\text{kin}}}{10^{56} \text{erg pc}^{-2}} = 1.46 \epsilon_{\text{SN}} \frac{\text{SFRD}}{M_\odot \text{yr}^{-1} \text{pc}^{-2}}, \quad (5.16)$$

$\log(y) = A + s \log(x)$		All galaxies			Subsample		
$x$	$y$	$s$	$A$	scatter	$s$	$A$	scatter
SFRD <sup>α</sup>	$\langle \sigma_v \rangle$	$0.16 \pm 0.03$	$2.45 \pm 0.31$	$0.09 \pm 0.02$	$0.14 \pm 0.06$	$2.23 \pm 0.58$	$0.08 \pm 0.02$
SFRD <sup>d</sup>	$\langle \sigma_v \rangle$	$0.14 \pm 0.02$	$2.11 \pm 0.14$	$0.05 \pm 0.02$	$0.13 \pm 0.04$	$2.07 \pm 0.24$	$0.05 \pm 0.03$
SFRD <sup>α</sup>	$\langle E_{\text{kin}}^\alpha \rangle$	$0.55 \pm 0.09$	$8.25 \pm 0.81$	$0.23 \pm 0.07$	$0.65 \pm 0.10$	$9.16 \pm 1.03$	$0.14 \pm 0.05$
SFRD <sup>d</sup>	$\langle E_{\text{kin}}^d \rangle$	$0.75 \pm 0.10$	$10.30 \pm 0.82$	$0.35 \pm 0.09$	$0.90 \pm 0.10$	$11.70 \pm 0.9$	$0.21 \pm 0.06$

**Table 5.7: Best fit parameters for the log-log linear relations between turbulence proxies (velocity dispersion and kinetic energy) and SFRD.**  $\langle \sigma_v \rangle$  is in units of  $\text{km s}^{-1}$ ,  $\langle E_{\text{kin}}^\alpha \rangle$  and  $\langle E_{\text{kin}}^d \rangle$  are in units of  $10^{43} \text{ erg pc}^{-2}$ , while the SFRD<sup>α</sup> and the SFRD<sup>d</sup> are in units of  $\text{M}_\odot \text{yr}^{-1} \text{pc}^{-2}$ . The details about these quantities can be found in the text.

where  $\epsilon_{\text{SN}}$  is the efficiency, i.e., the fraction of the SN energy effectively transferred to the ISM. If the turbulence is fed by the energy released in SN explosions we expect a linear relation  $E_{\text{kin}} \propto \text{SFRD}$  with a normalisation that depends on the efficiency  $\epsilon_{\text{SN}}$ . In Fig. 5.6 we plot the expected relation for three levels of efficiency (0.5, 0.1, 0.01, blue lines). Qualitatively, tuning the level of efficiency, the blue lines can be considered a good fit to the galaxies in the subsample (squares in Fig. 5.5 and Fig. 5.6), more quantitatively the posterior distributions of the slopes from the fit to the subsample (orange histograms in the subpanels) are compatible with the expected  $s = 1$  within  $3\sigma$  considering the  $\langle E_{\text{kin}}^\alpha \rangle$ -SFRD<sup>α</sup> relation and within  $1\sigma$  considering the  $\langle E_{\text{kin}}^d \rangle$ -SFRD<sup>d</sup> relation. All our galaxies are located below a level of efficiency  $\epsilon_{\text{SN}} = 0.5$ , interestingly Tenorio-Tagle et al. (1991) argued that this level of efficiency is an upper limit for the SN explosions.

The kinetic energy injected by the SNe depends on the assumed decay time scale for the turbulence (Eq. 5.15). As already said,  $\tau$  depends both on the turbulence driving scale,  $\lambda$ , and on the velocity dispersion as

$$\tau \simeq 9.8 \left( \frac{\lambda}{100 \text{ pc}} \right) \left( \frac{\sigma_v}{10 \text{ km s}^{-1}} \right)^{-1}. \quad (5.17)$$

Replicating the analysis presented in Tamburro et al. (2009), we evaluated Eq. 5.17 using a constant value both for  $\lambda$  and for  $\sigma_v$ . However, in Sec. 5.3.2 we found that  $\sigma_v$  and the SFRD are mildly correlated ( $\sigma_v \propto \text{SFRD}^{0.14-0.16}$ ). Taking into account this correlation, the expected relation between the kinetic energy and the SFRD is less steep with respect to a purely linear relation, in particular  $E_{\text{kin}} \propto \text{SFRD}^{0.84-0.86}$ . These slopes are even more compatible with what we found fitting our data, especially using the SFRD<sup>d</sup> as shown in Fig. 5.8 (see also Tab. 5.7 and the slope distributions in the insets of Fig. 5.6). The assumption of  $\lambda = 100 \text{ pc}$  has been obtained from hydrodynamical simulations considering the properties of our Galaxy (Joung & Mac Low, 2006; de Avillez & Breitschwerdt, 2007). It is not clear if in the presence of a shallower potential, as it is the case of dIrrs, the value of  $\lambda$  could be larger. We note that a factor 2 ( $\lambda = 200 \text{ pc}$ ) is enough to increase the normalisation

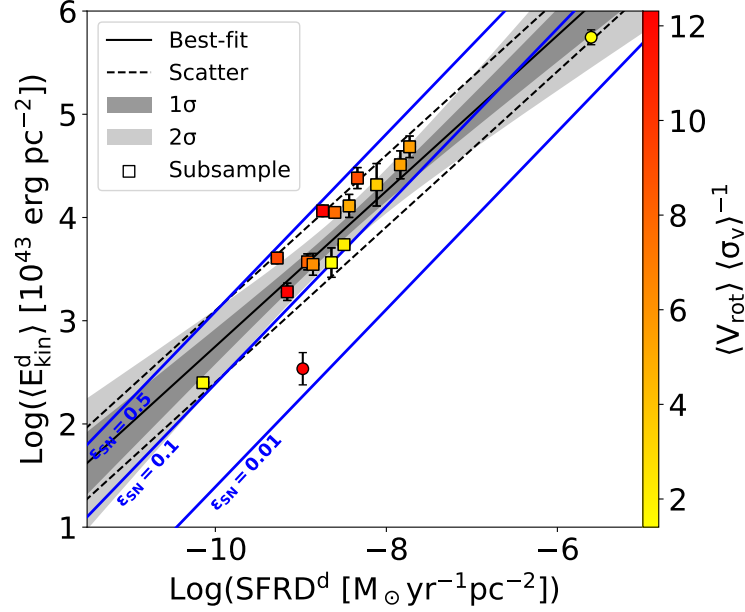


**Figure 5.8:** Same as right-hand panel of Fig. 5.6 but considering that the SN energy input in the ISM (blue lines) has a less steep dependence on the SFRD ( $E_{\text{kin}} \propto \text{SFRD}^{0.86}$ ), see text for details.

of the blue lines in Fig. 5.7 by about 0.3 dex; as a consequence, smaller values of the SN efficiency would be required to sustain the turbulence.

Moreover, the velocity dispersions used to calculate the kinetic energy contains both the thermal  $\sigma_{\text{Th}}$  and the turbulent  $\sigma_{\text{Tu}}$  components, so what we are really measuring is the total kinetic energy of the chaotic motion, rather than the kinetic energy of the turbulent motion  $E_{\text{Tu}}$ . The unbiased estimator of the turbulent energy can be calculated as  $\log E_{\text{Tu}} = \log E_{\text{kin}} + \log(1 - \sigma_{\text{Th}}^2/\sigma_v^2)$ . Since  $\sigma_{\text{Th}}^2 < \sigma_v^2$ , the last term is always negative and the points in Fig. 5.16 can be shifted down by 0.3-0.5 dex if most of the gas is the warm phase ( $\sigma_{\text{Th}}^2 \sim 6 - 8 \text{ km s}^{-1}$ ), approaching the efficiency of 0.1 or less. NGC 1569 is the only galaxy with a robust unbiased estimate of the turbulent kinetic energy, as it has  $\langle \sigma_v \rangle \sim 20 \text{ km s}^{-1}$  and the component of the thermal kinetic energy is negligible. Interestingly it is located very close to the line indicating the lowest level of efficiency ( $\epsilon_{\text{SN}} = 0.01$ ). Finally, we note that the observed value of  $\sigma_v$  can be further overestimated due to the possible presence of thick HI discs (see Fig. 4.9 and Sec. 4.3), hence the reported values of the kinetic energy in Fig. 5.6 can be considered upper limits of the value of the kinetic energy held in turbulent motions.

The colour code of the points in Fig. 5.6 shows the ratio between the mean of the outer part of the rotational velocity (calculated as the last three points of  $V_{\text{rot}}$ ) and the mean of the velocity dispersion calculated over the whole disc (see Tab. 3.8). A mild increase of the rotational support perpendicular to the relation appears; one

could speculate that, at fixed SFRD, galaxies more supported by rotation also have higher turbulent energy because when the rotation is significant part of the energy is due to other mechanisms such as rotational shear (e.g. Schaye 2004) and/or magneto rotational instability (e.g. Sellwood & Balbus 1999; Piontek & Ostriker 2005).

In this analysis, we have considered the properties of dIrr galaxies only within the region where star formation is currently ongoing. Outside  $R_{\text{H}\alpha}$  all the galaxies in our sample have velocity dispersion compatible with or even lower than  $\sim 8 \text{ km s}^{-1}$ , so we are in a regime where all the broadening of the HI line widths could be explained by thermal motion assuming that most of the HI is in the warm phase with  $T \approx 8000 \text{ K}$ .

## 5.4 Summary

In this Chapter, we have analysed correlations between global galactic properties for a sample of dIrrs. The main results of this Chapter are listed below.

1. We tested the baryonic Tully-Fisher relation in the low-mass regime ( $10^6 M_{\odot} \lesssim M_{\text{bar}} \lesssim 10^9 M_{\odot}$ ). We found that our results are compatible in slope, normalisation and scatter with the work of Lelli, McGaugh & Schombert (2016c) at higher mass ( $M_{\text{bar}} > 10^8 M_{\odot}$ ). In particular, there is no evidence for a break of the relation at the low-mass end as predicted in  $\Lambda$ CDM simulations (e.g. Brook, Santos-Santos & Stinson 2016; Sales et al. 2017).
2. We tested the radial acceleration relation (McGaugh, Lelli & Schombert, 2016) for dIrrs. We found that our results are compatible with the results obtained by Lelli et al. (2017) for larger galaxies. However, our data are also compatible with a constant value of the galactic acceleration ( $g_{\text{obs}} \simeq 1.8 \times 10^{-14} \text{ km s}^{-2}$ ), independently of the baryonic properties. This result is compatible with what Lelli et al. (2017) found for a sample of dSphs.
3. We found a correlation between proxies of the turbulence in the ISM (velocity dispersion and kinetic energy) and the star formation rate density. We also found that the kinetic energy ejected from the SN explosions is sufficient to cover the budget of kinetic energy held in the turbulent motions. These results suggest that the star formation activity is likely the main player in the feeding of the turbulence in the ISM of dIrrs.

## 5.A Rotation curve generated by the HI distribution

In this Appendix we estimate the rotation speed,  $V_{\text{HI}}$ , and the radial acceleration,  $g_{\text{HI}}$ , generated by the distribution of HI in the disc of the dIrrs analysed in [Chapter 3](#). The rotation speeds have been used in [Sec. 5.2](#) to test the radial acceleration relation for the dIrr galaxies in our sample.

We begin with the condition that the centrifugal acceleration ( $V_{\text{HI}}^2/R$ ) must exactly balance the gravitational attraction. Therefore the rotational velocity on the galactic plane ( $z=0$ ) expected from an HI disc is

$$V_{\text{HI}}(R) = \sqrt{-Rg_{\text{HI}}(R)}, \quad (5.18)$$

where  $g_{\text{HI}}$  is the radial component of the gravitational acceleration due to the HI distribution ([Eq. 4.22](#), see [Sec. 4.2.2](#)).

Assuming a razor-thin HI disc  $\rho_{\text{HI}} = \Sigma_{\text{obs}} \cos i \zeta(0)$ , where  $i$  is the inclination angle of the HI disc.  $\cos i$  takes into account the deprojection of the observed surface density profile  $\Sigma_{\text{obs}}$  and the vertical distribution  $\zeta$  is a Dirac  $\delta$  centred on  $z = 0$ , hence using [Eq. 4.22](#) we obtain

$$g_{\text{HI}}(R) = 4 G \Sigma_0 \cos i \int_0^\infty dR' \frac{2\sqrt{R'}}{\sqrt{R'p}} [K(p) - E(p)] \frac{\partial \tilde{\Sigma}_{\text{obs}}(R')}{\partial R'}, \quad (5.19)$$

where  $\tilde{\Sigma}_{\text{obs}}$  is the observed radial surface density profile normalised to  $\Sigma_0$ ,  $p = \epsilon - \sqrt{\epsilon^2 - 1}$  and

$$\epsilon = \frac{R^2 + R'^2}{2RR'}. \quad (5.20)$$

We can calculate the rotation curve expected for each of the HI disc analysed in [Chapter 3](#), using [Eq. 5.18](#), [Eq. 5.19](#) and the observed HI profile (see the Atlas in [Appendix 3.A](#)). The [Eq. 5.19](#) is solved numerically using our Python module `galpynamics`<sup>2</sup>, in order to avoid large artificial scatter due to the radial derivative inside the integral we use the functional form

$$\Sigma_{\text{obs}} = \Sigma_0 \left(1 + \frac{R}{R_d}\right)^\alpha \exp\left[-\frac{R}{R_d}\right] \quad (5.21)$$

to describe the radial trend of the surface density. In order to take into account the error on the intrinsic profile of the HI surface density (see [Figures and Tables](#) in [Appendix 3.A](#)) we used a method similar to the one used in [Sec. 3.3.3](#) to estimate the final errors of the circular velocities. This method consists of the following steps.

1. First, we make  $N$  realisations of the radial profile of the surface density. For

---

<sup>2</sup><https://github.com/iogiul/galpynamics>

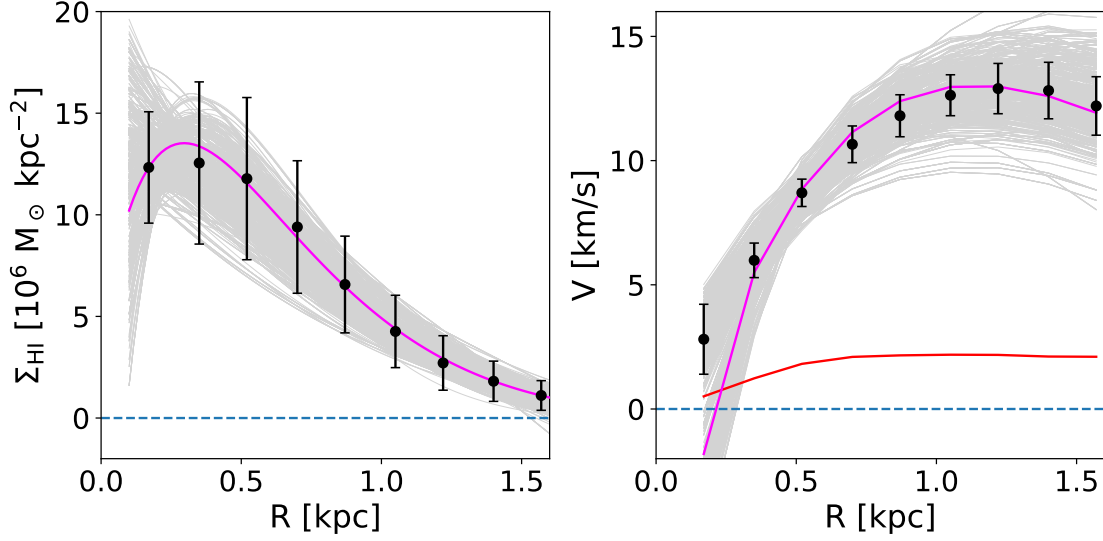


**Figure 5.9:** Rotation curve generated by the HI surface density distribution for CVn I dwA. **Left-hand panel:** the black points indicate the intrinsic surface density ( $\Sigma_{\text{obs}} \cos i$ ) obtained in [Chapter 3](#), the grey lines show the best-fits functional forms (Eq. 5.21) to the 1000  $\Sigma^j$  realisations (see text), while the magenta line shows the best-fit to the black points. **Right-hand panel:** The black points show the estimate of the rotation speed,  $V_{\text{HI}}$  generated by the HI surface density shown in the left-hand panel calculated as the median of the 1000  $V_{\text{HI}}^j$  estimates (grey lines), the errors are calculated using the MAD statistic (see text for further details); the magenta line shows the rotation curve expected for the surface density profile shown by the magenta line in the left-hand panel. The red line indicates the rotation curve due to the distribution of matter in the stellar disc, it is taken from the value reported in [Oh et al. \(2015\)](#) correcting for the mismatch between our and their assumption on the disc inclination (see [Sec. 5.2](#)).

each sampling radius  $R$  the values of a single realisation  $\Sigma_{\text{obs}}^j(R)$  are extracted randomly from a normal distribution with the mean and the dispersion taken respectively from the values and errors of the parent populations.

2. For each of the  $N$  realisations we fit  $\Sigma_{\text{obs}}^j(R)$  using the functional form in Eq. 5.21 as shown by the grey lines in the left-hand panel in [Fig. 5.9](#), then we calculate numerically the integral in Eq. 5.19 obtaining  $g_{\text{HI}}^j$  and  $V_{\text{HI}}^j$  using Eq. 5.18 (see grey lines in the right-hand panel in [Fig. 5.9](#)).
3. The final velocities are calculated as  $V_{\text{HI}} = \text{median}_j(V_{\text{HI}}^j)$ , while the associated errors are  $\delta_{V_{\text{HI}}}(R) = K \times \text{MAD}(V_{\text{HI}}^j)$  where the MAD is the median absolute deviation around the median (black points and error bars in [Fig. 5.9](#)). The factor  $K$  links the MAD with the standard deviation of the sample ( $K \approx 1.48$  for a normal distribution). We chose to use the median and the MAD because they are less biased by the presence of outliers with respect to the mean and the standard deviation.

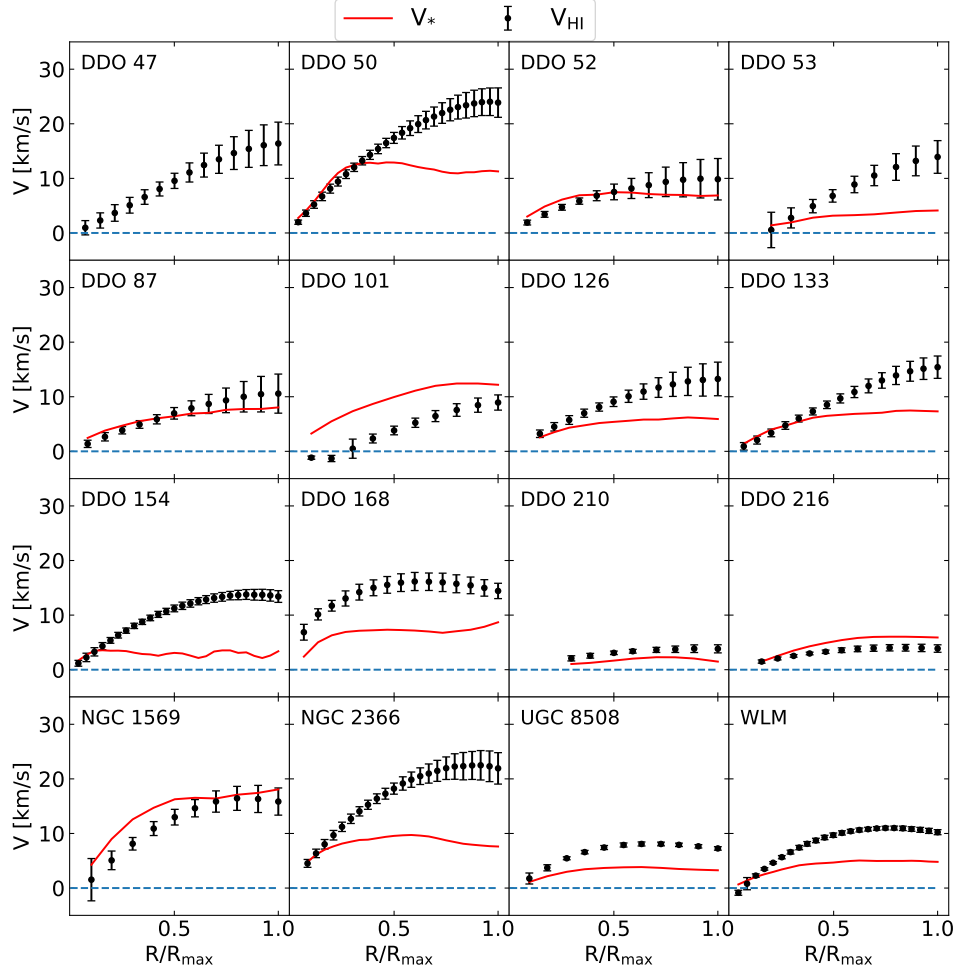


**Figure 5.10:** Black points and red lines are the same as in Fig. 5.9. Notice that DDO 47 does not have an estimate of the stellar rotation curve in Oh et al. (2015).

We found that  $N = 1000$  is enough to obtain a good description of the errors introduced by the uncertainties in the observed  $\Sigma_{\text{obs}}$ .

In Fig. 5.9 we show the results obtained with our method for the galaxy CVn I dwA (see Sec. 3.4 and Fig. 3.10), a summary plot with the  $V_{\text{HI}}$  estimated for all the other dIrrs presented in Chapter 3 can be found in Fig. 5.10. In some cases  $V_{\text{HI}}$  has a negative value (e.g. WLM or DDO 101), this is an artefact that we introduce when  $g_{\text{HI}} > 0$  and the argument of the square root in Eq. 5.18 becomes negative, hence a more general definition of  $V_{\text{HI}}$  is

$$V_{\text{HI}}(R) = -\text{sign}[g_{\text{HI}}(R)]\sqrt{|Rg_{\text{HI}}(R)|}. \quad (5.22)$$

The sign of  $g_{\text{HI}}$  is defined by the radial derivative of the HI surface density profile in Eq. 5.19, generally  $\Sigma_{\text{obs}}$  exhibits an exponential decrease and  $g_{\text{HI}}$  is always negative, i.e. directed inward causing a centripetal acceleration. However, in the very inner part of the disc some galaxies show a significant deficit of HI (e.g. WLM, see Fig. 3.26). In these cases, the value of  $\Sigma_{\text{obs}}$  increases with radius and  $g_{\text{HI}} > 0$ , the acceleration is direct outward and no centripetal acceleration is produced, hence Eq. 5.9 is not defined anymore. The negative  $V_{\text{HI}}$  that we introduce in Eq. 5.22 does not have physical meaning: an HI disc alone cannot rotate in the region where Eq. 5.22 predict negative velocities. However it is a useful “trick” in the study of galactic dynamics. In this sense, a negative velocity means just that we need more radial acceleration from other components (dark matter halo, stellar disc) to balance the observed rotation of the gas and the outward acceleration produced by the HI disc (see Sec. 4.2.2).



# Chapter 6

---

## Concluding remarks

Eventually, we have reached “safe and sound” the end of our “off piste tour” beyond the disc of the Milky Way. In this concluding Chapter, we summarise the contents and the results of this thesis (Sec. 6.1), then in Sec. 6.2, we briefly present related works that use results obtained in this thesis. In Sec. 6.3, we describe the improvement expected in our study of the halo with the next *Gaia* data release.

### 6.1 Summary

In the first part of this thesis we present a study of the distribution of stars in the inner part of the Galactic halo exploiting the unprecedented dataset of the first *Gaia* data release. Then, in the second part of the thesis we focus on the properties of the dwarf irregular galaxies (dIrrs) making use of the state-of-the art 3D fitting tool <sup>3D</sup>BAROLO (Di Teodoro & Fraternali, 2015) and developing a new original approach to take into account the HI disc thickness. The brief summaries and the main results of each Chapter are reported below

- In Chapter 2, we exploited the first *Gaia* data release to study the properties of the inner Galactic stellar halo as traced by RR Lyrae stars. We demonstrated that it is possible to select a pure sample of RR Lyrae stars using

only photometric information available in the *Gaia*+2MASS catalogue. The final sample contains about 21600 RR Lyrae stars covering an unprecedented fraction ( $\sim 60\%$ ) of the volume of the Galactic inner halo ( $R < 28$  kpc). We studied the morphology of the stellar halo by analysing the RR Lyrae stars distribution with parametric and non-parametric techniques. A consistent picture emerges: the inner halo is well reproduced by a smooth distribution of stars settled on triaxial density ellipsoids. The shortest axis is perpendicular to the Milky Way's disc, while the longest axis forms an angle of  $\sim 70^\circ$  with the axis connecting the Sun and the Galactic centre. The elongation along the major axis is mild ( $p = 1.27$ ), and the vertical flattening is shown to evolve from a squashed state with  $q \approx 0.57$  in the centre to a more spherical  $q \approx 0.75$  at the outer edge of our dataset. Within the radial range probed, the density profile of the stellar halo is well approximated by a single power-law with exponent  $\alpha = -2.96$ . We do not find evidence of tilt or offset of the halo with respect to the Galaxy's disc.

- In [Chapter 3](#), we studied the HI kinematics of 17 galaxies extracted from the ‘Local Irregulars That Trace Luminosity Extremes, The HI Nearby Galaxy Survey’ (LITTLE THINGS). Our approach differs significantly from previous studies in that we directly fit 3D models (two spatial dimensions plus one spectral dimension) using the software <sup>3D</sup>BAROLO, fully exploiting the information in the HI datacubes. For each galaxy we derived the geometric parameters of the HI disc (inclination and position angle), the radial distribution of the surface density, the velocity-dispersion ( $\sigma_v$ ) profile and the rotation curve. The circular velocity ( $V_c$ ), which traces directly the galactic potential, is then obtained by correcting the rotation curve for the pressure support in the HI disc. The final products of this work are high-quality, ready-to-use kinematic data ( $V_c, \sigma_v$ ).
- In [Chapter 4](#), we investigated the effect that the presence of thick gaseous layers can have on the study of the HI discs. In particular, we focused on discs with properties similar to the dIrrs studied in [Chapter 3](#). We found that, in the presence of a thick HI disc, if the effects of the thick disc is not accounted for, the observed surface density profile is shallower with respect to the intrinsic profile, the disc appears more face-on than it actually is and the parameters of the HI line profile (mean and standard deviation) are not a robust measurement of the kinematic properties (rotational velocity and velocity dispersion) of the gas in the meridional plane of the galaxy. In order to deal with the above observational biases, we presented, for the first time, a technique to analyse HI galaxies taking into account the presence of thick discs under the assumption of hydrostatic equilibrium. We applied this method to three galaxies already

analysed in [Chapter 3](#). We found that the thickness of the HI discs of these three galaxies is significant, both in absolute terms and relative to the radial scale length and the radial extent of the discs. However, the final rotation curves are compatible with the ones obtained in [Chapter 3](#) using <sup>3D</sup>BAROLO and assuming thin HI discs with a constant scale height ( $z_d \sim 100$  pc, for all the galaxies). Therefore, the presence of such thick discs does not have a significant impact in the study of the kinematics and dynamics. We can conclude that the results obtained in [Chapter 3](#) represent robust estimates of the properties of dIrrs in our sample. Finally, we also demonstrated that the excess of emission along the minor axis of some galaxies (e.g. WLM and UGC 8508) can be nicely explained by the presence of thick gaseous layers intercepted along the line of sight.

- In [Chapter 5](#), we presented three scaling relations of dIrrs using the results obtained in [Chapter 3](#). We used the circular velocities of the outer part of the HI discs to test the baryonic Tully-Fisher relation in the low-mass regime of dwarf galaxies, we found that the properties of the analysed galaxies are totally compatible with the relation found for larger spirals. The circular velocities and the HI surface densities have been used to test the radial acceleration relation between the acceleration obtained from the observed circular velocities,  $g_{\text{obs}}$ , and the one expected from the baryonic matter,  $g_{\text{bar}}$ . The values found for our dwarf galaxies are compatible with the relation found for larger spirals and elliptical galaxies at large  $g_{\text{bar}}$ , while at small  $g_{\text{bar}}$  our data seem to indicate the presence of a constant observed acceleration independent of the value of the baryonic acceleration as already found for a sample of dSphs by Lelli et al. (2017). Finally, we found that both the HI velocity dispersion and the HI “chaotic” kinetic energy per unit area ( $E_{\text{kin}} = \Sigma_{\text{HI}} \sigma_v^2$ ) show a relation with the star formation rate (SFR) of the galaxy. In particular,  $\sigma_v \propto \text{SFR}^{\sim 0.14-10.6}$  and  $E_{\text{kin}} \propto \text{SFR}^{\sim 0.55-0.75}$ . Studying these correlations, we found that the turbulence observed in the neutral medium of dIrrs can be sustained by the star formation activity assuming an average efficiency of about 30% in transferring the supernova explosions energy into the ISM.

## 6.2 Related works

In this thesis, we made use of state-of-the-art datasets and techniques and we further proposed new original approaches for data analysis giving a contribution to the field of kinematics and dynamics of HI discs and to the study of the Galactic stellar halo. Parts of the results of this thesis have been presented in accepted papers (Iorio et al. 2017b; Iorio et al. 2017a) and they have been already exploited in other works.

In a recent work (Boubert et al., 2017), we used the residuals between the dis-

tribution of stars in the halo and our best halo model to highlight the presence of a “genuine” excess of stars aligned with the Magellanic stream. This property suggests that this structure could contain either debris from a disrupted dwarf galaxy that was orbiting in the Vast Polar Structure (Pawlowski, Pflamm-Altenburg & Kroupa, 2012) or stars once belonging to the Small Magellanic Cloud, lost in a recent (3 Gyr) tidal interaction with the Large Magellanic Cloud.

The data and the techniques presented in Chapter 3 have been used in Read et al. (2016), where we analysed the observed diversity of the dwarf galaxy rotation curves. In particular, we applied the method described in Sec. 3.3 to a sample of dwarf galaxies from non-cosmological hydrodynamical simulations (Read, Agertz & Collins, 2016) and to four real dIrrs. We concluded that the large variations in shape and diversity of the rotation curves observed in dIrrs and in contrast with the “regularity” found in the  $\Lambda$ CDM simulations (Oman et al., 2015, 2016) owe only in few cases to the fact the gas is out of equilibrium. In general, the rotation curves trace the galactic potential very well as long as the inclination of the disc and the distance of the galaxy are properly determined.

In Read et al. (2017), we used the rotation curves derived in Chapter 3 to obtain an estimate of the virial mass for the dIrrs in our sample taking into account the cusp-core transformation of the DM density profile due to stellar feedback (Read, Agertz & Collins, 2016). Using these results, we found a monotonic relation with little scatter between the total stellar mass and the halo virial mass for the galaxies in our sample. This relation is totally compatible with what we obtained with the abundance matching technique comparing the stellar mass function of field galaxies from the Sloan Digital Sky Survey (Blanton et al., 2001) and the halo mass function from the  $\Lambda$ CDM Bolshoi simulation (Klypin, Trujillo-Gomez & Primack, 2011). Based on these results, we concluded that small scale cosmological problems, such as the “missing satellites” (e.g. Klypin et al. 1999; McConnachie 2012) or “too big to fail” (e.g. Read et al. 2006; Boylan-Kolchin, Bullock & Kaplinghat 2011) problems, are confined to group environment and must owe to “galaxy formation physics” rather than exotic cosmology.

The data obtained in Chapter 3 have been also already used by other groups, see Allaert, Gentile & Baes (2017); Santos-Santos et al. (2018).

Finally, we are currently exploiting the methodology presented in Chapter 4 to estimate the 3D density of HI discs and investigate the fundamental relation between the gas density and the star formation rate density in disc galaxies (Bacchini et al., in prep.)

### 6.3 Waiting for *Gaia* DR2

The *Gaia* collaboration announced the new data release (GDR2) for April 2018<sup>1</sup>. The GDR2 will have a series of important improvements with respect to the data that we used in [Chapter 2](#):

- the sky-coverage will be more uniform and the number of flux measurements ( $N_{\text{obs}}$ ) for each star will increase, thus making our simple variability estimator AMP (Eq. 2.1) more precise and more robust;
- the photometry for a large sample of variable stars will be used to fine-tune the selection cuts of RR Lyrae stars without relying only on external auxiliary datasets (Sec. 2.1.2);
- most importantly, two photometric colours will be available:  $G_{\text{RP}}$  in the red band ( $\sim 700 \text{ nm} - 1000 \text{ nm}$ ) and  $G_{\text{BP}}$  in the blue band ( $\sim 300 \text{ nm} - 600 \text{ nm}$ ). They will be used for RR Lyrae colour selection without cross-matching *Gaia* with other surveys (as we did with 2MASS in [Chapter 2](#)).

We envisage applying the method presented in [Chapter 2](#) to the GDR2, avoiding the necessity to rely on shallow 2MASS data and thus extending our analysis out to Galactocentric distances of about 100 kpc. This unprecedented volume coverage, combined with stellar proper motions, will allow us to trace the overall shape of the halo and to shed light on the substructures hidden in the Galactic halo and thus decipher the Galaxy's formation history.

---

<sup>1</sup><https://www.cosmos.esa.int/web/gaia/release>



# Bibliography

- Abazajian K. N. et al., 2009, ApJS, [182](#), [543](#)
- Abramowitz M., Stegun I. A., 1972, Handbook of Mathematical Functions
- Adams J. J. et al., 2014, ApJ, [789](#), [63](#)
- Akhter S., Da Costa G. S., Keller S. C., Schmidt B. P., 2012, ApJ, [756](#), [23](#)
- Allaert F., Gentile G., Baes M., 2017, A&A, [605](#), [A55](#)
- Allen R. J., Goss W. M., van Woerden H., 1973, A&A, [29](#), [447](#)
- Amorisco N. C., 2017, MNRAS, [464](#), [2882](#)
- Antoja T. et al., 2014, A&A, [563](#), [A60](#)
- Argyle E., 1965, ApJ, [141](#), [750](#)
- Armandroff T. E., 1989, AJ, [97](#), [375](#)
- Bacchini C., Iorio G., Fraternali F., Pezzulli G., in prep.
- Baillard A. et al., 2011, A&A, [532](#), [A74](#)
- Barnabè M., Ciotti L., Fraternali F., Sancisi R., 2006, A&A, [446](#), [61](#)
- Battaglia G., Fraternali F., Oosterloo T., Sancisi R., 2006, A&A, [447](#), [49](#)
- Battaglia G., Helmi A., Tolstoy E., Irwin M., Hill V., Jablonka P., 2008, ApJ, [681](#), [L13](#)
- Battaglia G., Sollima A., Nipoti C., 2015, MNRAS, [454](#), [2401](#)
- Begeman K. G., 1987, PhD thesis, , Kapteyn Institute, (1987)
- Begeman K. G., 1989, A&A, [223](#), [47](#)
- Begum A., Chengalur J. N., Karachentsev I. D., Sharina M. E., 2008a, MNRAS, [386](#), [138](#)
- Begum A., Chengalur J. N., Karachentsev I. D., Sharina M. E., Kaisin S. S., 2008b, MNRAS, [386](#), [1667](#)
- Belokurov V., Erkal D., Deason A. J., Koposov S. E., De Angeli F., Evans D. W., Fraternali F., Mackey D., 2017, MNRAS, [466](#), [4711](#)
- Belokurov V. et al., 2007a, ApJ, [657](#), [L89](#)
- Belokurov V. et al., 2007b, ApJ, [658](#), [337](#)

- Belokurov V. et al., 2006, *ApJ*, **642**, L137
- Benjamin R. A. et al., 2005, *ApJ*, **630**, L149
- Binney J., Tremaine S., 2008, *Galactic Dynamics: Second Edition*. Princeton University Press
- Bland-Hawthorn J., Freeman K., 2000, *Science*, **287**, 79
- Blanton M. R. et al., 2001, *AJ*, **121**, 2358
- Boomsma R., Oosterloo T. A., Fraternali F., van der Hulst J. M., Sancisi R., 2008, *A&A*, **490**, 555
- Bosma A., 1978, PhD thesis, PhD Thesis, Groningen Univ., (1978)
- Bosma A., 1981, *AJ*, **86**, 1791
- Bosma A., Goss W. M., Allen R. J., 1981, *A&A*, **93**, 106
- Boubert D., Belokurov V., Erkal D., Iorio G., 2017, [ArXiv e-prints](#)
- Bovy J. et al., 2012, *ApJ*, **759**, 131
- Boylan-Kolchin M., Bullock J. S., Kaplinghat M., 2011, *MNRAS*, **415**, L40
- Breddels M. A., Helmi A., 2013, *A&A*, **558**, A35
- Brinks E., Burton W. B., 1984, *A&A*, **141**, 195
- Brook C. B., Santos-Santos I., Stinson G., 2016, *MNRAS*, **459**, 638
- Bullock J. S., Johnston K. V., 2005, *ApJ*, **635**, 931
- Bullock J. S., Kolatt T. S., Sigad Y., Somerville R. S., Kravtsov A. V., Klypin A. A., Primack J. R., Dekel A., 2001, *MNRAS*, **321**, 559
- Bureau M., Carignan C., 2002, *AJ*, **123**, 1316
- Cai R.-G., Liu T.-B., Wang S.-J., 2017, [ArXiv e-prints](#)
- Carignan C., Purton C., 1998, *ApJ*, **506**, 125
- Carney B. W., Laird J. B., Latham D. W., Aguilar L. A., 1996, *AJ*, **112**, 668
- Carollo D. et al., 2007, *Nature*, **450**, 1020
- Casertano S., 1983, *MNRAS*, **203**, 735
- Casertano S., van Gorkom J. H., 1991, *AJ*, **101**, 1231
- Catelan M., 2009, *Ap&SS*, **320**, 261
- Chiba M., Beers T. C., 2000, *AJ*, **119**, 2843
- Citro A., Pozzetti L., Moresco M., Cimatti A., 2016, *A&A*, **592**, A19
- Cole A. A. et al., 1999, *AJ*, **118**, 1657
- Combes F., 2009, *A&A*, **500**, 119
- Cook D. O. et al., 2014, *MNRAS*, **445**, 881
- Côté S., Carignan C., Freeman K. C., 2000, *AJ*, **120**, 3027
- Crane J. D., Majewski S. R., Rocha-Pinto H. J., Frinchaboy P. M., Skrutskie M. F.,

- Law D. R., 2003, *ApJ*, **594**, [L119](#)
- Croxall K. V., van Zee L., Lee H., Skillman E. D., Lee J. C., Côté S., Kennicutt, Jr. R. C., Miller B. W., 2009, *ApJ*, **705**, [723](#)
- Cuddeford P., 1993, *MNRAS*, **262**, [1076](#)
- Da Costa G. S., 1992, in *IAU Symposium*, Vol. 149, *The Stellar Populations of Galaxies*, Barbuy B., Renzini A., eds., p. 191
- Dale D. A. et al., 2009, *ApJ*, **703**, [517](#)
- Danziger I. J., 1997, in *Astronomical Society of the Pacific Conference Series*, Vol. 117, *Dark and Visible Matter in Galaxies and Cosmological Implications*, Persic M., Salucci P., eds., p. 28
- Das P., Binney J., 2016, *MNRAS*, **460**, [1725](#)
- Das P., Williams A., Binney J., 2016, *MNRAS*, **463**, [3169](#)
- de Avillez M. A., Breitschwerdt D., 2007, *ApJ*, **665**, [L35](#)
- de Blok W. J. G., Bosma A., 2002, *A&A*, **385**, [816](#)
- de Blok W. J. G., Walter F., Brinks E., Trachternach C., Oh S.-H., Kennicutt, Jr. R. C., 2008, *AJ*, **136**, [2648](#)
- de Boer T. J. L., Belokurov V., Koposov S. E., 2017, [ArXiv e-prints](#)
- De Lucia G., Helmi A., 2008, *MNRAS*, **391**, [14](#)
- De Propris R., Harrison C. D., Mares P. J., 2010, *ApJ*, **719**, [1582](#)
- Deason A. J., Belokurov V., Erkal D., Koposov S. E., Mackey D., 2017a, *MNRAS*, **467**, [2636](#)
- Deason A. J., Belokurov V., Evans N. W., 2011, *MNRAS*, **416**, [2903](#)
- Deason A. J., Belokurov V., Evans N. W., Johnston K. V., 2013, *ApJ*, **763**, [113](#)
- Deason A. J., Belokurov V., Koposov S. E., Gómez F. A., Grand R. J., Marinacci F., Pakmor R., 2017b, *MNRAS*, **470**, [1259](#)
- Deason A. J., Mao Y.-Y., Wechsler R. H., 2016, *ApJ*, **821**, [5](#)
- Di Cintio A., Lelli F., 2016, *MNRAS*, **456**, [L127](#)
- Di Teodoro E. M., Fraternali F., 2015, *MNRAS*, **451**, [3021](#)
- Dib S., Bell E., Burkert A., 2006, *ApJ*, **638**, [797](#)
- Dickey J. M., Lockman F. J., 1990, *ARA&A*, **28**, [215](#)
- Drake A. J. et al., 2013, *ApJ*, **763**, [32](#)
- Drake A. J. et al., 2014, *ApJS*, **213**, [9](#)
- Duffau S., Zinn R., Vivas A. K., Carraro G., Méndez R. A., Winnick R., Gallart C., 2006, *ApJ*, **636**, [L97](#)
- Eggen O. J., Lynden-Bell D., Sandage A. R., 1962, *ApJ*, **136**, [748](#)
- Einasto J., 1965, *Trudy Astrofizicheskogo Instituta Alma-Ata*, **5**, [87](#)

- Elmegreen B. G., Elmegreen D. M., Leitner S. N., 2003, *ApJ*, **590**, 271
- Elmegreen B. G., Hunter D. A., 2015, *ApJ*, **805**, 145
- Elmegreen B. G., Leitner S. N., Elmegreen D. M., Cuillandre J.-C., 2003, *ApJ*, **593**, 333
- Elmegreen B. G., Scalo J., 2004, *ARA&A*, **42**, 211
- Epstein E. E., 1964, *AJ*, **69**, 490
- Ewen H. I., Purcell E. M., 1951, *Nature*, **168**, 356
- Falcón-Barroso J., Lyubenova M., van de Ven G., 2015, in *IAU Symposium*, Vol. 311, *Galaxy Masses as Constraints of Formation Models*, Cappellari M., Courteau S., eds., pp. 78–81
- Ferguson H. C., Binggeli B., 1994, *A&ARv*, **6**, 67
- Fermani F., Schönrich R., 2013, *MNRAS*, **432**, 2402
- Field G. B., Goldsmith D. W., Habing H. J., 1969, *ApJ*, **155**, L149
- Fiorentino G. et al., 2015, *ApJ*, **798**, L12
- Fitzpatrick E. L., 1999, *PASP*, **111**, 63
- Flores R. A., Primack J. R., 1994, *ApJ*, **427**, L1
- Foreman-Mackey D., Hogg D. W., Lang D., Goodman J., 2013, *PASP*, **125**, 306
- Francis C., Anderson E., 2014, *MNRAS*, **441**, 1105
- Fraternali F., Oosterloo T., Sancisi R., van Moorsel G., 2001, *ApJ*, **562**, L47
- Fraternali F., van Moorsel G., Sancisi R., Oosterloo T., 2002, *AJ*, **123**, 3124
- Frebel A., Christlieb N., Norris J. E., Thom C., Beers T. C., Rhee J., 2007, *ApJ*, **660**, L117
- Gaia Collaboration et al., 2016a, *A&A*, **595**, A2
- Gaia Collaboration et al., 2016b, *A&A*, **595**, A1
- García-Ruiz I., Sancisi R., Kuijken K., 2002, *A&A*, **394**, 769
- Gentile G., Burkert A., Salucci P., Klein U., Walter F., 2005, *ApJ*, **634**, L145
- Gentile G., Salucci P., Klein U., Vergani D., Kalberla P., 2004, *MNRAS*, **351**, 903
- Georgiev T. B., Karachentsev I. D., Tikhonov N. A., 1997, *Astronomy Letters*, **23**, 514
- Goodman J., Weare J., 2010, *Comm. App. Math. Comp. Sci.*, **5**, 65
- Graham A. W., Merritt D., Moore B., Diemand J., Terzić B., 2006, *AJ*, **132**, 2701
- Guth A. H., 1981, *Phys. Rev. D*, **23**, 347
- Harmsen B., Monachesi A., Bell E. F., de Jong R. S., Bailin J., Radburn-Smith D. J., Holwerda B. W., 2017, *MNRAS*, **466**, 1491
- Hawkins M. R. S., 1984, *MNRAS*, **206**, 433

- Haynes M. P., Giovanelli R., 1984, *AJ*, **89**, 758
- Heesen V., Brinks E., Leroy A. K., Heald G., Braun R., Bigiel F., Beck R., 2014, *AJ*, **147**, 103
- Heesen V., Rau U., Rupen M. P., Brinks E., Hunter D. A., 2011, *ApJ*, **739**, L23
- Helmi A., 2008, *A&ARv*, **15**, 145
- Helmi A., Cooper A. P., White S. D. M., Cole S., Frenk C. S., Navarro J. F., 2011, *ApJ*, **733**, L7
- Helmi A., Veljanoski J., Breddels M. A., Tian H., Sales L. V., 2017, *A&A*, **598**, A58
- Helmi A., White S. D. M., de Zeeuw P. T., Zhao H., 1999, *Nature*, **402**, 53
- Hennebelle P., Audit E., 2007, *A&A*, **465**, 431
- Hennebelle P., Audit E., Miville-Deschênes M.-A., 2007, *A&A*, **465**, 445
- Hernitschek N. et al., 2016, *ApJ*, **817**, 73
- Hill V. et al., 2002, *A&A*, **387**, 560
- Hubble E. P., 1936, *ApJ*, **64**
- Hunter D. A., Elmegreen B. G., 2004, *AJ*, **128**, 2170
- Hunter D. A., Elmegreen B. G., 2006, *ApJS*, **162**, 49
- Hunter D. A., Elmegreen B. G., Oh S.-H., Anderson E., Nordgren T. E., Massey P., Wilsey N., Riabokin M., 2011, *AJ*, **142**, 121
- Hunter D. A., Elmegreen B. G., van Woerden H., 2001, *ApJ*, **556**, 773
- Hunter D. A. et al., 2012, *AJ*, **144**, 134
- Ibata R., Martin N. F., Irwin M., Chapman S., Ferguson A. M. N., Lewis G. F., McConnachie A. W., 2007, *ApJ*, **671**, 1591
- Iorio G., 2014, Master's thesis, Master Thesis, University of Bologna
- Iorio G., Belokurov V., Erkal D., Koposov S. E., Nipoti C., Fraternali F., 2017a, [ArXiv e-prints](#)
- Iorio G., Fraternali F., Nipoti C., Di Teodoro E., Read J. I., Battaglia G., 2017b, *MNRAS*, **466**, 4159
- Ishiyama T., 2014, *ApJ*, **788**, 27
- Ivezić Ž. et al., 2000, *AJ*, **120**, 963
- Jarrett T. H., Chester T., Cutri R., Schneider S. E., Huchra J. P., 2003, *AJ*, **125**, 525
- Jeans J. H., 1915, *MNRAS*, **76**, 70
- Johnson M., Hunter D. A., Oh S.-H., Zhang H.-X., Elmegreen B., Brinks E., Tollerud E., Herrmann K., 2012, *AJ*, **144**, 152
- Johnston K. V., 2016, in *IAU Symposium*, Vol. 317, The General Assembly of Galaxy Halos: Structure, Origin and Evolution, Bragaglia A., Arnaboldi M., Rejkuba M.,

- Romano D., eds., pp. 1–8
- Jordi C. et al., 2010, *A&A*, [523](#), [A48](#)
- Joung M. K. R., Mac Low M.-M., 2006, *ApJ*, [653](#), [1266](#)
- Józsa G. I. G., Kenn F., Klein U., Oosterloo T. A., 2007, *A&A*, [468](#), [731](#)
- Jurcsik J., Kovacs G., 1996, *A&A*, [312](#), [111](#)
- Jurić M. et al., 2008, *ApJ*, [673](#), [864](#)
- Kalberla P. M. W., Dedes L., Kerp J., Haud U., 2007, *A&A*, [469](#), [511](#)
- Kamada A., Kaplinghat M., Pace A. B., Yu H.-B., 2017, *Physical Review Letters*, [119](#), [111102](#)
- Kamphuis J. J., 1993, PhD thesis, PhD Thesis, University of Groningen, (1993)
- Kamphuis P., 2008, PhD thesis, University of Groningen
- Kamphuis P., Józsa G. I. G., Oh S.-. H., Spekkens K., Urbancic N., Serra P., Koribalski B. S., Dettmar R.-J., 2015, *MNRAS*, [452](#), [3139](#)
- Karachentsev I. D., Makarov D. I., Kaisina E. I., 2013, *AJ*, [145](#), [101](#)
- Karim M. T., Mamajek E. E., 2017, *MNRAS*, [465](#), [472](#)
- Keller B. W., Wadsley J. W., 2017, *ApJ*, [835](#), [L17](#)
- Kennicutt, Jr. R. C., 1998, *ApJ*, [498](#), [541](#)
- Kinman T. D., Wirtanen C. A., Janes K. A., 1966, *ApJS*, [13](#), [379](#)
- Kirby E. N., Bullock J. S., Boylan-Kolchin M., Kaplinghat M., Cohen J. G., 2014, *MNRAS*, [439](#), [1015](#)
- Klypin A., Kravtsov A. V., Valenzuela O., Prada F., 1999, *ApJ*, [522](#), [82](#)
- Klypin A. A., Trujillo-Gomez S., Primack J., 2011, *ApJ*, [740](#), [102](#)
- Knapen J. H., Erroz-Ferrer S., Roa J., Bakos J., Cisternas M., Leaman R., Szymanek N., 2014, *A&A*, [569](#), [A91](#)
- Koposov S. E., Belokurov V., Torrealba G., 2017, [ArXiv e-prints](#)
- Koposov S. E. et al., 2015, *ApJ*, [811](#), [62](#)
- Kormendy J., Bender R., 2012, *ApJS*, [198](#), [2](#)
- Kormendy J., Djorgovski S., 1989, *ARA&A*, [27](#), [235](#)
- Kormendy J., Freeman K. C., 2016, *ApJ*, [817](#), [84](#)
- Krajnović D., Cappellari M., de Zeeuw P. T., Copin Y., 2006, *MNRAS*, [366](#), [787](#)
- Kroupa P., 2001, *MNRAS*, [322](#), [231](#)
- Krumholz M. R., Burkhardt B., 2016, *MNRAS*, [458](#), [1671](#)
- Kuzio de Naray R., Kaufmann T., 2011, *MNRAS*, [414](#), [3617](#)
- Lacey C., Cole S., 1994, *MNRAS*, [271](#), [676](#)
- Laurikainen E., Salo H., Buta R., Knapen J. H., Comerón S., 2010, *MNRAS*, [405](#),

1089

- Leaman R. et al., 2012, *ApJ*, **750**, 33
- Lelli F., Fraternali F., Sancisi R., 2010, *A&A*, **516**, A11
- Lelli F., McGaugh S. S., Schombert J. M., 2016a, *AJ*, **152**, 157
- Lelli F., McGaugh S. S., Schombert J. M., 2016b, *ApJ*, **816**, L14
- Lelli F., McGaugh S. S., Schombert J. M., 2016c, *ApJ*, **816**, L14
- Lelli F., McGaugh S. S., Schombert J. M., 2017, *MNRAS*, **468**, L68
- Lelli F., McGaugh S. S., Schombert J. M., Pawlowski M. S., 2017, *ApJ*, **836**, 152
- Lelli F., Verheijen M., Fraternali F., 2014a, *A&A*, **566**, A71
- Lelli F., Verheijen M., Fraternali F., 2014b, *MNRAS*, **445**, 1694
- Lelli F., Verheijen M., Fraternali F., Sancisi R., 2012a, *A&A*, **537**, A72
- Lelli F., Verheijen M., Fraternali F., Sancisi R., 2012b, *A&A*, **544**, A145
- Lepage G. P., 1978, *J. Comput. Phys*, **27**, 192
- Letarte B., 2007, PhD thesis, University of Groningen
- Lindegren L., Lammers U., Hobbs D., O’Mullane W., Bastian U., Hernández J., 2012, *A&A*, **538**, A78
- Liu C. et al., 2017, *Research in Astronomy and Astrophysics*, **17**, 096
- López-Corredoira M., Molgó J., 2014, *A&A*, **567**, A106
- Mac Low M.-M., 1999, *ApJ*, **524**, 169
- Makarova L., 1999, *A&AS*, **139**, 491
- Marchuk A. A., Sotnikova N. Y., 2017, *MNRAS*, **465**, 4956
- Mateo M. L., 1998, *ARA&A*, **36**, 435
- Mateu C., Vivas A. K., Downes J. J., Briceño C., 2011, in *Revista Mexicana de Astronomía y Astrofísica Conference Series*, Vol. 40, *Revista Mexicana de Astronomía y Astrofísica Conference Series*, pp. 245–246
- Mayer L., Governato F., Colpi M., Moore B., Quinn T., Wadsley J., Stadel J., Lake G., 2001, *ApJ*, **547**, L123
- McConnachie A. W., 2012, *AJ*, **144**, 4
- McGaugh S. S., 2012, *AJ*, **143**, 40
- McGaugh S. S., Lelli F., Schombert J. M., 2016, *Physical Review Letters*, **117**, 201101
- McGaugh S. S., Schombert J. M., 2014, *AJ*, **148**, 77
- McGaugh S. S., Schombert J. M., Bothun G. D., de Blok W. J. G., 2000, *ApJ*, **533**, L99
- McMillan P. J., Binney J. J., 2010, *MNRAS*, **402**, 934

- Meidt S. E. et al., 2014, *ApJ*, [788](#), [144](#)
- Miceli A. et al., 2008, *ApJ*, [678](#), [865](#)
- Morganson E. et al., 2016, *ApJ*, [825](#), [140](#)
- Mouhcine M., Rich R. M., Ferguson H. C., Brown T. M., Smith T. E., 2005, *ApJ*, [633](#), [828](#)
- Muller C. A., Oort J. H., 1951, *Nature*, [168](#), [357](#)
- Navarro J. F., Benítez-Llambay A., Fattahi A., Frenk C. S., Ludlow A. D., Oman K. A., Schaller M., Theuns T., 2017, *MNRAS*, [471](#), [1841](#)
- Navarro J. F., Frenk C. S., White S. D. M., 1996, *ApJ*, [462](#), [563](#)
- Nelan J. E., Smith R. J., Hudson M. J., Wegner G. A., Lucey J. R., Moore S. A. W., Quinney S. J., Suntzeff N. B., 2005, *ApJ*, [632](#), [137](#)
- Newberg H. J., Willett B. A., Yanny B., Xu Y., 2010, *ApJ*, [711](#), [32](#)
- Newberg H. J. et al., 2002, *ApJ*, [569](#), [245](#)
- O'Brien J. C., Freeman K. C., van der Kruit P. C., 2010, *A&A*, [515](#), [A62](#)
- Odenkirchen M. et al., 2001, *ApJ*, [548](#), [L165](#)
- Oh S.-H., de Blok W. J. G., Walter F., Brinks E., Kennicutt, Jr. R. C., 2008, *AJ*, [136](#), [2761](#)
- Oh S.-H. et al., 2015, *AJ*, [149](#), [180](#)
- Olling R. P., 1995, *AJ*, [110](#), [591](#)
- Olling R. P., 1996, *AJ*, [112](#), [481](#)
- Oman K. A. et al., 2015, *MNRAS*, [452](#), [3650](#)
- Oman K. A., Navarro J. F., Sales L. V., Fattahi A., Frenk C. S., Sawala T., Schaller M., White S. D. M., 2016, *MNRAS*, [460](#), [3610](#)
- Palma C., Majewski S. R., Siegel M. H., Patterson R. J., Ostheimer J. C., Link R., 2003, *AJ*, [125](#), [1352](#)
- Papastergis E., Giovanelli R., Haynes M. P., Shankar F., 2015, *A&A*, [574](#), [A113](#)
- Park O.-K., Staveley-Smith L., Koribalski B., Kalnajs A., Freeman K. C., Malin D., 2001, in *Astronomical Society of the Pacific Conference Series*, Vol. 240, *Gas and Galaxy Evolution*, Hibbard J. E., Rupen M., van Gorkom J. H., eds., p. 863
- Pawlowski M. S., Pflamm-Altenburg J., Kroupa P., 2012, *MNRAS*, [423](#), [1109](#)
- Peebles P. J. E., 1982a, *ApJ*, [259](#), [442](#)
- Peebles P. J. E., 1982b, *ApJ*, [263](#), [L1](#)
- Peebles P. J. E., 1982c, *ApJ*, [258](#), [415](#)
- Pérez-Villegas A., Portail M., Gerhard O., 2017, *MNRAS*, [464](#), [L80](#)
- Peters S. P. C., van der Kruit P. C., Allen R. J., Freeman K. C., 2017, *MNRAS*, [464](#), [65](#)

- Pietrukowicz P. et al., 2015, *ApJ*, **811**, 113
- Pila-Díez B., de Jong J. T. A., Kuijken K., van der Burg R. F. J., Hoekstra H., 2015, *A&A*, **579**, A38
- Pillepich A., Madau P., Mayer L., 2015, *ApJ*, **799**, 184
- Pineda J. C. B., Hayward C. C., Springel V., Mendes de Oliveira C., 2017, *MNRAS*, **466**, 63
- Piontek R. A., Ostriker E. C., 2005, *ApJ*, **629**, 849
- Planck Collaboration et al., 2016a, *A&A*, **594**, A20
- Planck Collaboration et al., 2016b, *A&A*, **594**, A13
- Posti L., Binney J., Nipoti C., Ciotti L., 2015, *MNRAS*, **447**, 3060
- Puche D., Westpfahl D., Brinks E., Roy J.-R., 1992, *AJ*, **103**, 1841
- Purcell C. W., Bullock J. S., Kazantzidis S., 2010, *MNRAS*, **404**, 1711
- Querejeta M. et al., 2015, *A&A*, **579**, L2
- Read J. I., Agertz O., Collins M. L. M., 2016, *MNRAS*, **459**, 2573
- Read J. I., Iorio G., Agertz O., Fraternali F., 2016, *MNRAS*, **462**, 3628
- Read J. I., Iorio G., Agertz O., Fraternali F., 2017, *MNRAS*, **467**, 2019
- Read J. I., Wilkinson M. I., Evans N. W., Gilmore G., Kleyna J. T., 2006, *MNRAS*, **367**, 387
- Renzini A., 2006, *ARA&A*, **44**, 141
- Rizzo F., Fraternali F., Iorio G., 2017, [ArXiv e-prints](#)
- Roberts M. S., 1962, *AJ*, **67**, 431
- Roberts M. S., 1975, *Radio Observations of Neutral Hydrogen in Galaxies*, Sandage A., Sandage M., Kristian J., eds., the University of Chicago Press, p. 309
- Robin A. C., Marshall D. J., Schultheis M., Reylé C., 2012, *A&A*, **538**, A106
- Roderick T. A., Jerjen H., Mackey A. D., Da Costa G. S., 2015, *ApJ*, **804**, 134
- Roderick T. A., Mackey A. D., Jerjen H., Da Costa G. S., 2016, *MNRAS*, **461**, 3702
- Rogstad D. H., Lockhart I. A., Wright M. C. H., 1974, *ApJ*, **193**, 309
- Rogstad D. H., Shostak G. S., 1971, *A&A*, **13**, 99
- Roman N. G., 1955, *ApJS*, **2**, 195
- Romanowsky A. J., Fall S. M., 2012, *ApJS*, **203**, 17
- Roychowdhury S., Chengalur J. N., Begum A., Karachentsev I. D., 2010, *MNRAS*, **404**, L60
- Rubin V. C., Ford, Jr. W. K., Thonnard N., 1980, *ApJ*, **238**, 471
- Ryan S. G., Norris J. E., 1991, *AJ*, **101**, 1865
- Sacchi E. et al., 2016, *ApJ*, **830**, 3

- Saha A., 1984, *ApJ*, **283**, 580
- Sales L. V. et al., 2017, *MNRAS*, **464**, 2419
- Samland M., Gerhard O. E., 2003, *A&A*, **399**, 961
- Sancisi R., 2004, in *IAU Symposium*, Vol. 220, *Dark Matter in Galaxies*, Ryder S., Pisano D., Walker M., Freeman K., eds., p. 233
- Santos-Santos I. M., Di Cintio A., Brook C. B., Macciò A., Dutton A., Domínguez-Tenreiro R., 2018, *MNRAS*, **473**, 4392
- Scalo J., Elmegreen B. G., 2004, *ARA&A*, **42**, 275
- Schaye J., 2004, *ApJ*, **609**, 667
- Schlegel D. J., Finkbeiner D. P., Davis M., 1998, *ApJ*, **500**, 525
- Schoenmakers R. H. M., Franx M., de Zeeuw P. T., 1997, *MNRAS*, **292**, 349
- Schombert J., McGaugh S., 2014, *Publ. Astron. Soc. Australia*, **31**, e036
- Schönrich R., 2012, *MNRAS*, **427**, 274
- Schwarz G., 1978, *Annals of Statistics*, **6**, 461
- Searle L., Zinn R., 1978, *ApJ*, **225**, 357
- Sellwood J. A., Balbus S. A., 1999, *ApJ*, **511**, 660
- Sesar B. et al., 2014, *ApJ*, **793**, 135
- Sesar B. et al., 2017, *AJ*, **153**, 204
- Sesar B. et al., 2010, *ApJ*, **708**, 717
- Sesar B. et al., 2007, *AJ*, **134**, 2236
- Sesar B. et al., 2013, *AJ*, **146**, 21
- Sesar B., Jurić M., Ivezić Ž., 2011, *ApJ*, **731**, 4
- Shanks T., Boyle B. J., Croom S., Loaring N., Miller L., Smith R. J., 2000, in *Astronomical Society of the Pacific Conference Series*, Vol. 200, *Clustering at High Redshift*, Mazure A., Le Fèvre O., Le Brun V., eds., p. 57
- Shetrone M. D., Côté P., Sargent W. L. W., 2001, *ApJ*, **548**, 592
- Shostak G. S., 1974, *A&A*, **31**, 97
- Sicking F. J., 1997, PhD thesis, PhD Thesis, University of Groningen, (1997)
- Simion I. T., Belokurov V., Irwin M., Koposov S. E., 2014, *MNRAS*, **440**, 161
- Skrutskie M. F. et al., 2006, *AJ*, **131**, 1163
- Snedden C., McWilliam A., Preston G. W., Cowan J. J., Burris D. L., Armosky B. J., 1996, *ApJ*, **467**, 819
- Sollima A., Valls-Gabaud D., Martínez-Delgado D., Fliri J., Peñarrubia J., Hoekstra H., 2011, *ApJ*, **730**, L6
- Soszyński I. et al., 2014, *Acta Astron.*, **64**, 177

- Soszyński I. et al., 2016, *Acta Astron.*, [66](#), [131](#)
- Spekkens K., Sellwood J. A., 2007, *ApJ*, [664](#), [204](#)
- Spitzer L., 1978, *Physical processes in the interstellar medium*
- Starkenburg T. K., Helmi A., Sales L. V., 2016, *A&A*, [587](#), [A24](#)
- Stil J. M., Israel F. P., 2002a, *A&A*, [392](#), [473](#)
- Stil J. M., Israel F. P., 2002b, *A&A*, [389](#), [42](#)
- Stokes G. H., Evans J. B., Vighh H. E. M., Shelly F. C., Pearce E. C., 2000, *Icarus*, [148](#), [21](#)
- Swaters R. A., 1999, PhD thesis, , Rijksuniversiteit Groningen, (1999)
- Swaters R. A., Bershady M. A., Martinsson T. P. K., Westfall K. B., Andersen D. R., Verheijen M. A. W., 2014, *ApJ*, [797](#), [L28](#)
- Swaters R. A., Sancisi R., van der Hulst J. M., van Albada T. S., 2012, *MNRAS*, [425](#), [2299](#)
- Swaters R. A., Schoenmakers R. H. M., Sancisi R., van Albada T. S., 1999, *MNRAS*, [304](#), [330](#)
- Tacconi L. J., Young J. S., 1987, *ApJ*, [322](#), [681](#)
- Tamburro D., Rix H.-W., Leroy A. K., Mac Low M.-M., Walter F., Kennicutt R. C., Brinks E., de Blok W. J. G., 2009, *AJ*, [137](#), [4424](#)
- Tassoul J., 1980, *Mercury*, [9](#), [21](#)
- Taylor C. L., Kobulnicky H. A., Skillman E. D., 1998, *AJ*, [116](#), [2746](#)
- Tenorio-Tagle G., Rozyczka M., Franco J., Bodenheimer P., 1991, *MNRAS*, [251](#), [318](#)
- Tissera P. B., Scannapieco C., Beers T. C., Carollo D., 2013, *MNRAS*, [432](#), [3391](#)
- Tolstoy E. et al., 2006, *The Messenger*, [123](#)
- Tolstoy E., Venn K. A., Shetrone M., Primas F., Hill V., Kaufer A., Szeifert T., 2003, *AJ*, [125](#), [707](#)
- Torrealba G. et al., 2015, *MNRAS*, [446](#), [2251](#)
- Tremonti C. A. et al., 2004, *ApJ*, [613](#), [898](#)
- Tully R. B., 1988, *Nearby Galaxies Catalog*. Cambridge: Cambridge University Press
- Tully R. B., Bottinelli L., Fisher J. R., Gougenheim L., Sancisi R., van Woerden H., 1978, *A&A*, [63](#), [37](#)
- Tully R. B., Fisher J. R., 1977, *A&A*, [54](#), [661](#)
- van Albada T. S., Bahcall J. N., Begeman K., Sancisi R., 1985, *ApJ*, [295](#), [305](#)
- van de Hulst H. C., 1945, *Ned. Tijdschr. Natuurkd.*, [11](#), [210](#)
- van de Hulst H. C., Raimond E., van Woerden H., 1957, *Bull. Astron. Inst. Netherlands*, [14](#), [1](#)

- van der Hulst J. M., Terlouw J. P., Begeman K. G., Zwitter W., Roelfsema P. R., 1992, in *Astronomical Society of the Pacific Conference Series*, Vol. 25, *Astronomical Data Analysis Software and Systems I*, Worrall D. M., Biemesderfer C., Barnes J., eds., p. 131
- van der Kruit P. C., 1981, *A&A*, [99](#), [298](#)
- van Eymeren J., Marcelin M., Koribalski B., Dettmar R.-J., Bomans D. J., Gach J.-L., Balard P., 2009, *A&A*, [493](#), [511](#)
- van Leeuwen F. et al., 2016, [ArXiv e-prints](#)
- Venn K. A., Irwin M., Shetrone M. D., Tout C. A., Hill V., Tolstoy E., 2004, *AJ*, [128](#), [1177](#)
- Verheijen M. A. W., 2001, *ApJ*, [563](#), [694](#)
- Verheijen M. A. W., Sancisi R., 2001, *A&A*, [370](#), [765](#)
- Vivas A. K., Zinn R., 2006, *AJ*, [132](#), [714](#)
- Vivas A. K. et al., 2004, *AJ*, [127](#), [1158](#)
- Vivas A. K. et al., 2001, *ApJ*, [554](#), [L33](#)
- Vivas A. K., Zinn R., Farmer J., Duffau S., Ping Y., 2016, *ApJ*, [831](#), [165](#)
- Volders L. M. J. S., Högbom J. A., 1961, *Bull. Astron. Inst. Netherlands*, [15](#), [307](#)
- Wada K., Meurer G., Norman C. A., 2002, *ApJ*, [577](#), [197](#)
- Walker M. G., Mateo M., Olszewski E. W., Peñarrubia J., Wyn Evans N., Gilmore G., 2009, *ApJ*, [704](#), [1274](#)
- Walter F., Brinks E., 2001, *AJ*, [121](#), [3026](#)
- Watkins L. L. et al., 2009, *MNRAS*, [398](#), [1757](#)
- Watson W. D., Deguchi S., 1984, *ApJ*, [281](#), [L5](#)
- Weisz D. R. et al., 2011, *ApJ*, [743](#), [8](#)
- Wetterer C. J., McGraw J. T., 1996, *AJ*, [112](#), [1046](#)
- White S. D. M., Rees M. J., 1978, *MNRAS*, [183](#), [341](#)
- Whiting M. T., 2012, *MNRAS*, [421](#), [3242](#)
- Willett K. W. et al., 2017, *MNRAS*, [464](#), [4176](#)
- Williams M. J., Bureau M., Cappellari M., 2010, *MNRAS*, [409](#), [1330](#)
- Willman B. et al., 2005, *ApJ*, [626](#), [L85](#)
- Wolfire M. G., Hollenbach D., McKee C. F., Tielens A. G. G. M., Bakes E. L. O., 1995, *ApJ*, [443](#), [152](#)
- Wolfire M. G., McKee C. F., Hollenbach D., Tielens A. G. G. M., 2003, *ApJ*, [587](#), [278](#)
- Xu Y. et al., 2018, *MNRAS*, [473](#), [1244](#)
- Xue X.-X., Rix H.-W., Ma Z., Morrison H., Bovy J., Sesar B., Janesh W., 2015,

- ApJ, [809](#), [144](#)
- Yanny B. et al., 2003, ApJ, [588](#), [824](#)
- Yanny B. et al., 2009, AJ, [137](#), [4377](#)
- Zhang H.-X., Hunter D. A., Elmegreen B. G., Gao Y., Schrubba A., 2012, AJ, [143](#), [47](#)
- Zibetti S., Ferguson A. M. N., 2004, MNRAS, [352](#), [L6](#)
- Zibetti S., White S. D. M., Brinkmann J., 2004, MNRAS, [347](#), [556](#)
- Zinn R., 1985, ApJ, [293](#), [424](#)
- Zolotov A., Willman B., Brooks A. M., Governato F., Brook C. B., Hogg D. W., Quinn T., Stinson G., 2009, ApJ, [702](#), [1058](#)
- Zschaechner L. K., Rand R. J., Heald G. H., Gentile G., Kamphuis P., 2011, ApJ, [740](#), [35](#)